Project #: YXM 0114

Investigating the Effects of Sensor Mass, Applied Heat, and Applied Pressure on Motion Artifact in Photoplethysmography within a Military Transport Environment

A Major Qualifying Project
submitted to the Faculty
of the
WORCESTER POLYTECHNIC INSTITUTE
in partial fulfillment of the requirements for the
Degree of Bachelor of Science
by

Corinne D. Nawn
Date: May 1, 2014

Professor Yitzhak Mendelson, Major Advisor

Table of Contents

Authorship 4

Abstract 5

Acknowledgements 6

Table of Figures 7

Table of Tables 9

Abbreviations 10

1. Introduction 11

2. Background 12

2.1. Photoplethysmography 12

2.2. Applications of Pulse Oximetry 13

2.3. Applications of Photoplethysmography 14

2.4. Modes of Pulse Oximetry 15

2.5. Limitations of Pulse Oximetry 15

2.6. Strategies for Reducing Motion Artifact 17

2.7. Current Devices for Reducing Motion Artifact 19

2.7.1. COTS Devices 19

2.7.2. Custom Devices 20

2.7.3. Investigated Variables 25

3. Design Approach 28

3.1. Purpose 28

3.2. Initial Client Statement 28

3.3. Design Parameters 29

3.3.1. Objectives 29

3.3.2. Constraints 30
3.4. Revised Client Statement 32
3.5. Design Alternatives 32
3.5.1. Bare Sensor 32
3.5.2. Sensor Weight 32
3.5.3. Applied Heat 33
3.5.5. Applied Pressure 35
3.5.6. Experimental Design 36
4. Methods 39
4.1. Final Prototype Design 39
4.1.1. Bare Sensor 39
4.1.2. Sensor Weight 40
4.1.3. Applied Heat 40
4.1.4. Applied Pressure 41
4.2. Experimental Design 42
4.3. Data Acquisition 43
4.4. Data Analysis 44
4.4.1. HR and SpO_2 Analysis 44
4.4.2. PPG Waveform Analysis 45
5. Results 46
5.1. Sensor Weight 48
5.2. Applied Heat 50
5.3. Applied Pressure 52
6. Discussion 55
6.1. Sensor Weight 55

6.2. Applied Heat 56
6.3. Applied Pressure 57
7. Conclusions 59
8. Recommendations 61
References 62
Appendix A: HR Bland-Altman Plots 65
Appendix B: SpO_2 Bland-Altman Plots 73
Appendix C: Sensor Weight HR Box Plots 81
Appendix D: Sensor Weight SpO_2 Box Plots 89
Appendix E: Applied Heat HR Box Plots 97
Appendix F: Applied Heat SpO_2 Box Plots 105
Appendix G: Applied Pressure HR Box Plots 113
Appendix H: Applied Pressure SpO_2 Box Plots 121
Appendix I: Sensor Weight Frequency Spectra 130
Appendix J: Applied Heat Frequency Spectra 137
Appendix K: Applied Pressure Frequency Spectra 144

Authorship

All sections were authored by Corinne Nawn and edited by Professor Mendelson.

Abstract

Despite the wide use of pulse oximetry as a clinical monitoring device for non-invasive measurement of hemoglobin oxygen saturation and heart rate, reports have shown its high sensitivity to motion artifact, rendering the device less accurate and reliable during field applications such as in military environments or ambulatory transport. This paper investigates the effects of sensor weight, localized heating and locally applied pressure on measurement accuracy of a prototype forehead pulse oximeter during a simulated military transport environment. The results yielded that increased sensor weight led to measurement errors and more severe signal corruption, while increased heat (up to 42^{o}C) and pressure (up to 60mmHg) decreased errors and improved signal fidelity.

Acknowledgements

I would like to thank the following people for their contributions to this project's success:

Professor Mendelson, for his consistent attention, insightful guidance and constructive criticism throughout the project.

Kristen M. Warren for providing assistance with the physical prototyping and testing

The 15 subjects who volunteered their time to participate in this study

Dr. Reed Hoyt, Dr. Nisha Charkoudian and my other colleagues at the US Army Research Institute of Environmental for their feedback and for the original inspiration for this project.

Lisa Wall for her technical support with laboratory equipment.

Table of Figures

Figure 1: Optical Absorption Spectra of HbO_2 and Hb 12
Figure 2: Optical Absorption of blood, skin, tissue and bone 13
Figure 3: Transmission Mode Pulse Oximetry 15
Figure 4: Reflectance Mode Pulse Oximetry [3] 15
Figure 5: Capillary Diagram with Arteriovenous Anastomoses 16
Figure 6: (a) Typical backscatter of reflectance configuration (b) Backscatter after sensor shift 17
Figure 7: Adaptive Noise Cancellation 18
Figure 8: Block Diagram of Additive Active Noise Cancellation Filter 21
Figure 9: Block Diagram of Logarithmic Active Noise Cancellation Filter 21
Figure 10: Diagram of IN-MONIT Sensing Component 22
Figure 11: Wireless Forehead Pulse Oximeter developed by Mendelson, Dao and Chon 23
Figure 12: Heated Pulse Oximeter Sensor developed by Mendelson and McGinn 24
Figure 13: Objectives Tree 29
Figure 14: Minco Thermofoil Heater 1" round, 37.4 ohms 33
Figure 15: Minco Thermofoil Heater, 1"x4" rectangle, 28.4 ohms 33
Figure 16: Schematic of Temperature Control Circuit 34
Figure 17: Applied Pressure Prototype (A) LEDs (B) Photodetector (C) Pressure Transducer ... 35
Figure 18: FlexiForce A401 with 1" sensing area (left) and Interlink FSR402 with 0.5" sensing area (right) 35
Figure 19: MPX5050GP Pressure Transducer (right) and Pin Out (left) 36
Figure 20: Sensor Mass Experiment Set-up (A) Prototype Pulse Oximeter (B) Masimo Tabletop Pulse Oximeter Monitor (C) Handheld Masimo Radical-57 Monitor (D) Finger Probe reference pulse oximeter (E) Serial cable (F) National Instruments DAQ 37
Figure 21: Bare Sensor with LEDs (A), photodetector (B) and adhesive wings (C) 39
Figure 22: Prototype position on forehead 39
Figure 23: Applied Heat Prototype 40
Figure 24: Temperature Control Circuit on Perfboard in Plastic Black Box 40
Figure 25: Temperature Control and Pressure Sensing Circuit Schematic (red box denotes pressure sensing amplification circuit) 41
Figure 26: Pressure Sensing Circuit, Air Displacement Bulb, and Silicon Tubing 42

Figure 27: Example of Experimental Set-up 43
Figure 28: Flow Chart of Data Analysis for HR and SpO_2 Normalized Error Calculation..... 46
Figure 29: Example Bland-Altman Plots of HR (left) and SpO_2 (right) measurements during rest (Subject C11) 47
Figure 30: Example Box Plots of normalized HR (left) and SpO_2 (right) error during random motion (Subject M2) with mean (blue text) and median (red text) numbers displayed above each data set. 48
Figure 31: Bar Graph Comparing Mean Normalized HR and SpO_2 Errors..... 48
Figure 32: Example Frequency Spectra Corresponding for different Sensor Weights (Subject L14)..... 49
Figure 33: Example Box Plots of Normalized HR (left) and SpO_2 (right) errors during Random Motion..... 50
Figure 34: Mean Error of Prototype Measurements versus Applied Heat..... 51
Figure 35: Example Frequency Spectrum for Applied Heat Data Set (Subject L14)..... 52
Figure 36: Example Box Plot for Applied Pressure Data Set during Random Motion (Subject K) 52
Figure 37: Mean Error of Prototype Sensor Measurements versus Applied Pressure..... 53
Figure 38: Example Frequency Spectra Comparing Applied Pressures (Subject L14)..... 53

Table of Tables

Table 1: Pairwise Comparison Chart 29
Table 2: Average P_w Values for each weight level versus the bare sensor 50
Table 3 Average P_p values for Applied Pressure versus 0mmHg 54

Abbreviations

AC: Alternating Current (Time-Variant Component of a signal)

ACC: Accelerometer

ANC: Adaptive Noise Cancellation

bpm: beats per minute

^{o}C: degrees Celsius (unit of temperature)

COTS: Commercial-off-the-Shelf

DC: Direct Current (Time-Invariant Component of a signal)

FSR: Force Sensitive Resistor

g: grams (units of mass)

Hb: Reduced Hemoglobin

HbO_2: Oxyhemoglobin

HR: Heart Rate

IR: Infrared

IRB: Institutional Review Board

LBNP: Lower Body Negative Pressure

LED: Light Emitting Diode

LMS: Least Mean Squares

MEMS: Microelectromechanical Systems

mmHg: Millimeters Mercury (units of pressure)

OEM: Original Equipment Manufacturer

PD: Photodetector

PPG: Photoplethysmogram

R: Red

RLS: Recursive Least Squares

SET®: Signal Extraction Technology

SNR: Signal-to-Noise Ratio

SpO_2: Oxygen Saturation

USARIEM: United States Army Research Institute of Environmental Medicine

1. Introduction

Photoplethysmography (PPG) measures the volumetric changes in arteries during the cardiac cycle. Pulse Oximetry uses this optical measurement to calculate the hemoglobin oxygen saturation (SpO_2) and stands as the most widely used non-invasive, clinical method for blood-oxygen analysis. In addition to arterial oxygen saturation, the PPG waveform yields information about the patient's heart rate. Recently, studies have also correlated the morphological characteristics of the PPG waveform to early indicators of hypovolemia, or the loss of central blood pressure [1]. The discovery of this relationship opens up PPG sensors as a potential tool for triage in cases with severe hemorrhaging, stimulating interest from the military to potentially equip foot soldiers with these PPG sensors. Despite the beneficial potential as a monitoring device for soldiers, the optical configuration of the sensor and the principles behind the calculations cause the resulting PPG signal to be highly sensitive to corruption due to subject motion, otherwise known as "motion artifact"[2]. Consequently, the data gathered by the sensor often yields inaccurate or impractical analysis of the patient's condition rendering it unreliable.

In order to design a device for military applications, the true sources of motion artifact must be investigated with regards to the sensor/skin interface itself as well as within a military transport environment, given the sensor's potential application as a wearable military device. By identifying the elementary causes of motion artifact during simulated military transport, we hope to develop a wearable pulse oximeter sensor that can minimize interferences. Therefore, this study aimed to investigate how sensor weight, locally applied heat, and locally applied pressure may affect the quality of the PPG waveform and accuracy of determining SpO_2 and HR. To explore these variables, a prototype sensor was designed to isolate and investigate the effects of each respective variable during random motion while collecting HR, SpO_2 and the PPG waveform from the prototype device. Since the inspiration for this study came from using pulse oximetry as a physiological monitoring device in a military application, the exploration of motion artifact during "random motion" aimed to simulate a military transport environment in hopes to expose new information on the impacts of motion artifact within a non-uniform setting. The gathered results and study conclusions aim to suggest optimal specifications for the future design of an effective, motion-tolerant pulse oximeter for a battlefield environment.

2. Background

2.1. Photoplethysmography

Photoplethysmography (PPG) stands as the most widely used clinical method for non-invasive measurement arterial hemoglobin oxygen saturation (SpO_2), also called pulse oximetry. Photoplethysmography revolves around the fundamental concept of measuring relative light absorption in the blood. The measurement of light absorption in a solution can be determined by the Beer-Lambert Law:

$$I_t = I_0 * 10^{-\varepsilon c d} \quad (1)$$

I_t is the intensity of the transmitted light, I_o is the intensity of the incident light, ε is the extinction coefficient of the sample, c is the concentration of the sample, and d represents the light path length through the sample [3]. Since oxygenated hemoglobin (HbO_2) and deoxygenated hemoglobin (Hb) have different absorption characteristics (Figure 1), the amount of oxygen in the blood can be determined by the difference in light absorption between two wavelengths of light. For examining blood as a homogenous mixture of Hb and HbO_2, the near-IR (940nm) and red (660nm) light spectrum display the greatest difference in absorption between Hb and HbO_2.

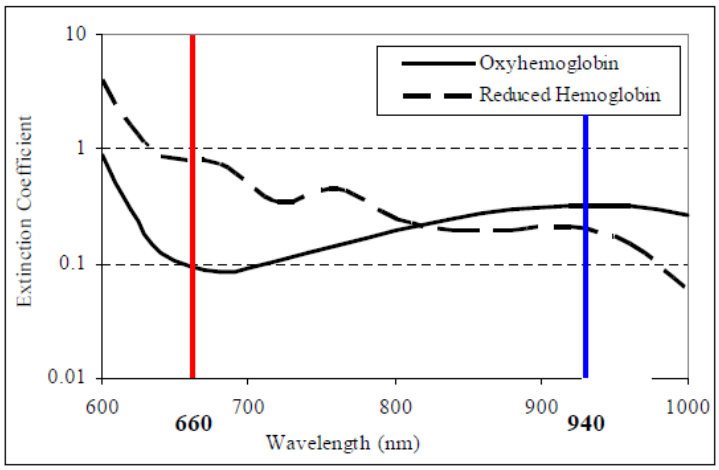

Figure 1: Optical Absorption Spectra of HbO_2 and Hb

Utilizing these principles, pulse oximetry measures oxygen content by illuminating a region of tissue with red and infrared light emitting diodes (LED) and comparing the amount of each wavelength absorbed based upon the light captured by a photodetector (PD). SpO_2 can be calculated using the relationship:

$$SpO_2 = A - B[I_r(red)/I_r(infrared)] \quad (2)$$

A and *B* are constants determined empirically through in vivo studies to establish an appropriate calibration for an average, healthy individual [3].

Aside the arterial blood being measured, various additional physiological features such as skin, venous blood, tissue and bone contribute to the absorption of the projected light. Consequently, the resulting waveform is composed of a time variant (AC) and time invariant (DC) portion (Figure 2).

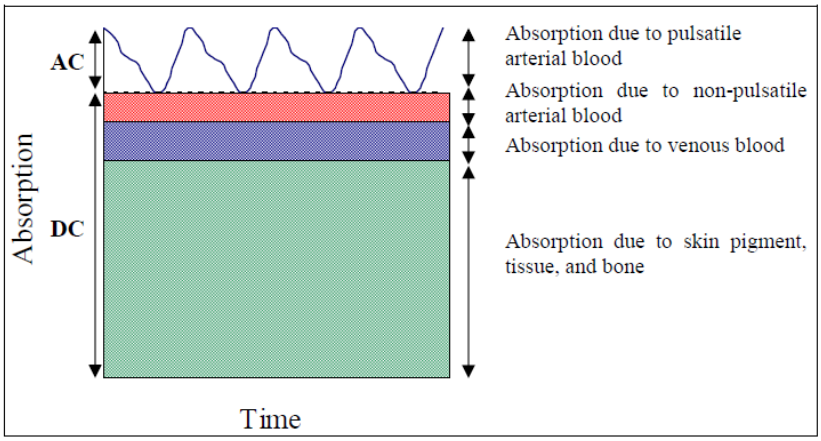

Figure 2: Optical Absorption of blood, skin, tissue and bone

The DC component involves the non-pulsatile arterial blood, venous blood, skin, tissue and bone while the AC component is solely composed of the pulsatile arterial blood. The AC component represents the familiar waveform that is typically examined for insight into the patient's cardiac state. Closely resembling an inverted blood pressure waveform, the rapid increase correlates to the increased blood volume present in the arteries during systole, while the downslope represents the draining of the blood from the arteries during diastole [4].

2.2. Applications of Pulse Oximetry

Much advancement in early pulse oximetry came about during World War II as a rapid and non-invasive way to monitor pilots' oxygen content, as they were in danger of hypoxic conditions. Clinically, pulse oximeters were also initially developed as an optical way to monitor patients' oxygenation during anesthesia to safeguard against post-surgery brain damage due to hypoxia [2]. In modern day, pulse oximeters are still widely used in clinical settings to monitor patients' heart rates and SpO_2, particularly during anesthesia, surgery, critical care, and infant care. Additionally, a desire exists for reliable pulse oximeters during critical care and transport settings where patients are most likely subject to vibrations from vehicular motion or motion from their own personal distress. In these situations, clinicians tend to abandon pulse

oximetry and completely remove the device due to inaccurate readings or false alarms [5]. More recently, pulse oximetry has been suggested as a home monitor for sudden infant death syndrome (SIDS) or apnea in the elderly. Despite the usefulness of "at home" or "continuous" monitoring, frequent false alarms caused by motion and physiological changes limit the use of pulse oximetry in non-clinical settings [2]. The Biophysics and Biomedical Modeling Division of the U.S. Army Research Institute for Environmental Medicine has also expressed an interest in pulse oximeters for war fighters stationed at altitude in order to monitor their oxygenation status. Thus, a need exists for an accurate, motion tolerant device to enable continuous and remote monitoring in the scenarios where blood oxygen saturation could provide vital insight.

2.3. Applications of Photoplethysmography

As detailed previously, Photoplethysmography (PPG) has primarily been applied to pulse oximetry; however, recent research suggests that the fluctuations and morphology of PPG waveform itself could also hold valuable insight into a patient's cardiac condition. Examining cases of severe trauma, such as hemorrhaging, standard ambulatory devices have proved insufficient in detecting precursory signs of hypovolemia [1]. Despite this shortcoming, hemorrhaging has been stated as the leading cause of death in both civilian and military trauma, making earlier detection of hypovolemia a crucial investigation for ambulatory treatment [6]. Studies exposing humans to lower body negative pressure (LBNP) have been conducted to simulate the onset of central hypovolemia and have found that elements of the time-domain PPG morphology can provide early indication of potential cardiac collapse [1]. Specifically, changes in PPG waveform characteristics, such as pulse amplitude, pulse width, and the area under the pulse curve, have strongly correlated to reduction in stroke volume and thereby serve as early indicators of blood loss [6]. To apply the research for practical use, advanced machine learning algorithms have recently been developed to evaluate these pulse characteristics and detect decompensating central blood pressure as a result of hemorrhaging [7]. Despite these advances, these algorithms rely on a clean PPG waveform in order to properly diagnose the patient who will most likely be a soldier on the battlefield or a victim in transport. As detailed later, these environments present many challenges that would greatly interfere with the fidelity of the PPG signal captured and prevent the true morphology of the waveform to be detected.

2.4. Modes of Pulse Oximetry

Traditionally, PPG sensors are configured in a transmission mode, where the LEDs and photodetector are positioned on opposite sides of the tissue (Figure 3). For this arrangement, the LEDs project light through the tissue and the photodetector collects the amount of light transmitted through the media. Since this configuration requires illumination to pass through the tissue, only certain sites of the body can be monitored with transmission mode, such as fingertips, earlobes, or hands and feet in infants.

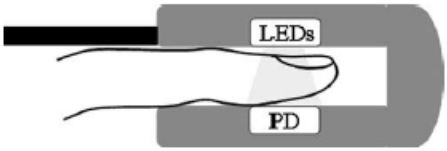

Figure 3: Transmission Mode Pulse Oximetry

To overcome the limited nature of the transmission mode, investigation into applying the same optical principles with skin reflectance began in 1949 by Brinkman and Zijlstra [8]. By using this skin reflectance spectrophotometry, the LEDs and photodetectors were placed on the same side of the media, with the (Figure 4) LEDs projecting light into the tissue and the photodetector capturing the reflected (backscattered) light intensity. Compared to transmission mode, reflectance mode enables a wider variety of body locations to be monitored, such as the forehead, chest, or limbs [2]. On the other hand, early reflectance oximeters encountered many difficulties with accuracy and calibration. While major advancements have been made in reflectance pulse oximetry, a sensor that can perform reliably on any location of the skin is not yet available [8]. For the purposes of this study, the focus will remain on reflectance mode in order to investigate alternate bodily locations.

Figure 4: Reflectance Mode Pulse Oximetry [3]

2.5. Limitations of Pulse Oximetry

Due to the fragility of both transmission and reflectance mode, pulse oximeters are highly susceptible to corruption from various sources. Internally, low peripheral vascular perfusion, such as in hypotension or vasoconstriction, can result in a poor signal since the measurements depend on the detection of a sufficiently strong arterial pulsation [2]. Additionally, the extraction

of the PPG signal relies on the assumption that the arterial blood is the only variable component in the underlying media, consisting of skin, tissue, bone and blood, any alteration of the time variant (AC) and time invariant (DC) components will compromise the accuracy and reliability of the measurements. Low peripheral vascular perfusion, such as in hypotension or vasoconstriction, yields a weaker pulsatile blood flow in peripheral regions, which ultimately results in a weaker PPG signal [2].

Additionally, the detection of a PPG signal relies on the assumption that the arterial blood is the only variable component in the underlying tissue. While skin pigment, tissue and bone are motionless, venous blood still actively circulates as a part of the cardiac cycle. Some studies have cited "venous pulsations" as contributing factors to corrupted PPG signals; however, the fundamental properties of the vascular system do not explain pulsatile blood in the veins. The elasticity of the arteries acts similar to a hydraulic filter: the compliant walls control the pulsatile blood flow generated by the "intermittent pump" of the heart, thereby evening out to a steady venous flow. Despite this physiological regulation, studies have still identified pulsations in venous blood [9]. While the phenomenon did not greatly affect the calculation of heart rate, the calculated SpO_2 levels measured much lower than the correct, invasive SaO_2 measurements. These instances of pulsation result from influences such as applied pressure or constriction that shunt arterial blood through arteriovenous anastomoses (Figure 5), small connecting channels between arteries and veins, thereby creating the illusion of pulsating venous blood [9]. Since venous blood contains significantly lower oxygen content than arterial blood, the pulsations include the venous blood in the SpO_2 calculations and result in a false low SpO_2 reading.

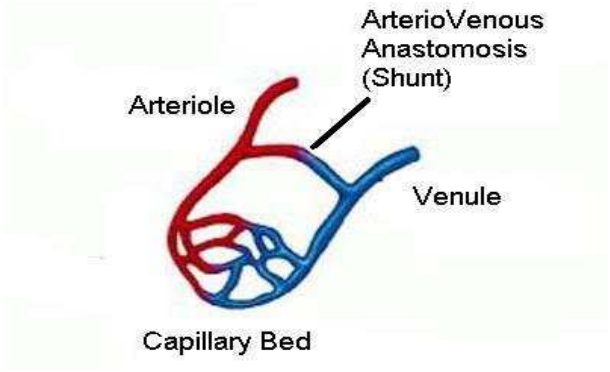

Figure 5: Capillary Diagram with Arteriovenous Anastomoses

Speculations have also hypothesized that motion artifact can stem from minute changes in sensor position relative to the skin [2], predominantly in reflectance-mode pulse oximetry. As shown in Figure 6, minor shifts in sensor position could severely alter the amount of backscattered light that reaches the photodetector [10]. Few studies have directly targeted the consequences of the relative motion present at the sensor/skin boundary. Therefore, the present study aims to closely examine this relationship within the context of variable sensor mass.

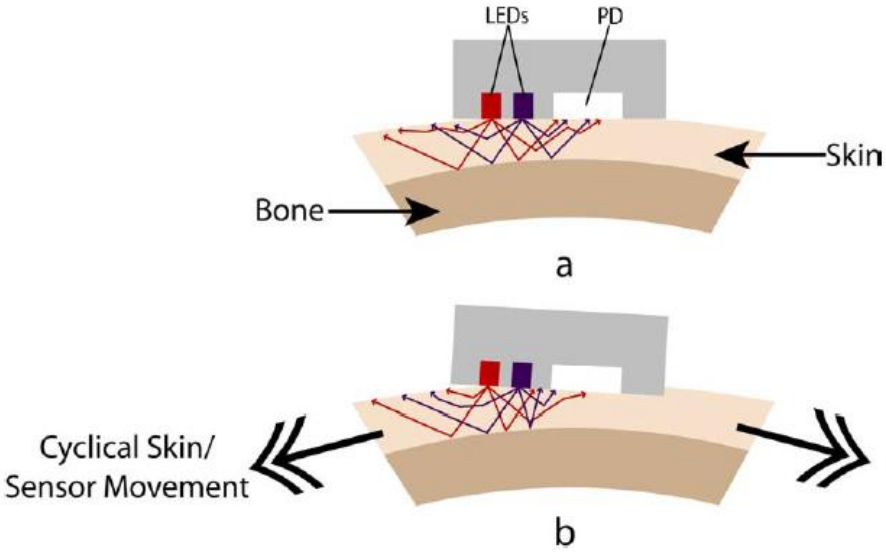

Figure 6: (a) Typical backscatter of reflectance configuration (b) Backscatter after sensor shift

2.6. Strategies for Reducing Motion Artifact

Since the advent of pulse oximeters, many research efforts have investigated ways to enhance the signal quality by reducing the effects of motion artifact and compensating for the limitations mentioned above. Although some of these methods have led to improvements in the accuracy of measurements, they often salvage just enough from the corrupted signal to be able to determine SpO_2 and heart rate at best. Given the recent developments that attribute additional details about a patient's cardiac state to the PPG waveform [7], preserving the morphology of the signal has become an equally important objective as well.

One of the most common approaches to recover physiological measurements is signal processing. Numerous algorithms have been developed that attempt to reduce the noise or separate the arterial pulsation signal from the noise signal through various filtering or digital signal processing techniques [11]. Some utilize solely mathematical principles, while others

utilize adaptive filtering techniques, such as Adaptive Noise Cancellation (ANC), to factor out the noise from the true signal. ANC assumes that the captured signal (Signal Source) is composed of the true signal (s) plus the motion artifact (n_o). A second signal (Noise Source) is captured and assumed to correlate to the noise of the signal (n_1) without correlating to the true signal. The Adaptive Noise Canceller (Figure 7) uses the information from the Noise Source to adjust the filter coefficients and cancel out the noise from the signal source (n_o) [11].

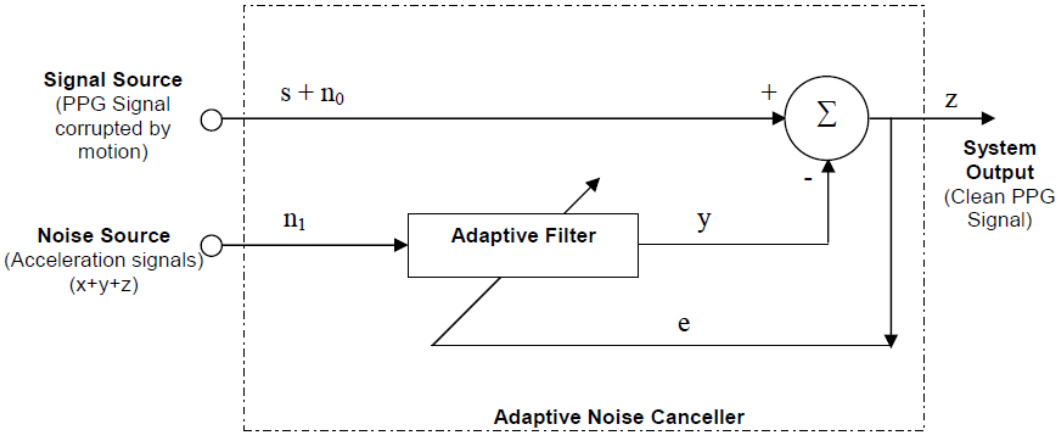

Figure 7: Adaptive Noise Cancellation

Another approach to minimizing motion artifact involves attempting to capture the PPG signal from atypical locations on the body, leading to prototypes investigating areas such as the inner ear, chest, forearm, calf and forehead [10, 13]. However, different bodily locations, such as the chest and limbs, can have lower blood perfusion and therefore are more greatly subject to motion artifact. To combat this limitation, studies have investigated localized heating techniques and have found the approach relatively successful at increasing vasodilation in the targeted tissue area [13]. Increasing the volume of the blood vessels aims to increase the strength of the reflected signal and plays into another method of improving the PPG signal: increasing the signal-to-noise ratio (SNR). SNR is defined as:

$$SNR = \frac{P_{signal}}{P_{noise}} = \left(\frac{A_{signal}}{A_{noise}}\right)^2 \quad (3)$$

where, P is the power and A is the amplitude of the signal. Research has shown that by capturing a signal containing a stronger signal element (PPG in this case) than noise element, the true component will be more easily extracted [10]. Therefore, increasing the power or amplitude of the true signal or decreasing the power or amplitude of the noise will result in a higher SNR.

While some devices and strategies have posed more promise than others, none have been able to successfully yield a clean PPG waveform from a moving patient. The following section comprises a more detailed analysis of the current products and methods aimed at reducing motion artifact in pulse oximetry.

2.7.Current Devices for Reducing Motion Artifact

2.7.1. COTS Devices

Various Commercial-off-the-shelf (COTS) pulse oximeters exist that claim to reduce motion artifact.

2.7.1.1. Nonin

Deriving their company name from "Noninvasive", Nonin advertises themselves as "Leaders in Noninvasive Medical Monitoring" and specializes in oximeters for various medical uses. Targeting clinical settings, the majority of Nonin's sensors are designed for location on the finger. In particular, the Onyx II 9550 wireless finger pulse oximeters has received US Army and US Military Airworthiness Certifications for use in helicopters. The PalmSAT 2500 series handheld pulse oximeters has also received this certification and has options of attachable ear, finger or forehead probes and. For both devices, no results or details were published regarding the devices' performances in the tests. Alongside fully developed pulse oximeters, Nonin also sells their probes as OEM solutions.

To combat motion artifact or other noise inducing factors, Nonin implements their PureLight® sensors and PureSAT® Technology. The PureLight® sensors use LEDs that produce a high-intensity, pure light spectrum, which claim to reduce variability in readings between patients or sensors. The PureSAT® Technology encompasses Nonin's software approach to de-noising the PPG signal, claiming "intelligent pulse-by-pulse filtering" to achieve a precise measurement even during limiting conditions such as motion or low perfusion. Due to proprietary reasons, more details on the underlying principles for both the PureLight® sensors and PureSAT® algorithms are not publically available. While Nonin sensors have reduced motion artifact to some extent, their only reflectance-based sensor involves a forehead probe that plugs into the PalmSAT 2500 handheld device. Despite the PalmSAT's US Military Airworthiness Certification, the wired forehead probe would not assimilate smoothly into war fighter's uniforms for a battlefield casualty scenario. Furthermore, with the current focus on the

quality of the PPG waveform, the performance of the forehead probe in these regards is unknown. Lastly, the Nonin devices physically interfere with a patient's daily functioning too much for long term, continuous monitoring.

2.7.1.2. Masimo

Masimo is another leader in pulse oximeters implementing signal reduction technology. Aside oxygen content, Masimo also targets other gases in the blood to monitor firefighters for signs such as CO content. The sensor probes are designed for transmission mode at locations such as the ear, fingers, or infant feet; so, the sensors themselves are thin, flexible and adhesive for wrapping around the area then plug into a remote processing media. Alongside the securely fastened sensors, Masimo counters motion artifact through their Signal Extraction Technology (SET). Masimo SET uses patented adaptive filtering techniques by applying DST®, SST™, FST™ and MST™ in parallel processing with conventional R/IR pulse oximetry calculation.

Similarly to the Nonin sensors, the Masimo sensors are physically intrusive and the only reflectance-based sensor is a wired probe for the forehead. Unlike Nonin's handheld interface, Masimo's forehead probe plugs into a much larger processing device, making it less conducive for a battlefield environment. On the other hand, this processing unit displays the captured and filtered PPG waveform, but therefore reveals that the waveform becomes greatly corrupted even with slight motion.

2.7.2. Custom Devices

In an attempt to pursue continuous pulse oximetry monitoring of patients, either clinically or in a battlefield setting, many studies have been performed to assess the feasibility and success of pulse oximeters at non-intrusive locations on the body.

2.7.2.1. Ring Sensor

Since most people would be receptive to wearing a ring for an extended period of time, Haruhiko H. Asada developed a pulse oximeter designed in the form of a ring to facilitate continuous patient monitoring. Due to the location at the base of the finger, the device could implement both reflectance and transmittal configurations of the LEDs and PDs; but, chose transmittal mode since reflectance mode proved more susceptible to corruption due to motion [14]. Another design consideration surrounded keeping the power requirements low due to the small space available at the finger base. Transmittal PPG requires a more powerful LED to

strongly send enough photons through the tissue to the PD; however, the power requirement can be reduced with light modulation techniques by quickly switching high-speed LEDs and PDs on and off. Alongside saving power, the light modulation also prevents any burning of the patient's finger from too powerful of an LED [14]. To further improve the SNR of the PPG signal, the application of pressure at the area aimed to increase the pulsatile amplitude in the targeted artery. When evaluating the optimal pressure for the greatest amplitude measurements without occluding blood, the pressure was too great to apply for an extended period without causing capillary collapse. Locally applying pressure at one of the photodetectors created sufficient amplification in the PPG waveform without compromising the tissue perfusion since the second artery remained open [14].

Alongside the physical design considerations, a MEMS accelerometer was also attached to the ring in order to serve as a noise reference in an active noise cancellation algorithm. After an initial correlation between PPG and MEMS-ACC data, assumptions had to be made about the relationship between noise and the true PPG signal in order to utilize the accelerometer signal for adaptive noise cancellation. One proposed model claims that noise is additive (Figure 8), while the other entertains the possibility that noise is logarithmic (Figure 9).

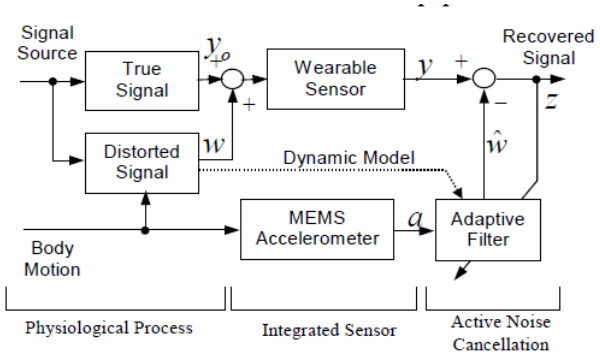

Figure 8: Block Diagram of Additive Active Noise Cancellation Filter

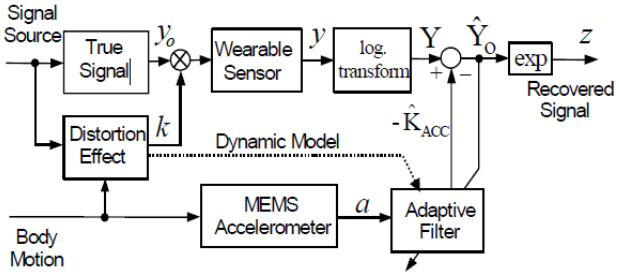

Figure 9: Block Diagram of Logarithmic Active Noise Cancellation Filter

Testing the ring sensor on a jogger on a treadmill, the PPG signal was reconstructed using both the logarithmic and additive methods then compared the correct reference PPG. Based upon a waveform clip shown in the study results, both the additive and logarithmic adaptive noise cancellation algorithms sufficiently preserved the morphology of the PPG signal in their reconstructions [15]. While the algorithms appeared quite successful, the device's performance in the situation where heart rate corresponded closely to step rate was not detailed. Other studies have found during walking or jogging tests that accelerometer-based noise cancellation techniques can undesirably cancel out the true PPG signal if the step rate and heart rate coincide [11, 16]. When evaluating the device in the specific context of a battlefield or ambulatory environment, the ring sensor's performance in the presence of abrupt movements, vibrations or large pressures was not reported. Additionally, the fingers are not an optimal location for a war fighter application since they are highly prone to motion as well as casualty during missions.

2.7.2.2. IN-MONIT

Initially developed by Vogel et al, the IN-MONIT device aims to serve as a wearable "In-Ear 24/7 monitoring system for vital signs" [16]. The miniaturization and incorporation of the device's sensing component into a customized housing enables the reflectance sensor to be worn inconspicuously inside the auditory canal. The auditory canal was targeted as a novel location for measuring reflective PPG signals that could provide a closer contact, hoping to encounter less motion and sufficient vascular perfusion [12]. The optoelectronic component, most recently implemented by Venema et al, is comprised of silicon chip containing two inversely connected LEDs (red and infrared) as well as a photodetector placed at least 3mm away from the LEDs to prevent direct cross talk [17]. Additionally, the LEDs and photodetectors are separated by an optical barrier, shown in Figure 10.

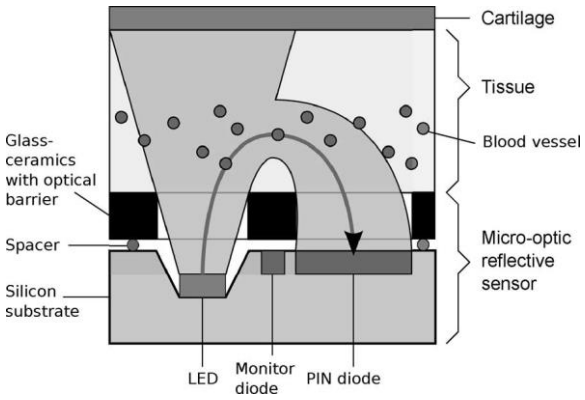

Figure 10: Diagram of IN-MONIT Sensing Component

While the sensing unit does not incorporate an accelerometer, Vogel attempted to use accelerometers located at the subject's hip and the top of the subject's head to measure the primary motion influencing the PPG signal during walking as well as jaw motions. During walking motions, the artifacts could be identified as separate from the PPG signal, which could then be evaluated as a pulsatile-controlled signal. On the other hand, if the subject's heart rate coincided with step rate, the artifact was incorporated within the PPG signal and dominated the morphology and frequency. Similarly, during jaw motion the PPG signal was largely dominated by the chewing frequency and a pulsatile signal could not be detected. Additionally, neither accelerometer could register any reference signal to measure the artifact during the chewing tests [16]. Despite the inability to produce an accurate PPG signal amidst various motion-inducing conditions, the highly miniaturized sensor design presents promise for reflective sensors.

2.7.2.3. Multi-Channel Forehead Pulse Oximeter

The application of a reflective, forehead pulse oximeter to reduce motion artifact has been largely investigated as another measurement site that could hold promise for yielding a consistent PPG signal. Due to the maintenance of a relatively stable level of vascular perfusion and the flat bone of the skull serving as a solid reflector, the physical properties of the forehead hold promise for stronger PPG reflectance SNR [18]. To further increase the SNR, a wireless forehead pulse oximeter device employs a photodetector array surrounding a central pair of LEDs (Figure 11).

Figure 11: Wireless Forehead Pulse Oximeter developed by Mendelson, Dao and Chon

In reflectance mode with only one photodetector, a large amount of light is lost in backscatter due to the diffusion by the underlying tissues and lateral LED-PD position. By concentrically surrounding the central LEDs with multiple photodetectors, a greater proportion of the scattered light can be captured and multiple viewpoints of the PPG signal can be obtained [19]. In addition, the device incorporates a tri-axial MEMS accelerometer to measure the physical motion of the sensor and provide a reference signal for adaptive noise cancellation

(ANC). Various algorithms exist for adaptive filtering: Least Mean Square (LMS), Time Varying LMS, Normalized LMS, Modified Normalized LMS and Recursive Lease Squares (RLS). Research comparing the performance of the algorithms in real-time adaptive filtering for the multi-channel forehead pulse oximeter found that major tradeoffs exist between the measurement accuracy, convergence rate and filter order. For example, the RLS algorithm had a faster convergence rate than the LMS algorithm; but, the RLS algorithm had a longer computation time since it requires M^2 (M is filter order) operations per iteration [11]. While the Time Varying LMS, Normalized LMS and RLS algorithms exhibit better overall performance than the traditional LMS algorithm, practical considerations for real-time implementation such as computation time and simplicity make the LMS algorithm the most conducive in the multi-channel forehead pulse oximeter [11].

The real-time ANC in the device significantly reduced motion artifact, resulting in decreased errors for heart rate and SpO_2 and signifying more reliable measurements. Despite the relative success, the accelerometer-based ANC approach is limited by the type of motion artifact present. Since the technique aims to predict the noise by adapting to the noise reference captured from the accelerometer, spontaneous or less repetitive motions could prove difficult to cancel or take longer to adapt if the noise frequency shifts greatly [11]. Additionally, the situation where cardiac and noise frequencies overlap still hinders the effectiveness of the adaptive filtering.

2.7.2.4. Heated Pulse Oximeter

To combat the limitation of poor vascular perfusion at alternate bodily locations (i.e. chest, limbs), Mendelson and McGinn prototyped a reflectance pulse oximeter configured with a heating element to stimulate localized vasodilation (Figure 12).

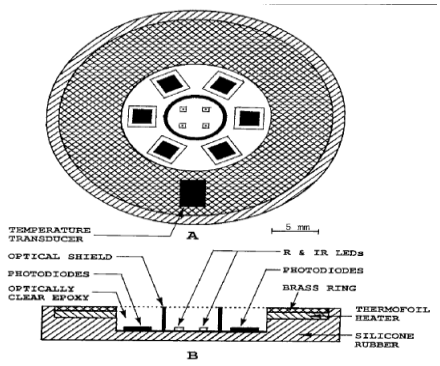

Figure 12: Heated Pulse Oximeter Sensor developed by Mendelson and McGinn

By increasing the size of the arteries, the reflected light will interact with more pulsatile blood and thereby increase the SNR by increasing the power and amplitude of the desired signal. Similar to the multi-channel forehead pulse oximeter, this device employed a concentric PD configuration around a central pair of LEDs. Outside the optical sensing unit, a thermofoil heater disk with a brass ring on the skin side was incorporated to stimulate the heating of the skin. A temperature transducer was also included on top of the brass ring to monitor the skin temperature in order to maintain a comfortable and optimal temperature.

The device was subject to a motionless, induced-hypoxia test at the forearm and calf locations, securing the sensor with double-sided sticky tape and maintaining the skin temperature around 40^{o}C for the entirety of data collection. While the heated sensor did show that local skin heating could be used as a practical method for improving the SNR of reflectance PPG sensors, the forearm and calf locations still recorded weaker signals than unheated signals captured from the forehead. The research did suggest that a skin temperature of around 40^{o}C is generally adequate for improved signal strength without skin damage [8]. While the sensor was not subject to motion and signal processing techniques were not used, the application of localized heating still presents promise as a technique for improving PPG signals from sparsely perfused areas alongside additional motion artifact reduction methods.

2.7.3. Investigated Variables

Several studies using non-unique devices have examined additional variables affecting PPG signals. The findings serve as important insight for design considerations to be made for this study.

2.7.3.1. Contact Pressure

By examining the PPG signal resulting from progressive pressure increases on the sensor itself, relationships arose between the contact force and various AC/DC components of the signal. Isolating the AC component, the first notable finding exposed that different subjects achieved maximum AC amplitude at different absolute pressures. Consequently, the AC amplitudes had to be normalized then subject-averaged in order to effectively compare data. After this normalization, data showed that AC amplitude exhibited a slight initial increase from 0.21N to 0.4N of contacting force with a comparatively drastic decrease above 0.4N of contacting force [20]. This phenomenon can be explained by the physiological variable of transmural pressure, or the difference between the internal and external pressure of the arteries.

When the transmural pressure approaches 0, the AC amplitude will be at a maximum; so, the initial values of contacting force will flatten the arterial wall as the external pressure approaches the intra-arterial pressure. This concept also explains the difference between subject's optimal contacting pressures, since each subject has a unique blood pressure [22]. Isolating the DC component, studies observed that increasing external pressure led to an increase in DC amplitude [20].

In a practical setting, these relationships translate to potential aids as well as oppositions to reducing motion artifact. While imposing an optimal pressure on the PPG sensor could improve the signal's amplitude and therefore the SNR, constantly maintaining a static pressure in the unpredictable ambulatory and battlefield environments would prove especially difficult. One attempt to account for the effects pressure imposes on the signal has approached the consideration by designing specialized "housing" units for the PPG sensor to maintain blood supply through blood flow channels during events of high pressure. When compared to a non-housed sensor, the housing resulted in a more gradual decrease in PPG amplitude of the signal under higher pressures. Despite the comparative difference, a greater reduction in amplitude than anticipated occurred. Future recommendations to prevent undesired vascular occlusion involved designing the housing with a flexible molded plastic to conform to the subject's head [10].

2.7.3.2. Separation Distance Between LED and Photodetector

In reflectance mode, most of the LED light is actually diffused by the skin and other tissue in a forward-scattering pattern and only a small portion of the light is backscattered. Therefore, maximizing the light captured by the photodetector serves as a crucial point in collecting a sufficiently strong signal. Typically, backscattered light is spread concentrically around the LEDs, with its intensity inversely proportional to the square distance from the location of the LEDs [3]. Consequently, the distance separating the PD and LED as well as the intensity of the projected light greatly affect the strength and quality of the signal captured. Research has shown that a greater diving current of the LED results in a more effective penetration depth of the incident light, translating to a greater interaction with the underlying tissue and a greater AC component of the signal [8]. Despite this advantage, practical considerations of power consumption in a stand-alone device limit the driving current for each LED. Additionally, if the PD and LED are placed too closely, there is a potential for undesired

talk directly between the LED light and the PD [17]. The shortcut of the detected light would fail to interact with any of the underlying vascular bed and result in the addition of a large DC component, further dominating the AC component [8].

Evaluating an optimal photodetector and LED separation, research has found that larger PPG signals were detected with a farther distance between LED and PD. Increasing the distance from 4mm to 11mm yielded a two-fold increase in pulse amplitude of the infrared PPG as well as a decrease in beat-to-beat variation from 7 to 3 percent. In spite of the advantages involved in longer LED-PD separation, higher driving currents are needed to counteract the absorption encountered over the longer optical path [8]. Consequently, the tradeoff between distance and LED drive current presents a design choice that depends on the specific prototype constraints.

3. Design Approach

3.1. Purpose

While studies have aimed at counteracting motion artifact using accelerometers, signal processing, or novel sensor locations [14, 19, 21], few have targeted how the physical interface between the sensor and the skin itself might contribute to motion artifact. Additionally, no study was conducted that explored motion artifact in PPG signals during random motion. Given the potential aim of developing a "motion-tolerant" pulse oximeter for a soldier in a military environment, the effects of vibration and sporadic movements could provide valuable situational information for military transport beyond the previously collected data from a subject running on a treadmill which induces a uniform type of motion artifact.

Sensor motion, movement of the capillary beds and weak signal strength stand out as the primary antagonists of motion artifact; therefore, the present study aimed at extracting deeper insight into their instigating variables at the sensor-skin boundary. The first hypothesis of the present study holds that the weight of the sensor itself could correlate to the degree of movement relative to the skin. Therefore, the first variable investigated whether the sensor's weight contributed to the relative motion artifacts. A second hypothesis holds that false low SpO_2 readings during motion stem from the undesirable inclusion of venous blood in the time-variant component. So, the second variable investigated whether locally applied heat could combat the inclusion of the lower oxygen content of the venous blood by promoting blood "arterialization". Finally, the third hypothesis holds that the beneficial effects of externally applied pressure on PPG amplitudes observed at rest would strengthen the PPG signal component during motion. Thus, the third variable targeted the investigation of various levels of applied pressure during random motion. By investigating these three variables (sensor weight, applied heat, and applied pressure), a more reliable wearable pulse oximeter can then be developed that addresses the most significant factors that degrade the accuracy of a reflectance type pulse oximeter.

3.2.Initial Client Statement

Within the context of the aforementioned purpose, the initial client statement was:

"Investigate the true sources of motion artifact in reflective pulse oximetry"

The theory behind this investigation was that by identifying which variables affect the PPG signal the greatest during motion, a more optimal motion tolerant device could be designed to optimize the variables appropriately.

3.3.Design Parameters

3.3.1. Objectives

In order to investigate the true sources of motion artifact in pulse oximetry, a prototype device had to be created that isolated each of the above variables of interest. An Objectives Tree was created to organize the necessary elements of the prototypes (Figure 13), which were then ranked using a Pairwise Comparison Chart (Table1). The pairwise comparison chart was ranked by comparing each of the variables in the rows against those in the column. If the row variable was regarded as more important than the column variable, a 1 was assigned in the box; otherwise, a 0 was placed in the box to indicate a lesser importance. After comparing all the variable combinations, the values for each row were totaled in the "total" column on the right with the sum corresponding to each variable's priority: the greatest number representing the most important and the lowest representing the lowest.

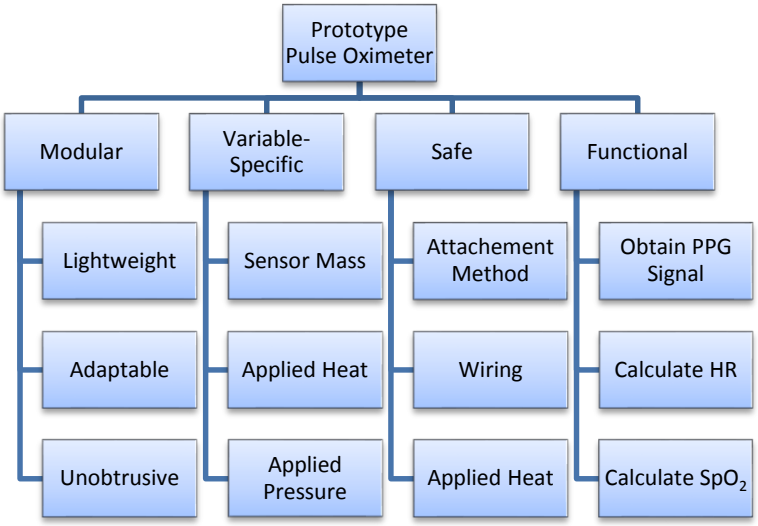

Figure 13: Objectives Tree

Table 1: Pairwise Comparison Chart

	Modular	Variable-Specific	Safe	Functional	Final
Modular		0	0	0	0
Variable-Specific	1		1	0	2
Safe	1	0		0	1
Functional	1	1	1		3

The modularity of the prototype remained extremely important for the feasibility of the testing. Creating a completely unique and different prototype to investigate each variable would have been impractical for the completion of the project. Furthermore, the results gathered would not be as cohesive if they were collected from unrelated prototypes. The ideal investigatory device would employ a modular base sensor upon which minor alterations or additions could be made between variable tests so that the same fundamental components and signal processing would be collecting data for all the tests, thereby minimizing the variables introduced and the overall testing time.

With regards to the targeting of variables, the testing scenarios must be variable-specific in order to collect data that successfully examines the effects of each variable on the PPG signal. While uncontrollable variables exist, primarily from sources pertaining to the individuality of subjects, the optimal prototype will control all variables possible in order to investigate the one at hand. For example, the additions made to the base prototype in order to investigate applied heat cannot be bulky since that would increase the sensor weight and cross-contaminate investigations.

Since the tests were conducted *in vivo* in order to explore the variables existing at the intimate sensor-skin relationship, the prototype had to be safe and impose no harm or damage to the subjects. Exploring variables that require the application of pressure or heat, the introduction of such factors could not damage the subject's skin.

Most importantly, the prototypes had to be functional. Obtaining a PPG signal, calculating HR and calculating SpO_2 are the basic functions of a pulse oximeter. Therefore, a successful prototype had to be able to adequately perform those tasks, otherwise it would not be able to collect the necessary data to assess the effects of the variables. Thus, the purpose of the study would not have been possible to conduct.

3.3.2. Constraints

The project constraints arose from the practical implication of the testing procedure itself as well as from the future application of the technology as a military device to be used in the battlefield. As previously mentioned, the locations at which transmission mode (Section 2.1 Figure 3) can be applied (fingers, toes and ears) are too vulnerable for military application and

also are more subject to poor blood perfusion during cold or severe blood loss. Therefore, the prototype pulse oximeter needed to be configured in reflectance mode in order to focus the present study on supporting a future military application. For the investigation of the three variables, the prototype had to be able to incorporate a certain range pertaining to each respective variable. For exploring the effects of sensor weight, the prototype had to incorporate a method for collecting data at as "near-zero" weight as possible, then increasing the weight of the sensor up to approximately 30g. The upper bound of 30g was chosen from the weight of the current reflective pulse oximeter developed in Professor Mendelson's lab that includes the battery and sensor housing (Section 2.7.2 Figure 11). For the investigation of applied heat, the device had to safely heat up and maintain the forehead skin temperature at a safe setting. Since background research revealed that increasing localized skin temperature to 42^0C could promote "blood arterialization", this temperature was chosen as the upper bounds to target the arterialization effect without causing the subject discomfort. Finally, the applied pressure by the sensor should not exceed 80mmHg of force on the forehead, since that has been shown to occlude blood flow within the fragile framework of the capillary beds.

Additional constraints existed within the testing protocol and environments. In order to practically compare the data gathered by the investigatory prototype, a reference device had to be implemented in order to gather "correct" values for HR and SpO_2. As uncovered by the background research, there has not been a truly motion tolerant pulse oximeter developed. While some high-grade clinical devices have very advanced signal processing techniques to compensate for noisy signals, drastic movements would still adversely affect the readings. Consequently, the testing protocol was constrained by the detail that the reference pulse oximeter had to be kept as stationary as possible during the protocol. In addition, the testing protocol had to be safe for the human subjects and conducted in accordance with an IRB approved protocol. With the ideal testing environment targeting simulated military transport, the vibrations must be imposed safely and without increased risk to the subjects. In the interest of the volunteer subjects, the testing protocol itself had to involve a reasonable total testing time, ideally requiring no more than an hour and a half of their time. Consequently, tradeoffs among the levels of investigation, length of testing time, and transitions between variables had to be optimized in order to fit a reasonable testing time.

3.4. Revised Client Statement

After extensive background research and evaluation of the design parameters, the initial client statement was revised to the following:

"Design prototypes and testing scenarios to investigate the effects of sensor mass (by testing with varying sensor weights from 5g to 34g), applied heat (by locally heating the skin around the sensor to 38^{O}C, 40^{O}C and 42^{O}C), and applied pressure (by externally applied pressure on the sensor up to 60mmHg) on motion artifact in reflective pulse oximetry"

3.5.Design Alternatives

3.5.1. Bare Sensor

In order to fit the constraints of the sensor weight study, the base prototype had to be designed for minimal weight; thus, the components at the sensing site were limited to the essential components of LEDs, a photodetector, a method of attachment, and a method of transmitting the signal. Due to the ease of integration and cost-effectiveness, commercially available adhesive sensors were chosen to reuse the optical components and adhesive attachment. In addition, the wiring from the adhesive sensor enabled a connection to a signal processing unit for HR and SpO_2 calculation as well as basic noise filtering for the PPG signal. Initially, the optical components from Masimo LNCS sensors were reconfigured from transmission mode by placing the LEDs and photodetector closer together, approximately 8mm apart in accordance with previous findings [8]. The Masimo LNCS sensor also connected to a benchtop Masimo Radical Pulse Oximeter monitor, chosen for its advanced Signal Extraction Technology (SET®) which is currently regarded as the most sophisticated on the market.

3.5.2. Sensor Weight

While employing just the adhesive material for the method of sensor attachment stands as the lightest method, adhesive material has shown poor performance in sticking to oily skin or for longer durations of time [10]. In addition, the bare adhesive sensor did not provide an adequate platform for the incorporation of increasing weights up to the desired upper bounds of 30g. Therefore, the bare adhesive sensor was sewn into an ACE bandage to provide a more secure method of attachment for the repeated application and removal between subjects and tests. To simulate the increase in sensor weight, multiples of weights (approx. 5g each) were taped on the

outside of the headband on the opposite side of the sensing site. The material was chosen so that each weight was around the size of a 3.6V Lithium Battery in order to mimic the size of the current wireless pulse oximeter.

3.5.3. Applied Heat

The application of heat involved the two-fold implementation: heating up the forehead skin as well as maintaining the localized temperature. Based off the upper bounds of 42°C and the constraint of reasonable testing time, the three heat levels of 38°C, 40°C and 42°C was chosen to investigate enough of a temperature range to observe difference between the levels without requiring long testing procedures.

3.5.3.1. Prototype Components

To heat the skin, a thin thermofoil heater was incorporated behind the optical components of the sensor and inside of the ACE bandage. This enabled adequate localized heating without burning the subject's forehead with direct contact. Additionally, the choice of a thermofoil material served to maintain the low sensor weight so as to satisfy the variable-specific objective. Two different sizes and shapes of Minco thermofoil heaters were assessed as a part of the design alternatives (Figure 14 and 15).

Figure 14: Minco Thermofoil Heater 1" round, 37.4 ohms

Figure 15: Minco Thermofoil Heater, 1"x4" rectangle, 28.4 ohms

In order to maintain the skin temperature, a Biopac fast response thermistor (TSD202A) was incorporated near the optical components to sense the localized temperature. The resistance vs. temperature relationship for the thermistor was developed by placing the prototype (with the thermistor and the heating strip) on the forehead and measuring the resistance of the thermistor while using a COTS wired temperature probe as a validation of the true skin temperature.

3.5.4. Temperature Control Circuit

The resistance of the thermistor was used as feedback for a custom temperature control circuit (R5 in Figure 16) that regulated the flow of current through the heater (U4 in Figure 16) based upon the sensed temperature.

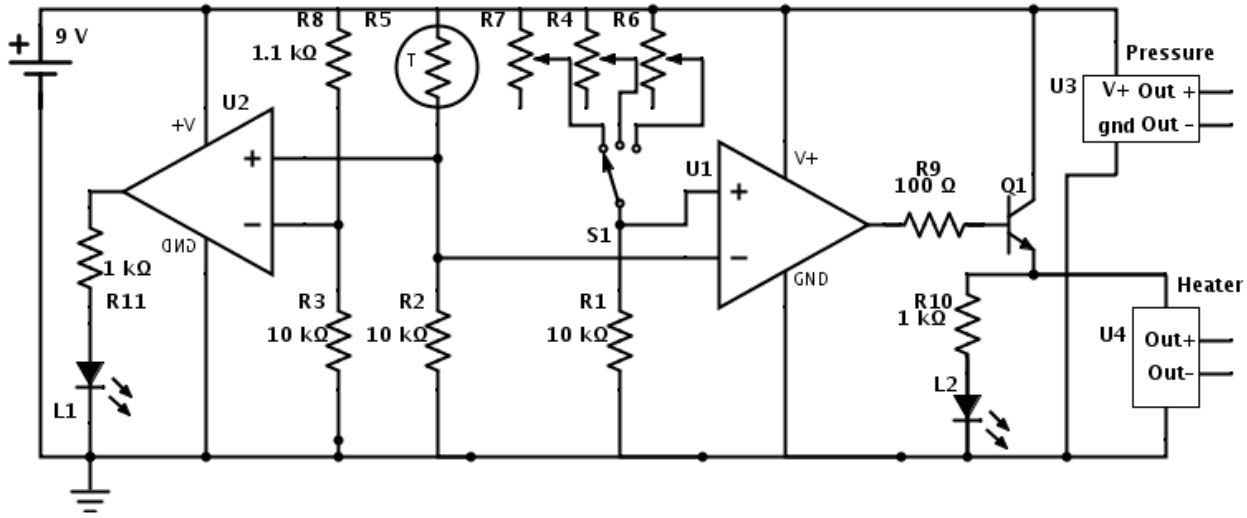

Figure 16: Schematic of Temperature Control Circuit

The resistances of the potentiometers (R7, R4, R6) in the circuit were adjusted to match each of the three previously calibrated resistance vs. temperature values for 38°C, 40°C and 42°C. A rotary switch (S1) was implemented to switch between the three potentiometers in order to select the desired resistance against which the thermistor's resistance would be compared. This comparison was implemented using a Wheatstone Bridge configuration, involving the thermistor (R5) as the top left branch, a 10kΩ resistor as the bottom left branch (R2), the potentiometers as the top right branch (R7, R4, R6), and another 10kΩ resistor (R1) as the bottom right branch. The voltage between the resistors of the left branch (between R5 and R2) and the voltage between the resistors of the right branch (between S1 and R1) was passed into the positive and negative inputs of a LM741 operational amplifier (U1) configured as a comparator. If the thermistor resistance was greater than that of the selected potentiometer,

indicating the sensed temperature was less than the desired temperature, the op amp output 9V, thereby causing current to run through the heater (U4) and through the green LED (L2) to indicate to the investigator that the heater was "on". If the temperature sensed by the thermistor was greater than the desired setting, the op amp would output 0V, rendering both the heater and the green LED "off". In addition, a red safety LED (L1) was implemented with a second LM741 operational amplifier (U2) configured as a comparator to turn on the LED if the resistance of the thermistor dropped below a set resistance (R8) corresponding to 43ºC. This safety mechanism was tested by forcing the heater to remain on and heat up the forehead until just above the 43ºC point. The circuit was powered by a 9V battery, chosen to allow for containment of the entire unit.

3.5.5. Applied Pressure

In order to satisfy the variable-specific constraint ad allow the prototype to still functionally collect data, the pressure sensing mechanism had to be lightweight (< 2g) and unobtrusive. Thin, inexpensive COTS Force Sensitive Resistors (FSRs) were available that could be placed proximal to the optical components (Figure 17) and sense the localized force while the ACE bandage was tightened to the various levels. Two different FSRs were tested: FlexiForce A401 and Interlink FSR402 (Figure 18).

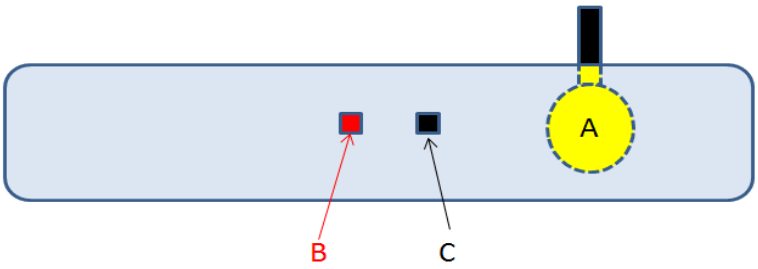

Figure 17: Applied Pressure Prototype (A) LEDs (B) Photodetector (C) Pressure Transducer

Figure 18: FlexiForce A401 with 1" sensing area (left) and Interlink FSR402 with 0.5" sensing area (right)

In order to calibrate the output of the FSRs, three different weights were placed on the sensing area ten separate times. A clay round was shaped to match the sensing area and served as a platform upon which to place the weight and allow for even dispersion of pressure; however, neither FSR was capable of reproducing a consistent and stable output corresponding to the applied force.

Pressure transducers stand as a more consistent and sensitive method of quantifying pressure through air displacement. A thin bulb was placed the same as the previous FSR configuration and connected to the input port of a pressure transducer (Figure 19) via thin silicon tubing. The differential output between pin 2 and 4 was measured and calibrated directly to mmHg by connecting the tubing to a blood pressure cuff and inflating the cuff to specified pressures. With this calibration method, the pressure transducer consistently yielded an output of 1mV per 10mmHg of applied pressure.

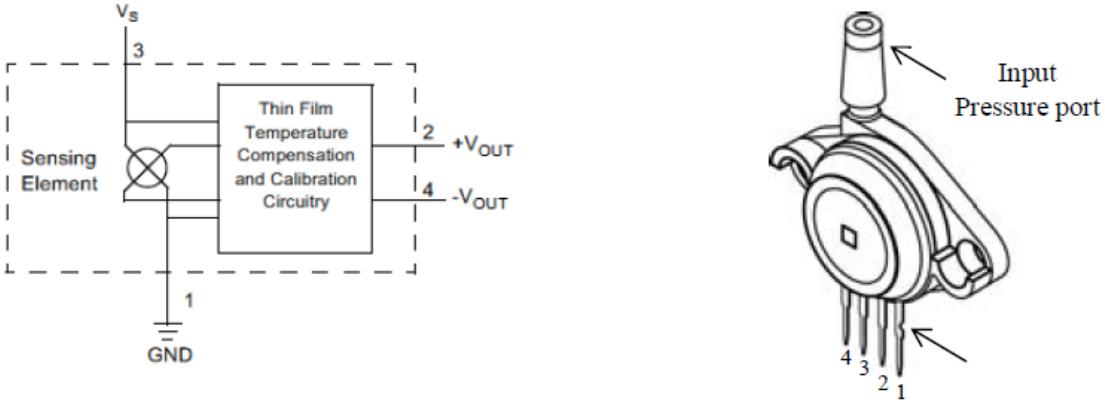

Figure 19: MPX5050GP Pressure Transducer (right) and Pin Out (left)

3.5.6. Experimental Design

A request for IRB approval was submitted and approved, allotting for a maximum of ten male and ten female volunteers. The subjects were instrumented with the prototype sensor on their forehead, with the wire extending from the sensor secured near their temple with tape in order to prevent the wire from pulling on the sensor during the tests. The prototype sensor was connected to the Masimo Benchtop Radical Pulse Oximeter, from which HR and SpO_2 values were collected using the serial port connected to a PC, while the analog PPG signal was acquired with a National Instruments DAQ. In addition, a Masimo Radical-57 handheld pulse oximeter with a finger transmission sensor was used as a reference to simultaneously acquire HR and SpO_2 readings, which were extracted from the device's memory after the test. A diagram of the

overall configuration of the prototype and reference sensor is depicted in Figure 20. Initially, the internal clocks of both Masimo monitors were to be synced so that the time stamps of the digital outputs were the same in order to be directly compared.

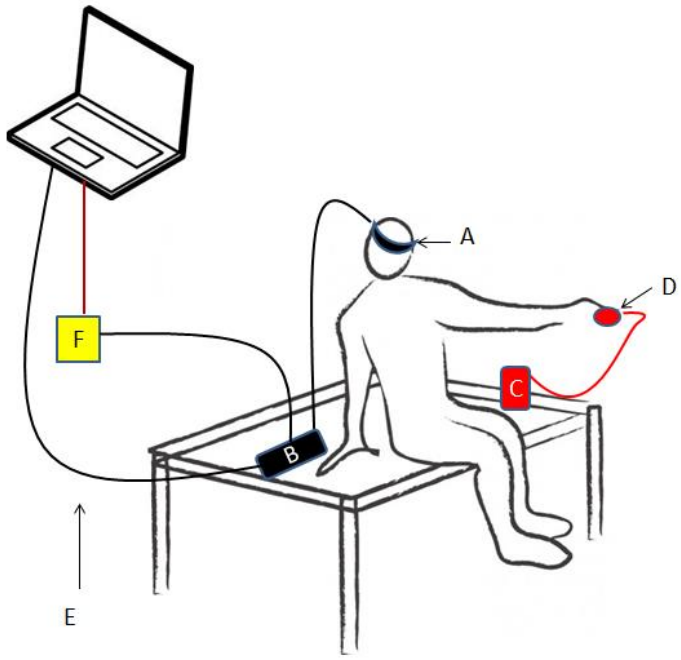

Figure 20: Sensor Mass Experiment Set-up (A) Prototype Pulse Oximeter (B) Masimo Tabletop Pulse Oximeter Monitor (C) Handheld Masimo Radical-57 Monitor (D) Finger Probe reference pulse oximeter (E) Serial cable (F) National Instruments DAQ

Since a focus of the testing protocol stood to explore motion artifact in a military transport environment, preliminary discussions with collaborators at USARIEM and Lincoln Laboratories explored the prospect of testing subjects in the back of military HUMVEEs. Due to foreseen physical difficulties involving the management of the signal processing monitors and reference sensor as well as the logistical difficulties involving IRB approval and gaining access to HUMVEEs, a laboratory alternative was chosen to simulate a military transport environment. Ideally, the simulation was to be conducted on whole body vibration tables that could be uploaded with the vibration signatures of military-grade vehicles; however, the table's remote location and physical dimensions rendered testing human subjects on it impractical.

Given the eventual testing environment of laboratories available on the WPI campus, the testing protocol comprised of subjects performing various movements to mimic ambulatory field transport involving head movements (side-to-side and up-and-down), bouncing (calf raises) and

random motion. To facilitate consistency among subjects' head movements and bouncing, particular rates were specified. In order to prevent the introduction of motion artifact in the reference pulse oximeter during these movements, the subject's hand instrumented with the reference sensor was kept stationary by securing the arm on a table of appropriate height. Choosing a table height based on subject and testing movement phase served as a way to enable the subject's arm to remain at a comfortable height when performing some of the larger movements like sitting or standing up. To safely simulate the vehicular transport within a laboratory setting, random motion was explored by placing human volunteers on an air mattress while wearing the prototype on their forehead and the reference sensor on their finger. The investigator then bounced the subject at random amplitudes and frequencies while the reference sensor was kept stationary by securing the instrumented hand off the air mattress and resting on a low platform.

4. Methods

4.1. Final Prototype Design

4.1.1. Bare Sensor

Preliminary experimentation revealed that the advanced SET® in the Masimo Radical Benchtop Monitor did not necessarily report the real-time calculated HR or SpO_2 measurements. In the event of extreme motion artifact, the SET® would hold the last known confident value. This proved difficult particularly in the investigation of applied heat since the false low SpO_2 values could not be observed even during severe waveform corruption; thus, no comment could be made on the effects of heat since all SpO_2 levels remained within 96%-100%. Therefore, the benchtop monitor was changed to a Nellcor benchtop pulse oximeter that displayed the real-time calculated values and output the raw red and infrared signals. Consequently, the bare sensor for the final prototype (Figure 21) used Nellcor™ Adult SpO_2 adhesive sensors with reconfigured optical components as previously specified. The sensor was sewn into an ACE bandage with a hole cut in the bandage in order to allow the wire from the sensor to run along the outside of the bandage and pinned to the headband at the back of the subject's head using a bobby pin in order to prevent the connector from pulling the sensor. In addition, Velcro strips were sewn at the ends of the ACE bandage to facilitate customizable attachment for each subject (Figure 22).

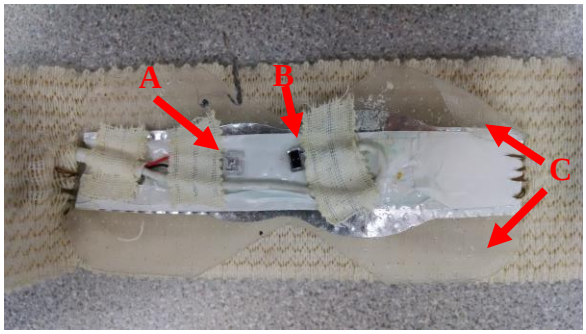

Figure 21: Bare Sensor with LEDs (A), photodetector (B) and adhesive wings (C)

Figure 22: Prototype position on forehead

4.1.2. Sensor Weight

The bare sensor previously described weighed 5.6g at the sensing site, thereby representing the lowest weight level of investigation. Quarters (25 cents) were chosen to serve as the weights due to their size, availability, and standardization. According to the US Mint, quarters are manufactured to weigh 5.6g and measure 0.955" in diameter and 1.75mm thick. The physical dimensions allowed for easy attachment with tape in a pyramidal fashion and the weight fell around the desired incremental range. In order to investigate up to the upper bounds of 30g, one quarter at a time was added to the bare sensor and tested up to five quarters, or 33.6g.

4.1.3. Applied Heat

The 1"x4" rectangular thermofoil heater was chosen due to its ability to heat up the entire sensing area. In addition, the physical dimensions matched that of the adhesive sensor and allowed smooth incorporation behind the optical components (Figure 23).

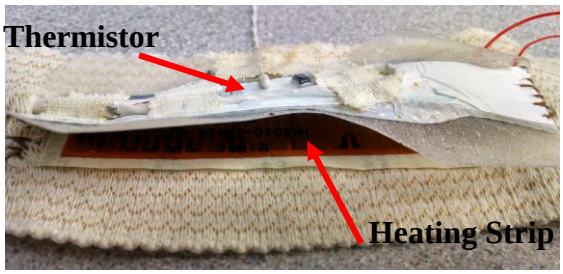

Figure 23: Applied Heat Prototype

Preliminary experimentation yielded that the 9V battery could not maintain sufficient voltage across the heater to maintain a forehead skin temperature for 40ºC or 42ºC. Since the testing was in a lab setting, the benchtop power supply was used to power the circuit at 10V. The circuit (Section 3.3.3, Figure 16) was soldered to a 3"x6" perfboard and placed in a 3"x7"x3" plastic black box (Figure 24).

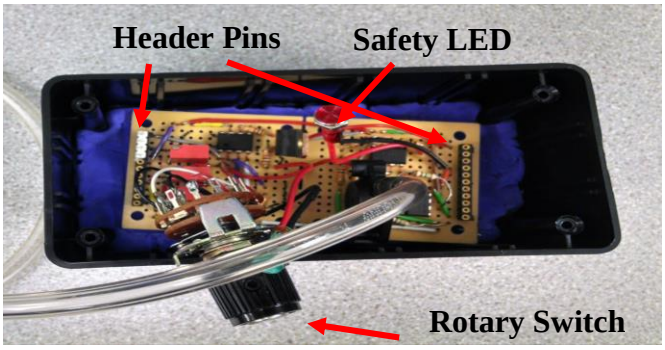

Figure 24: Temperature Control Circuit on Perfboard in Plastic Black Box

Header pins were soldered on the edges to enable cable connections for the inputs of the thermistor and power supply on one side and the output of the heater on the opposite.

4.1.4. Applied Pressure

Due to the stretching and pressure dispersing properties of the ACE bandage, an additional headband had to be applied over the ACE bandage prototype in order to apply sufficient pressure. To quantify the pressure, the pressure transducer described in Section 3.3.4 was soldered to the same perfboard as the previous temperature control circuit and connected to an amplifier circuit to yield a 1V output per 10mmHg of sensed pressure (Figure 25). Building upon the temperature control circuitry, the same +10V power supply was used. The differential output from the MPX5050GP pressure sensor (Section 3.3.4 Figure 19) was connected to the + and – terminals of another LM741 operational amplifier with the resistors R12, R12, R14 and R15 chosen for an gain of 1,000 in order to map the 1-10mV output range of the pressure sensor to a 1-10V output of the circuit.

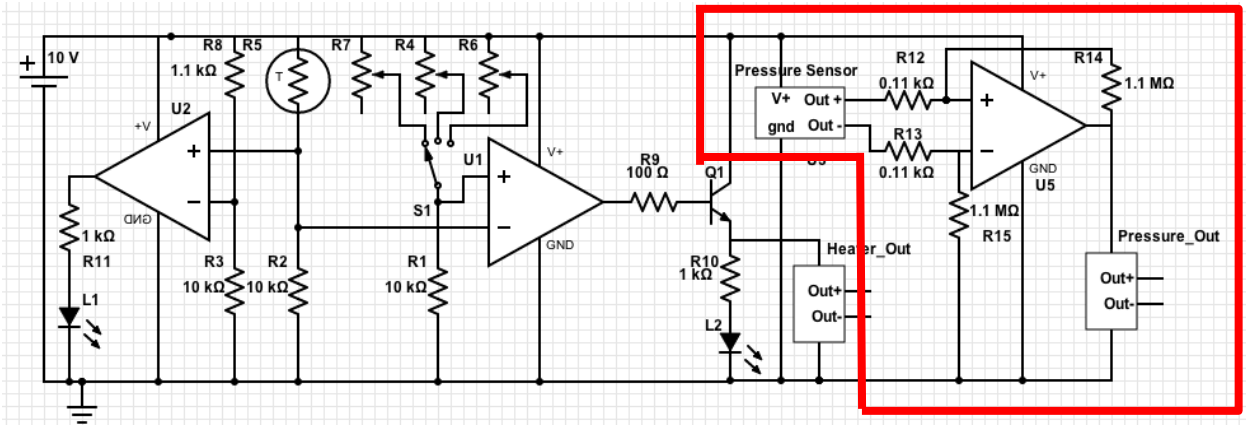

Figure 25: Temperature Control and Pressure Sensing Circuit Schematic (red box denotes pressure sensing amplification circuit)

A small oval bulb from a squeaker toy was chosen to serve as the air displacement sensor and was connected to the input port of the pressure transducer with one foot of silicon tubing (Figure 26). The silicon tubing was chosen to have a stiff wall while still allowing for a suction fit on connectors on both ends in order to enable an air tight connection but not decrease the sensitivity by increasing the compliance of the tubing.

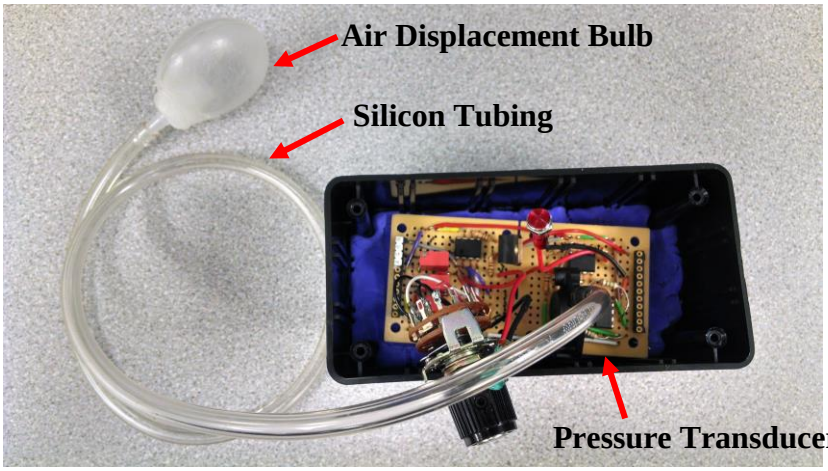

Figure 26: Pressure Sensing Circuit, Air Displacement Bulb, and Silicon Tubing

Before testing, the air displacement sensor was placed on the subject's forehead in place of the prototype sensor and a thick Velcro strap was wrapped around both the bulb and the subject's forehead. The strap was then tightened while the output from the pressure sensing circuit was measured in order to determine the headband lengths corresponding to 20mmHg, 40mmHg and 60mmHg. With the headband length-to-pressure relationship calibrated for each subject before testing, the headband was applied directly over the prototype sensor during testing and tightened to the predetermined lengths. Since the applied pressure was to remain consistent throughout the testing, there was no need the need for a pressure sensor during testing thereby maintaining the variable-specific constraint by not introducing bulky components that could induce their own corruption into the signal.

4.2.Experimental Design

In order to target the desired levels of investigation and still maintain a reasonable testing time, the testing protocol was focused solely on random motion. The subject laid their upper torso on an air mattress with a pillow supporting their head, simulating the slight incline of a stretcher during ambulatory transport. Each test began with 20 seconds of data collected at rest in order to provide a controlled data set against which the following 60 seconds of random

motion could be compared. During the random motion phase, the investigator bounced on the rest of the air mattress at random amplitudes and frequencies. For the reference measurements, one of the subject's fingers was instrumented with a finger probe connected to a Masimo Radical-57 Handheld Pulse Oximeter. The subject laid so that the arm of the instrumented finger was kept off the mattress and held stationary throughout the testing. An example of the experimental set-up is shown in Figure 27.

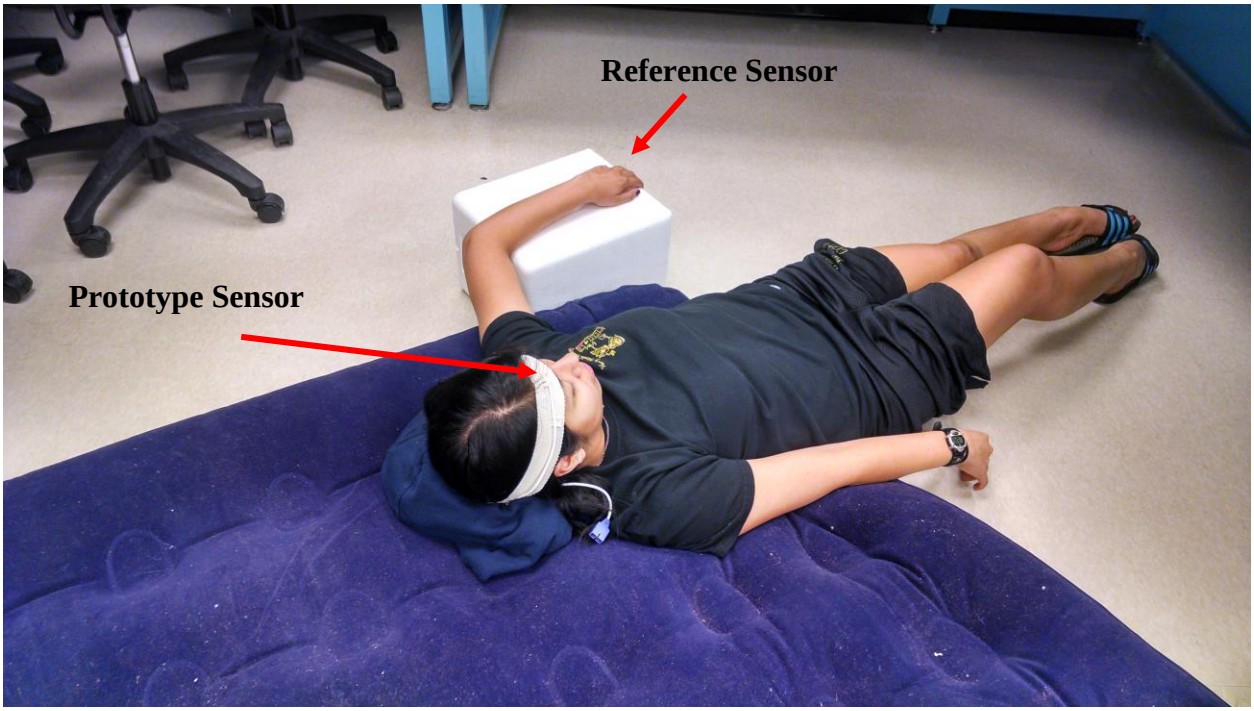

Figure 27: Example of Experimental Set-up

4.3.Data Acquisition

Preliminary experimentation revealed that the advanced SET® in the Masimo Radical Benchtop Monitor did not report the real-time calculated HR or SpO_2 measurements. In the event of extreme motion artifact, the SET® would hold the last known confident value. This proved difficult particularly in the investigation of applied heat since the false low SpO_2 values could not be observed even during severe waveform corruption; thus, no comment could be made on the effects of heat since all SpO_2 levels remained within 96%-100%. Therefore, the benchtop monitor was changed to a Nellcor benchtop pulse oximeter that displayed the real-time calculated values and output the raw red and infrared signals. The Nellcor was connected to a separate interface via a fiber optic cable in order to extract the HR and SpO_2 values via a BNC cable to the NI-DAQ. A LabVIEW VI was created to collect and plot the HR, SpO_2 and R and

IR PPG waveforms during testing. The NI-DAQ was sampled at 500Hz. Each subject's data were assigned and stored under a random alphanumeric code under the investigator's password protected account in accordance with the IRB approval. At the completion of all the variable test for each subject, the data from the reference sensor were imported as a .csv file using the TrendCom™ program and the data trend was cleared from the sensor's memory.

4.4.Data Analysis

4.4.1. HR and SpO_2 Analysis

For each subject, both the prototype and reference measurements were imported into MATLAB. Since the reference sensor recorded time-stamped measurements every 2 seconds (0.5Hz) and the prototype sensor was sampled through a NI-DAQ at 500Hz, the reference measurement vector was interpolated using MATLAB's spline function to a vector of 80 data points (one data point per second) while the prototype measurement vector was down-sampled to match. The normalized error was calculated at each data point for both HR and SpO_2 from the relationship

$$\%\ Normalized\ Error = \frac{|reference - prototype|}{reference}\ x\ 100\% \quad (4)$$

This resulted in a normalized error vector of 80 data points for each test, including both the first 20 seconds of rest and the 60 seconds of random motion. Since Bland-Altman plots stand as a beneficial tool to compare the correlation between two measurement methods, Bland-Altman plots were generated from each subject's HR and SpO_2 rest measurements by compiling the first 20 data points from the prototype and reference sensor in each test and plotting the mean versus the difference for each data point. These plots served to validate the prototype's measurement readings in a controlled setting before introducing motion artifact to the forehead sensor. The error during rest was then subtracted from the error during random motion for each subject to account for the innate differential between the reference and the prototype calculations. The resulting errors were then averaged to yield a mean normalized error for each level of investigation.

Box plots were also generated from the 60 data points during random motion for each subject for each variable, juxtaposing each level of investigation within the same plot. In the box plots, the top and the bottom of the box represented the third and first quartiles, respectively, while the red line represented the median and a blue dot represented the mean. The dotted lines extending

from the top and bottom of the box represented the maximum and minimum of the data set, not including the "outliers" which were represented by the red plus signs. Box plots served to visualize the distribution of each measurement (one per second) throughout the random motion rather than solely analyzing the average error of a data set which does not expose additional characteristics of the data set, such as distribution, relationship of the median and outlier points.

4.4.2. PPG Waveform Analysis

The frequency spectrum for each test were computed using MATLAB's *fft*() and plotting the spectrum up to 3Hz, chosen as the upper bounds after preliminary inspection of the frequency spectrums showed little magnitude at frequencies greater than 3Hz. Physiologically, 3Hz would correspond to a HR of 180 beats per minute (bpm) which lies safely above a reasonable resting HR that the subjects may have. Additionally, the random frequencies at which the investigator bounced on the air mattress most likely remained under 3 cycles per second. The area under the spectrum was taken +/-20% of the mean heart rate (A_{in}), accounting for the possibility of minor changes in heart rate throughout the test. The resulting area was then compared to the area under the rest of the spectrum (A_{out}) within the interval 0.25Hz to 3Hz, as depicted in equation 5. The lower bounds of the A_{out} interval was chosen as 0.25Hz since that would correspond to a HR of 20bpm and also stands as an unreasonable resting HR. Preliminary investigation showed high magnitudes at these low frequencies that interfered with the focus on analyzing frequencies that could be representative of either motion or HR. Physiologically, this extremely low frequency component could stem from the subjects respiratory rate which is not of interest with regards to exploring motion artifact during random motion. MATLAB's *trapz()* function was used to approximate the area.

$$A_{in}/A_{out} = \int_{0.8MHR}^{1.2MHR} FFT \Big/ \left[\int_{0.25Hz}^{0.8MHR} FFT + \int_{1.2MHR}^{3.0Hz} FFT\right] \quad (5)$$

While the relative quality of the PPG waveform morphology was a point of comparison among the various levels of investigation, quantitative methods were necessary to extract measureable comparisons that related to the quality. Since the PPG waveform corresponds with the cardiac cycle, the relative prominence of the HR frequency versus other frequencies served as a quantitative indicator of whether the PPG waveform morphology was representative of the cardiac cycle or whether the morphology was corrupted from the influences of motion.

5. Results

Full data sets for each level of investigation for each of the three variables were collected from 16 subjects. Each test began with 15-20 seconds of data collection at rest followed by 60 seconds of induced random motion. For the entire testing period (approx. 80 seconds), the subject's HR and SpO_2 measurements were collected simultaneously from the reference and the prototype sensors. In addition, the infrared and red PPG waveforms were collected from the prototype sensor. All prototype data (HR, SpO_2, PPG waveforms) were collected in real-time with a LabVIEW VI and stored in .lvm files, while the time-stamped reference sensor measurements were imported into a .csv file after each subject's testing.

The normalized error vectors of 80 data points were calculated for each test according to the flow chart in Figure 28 and according to Equation 4 in Section 4.4.1, resulting in normalized error vectors of 80 data points (one data point per second) for HR and SpO_2 for each test for each subject.

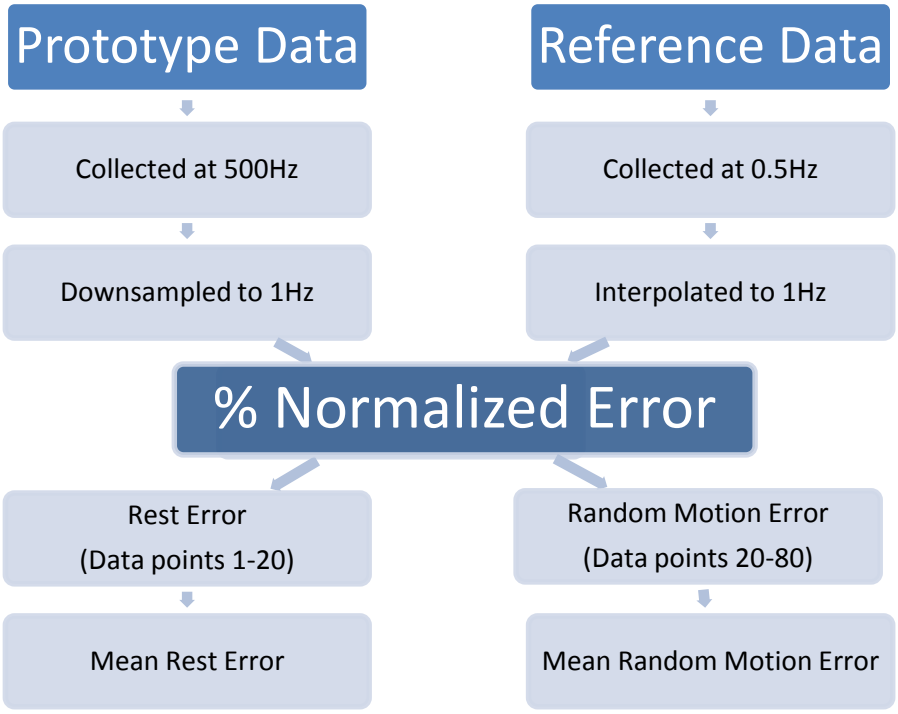

Figure 28: Flow Chart of Data Analysis for HR and SpO_2 Normalized Error Calculation

To verify the prototype's accuracy, Bland-Altman plots were generated for each subject's HR and SpO_2 rest measurements by compiling the first 20 data points from the prototype and reference sensors in each test and plotting the mean versus the difference for each data point.

Figure 29 shows example Bland-Altman plots for HR and SpO_2 rest data, while Appendix A and B contains the plots generated for all subjects.

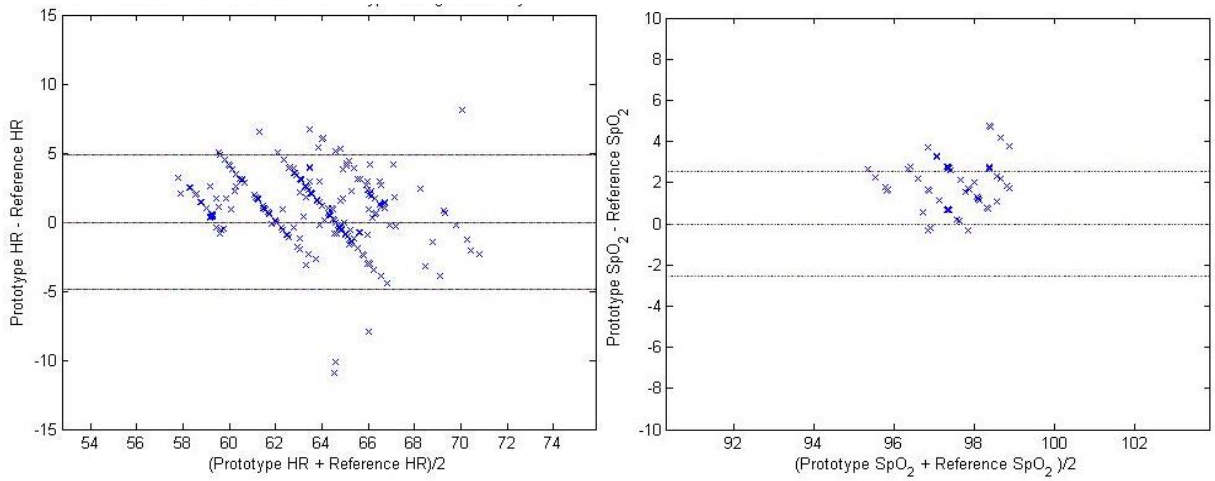

Figure 29: Example Bland-Altman Plots of HR (left) and SpO_2 (right) measurements during rest (Subject C11)

The mean normalized error was calculated during the random motion period for each subject by averaging the 60 data points and the mean normalized error from the previous data collected at rest count for the innate differential between the reference and the prototype calculations. The resulting errors were then averaged to yield a mean normalized error for each level of investigation. Statistical significance was calculated using MATLAB's built-in *ttest()* function to compare the mean normalized errors for all subjects between two adjacent levels of investigation. The two levels were determined statistically significant if the resulting correlation remained below a P value of 0.05.

5.1.Sensor Weight

Box plots were then generated from the normalized errors for each subject's HR and SpO_2 measurements during random motion, juxtaposing the data sets for each weight level. Figure 30 shows example box plots for HR and SpO_2 data, exhibiting the overall trend of an increase in normalized error with the increase in sensor weight. The box plots of all the subjects are included in Appendix C and D.

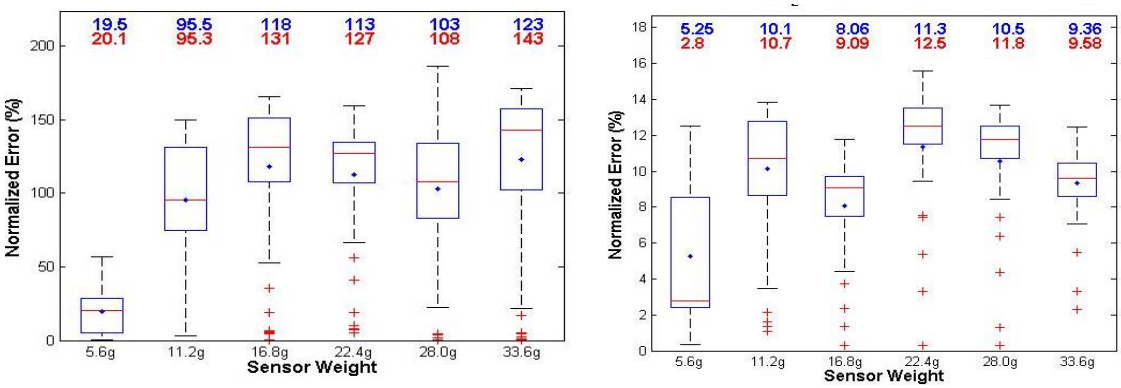

Figure 30: Example Box Plots of normalized HR (left) and SpO_2 (right) error during random motion (Subject M2) with mean (blue text) and median (red text) numbers displayed above each data set.

Figure 31 shows a bar graph depicting the mean of all the subjects' mean normalized errors during random motion, exhibiting an increase in percent normalized HR error with the increase in sensor weight. The bars with the bold red labels above denote the weight levels that represented a statistical difference when compared to the mean error of the previous sensor weight.

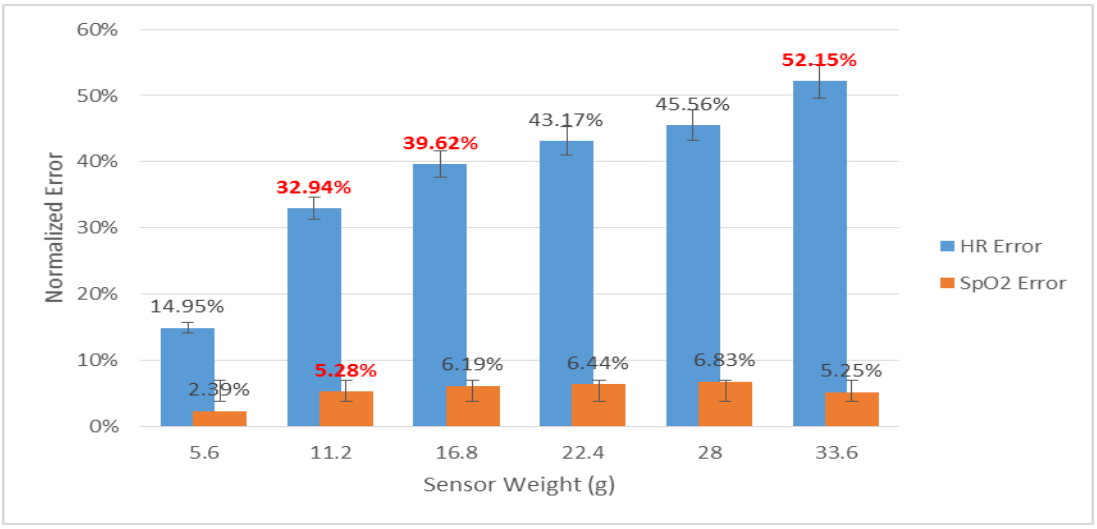

Figure 31: Bar Graph Comparing Mean Normalized HR and SpO_2 Errors

The 17.41% increase in error from 5.6g to 11.2g and the 8.47% increase in error from 11.2g to 16.8g shows a significant difference between the weight levels. As the sensor weight increased to 22.4g and 28.0g, the increasing weight did not indicate statistically different increases in error; however, the final weight level of 33.6g showed another jump in error, increasing by 6.59%. Figure 32 shows the relative SpO_2 errors at each weight level. Comparing each progressive weight level, the only statistical difference can be attributed to increasing the weight from 5.6g to 11.2g. The relative errors for 11.2g to 33.6g only differ by 1.58% overall.

To quantitatively evaluate the relative quality of the PPG waveforms, the Fourier Transform was computed and the resulting frequency spectrum analyzed at each weight level. Figure 32 shows an example frequency spectra for each weight level for Subject L14, while Appendix I contains all the generated spectra.

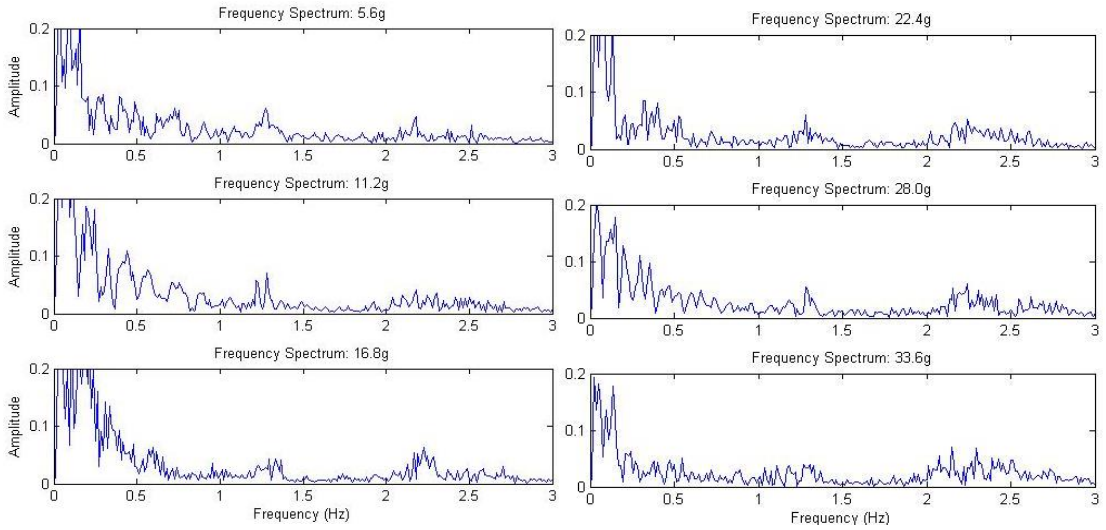

Figure 32: Example Frequency Spectra Corresponding for different Sensor Weights (Subject L14)

Since preliminary inspection of the plots showed little magnitude at frequencies greater than 3Hz, the frequency spectrums were only plotted and analyzed up to 3Hz. Physiologically, 3Hz would correspond to a HR of 180 beats per minute (bpm) which lies safely above a reasonable resting HR that the subjects may have. Additionally, the random frequencies at which the investigator bounced on the air mattress most likely remained under 3 cycles per second. The area under the spectrum was taken +/-20% of the mean heart rate (A_{in}), accounting for the possibility of minor changes in heart rate throughout the test. The resulting area was then compared to the area under the rest of the spectrum (A_{out}) within the interval 0.25Hz to 3Hz, as depicted in equation 5. The lower bounds of the A_{out} interval was chosen as 0.25Hz since that

would correspond to a HR of 20bpm and also stands as an unreasonable resting HR. Preliminary investigation showed high magnitudes at these low frequencies that interfered with the focus on analyzing frequencies that could be representative of either motion or HR. Physiologically, this extremely low frequency component could stem from the subjects respiratory rate which is not of interest with regards to exploring motion artifact during random motion.

Each subject's spectra were further analyzed by calculating the A_{in}/A_{out} ratio at each weight level. The A_{in}/A_{out} ratios for 11.2g and above were each compared against the base sensor's ratio for each subject to observe the proportional change of each weight level's A_{in}/A_{out} ratio relative to that of the minimal weight level. Equation 6 expresses this calculated proportion where the subscript *w* represents the weighted level that is being compared. These P_w values were then averaged across all the subjects to determine a mean proportion for each weight level. It was observed that with the increasing weight, the corresponding proportions decreased, as seen in Table 2.

$$P_w = \left(\frac{A_{in}}{A_{out}}\right)_w \Big/ \left(\frac{A_{in}}{A_{out}}\right)_{5.6g} \tag{6}$$

Table 2: Average P_w Values for each weight level versus the bare sensor

	11.2g v. 5.6g	16.8g v. 5.6g	22.4g v. 5.6g	28.0g v. 5.6g	33.6g v. 5.6g
P_w	0.91	0.92	0.87	0.84	0.89

5.2.Applied Heat

Box plots were again generated from the normalized errors for each subject's HR and SpO_2 measurements during random motion. Figure 33 shows example Box Plots for HR and SpO_2 data, exhibiting an overall trend of a decrease in normalized error with the application of heat.

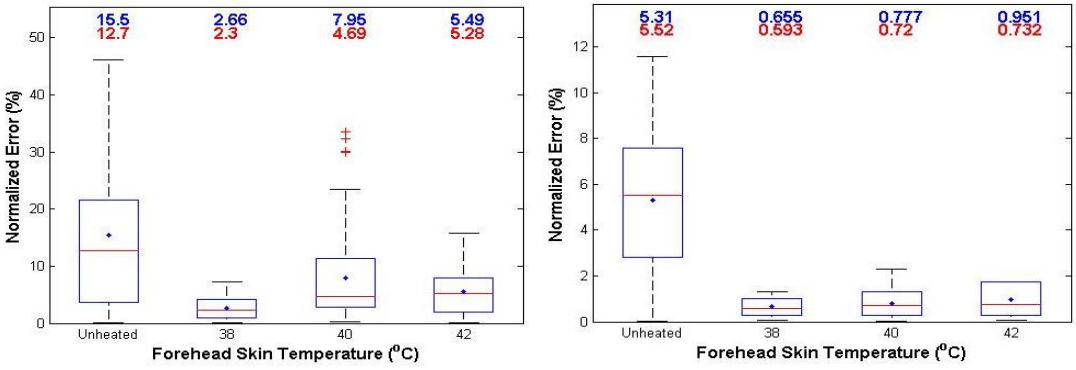

Figure 33: Example Box Plots of Normalized HR (left) and SpO_2 (right) errors during Random Motion

Figure 34 shows the changes in mean normalized HR and SpO_2 measurement error relative to the application of heat to the forehead. The initial introduction of heat, from unheated to 38°C, shows a significant decrease in measurement errors, -8.66% in HR error and -2.00% in SpO_2 error. Among the three heated data sets, little statistical difference existed with errors remaining within a range of 2.25% for HR and 1.62% for SpO_2. While the SpO_2 error at 42°C is only 1.62% below the SpO_2 error at 40°C, the bar is denoted by a red bold to denote its statistical significance in comparison to the unheated data as well as to highlight the fact that its mean relative error falls below 0.5%.

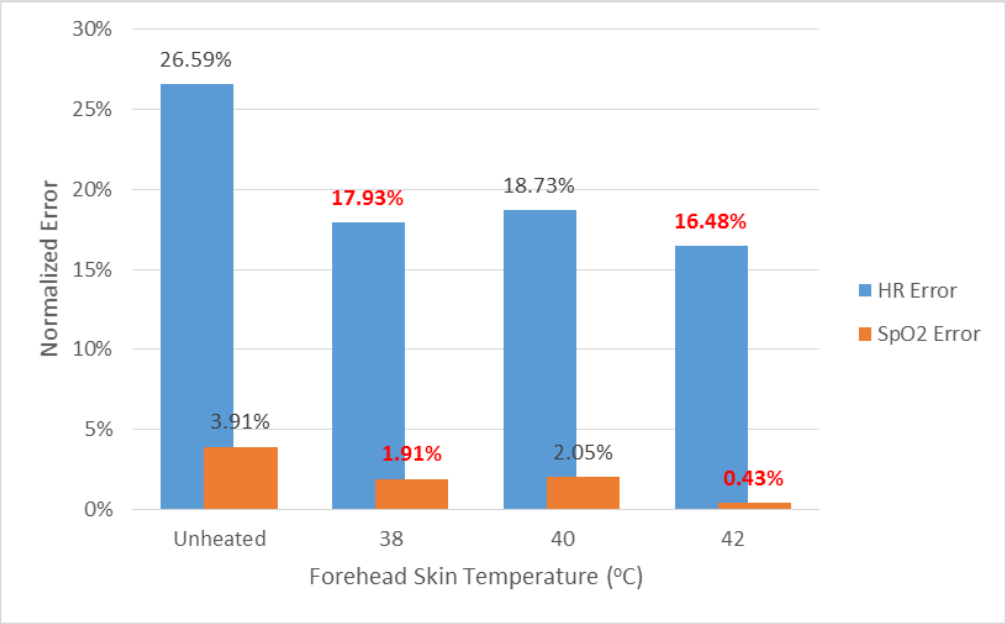

Figure 34: Mean Error of Prototype Measurements versus Applied Heat

The quality of the PPG waveforms was again analyzed by plotting the frequency spectrum for the unheated and heated data sets. The example plot (Figure 35) exhibits the observed trend of increased overall peak magnitude corresponding with the increase in heat. While the A_{in}/A_{out} ratio increased with the application of heat, the progression of increasing heat at 38°C, 40°C, and 42°C did not suggest a strong correlation to a consistent A_{in}/A_{out} trend.

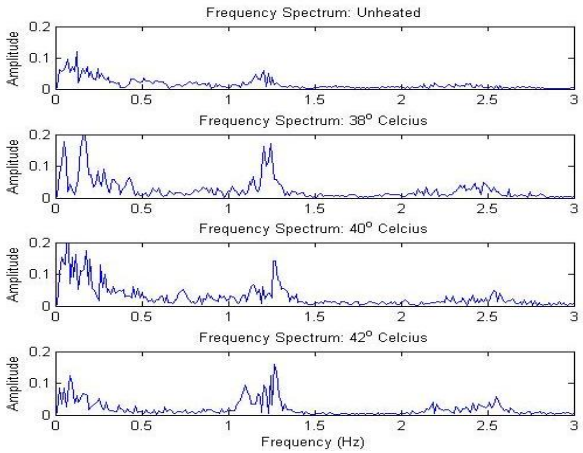

Figure 35: Example Frequency Spectrum for Applied Heat Data Set (Subject L14)

5.3.Applied Pressure

Similar to the sensor weight and applied heat data sets, box plots were again generated from the normalized errors for each subject's HR and SpO_2 measurements during random motion, juxtaposing the data sets for each pressure level. Figure 37 shows example box plots for HR and SpO_2 data, exhibiting the observed trend of an initial increase in normalized HR error at 20mmHg followed by a steep decrease in HR error. The box plots of all the subjects are included in Appendix G and H.

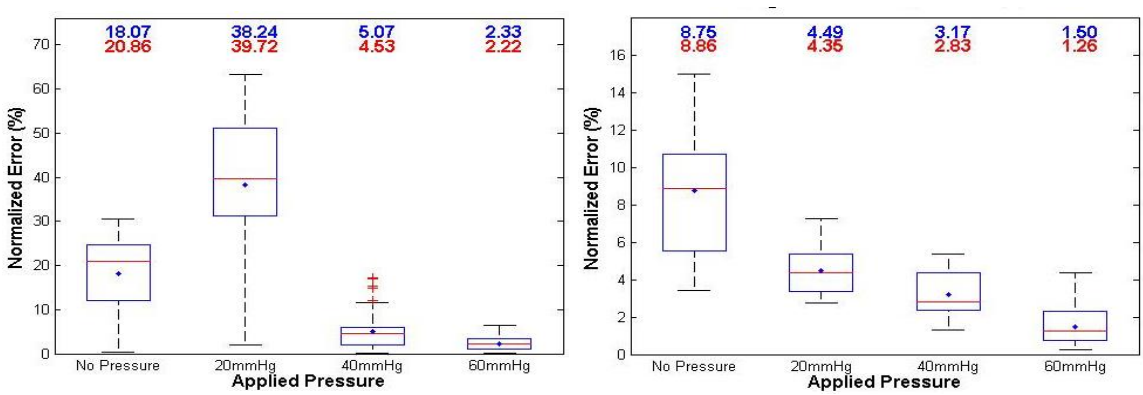

Figure 36: Example Box Plot for Applied Pressure Data Set during Random Motion (Subject K)

Figure 37 shows the mean HR and SpO_2 errors relative to the increase in applied pressure, indicating with bold, red labels the bars that exhibit a statistically significant difference from the previous pressure level. While the SpO_2 errors did not show a significant difference between any of the pressure levels, the mean error remained below 1% for 60mmHg. Conversely, the mean HR error changed significantly between each pressure level, initially increasing by 14.02% from no pressure to 20mmHg, then progressively decreasing by 10.59% to 40mmHg and finally 15.42% to 60mmHg.

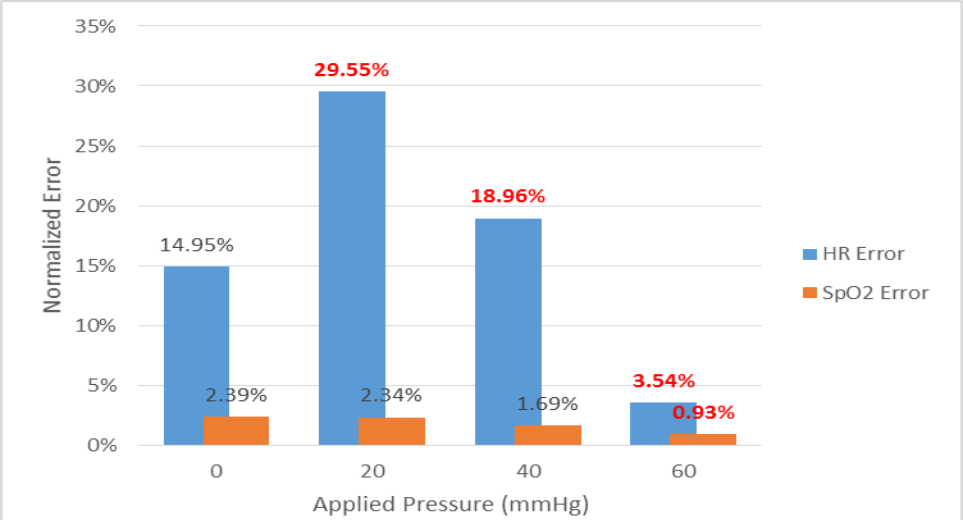

Figure 37: Mean Error of Prototype Sensor Measurements versus Applied Pressure

Similar to the data analysis for sensor weight, the frequency spectra were evaluated between 0-3Hz for each pressure level. Figure 38 shows a representative plot of the frequency spectrums, while Appendix contains all the applied pressure frequency spectra. Qualitatively, the peaks outside the mean heart rate peak were mostly suppressed with the increase in applied pressure.

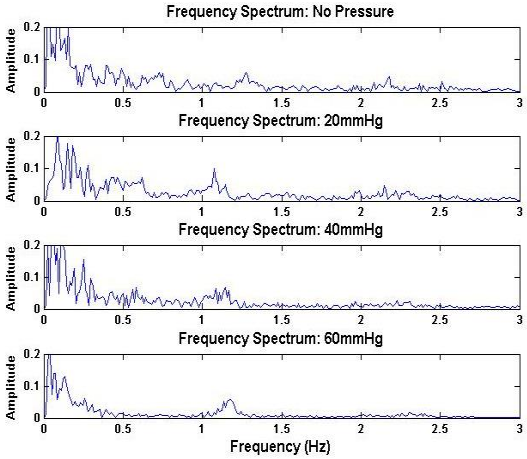

Figure 38: Example Frequency Spectra Comparing Applied Pressures (Subject L14)

Again, the A_{in}/A_{out} ratios were calculated for each pressure level and the corresponding proportional value to the A_{in}/A_{out} ratio for 0mmHg as shown in Equation 7, where the subscript *p* denotes the pressure level being compared. The P_p values for each level of pressure were averaged across all subjects to obtain a mean proportion comparing the A_{in}/A_{out} ratio of each pressure level versus that of minimal applied pressure (Table 3).

$$P_p = \left(\frac{A_{in}}{A_{out}}\right)_p \Big/ \left(\frac{A_{in}}{A_{out}}\right)_{0mmHg} \tag{7}$$

Table 3 Average P_p values for Applied Pressure versus 0mmHg

	20mmHg v. 0mmHg	40mmHg v. 0mmHg	60mmHg v. 0mmHg
P_p	1.21	1.39	1.45

6. Discussion

Since Bland-Altman plots stand as a beneficial tool to compare the correlation between two measurement methods, Bland-Altman plots were generated from the prototype and reference data points collected during rest to verify that the prototype is collecting accurate data before the introduction of motion artifact. As seen from the plots (Appendix A and B), the majority of the data points taken at rest lie within the 95% limits of agreement (denoted by the upper and lower dotted lines located at $\pm$1.96SD) and, thereby, supports the prototype sensor as a reliable pulse oximeter under controlled conditions. Futhermore, the normalized error data calculated during rest establish a general "offset" characteristic that represents the innate difference between the two different sensing sites. This proves useful in adjusting the relative normalized error during random motion by subtracting the mean rest error from the mean random motion error in order to account for these innate differences. Particularly with SpO_2, the prototype sensor often read a higher oxygen content than the finger reference sensor. This is consistent with previous findings that observed a stronger relative ventilation effect on PPG waveforms gathered from the head versus the finger [23].

6.1. Sensor Weight

The overall trend of increased normalized HR error during random motion corresponding to the increased weight, as shown in the box plots (Appendix C) and the graph of mean normalized errors (Section 5.1 Figure 31), suggest that the progressive increase in weight contributes to increased mean normalized HR error for the forehead sensor. Examining the statistical differences between weight levels shows that increases within the first three weight levels (5.6g-16.8g) yield a more drastic consequence in normalized HR error per gram of added weight (2.20% error per gram) compared to the 16.8g-33.6g range (0.56% error per gram). For normalized SpO_2 error, any additional weight beyond the 5.6g bare sensor yielded a significant increase in error, but, did not statistically differ among the 11.2g through 33.6g weight levels. Consequently, the results examining both normalized HR and SpO_2 error suggest that the sensor's accuracy for both HR and SpO_2 measurement is highly subject to any addition of components beyond the minimal weight of the bare optical components, indicated by the greatest % normalized HR error per gram occurring below a sensor weight of approximately 17g and the observed SpO_2 sensitivity to any additional weight beyond the base weight level (5.6g).

The further investigation of the frequency spectra of the PPG waveforms at each weight level provided a method of quantitatively analyzing the primary physiological features of the PPG waveform. While the detriment in PPG waveform characteristics corresponding to the increase in sensor weight could be visibly seen, a more definitive method of evaluation was necessary to provide quantitative support to the qualitative observations. Thus, the frequency spectrum analysis (Section 5.1 Figure 32 and Appendix I) exposes the relative presence of existing frequencies in each waveform, within the target range of 0Hz-3Hz. With the increase of sensor weight, frequency peaks ranging around the 2-3Hz range were introduced and amplified during motion. Quantitatively, this observation is supported by the decrease in proportional A_{in}/A_{out} ratios (Table 1), thereby suggesting an increasing prevalence in frequencies that do not correspond to the subject's true mean HR (calculated from the reference sensor). The correlation between increasing weight and increasing non-HR frequency components suggest that the increased weight amplifies the signal corruption due to motion artifact. Most likely, this effect stems from the increased sensor momentum at the sensing site due to the increased weight, thereby causing greater motion of the optical components relative to the skin and supporting the initial hypothesis.

6.2.Applied Heat

As shown in the box plots (Appendix E and F) and bar graph of the mean normalized errors (Section 5.2 Figure 34), the application of heat yielded a statistically significant decrease in normalized HR and SpO_2 error compared to the unheated data set. The lack of statistical significance in normalized HR error among the three heated levels suggests that the increase in forehead skin temperature from 38^{o}C to 42^{o}C does not provide a beneficial advantage for HR determinations. The improvement of normalized HR errors in the transition between unheated and heated data could be due to the increased PPG signal strength stimulated by local vasodilation, thus resulting in greater changes in blood volume per pulse and thereby greater AC signal amplitudes. The presence of vasodilation is supported by the overall increase in magnitude of the frequency components, indicating the increased PPG signal strength.

Despite the increase in signal-to-noise ratio, false low SpO_2 readings can still occur as a result of venous blood inclusion during motion since the vasodilation would affect both venous and arterial blood. However, the observed results show a continued decrease in normalized SpO_2 error occurring at 42^{o}C with a less than 0.5% normalized SpO_2 error. Juxtaposed with the lack in

change with the normalized HR error, this trend suggests that the increased heat of 42°C could provide additional benefit to combat the false SpO_2 readings, such as in the previously explored concept of blood arterialization.

6.3.Applied Pressure

The box plots (Appendix G and H) and mean normalized errors (Section 5.3 Figure 37) indicate a strong correlation between the application of pressure and the accuracy of HR readings, with the lowest normalized HR error across all three variable's data sets at 60mmHg. This finding corroborates the observation by Dresher, who concluded that an applied pressure between 60-80mmHg at the sensing site exhibited beneficial effects on the stability of PPG waveforms during rest [10]. Since several subjects in this study conveyed discomfort with a headband tightened beyond 60mmHg of pressure at the sensing site, pressure levels beyond 60mmHg were not investigated. In addition, pressures beyond 60mmHg will collapse the fragile capillary beds and could occlude blood flow, especially with the current form using a headband to secure the sensor. Dresher observed contact pressure by applying the pressure solely to the area of the optical components at rest rather than with a headband, so, the subjects most likely had a greater tolerance for the applied pressure without the constricting nature of the pressure and the ability for the blood to circumvent the locally occluded area. Due to the imperfect shape of the human head, it is very possible that in order to apply 60mmHg of pressure at the sensing site the headband applied greater levels of pressure at different areas of the head thereby causing the discomfort. The initial increase in HR error as a result of the application of 20mmHg pressure demonstrates an inconsistency with previous findings; however, at such a light pressure, the headband applying the pressure most likely contributed more as an additional weight rather than an application of pressure. As the pressure increased to 40mmHg and 60mmHg, the effects of the additional weight were overshadowed by the effects of the applied pressure.

Examining the PPG waveforms' frequency spectrums (Appendix K), an overall suppression of frequency components outside the mean HR frequency was observed at 40mmHg and 60mmHg of applied pressure. This observation is corroborated by the increasing mean A_{in}/A_{out} ratio proportional to the A_{in}/A_{out} ratio at 0mmHg (Table 3), thereby indicating an increasing relative prevalence of the HR frequency component and a reduction in the effects of extraneous motion. In addition to the stabilizing transmural pressure, the application of pressure with the headband could have contributed to the stabilization of the underlying capillary beds during the

random motion. The slight compression of the forehead skin could also contribute to the decreased distance between the optical components and the underlying bone reflecting the light, thus increasing the photodetector's ability to detect a greater amount of backscattered light.

7. Conclusions

The present study investigated the sources of motion artifact in reflective forehead pulse oximetry in a "simulated military transport environment" by exploring the relative effects of sensor weight, applied heat and applied pressure during random motion. In accordance with IRB approval, HR, SpO_2 and PPG measurements were collected from 15 human volunteers using an investigational forehead prototype pulse oximeter. Comparing the error of the measurements from the forehead prototype with the reference measurements simultaneously collected from a reference sensor, the results of the sensor weight study showed that increased weight leads to increased HR and SpO_2 error. Additionally, analysis of the PPG waveform indicated an increase in sensor movement corresponding to increased weight, thereby supporting the hypothesis that the increased measurement error stems from increased sensor movement relative to the underlying tissue. For applied heat, the application of heat in the 38°C-42°C range corresponded to a decrease in HR and SpO_2 error, due to the presence of localized vasodilation; however, little difference in HR accuracy was observed among the forehead skin temperatures of 38°C, 40°C and 42°C. A continued decrease in normalized SpO_2 error was observed at 42°C (mean normalized error below 0.5%), potentially indicative of the effects of "blood arterialization." Lastly, data collected during the exploration of applied pressure showed a decrease in normalized HR error with applied pressures of 40mmHg and 60mmHg, the latter of which corresponded to a mean normalized error of 3.5%. The frequency spectrum analysis of the PPG waveforms at each pressure level exhibited a suppression of interfering frequency components at 40mmHg and 60mmHg, thereby indicating a reduction in the effects of extraneous motion with the application of 40mmHg and 60mmHg of applied pressure.

Assessing the normalized errors within the context of physiological equivalents, the percent normalized SpO_2 error can be directly to the percent measurement of SpO_2, with 1% normalized error correlating to 1% SpO_2. On the other hand, since the HR of each subject varied, the correlation between percent normalized error (%) and absolute HR error (bpm) varied per subject. Therefore, an average all the subject's HR was calculated to be approximately 76.31 bpm in order to develop the average relationship of 1% normalized HR error correlating to an error of 0.76 bpm. Current clinical devices, such as Nonin, have a measurement accuracy of $\pm$ 2% for SpO_2 and $\pm$3 bpm for HR. Within the context of normalized error in the present study, these specifications correlate to roughly 2% normalized SpO_2 error and 3.94% normalized HR

error. The average normalized SpO_2 errors observed in the 5.6g, 38°C, 40°C, 42°C, 40mmHg and 60mmHg data sets remain at or below a measurement accuracy of 2% normalized SpO_2 error. On the other hand, the 60mmHg data set was the only that remained within a $\pm$ 3bpm measurement accuracy. The next lowest average percent normalized HR error was recorded by the 5.6g data set, correlating to an average measurement accuracy of $\pm$11.36 bpm which still remains too significant of an inaccuracy for a field device. Therefore, given the evaluation of the variables with regards to an acceptable measurement accuracy range, the present findings support applying a pressure of 60mmHg at the sensing site with a headband as the most influential variable in combatting the effects of motion artifact. However, it should be noted that the 60mmHg data set was conducted with minimal sensor weight.

8. Recommendations

Since the purpose of the present study was to investigate the relative effects of sensor weight, locally applied heat and pressure on motion artifact, the reported results suggest design guidelines for the development of a more motion-tolerant forehead pulse oximeter. The exploration of sensor weight proposes that an optimal design would reduce the sensor weight at the sensing site to at or below 5.6g to minimize HR and SpO_2 measurement error. For military applications, additional components for signal processing, wireless transmission and power will most likely be necessary in order to enable remote monitoring and transmit data. With the present technology, these additional components will introduce a weight component greater than the recommended value. However, these components could be located elsewhere on the body (i.e. back of the head) and connected to the optical components located at the sensing site by a thin and flexible shielded wire. Additionally, the results suggest that applying and maintaining a localized forehead skin temperature of 42^{o}C would be the most beneficial for reducing HR error through vasodilation and combating false low SpO_2 errors through stimulating blood arterialization. Practically, maintaining a forehead skin temperature at 42^{o}C for extended periods of time could prove uncomfortable for a subject and would increase power consumption, requiring more battery power or decreasing wireless sensor life. Therefore, maintaining a forehead skin temperature between 38^{o}C-42^{o}C will still prove sufficient since +/-3% in SpO_2 measurement for a field application would still lie within an acceptable medical tolerance. Lastly, the results from the exploration of applied pressure suggest that a motion tolerant sensor should apply 60mmHg of pressure at the sensing site to reduce HR measurement error and increase PPG waveform stability. Optimally, this pressure would be applied with a headband, such as in the present study. Within the context of field applications, this serves as a practical implementation for an improved wearable pulse oximeter. However, in the case of military applications, soldiers often wear helmets which could introduce additional pressure on the forehead depending on the fit of the helmet. Thus, in the given military setting, additional care must be paid to ensure approximately 60mmHg of pressure at the sensing site.

References

[1] Cox, P., Madsen, C., Ryan, K. L., Convertino, V. A., & Jovanov, E., "Investigation of photoplethysmogram morphology for the detection of hypovolemic states." Paper presented at the *Engineering in Medicine and Biology Society, EMBS 2008. 30th Annu. Int. Conf IEEE, pp.* 5486-5489.

[2] Mendelson, Y. "Pulse oximetry: Theory and applications for noninvasive monitoring." *Clinical Chemistry,* vol. 38, pp. 1601-1607, 1992.

[3] Mendelson, Y. "Pulse oximetry." *Wiley encyclopedia of biomedical engineering*. John Wiley & Sons, Inc. 2006.

[4] Mannheimer, P.D., "The Light-Tissue Interaction of Pulse Oximetry," *Anesthesia & Analgesia,* vol, 105, no. 6, Dec, 2007.

[5] Barker, S.J., "'Motion-Resistant' Pulse Oximetry: A Comparison of New and Old Models," *Anesthesia & Analgesia,* vol. 95, no. 4, Oct 2002.

[6] McGrath, S.P., Ryan, K.L., Wendelken, S.M, Rickards, C.A. & Convertino, V.A., "Pulse Oximeter Plethysmographic Waveform Changes in Awake, Spontaneously Breathing, Hypovolemic Volunteers," *Anesthesia & Analgesia*, vol. 112, no. 2, Feb 2011.

[7] Convertino, V.A., Moulton, S.L., Grudic, G.L., Rickards, C.A. Hinojosa-Laborde, C., Gerhardt, R.T., & Ryan, K.L. "Use of advanced machine-learning techniques for noninvasive monitoring of hemorrhage," *Journal of Trauma-Injury, Infection, and Critical Care,* vol. 71, no. 1, p. S25-S32, 2011.

[8] Mendelson, Y., & Ochs, B. "Noninvasive pulse oximetry utilizing skin reflectance photoplethysmography." *IEEE Trans. on Biomed. Eng.,* vol. 35, no. 10, pp. 798-805, 1988.

[9] Kim, J., Arakawa, K., Benson, K., & Fox, D. "Pulse oximetry and circulatory kinetics associated with pulse volume amplitude measured by photoelectric plethysmography." *Anesthesia & Analgesia,* vol. 65, pp. 1333-13339, 1986.

[10] Dresher, R. *Wearable forehead pulse oximetry: Minimization of motion and pressure artifacts.* (Thesis). Worcester Polytechnic Institute: Mendelson, Yitzhak. 2006.

[11] Comtios, G., Mendelson, Y., and Ramuka, P., "A Comparative Evaluation of Adaptive Noise Cancellation Algorithms for Minimizing Motion Artifacts in a Forehead-Mounted Wearable Pulse Oximeter," *Proc. 29th Annu. Int. Conf. IEEE EMBS,* Cité Internationale, Lyon, France, 2007, pp. 1529-1531

[12] Vogel, S., Hulsbusch, M., Diermar, S. & Leonhardt, S. " A System for Assessing Motion Artifact in the Signal of a Micro-Optic In-Ear Vital Signs Sensor," *30th Annu. Int. IEEE EMBS Conf.,* Vancouver, B.C., Canada, 2008.

[13] Mendelson, Y., and McGinn, M.J., "Skin Reflectance Pulse Oximetry: In Vivo Measurements from the Forearm and Calf," *Journal of Clinical Monitoring*, vol. 7, no. 1, Jan 1991.

[14] Asada, H.H. et al, "Mobile Monitoring with Wearable Photoplethysmographic Biosensors" *IEEE Engineering in Medicine and Biology Magazine,* May/Jun 2003.

[15] Gibbs, P. & Asada, H.H, "Reducing Motion Artifact in Wearable Biosensors Using MEMS Accelerometers for Active Noise Cancellation,"*2005 American Control Conf.,* Portland, OR, 2005.

[16] Vogel, S., Hulsbusch, M., Henning, T., Blazek, V., & Leonhardt, S. "In-ear vital signs monitoring using a novel microoptic reflective sensor." *IEEE Transaction on Information Technology in Biomedicine,* vol. 13(6), pp. 882-889, 2009.

[17] Venema, B., Blanik, N., Blazek, V., Gehring, H., Opp, A., & Leonhardt, S., "Advances in Reflective Oxygen Saturation Monitoring with a Novel In-Ear Sensor System: Results of a Human Hypoxia Study," *IEEE Trans. Biomed. Eng.,* vol. 59, no. 7, Jul 2012.

[18] Nagre, A., & Mendelson, Y. "Effects of motion artifacts on pulse oximeter readings from different facial regions." Paper presented at the *Bioengineering Conference, 2005. Proceedings of the IEEE 31st Annual Northeast,* 220-222.

[19] Mendelson, Y., Dao, D. K., & Chon, K. H. "Multi-channel pulse oximetry for wearable physiological monitoring." Paper presented at the *Body Sensor Networks (BSN), 2013 IEEE International Conference.* 2013.

[20] Teng, X. F., & Zhang, Y. T. "The effects of contacting force on photoplethysmographic signals." *Physiological Measurement,* vol. 25, pp.1323-1335, 2004.

[21] Santos, S.A., Venema, B., & Leonhardt, S., "Accelerometer-assisted PPG Measurement During Physical Exercise Using the LAVIMO Sensor System," *Acta Polytechnica,* vol. 52, no. 5, pp. 80-85, 2012.

[22] Santos, P., Almeida, V., Cardoso, J., & Correia, C. "Photoplethysmographic logger with contact force and hydrostatic pressure monitoring." *3rd Portuguese Bioengineering Meeting,* University of Minho. 2013.

[23] Shelley, K.H., Jablonka, D.H., Awad, A.A., Stout, R.G., Rezkanna, H., Siverman, D.G., "What is the Best Site for Measuring the Effect of Ventilation on the Pulse Oximeter Waveform?" *Anesthesia & Analgesia*, vol. 103, no. 2, p.372-277, Aug. 2006.

Appendix A: HR Bland-Altman Plots

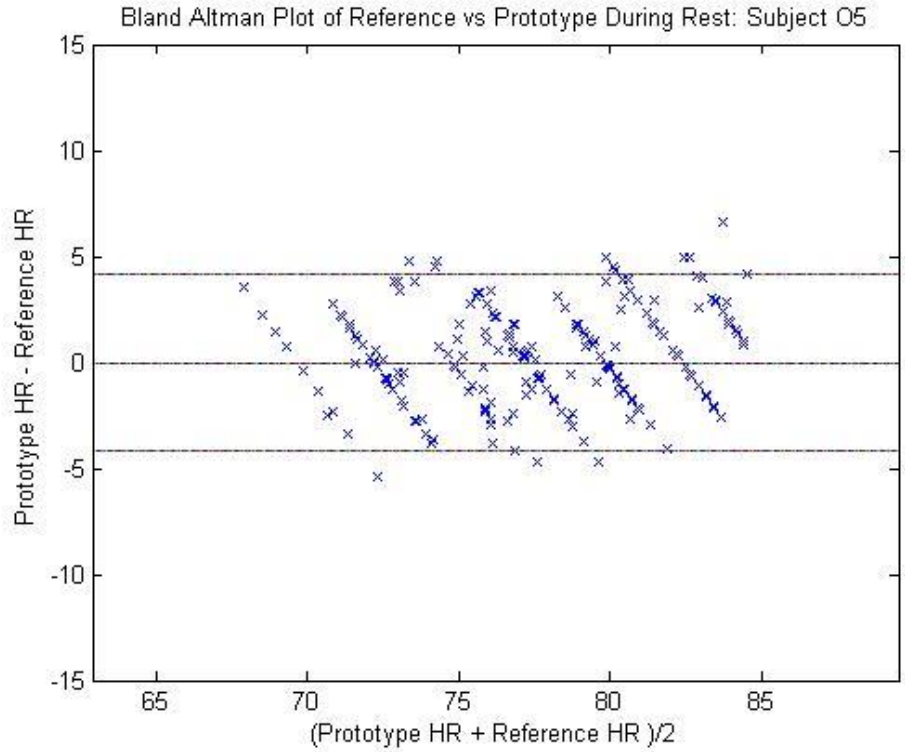

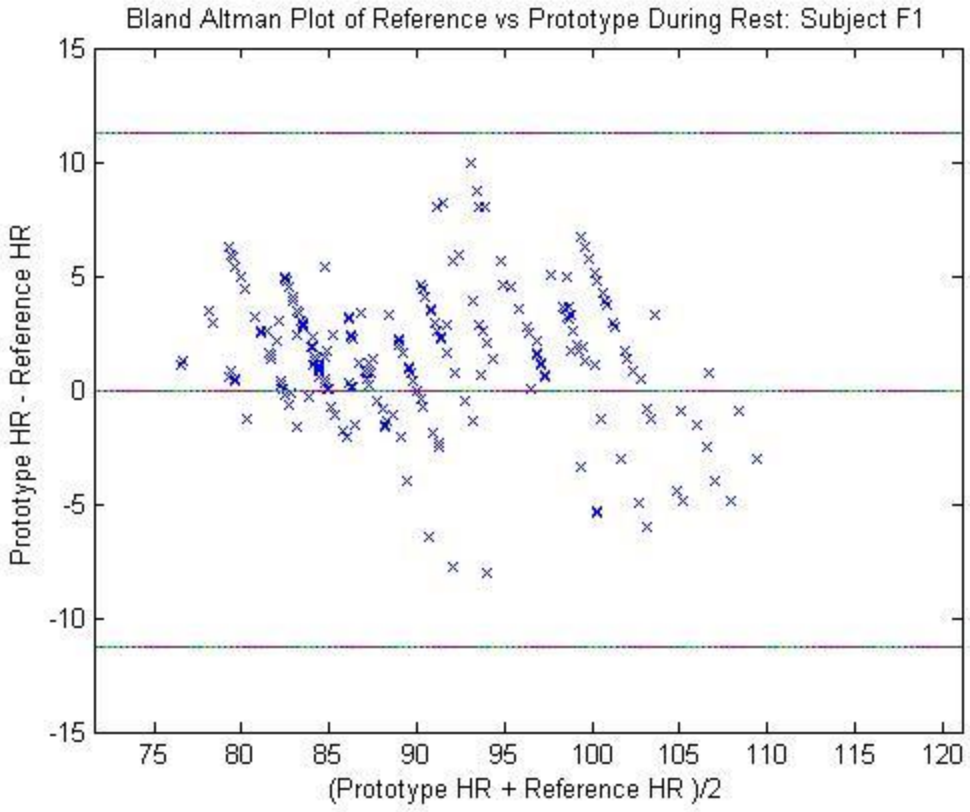

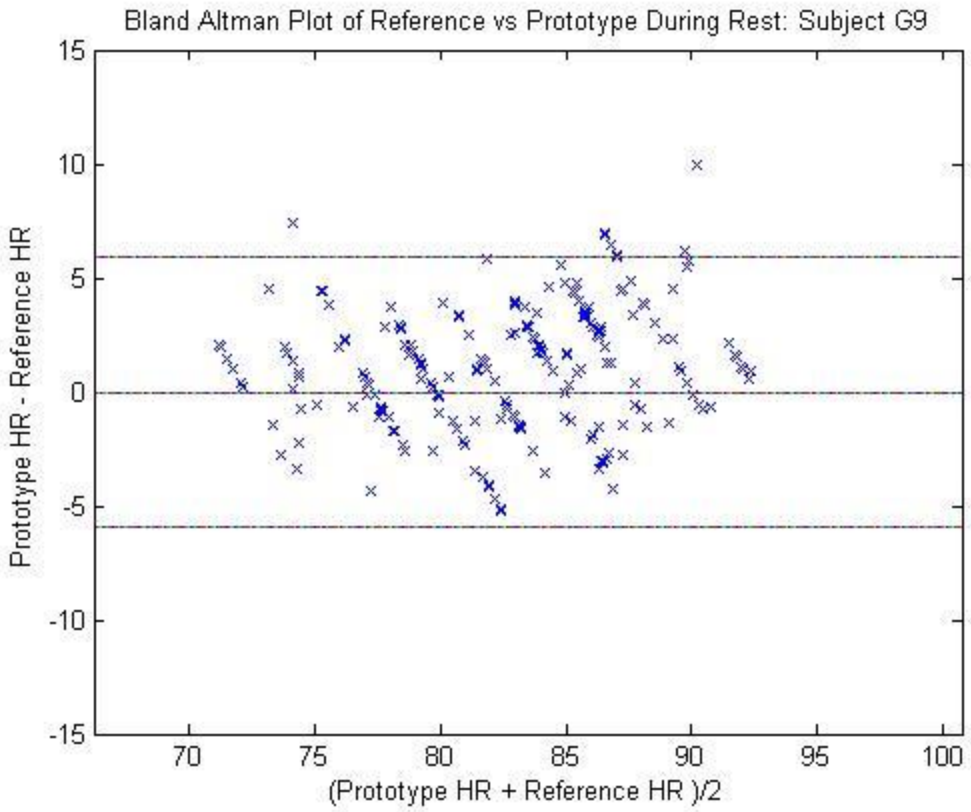
Bland Altman Plot of Reference vs Prototype During Rest: Subject G9
Prototype HR - Reference HR
(Prototype HR + Reference HR)/2
15
10
5
0
-5
-10
-15
70
75
80
85
90
95
100

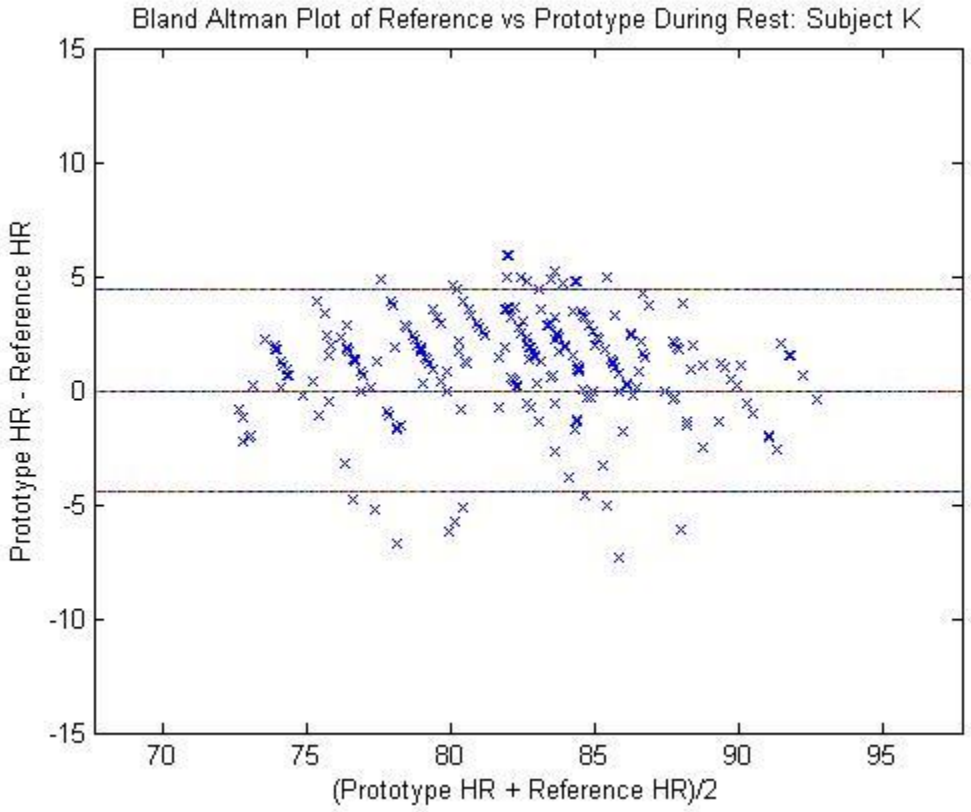
Bland Altman Plot of Reference vs Prototype During Rest: Subject K
Prototype HR - Reference HR
(Prototype HR + Reference HR)/2
15
10
5
0
-5
-10
-15
70
75
80
85
90
95

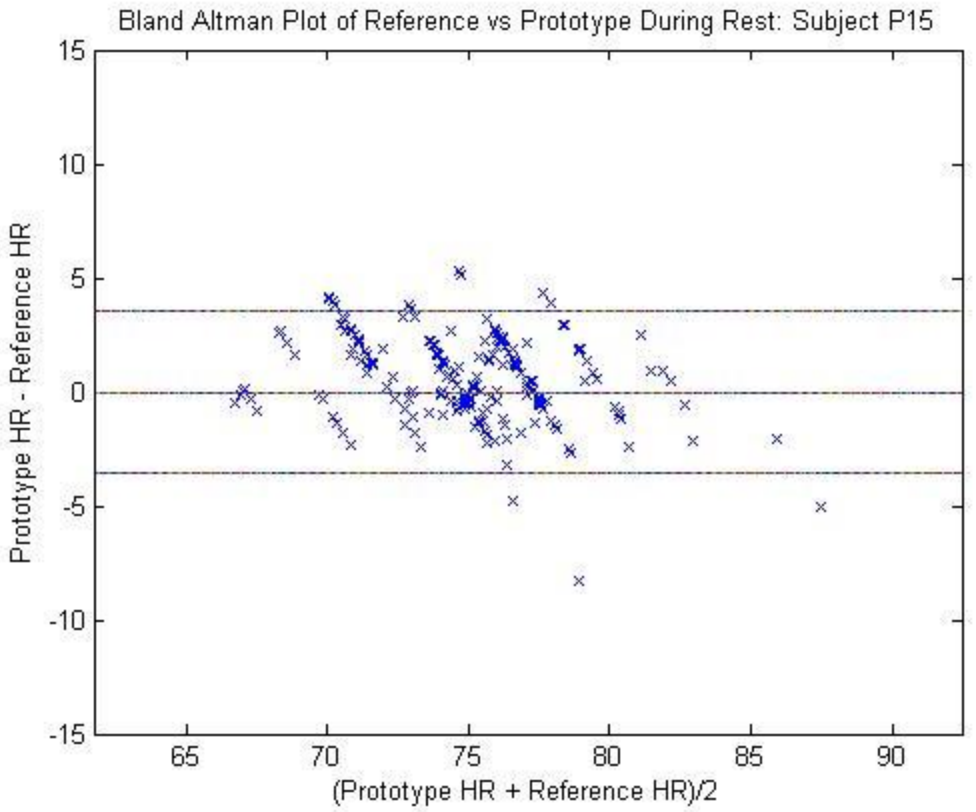
Bland Altman Plot of Reference vs Prototype During Rest: Subject P15
Prototype HR - Reference HR
(Prototype HR + Reference HR)/2
15
10
5
0
-5
-10
-15
65
70
75
80
85
90

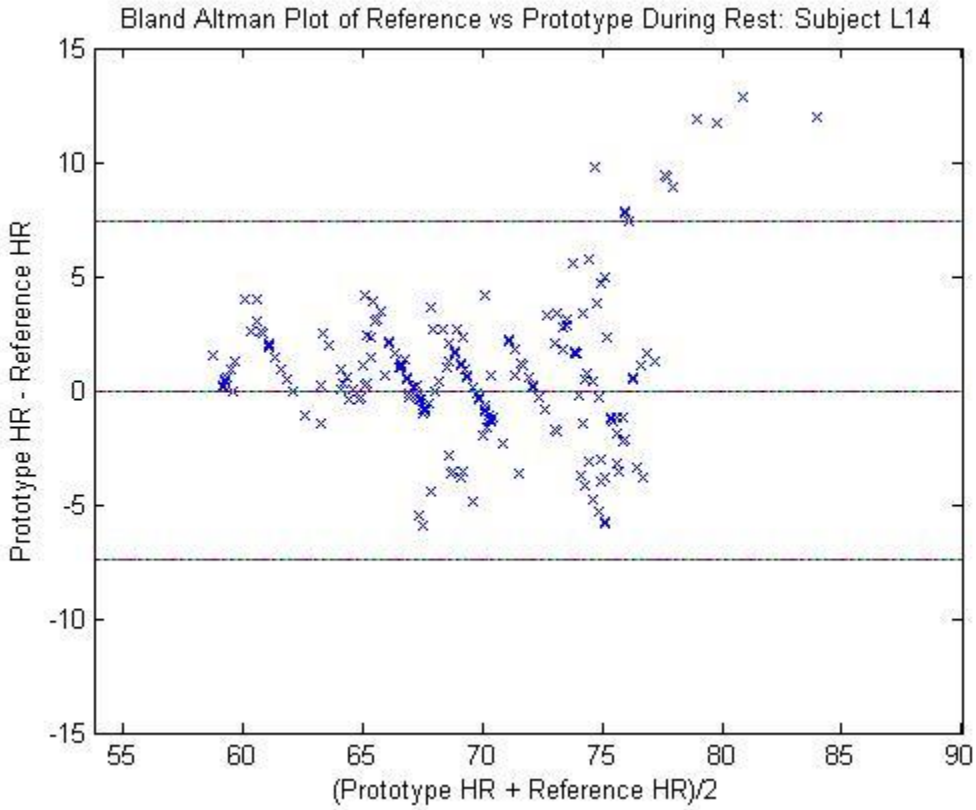
Bland Altman Plot of Reference vs Prototype During Rest: Subject L14
Prototype HR - Reference HR
(Prototype HR + Reference HR)/2
15
10
5
0
-5
-10
-15
55
60
65
70
75
80
85
90

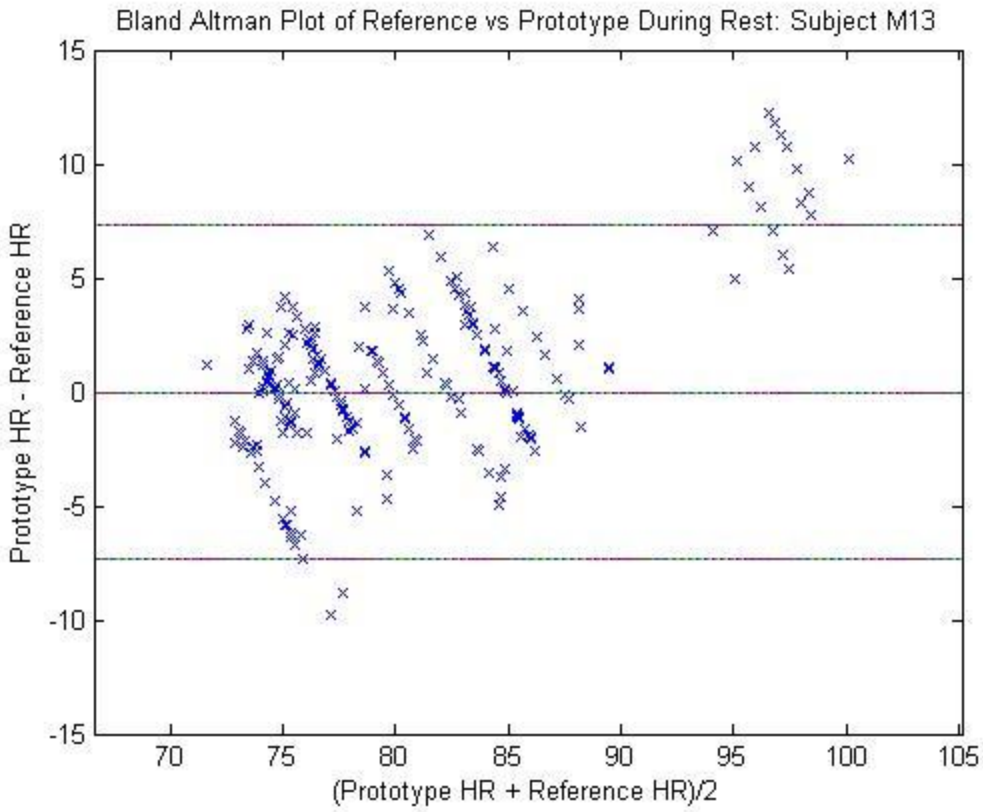
Bland Altman Plot of Reference vs Prototype During Rest: Subject M13
Prototype HR - Reference HR
(Prototype HR + Reference HR)/2
15
10
5
0
-5
-10
-15
70
75
80
85
90
95
100
105

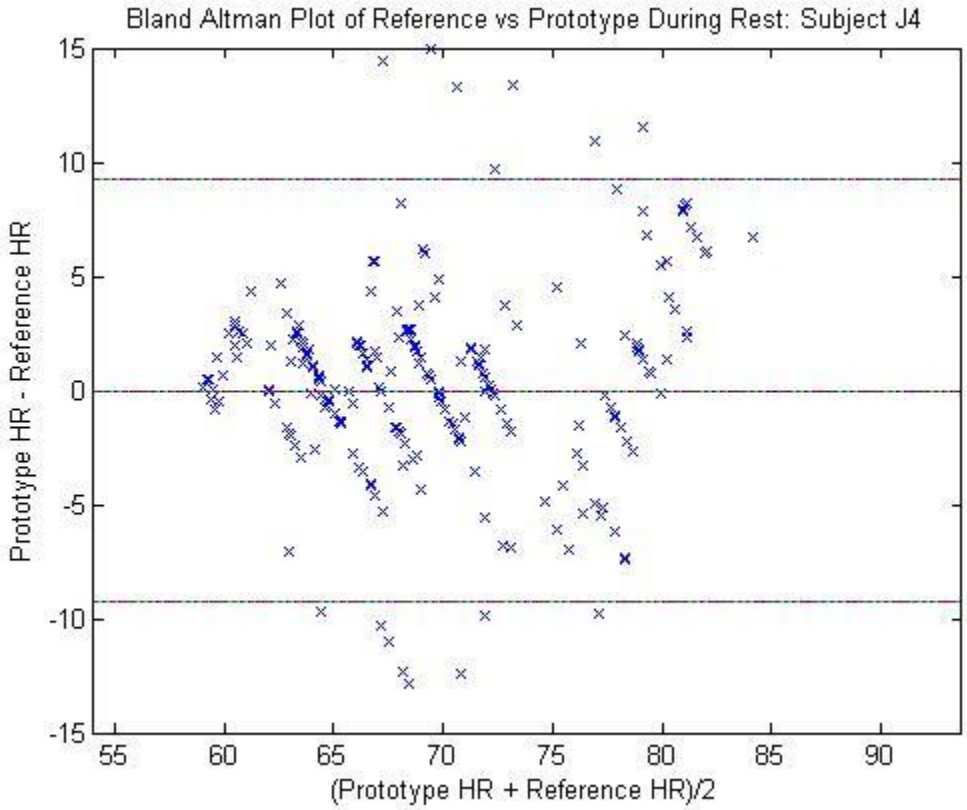
Bland Altman Plot of Reference vs Prototype During Rest: Subject J4
Prototype HR - Reference HR
(Prototype HR + Reference HR)/2
15
10
5
0
-5
-10
-15
55
60
65
70
75
80
85
90

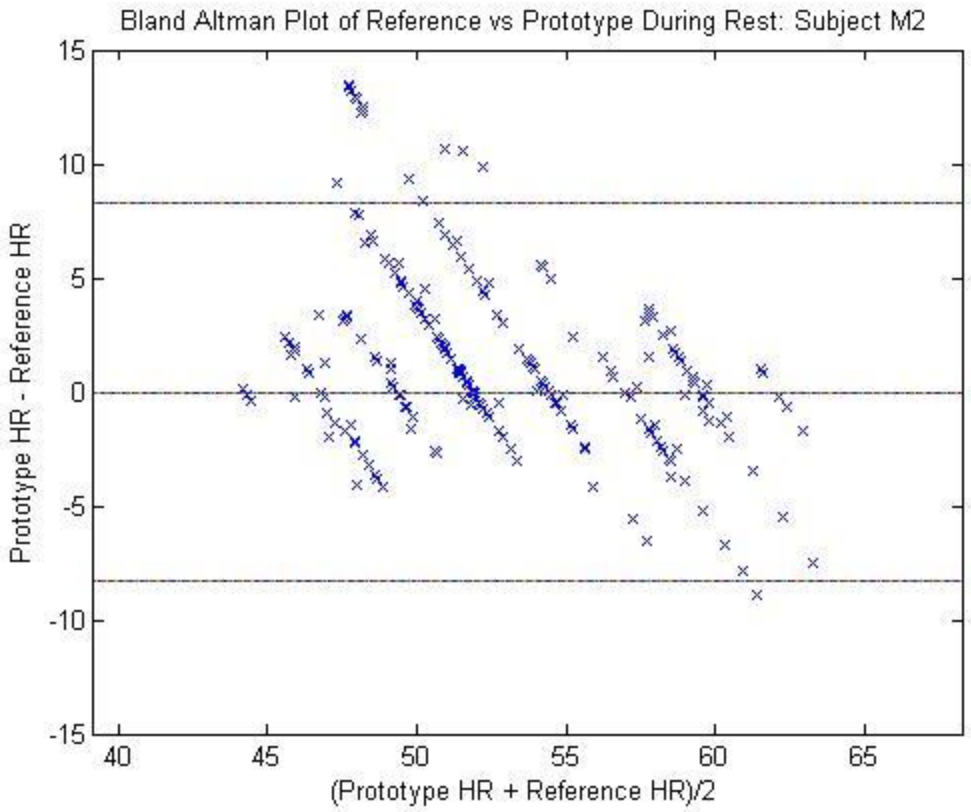
Bland Altman Plot of Reference vs Prototype During Rest: Subject M2
Prototype HR - Reference HR
(Prototype HR + Reference HR)/2
15
10
5
0
-5
-10
-15
40
45
50
55
60
65

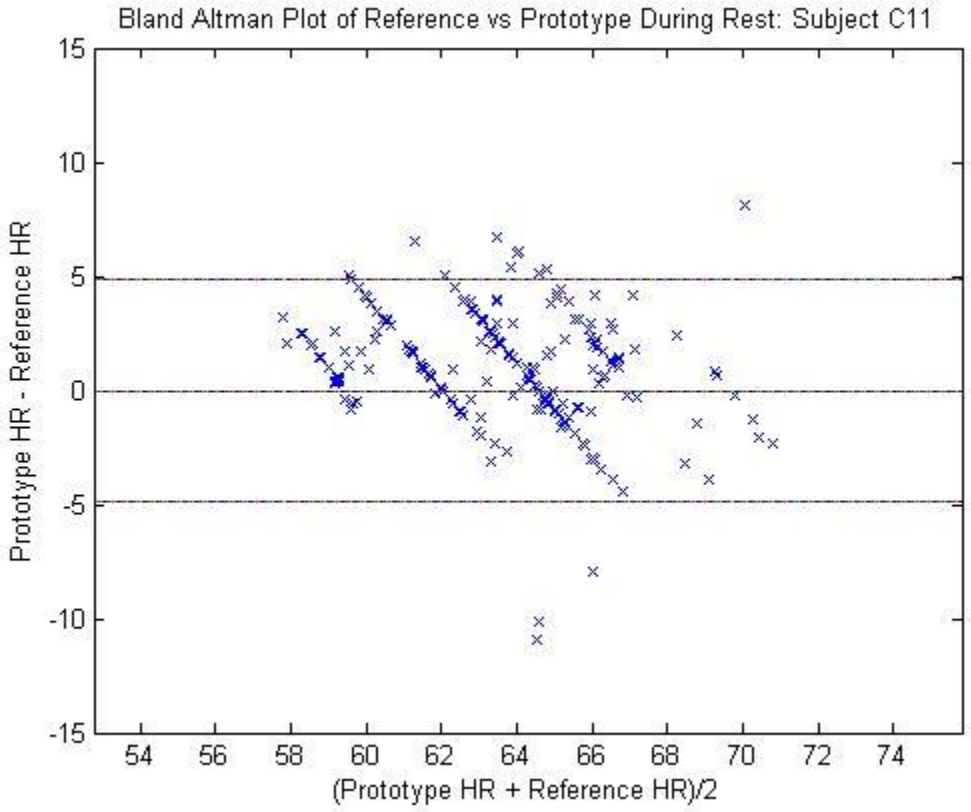
Bland Altman Plot of Reference vs Prototype During Rest: Subject C11
Prototype HR - Reference HR
(Prototype HR + Reference HR)/2
15
10
5
0
-5
-10
-15
54
56
58
60
62
64
66
68
70
72
74

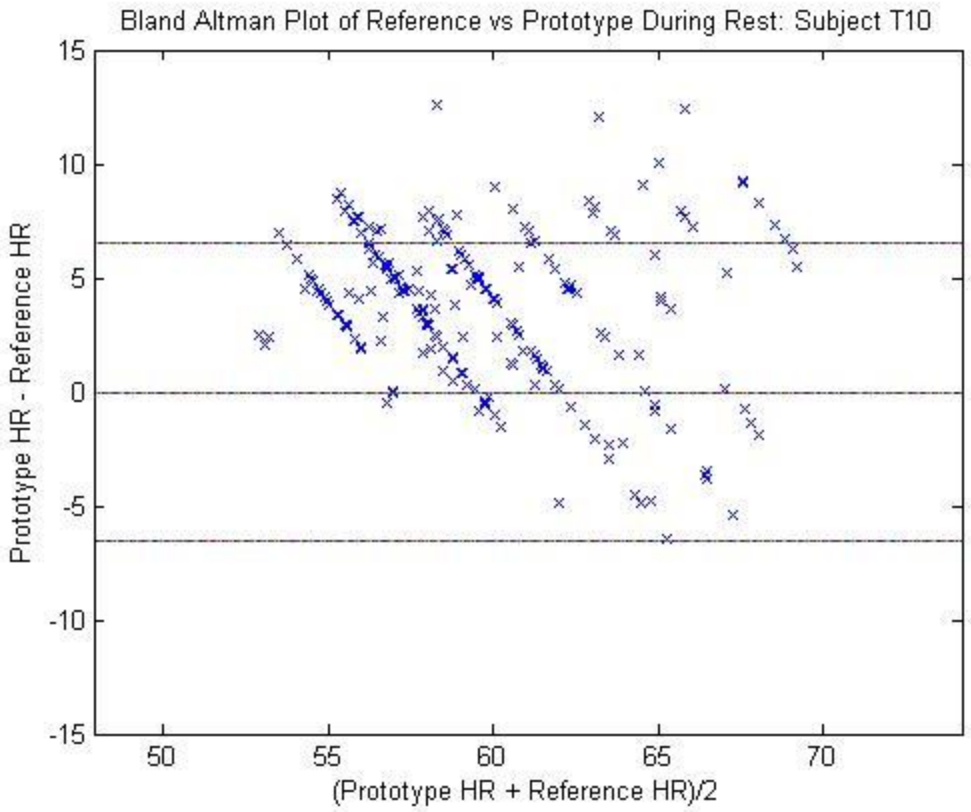
Bland Altman Plot of Reference vs Prototype During Rest: Subject T10
Prototype HR - Reference HR
(Prototype HR + Reference HR)/2
15
10
5
0
-5
-10
-15
50
55
60
65
70

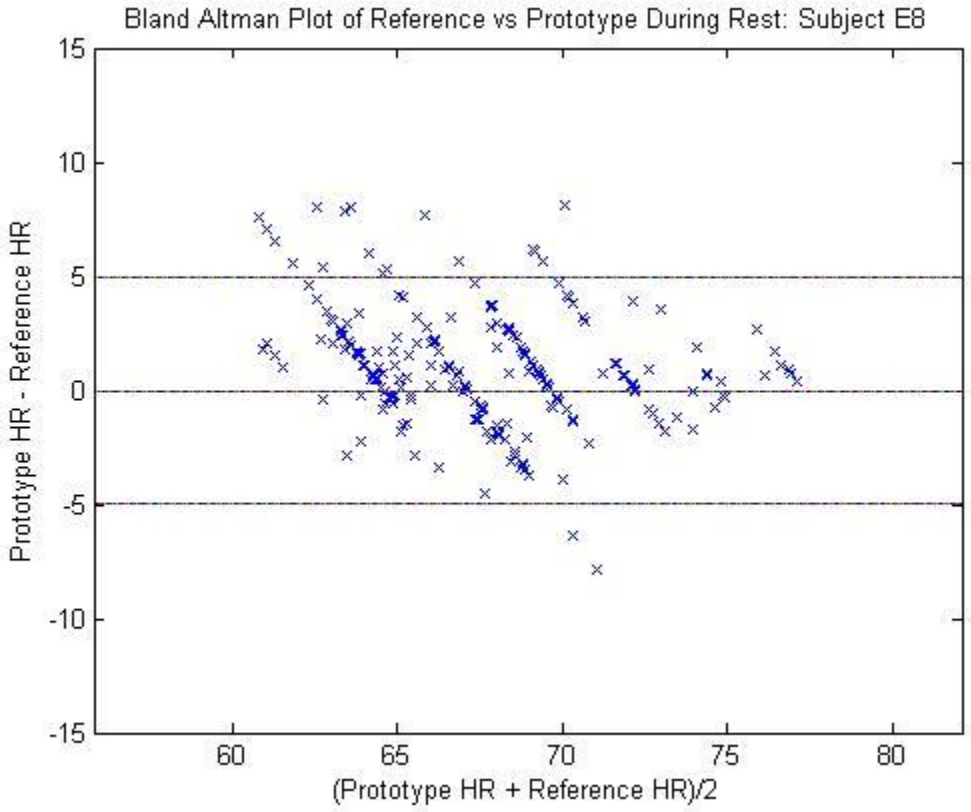
Bland Altman Plot of Reference vs Prototype During Rest: Subject E8
Prototype HR - Reference HR
(Prototype HR + Reference HR)/2
15
10
5
0
-5
-10
-15
60
65
70
75
80

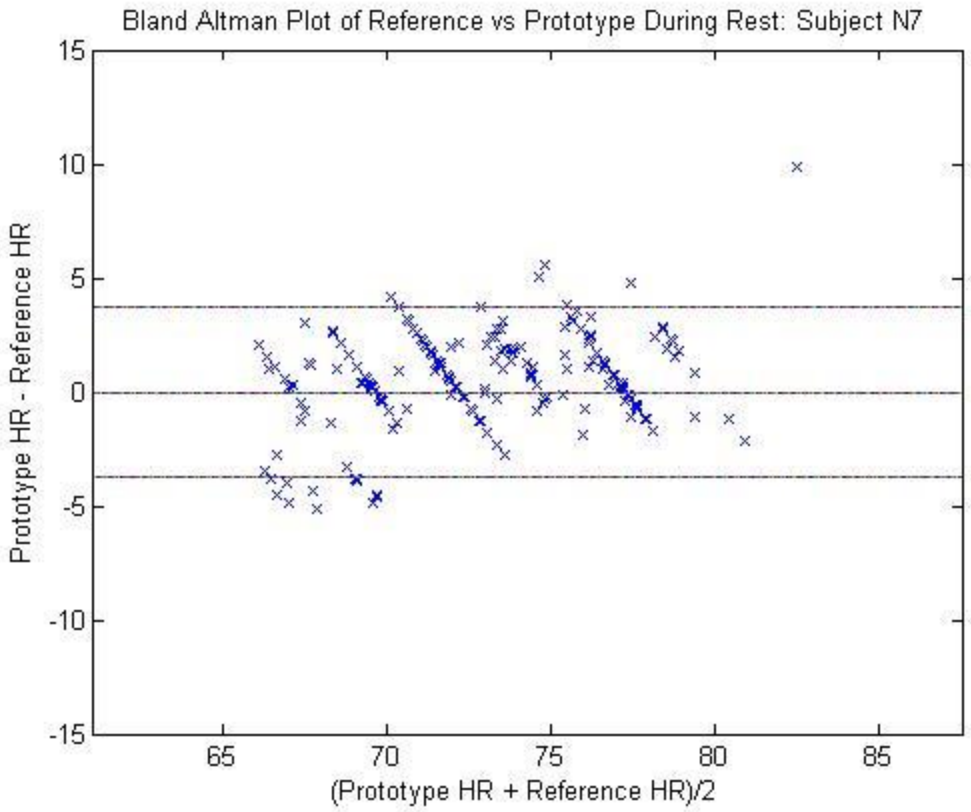
Bland Altman Plot of Reference vs Prototype During Rest: Subject N7
Prototype HR - Reference HR
(Prototype HR + Reference HR)/2
15
10
5
0
-5
-10
-15
65
70
75
80
85

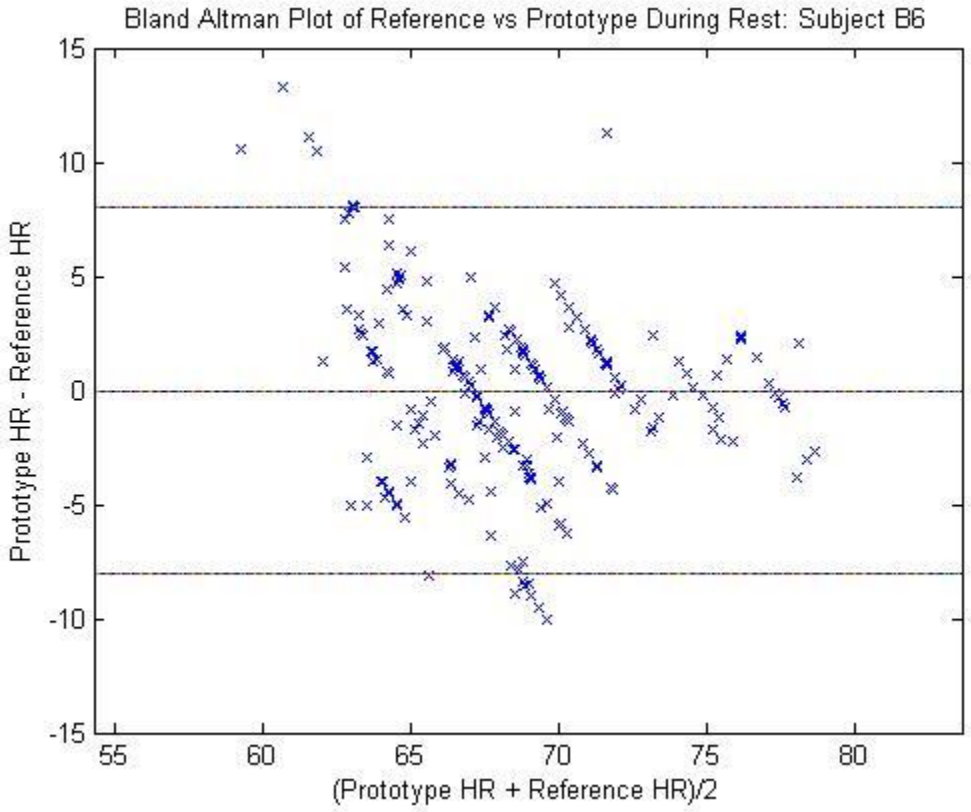
Bland Altman Plot of Reference vs Prototype During Rest: Subject B6
Prototype HR - Reference HR
(Prototype HR + Reference HR)/2
15
10
5
0
-5
-10
-15
55
60
65
70
75
80

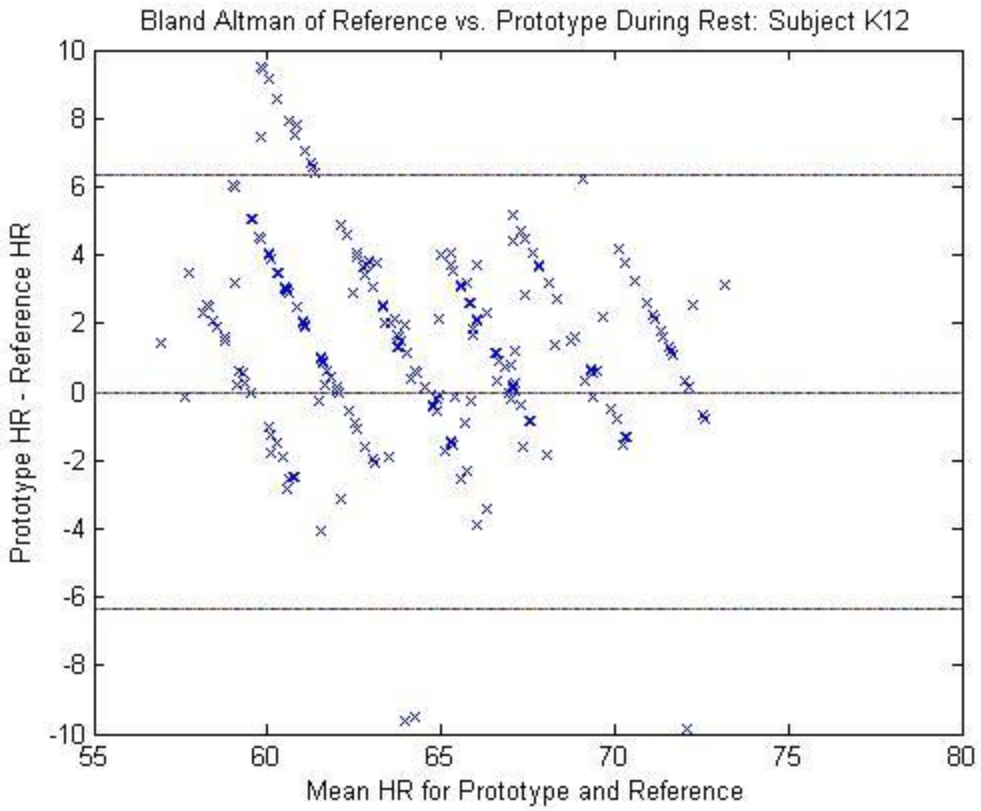
Bland Altman of Reference vs. Prototype During Rest: Subject K12
Prototype HR - Reference HR
Mean HR for Prototype and Reference
10
8
6
4
2
0
-2
-4
-6
-8
-10
55
60
65
70
75
80

Appendix B: SpO_2 Bland-Altman Plots

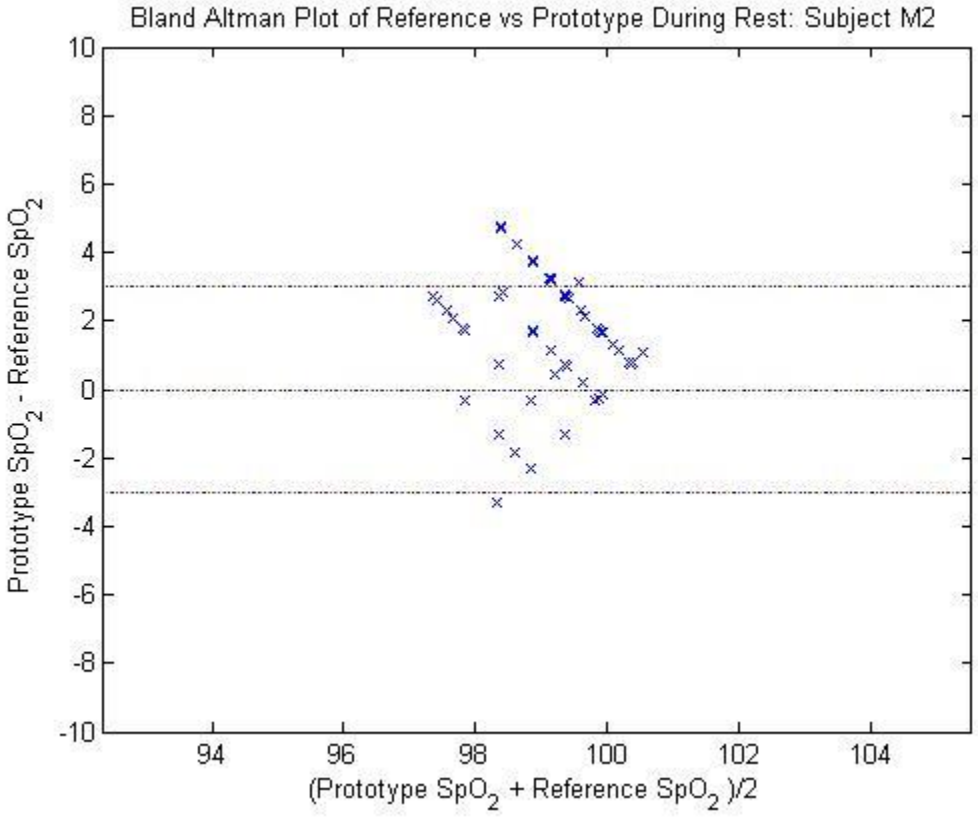

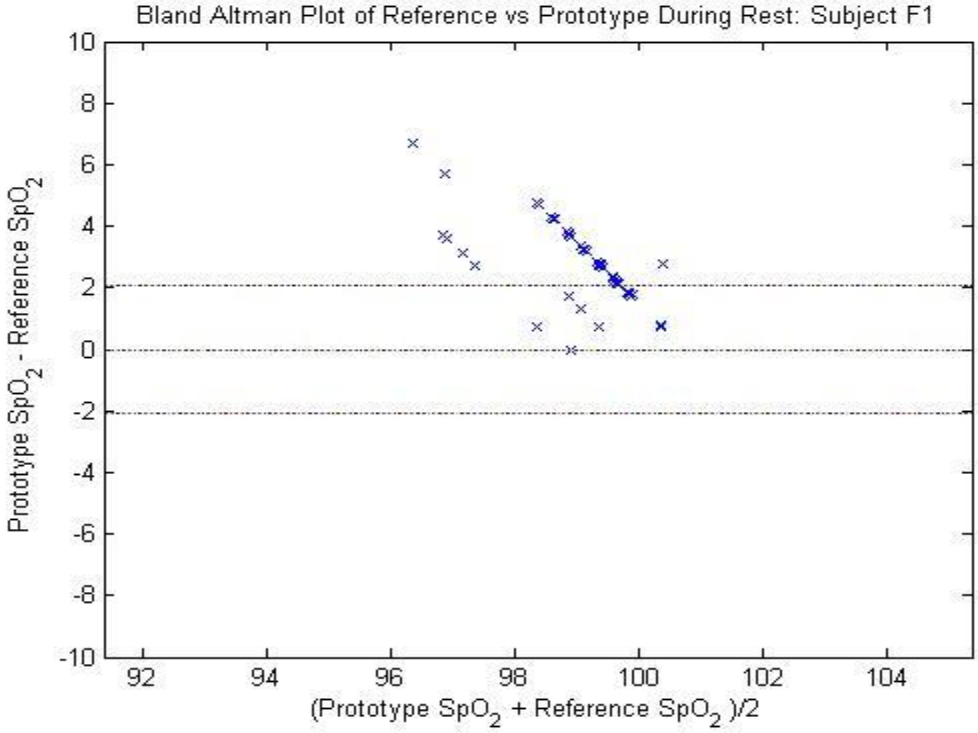

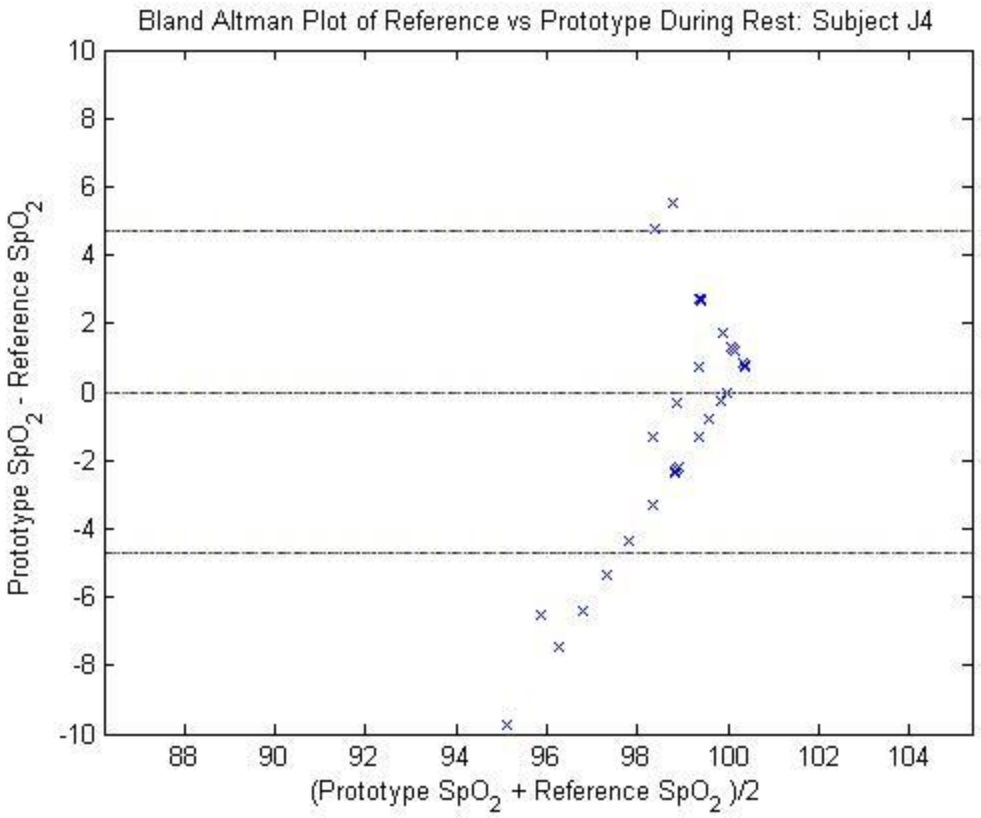
Bland Altman Plot of Reference vs Prototype During Rest: Subject J4
Prototype SpO2 - Reference SpO2
(Prototype SpO2 + Reference SpO2)/2
10
8
6
4
2
0
-2
-4
-6
-8
-10
88
90
92
94
96
98
100
102
104

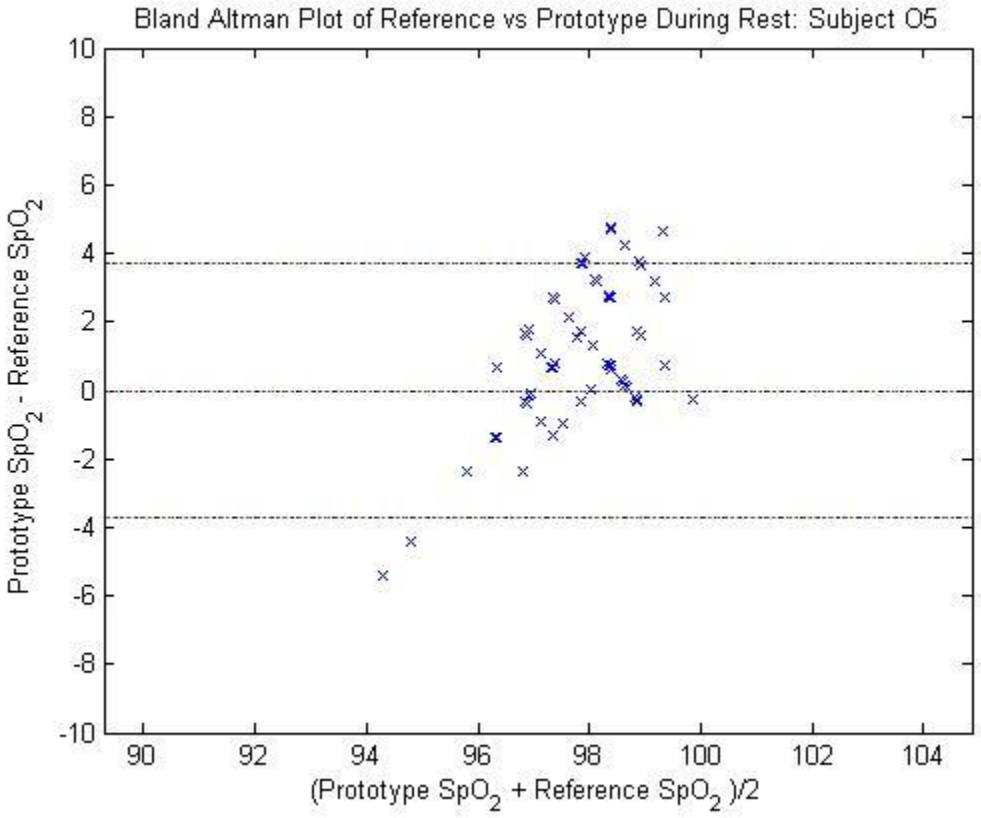
Bland Altman Plot of Reference vs Prototype During Rest: Subject O5
Prototype SpO2 - Reference SpO2
(Prototype SpO2 + Reference SpO2)/2
10
8
6
4
2
0
-2
-4
-6
-8
-10
90
92
94
96
98
100
102
104

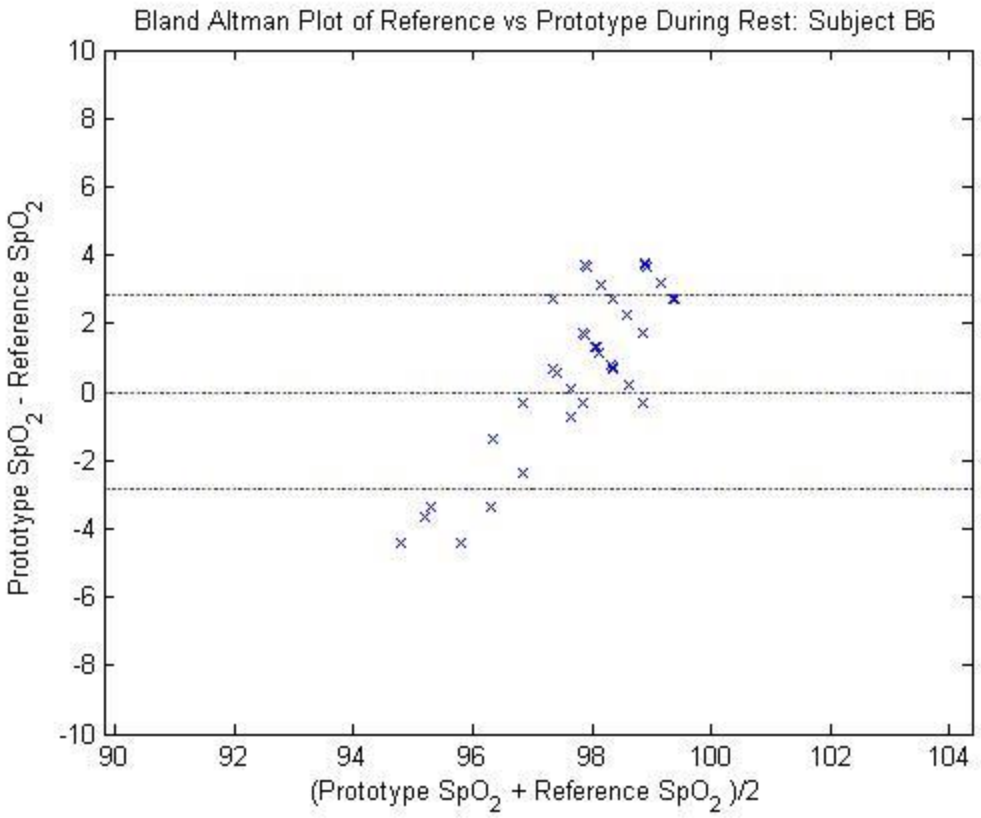
Bland Altman Plot of Reference vs Prototype During Rest: Subject B6
Prototype SpO2 - Reference SpO2
(Prototype SpO2 + Reference SpO2)/2
10
8
6
4
2
0
-2
-4
-6
-8
-10
90
92
94
96
98
100
102
104

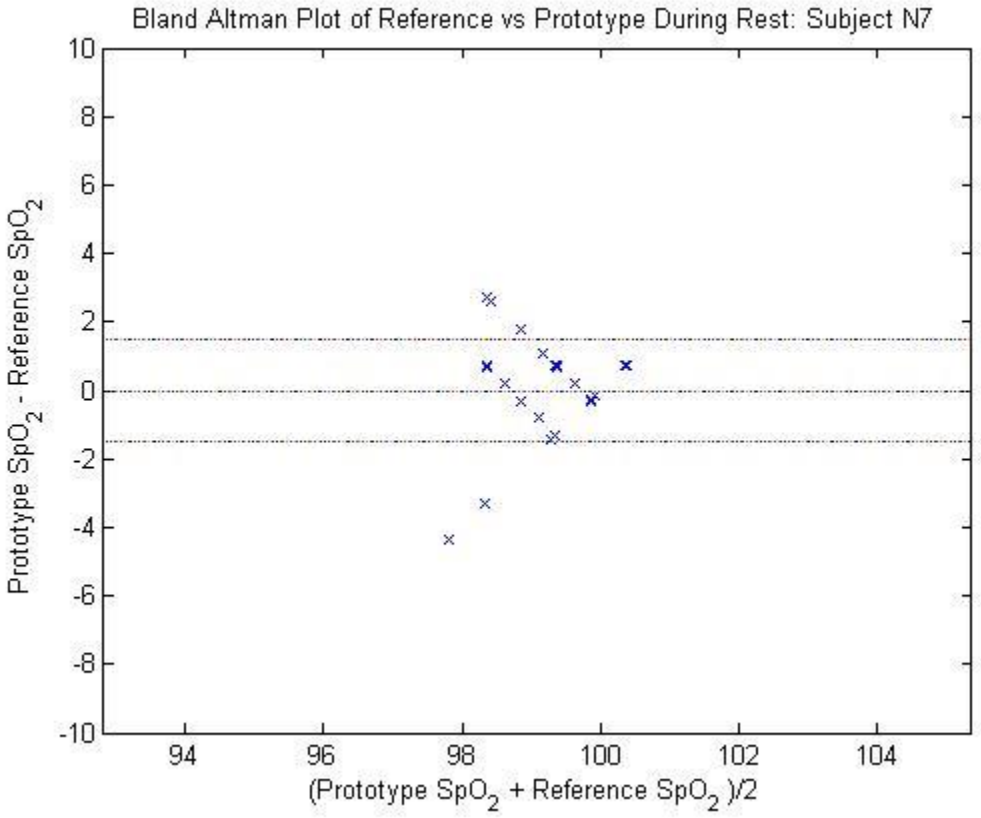
Bland Altman Plot of Reference vs Prototype During Rest: Subject N7
Prototype SpO2 - Reference SpO2
(Prototype SpO2 + Reference SpO2)/2
10
8
6
4
2
0
-2
-4
-6
-8
-10
94
96
98
100
102
104

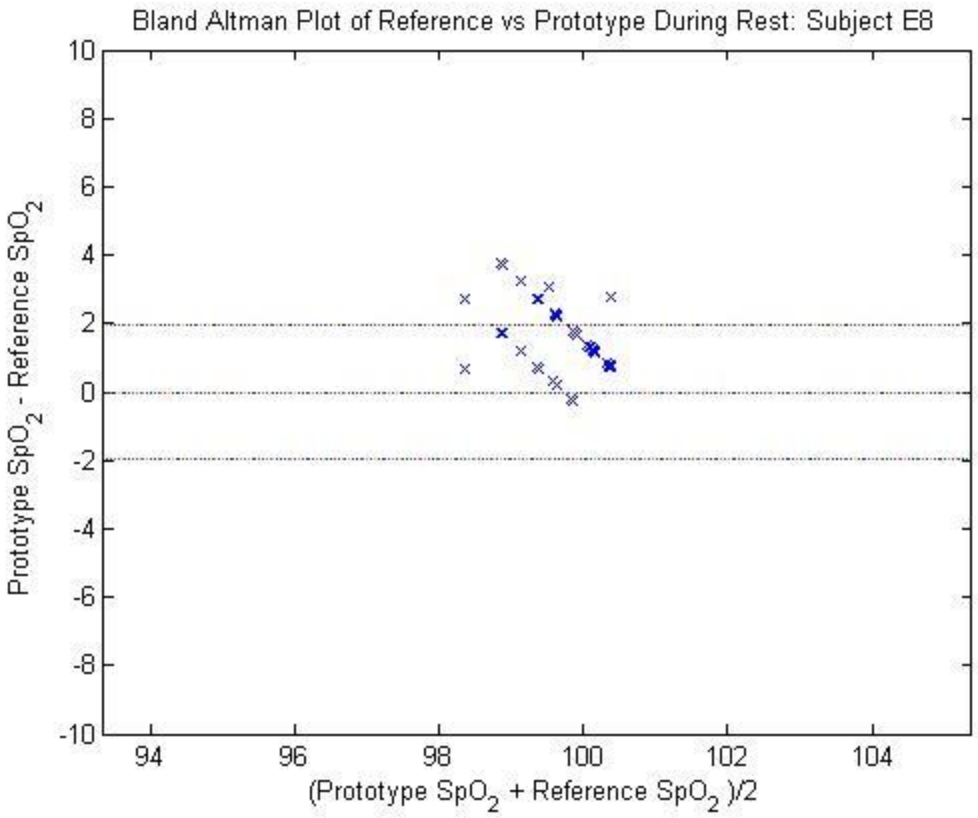
Bland Altman Plot of Reference vs Prototype During Rest: Subject E8
Prototype SpO2 - Reference SpO2
(Prototype SpO2 + Reference SpO2)/2
10
8
6
4
2
0
-2
-4
-6
-8
-10
94
96
98
100
102
104

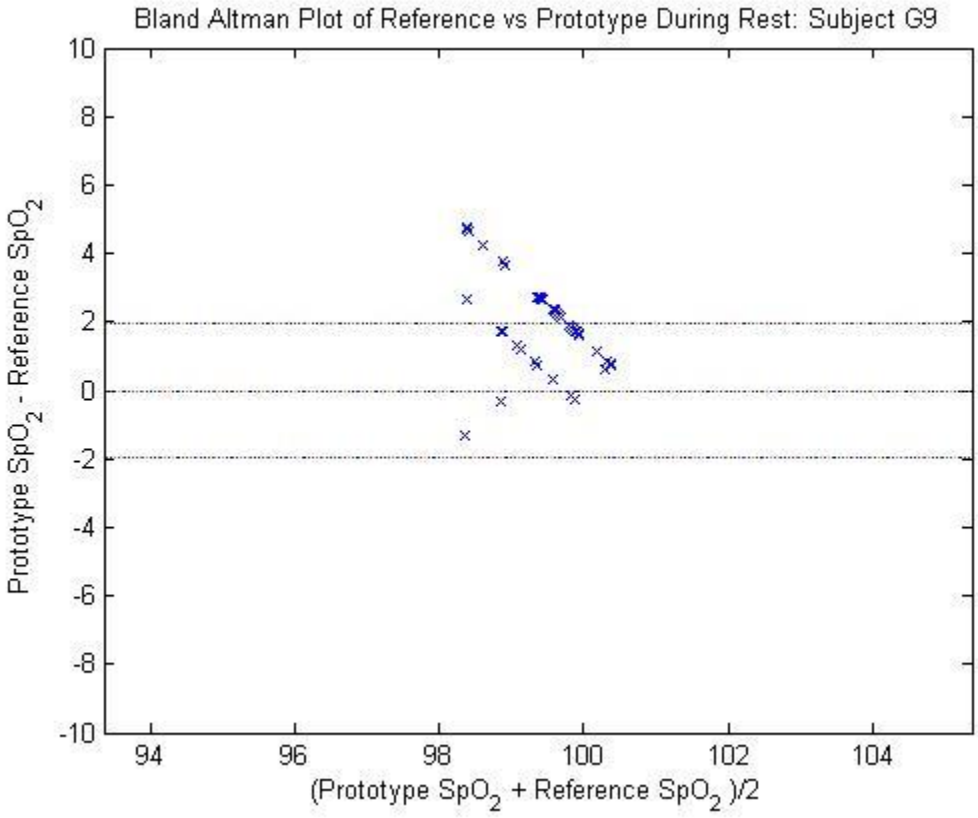
Bland Altman Plot of Reference vs Prototype During Rest: Subject G9
Prototype SpO2 - Reference SpO2
(Prototype SpO2 + Reference SpO2)/2
10
8
6
4
2
0
-2
-4
-6
-8
-10
94
96
98
100
102
104

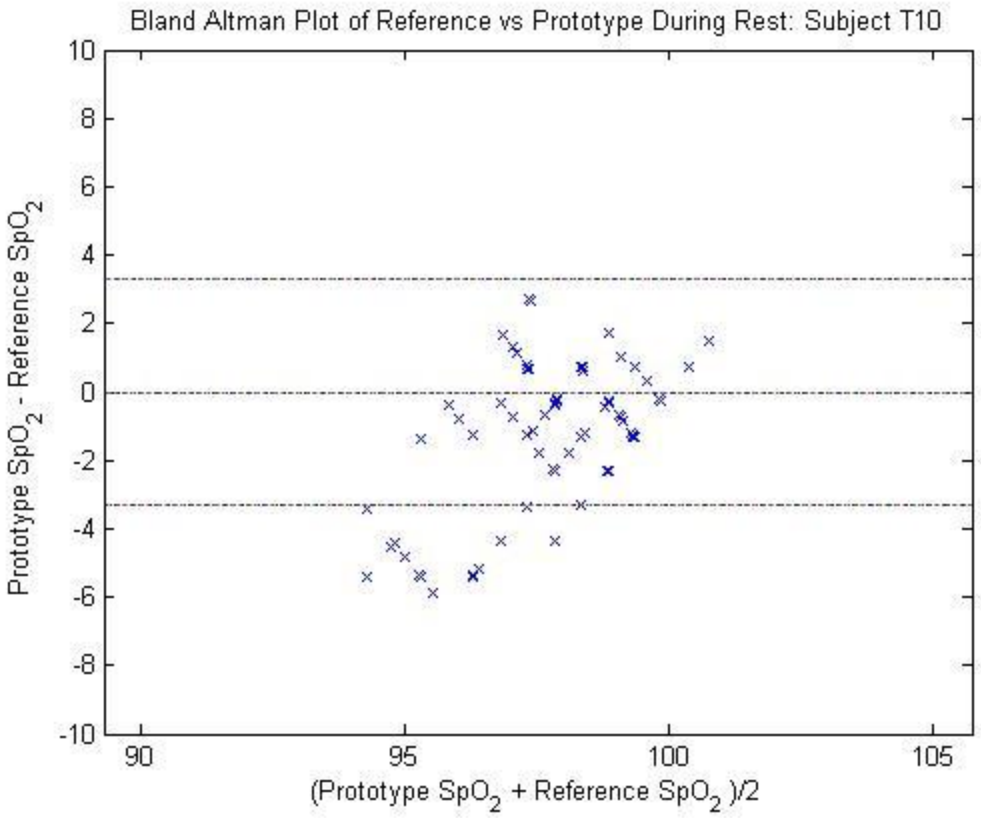
Bland Altman Plot of Reference vs Prototype During Rest: Subject T10
Prototype SpO2 - Reference SpO2
(Prototype SpO2 + Reference SpO2)/2
10
8
6
4
2
0
-2
-4
-6
-8
-10
90
95
100
105

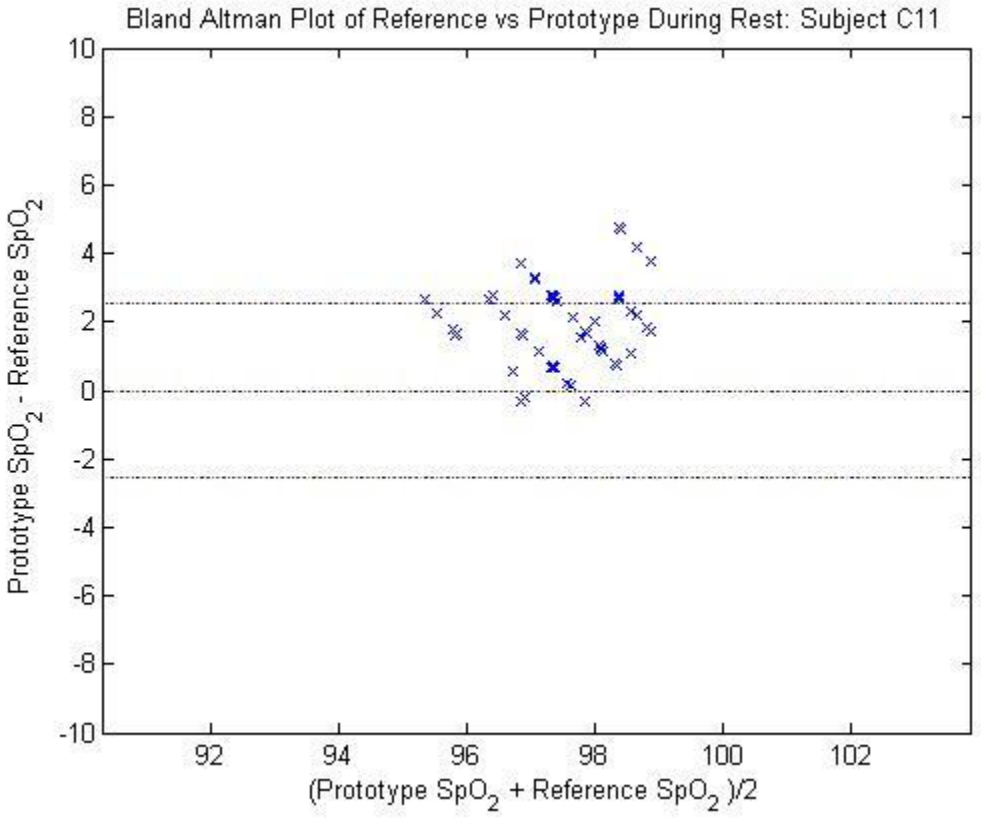
Bland Altman Plot of Reference vs Prototype During Rest: Subject C11
Prototype SpO2 - Reference SpO2
(Prototype SpO2 + Reference SpO2)/2
10
8
6
4
2
0
-2
-4
-6
-8
-10
92
94
96
98
100
102

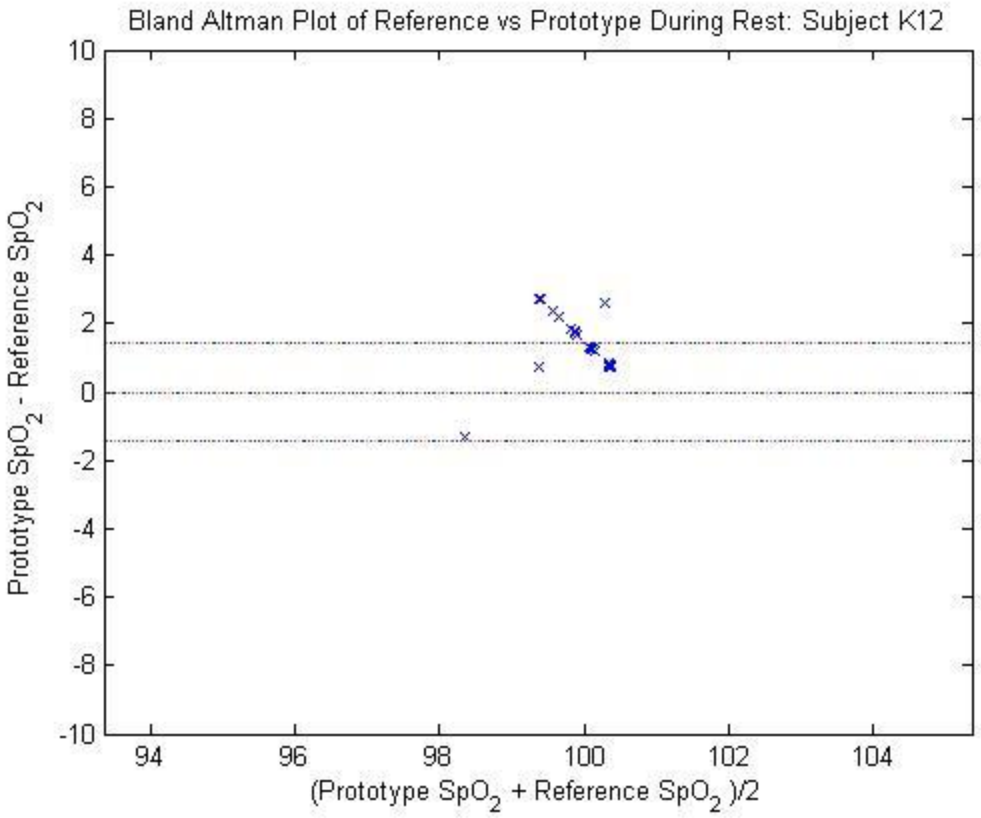
Bland Altman Plot of Reference vs Prototype During Rest: Subject K12
Prototype SpO2 - Reference SpO2
(Prototype SpO2 + Reference SpO2)/2
10
8
6
4
2
0
-2
-4
-6
-8
-10
94
96
98
100
102
104

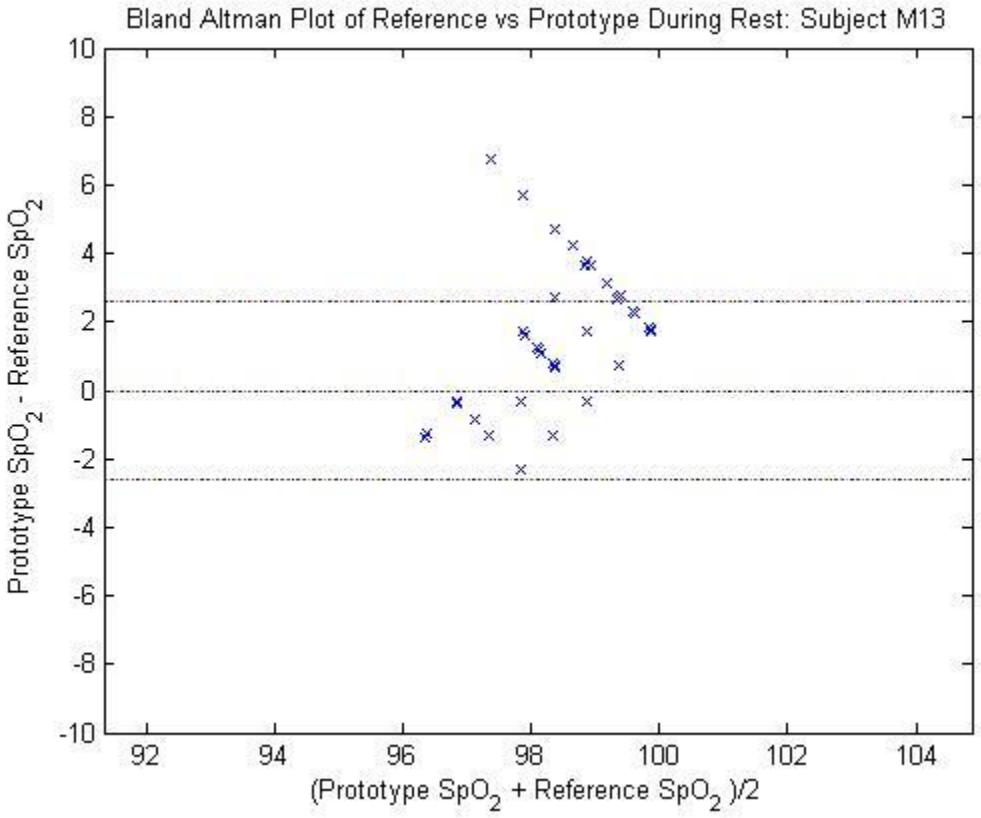
Bland Altman Plot of Reference vs Prototype During Rest: Subject M13
Prototype SpO2 - Reference SpO2
(Prototype SpO2 + Reference SpO2)/2
10
8
6
4
2
0
-2
-4
-6
-8
-10
92
94
96
98
100
102
104

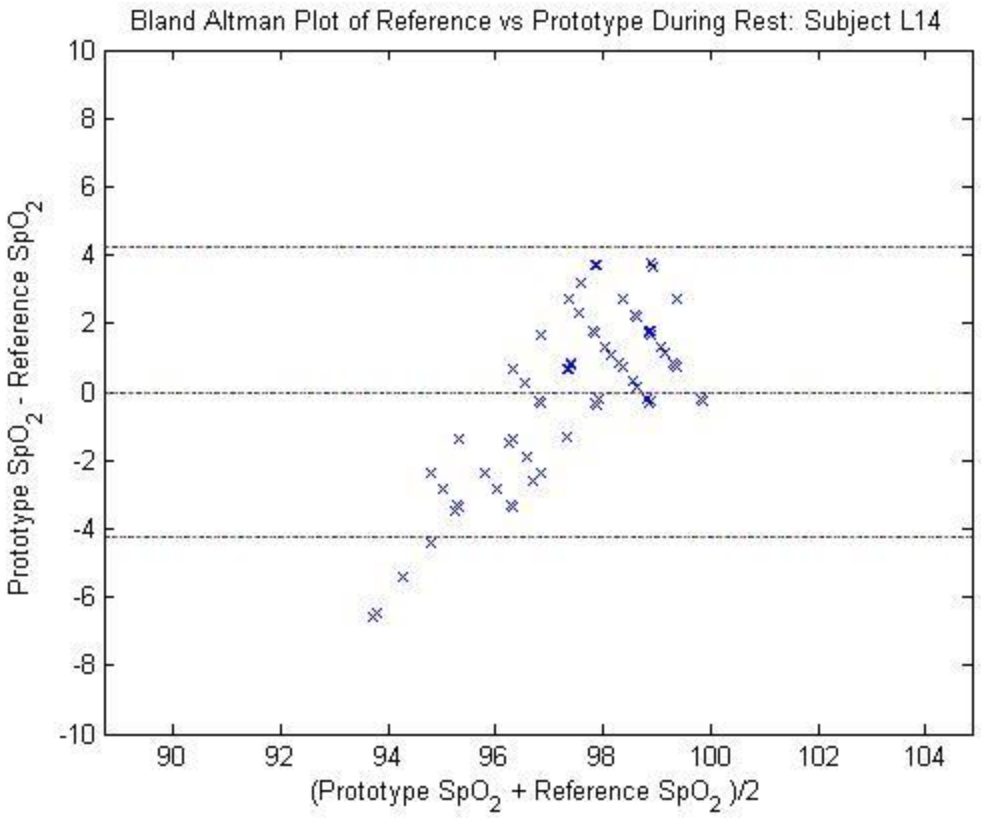
Bland Altman Plot of Reference vs Prototype During Rest: Subject L14
Prototype SpO2 - Reference SpO2
(Prototype SpO2 + Reference SpO2)/2
10
8
6
4
2
0
-2
-4
-6
-8
-10
90
92
94
96
98
100
102
104

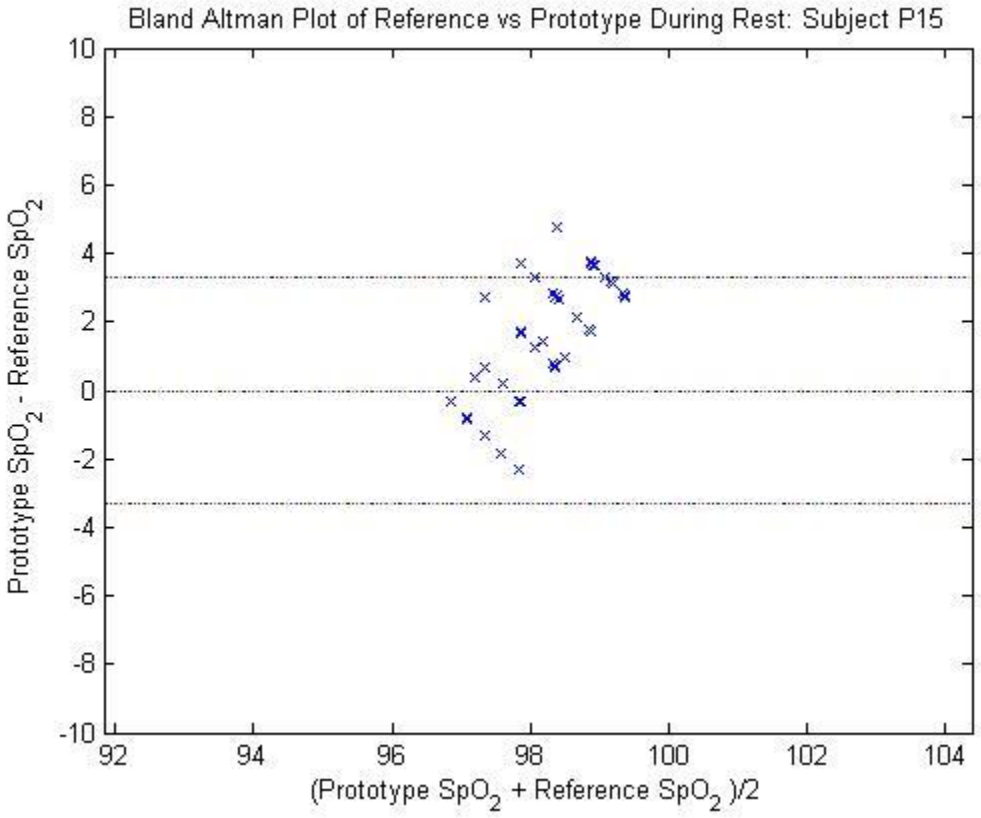
Bland Altman Plot of Reference vs Prototype During Rest: Subject P15
Prototype SpO2 - Reference SpO2
(Prototype SpO2 + Reference SpO2)/2
10
8
6
4
2
0
-2
-4
-6
-8
-10
92
94
96
98
100
102
104

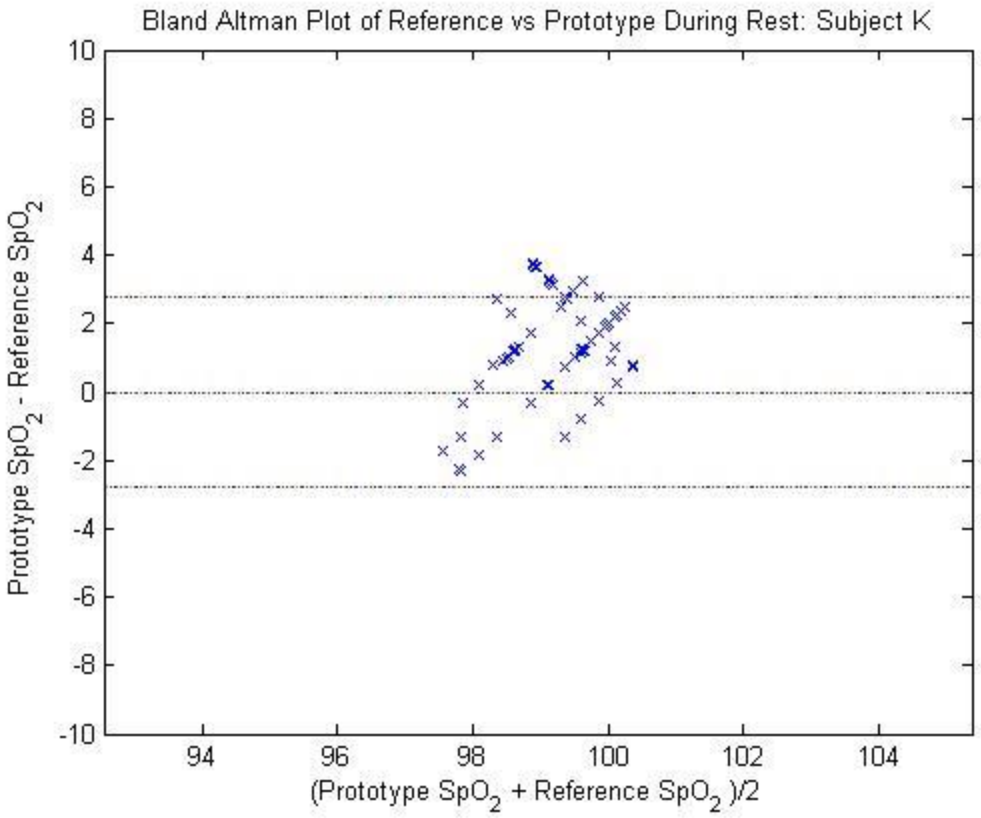
Bland Altman Plot of Reference vs Prototype During Rest: Subject K
Prototype SpO2 - Reference SpO2
(Prototype SpO2 + Reference SpO2)/2
10
8
6
4
2
0
-2
-4
-6
-8
-10
94
96
98
100
102
104

Appendix C: Sensor Weight HR Box Plots

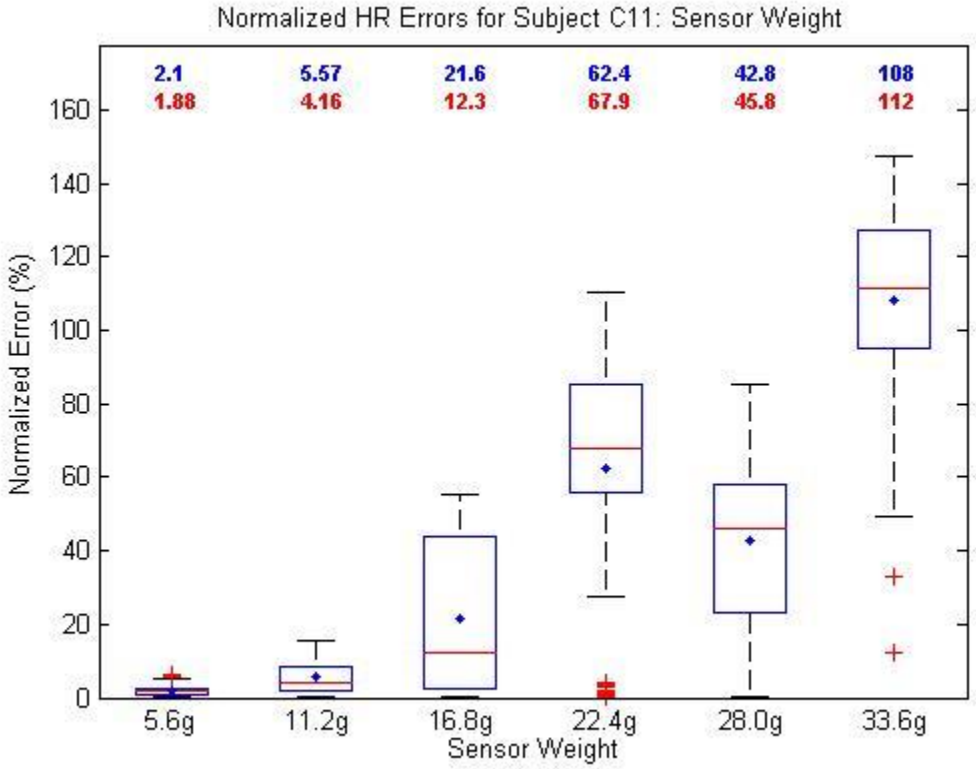

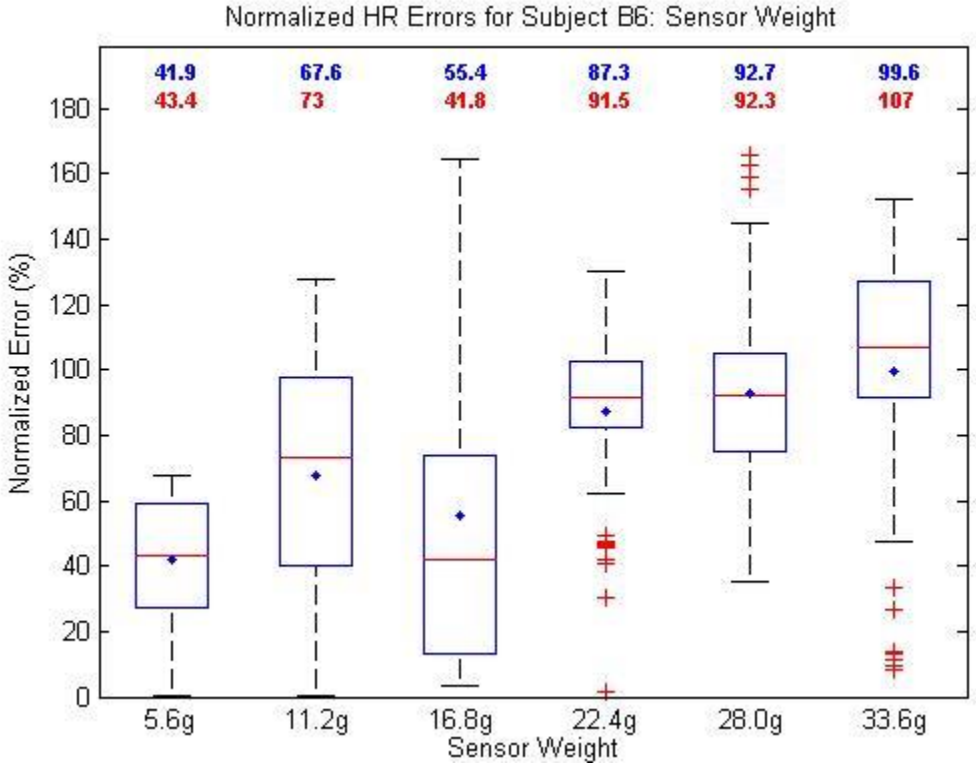

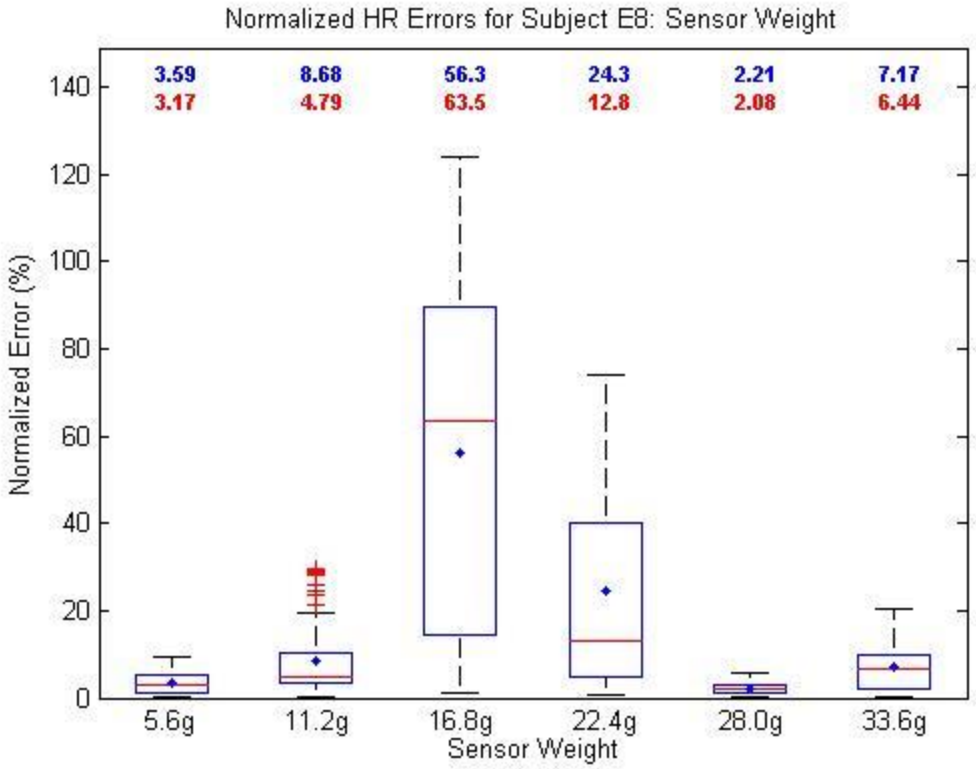
Normalized HR Errors for Subject E8: Sensor Weight
3.59
8.68
56.3
24.3
2.21
7.17
3.17
4.79
63.5
12.8
2.08
6.44
Normalized Error (%)
0
20
40
60
80
100
120
140
5.6g
11.2g
16.8g
22.4g
28.0g
33.6g
Sensor Weight

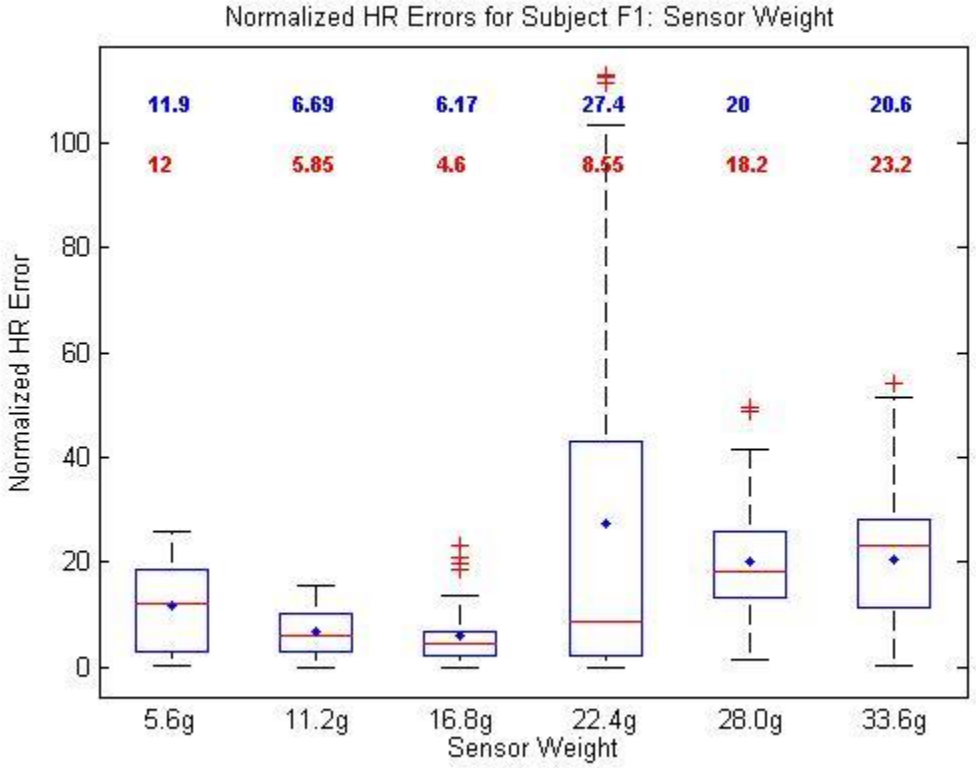
Normalized HR Errors for Subject F1: Sensor Weight
11.9
6.69
6.17
27.4
20
20.6
12
5.85
4.6
8.55
18.2
23.2
Normalized HR Error
0
20
40
60
80
100
5.6g
11.2g
16.8g
22.4g
28.0g
33.6g
Sensor Weight

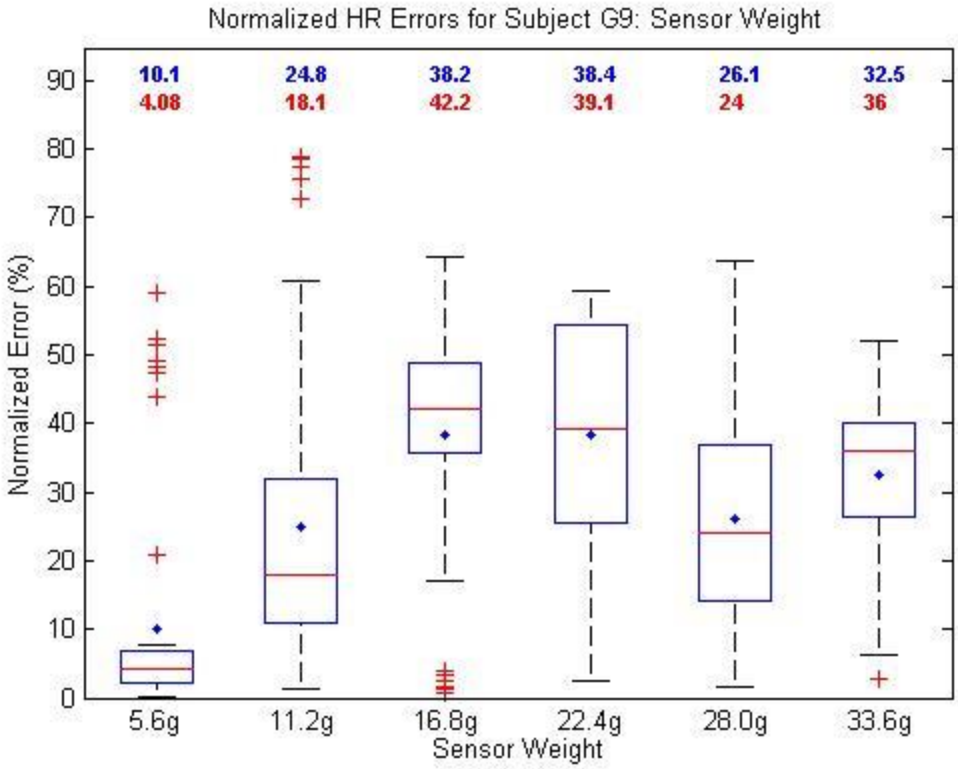
Normalized HR Errors for Subject G9: Sensor Weight
10.1
4.08
24.8
18.1
38.2
42.2
38.4
39.1
26.1
24
32.5
36
Normalized Error (%)
0
10
20
30
40
50
60
70
80
90
5.6g
11.2g
16.8g
22.4g
28.0g
33.6g
Sensor Weight

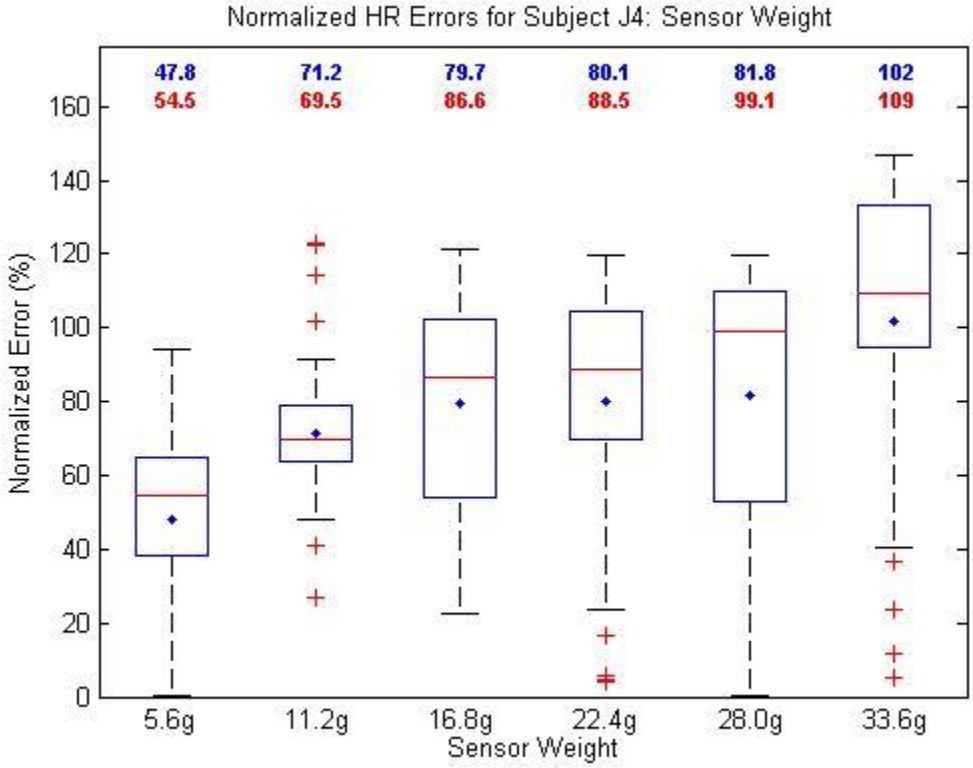
Normalized HR Errors for Subject J4: Sensor Weight
47.8
54.5
71.2
69.5
79.7
86.6
80.1
88.5
81.8
99.1
102
109
Normalized Error (%)
0
20
40
60
80
100
120
140
160
5.6g
11.2g
16.8g
22.4g
28.0g
33.6g
Sensor Weight

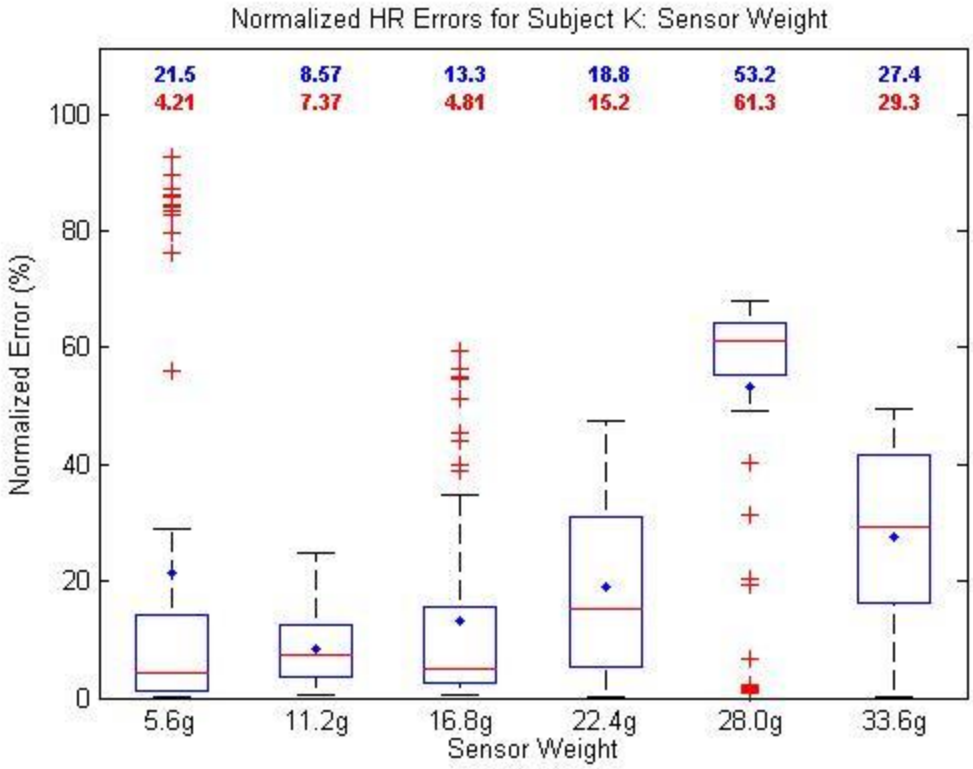
Normalized HR Errors for Subject K: Sensor Weight
21.5
8.57
13.3
18.8
53.2
27.4
4.21
7.37
4.81
15.2
61.3
29.3
Normalized Error (%)
0
20
40
60
80
100
5.6g
11.2g
16.8g
22.4g
28.0g
33.6g
Sensor Weight

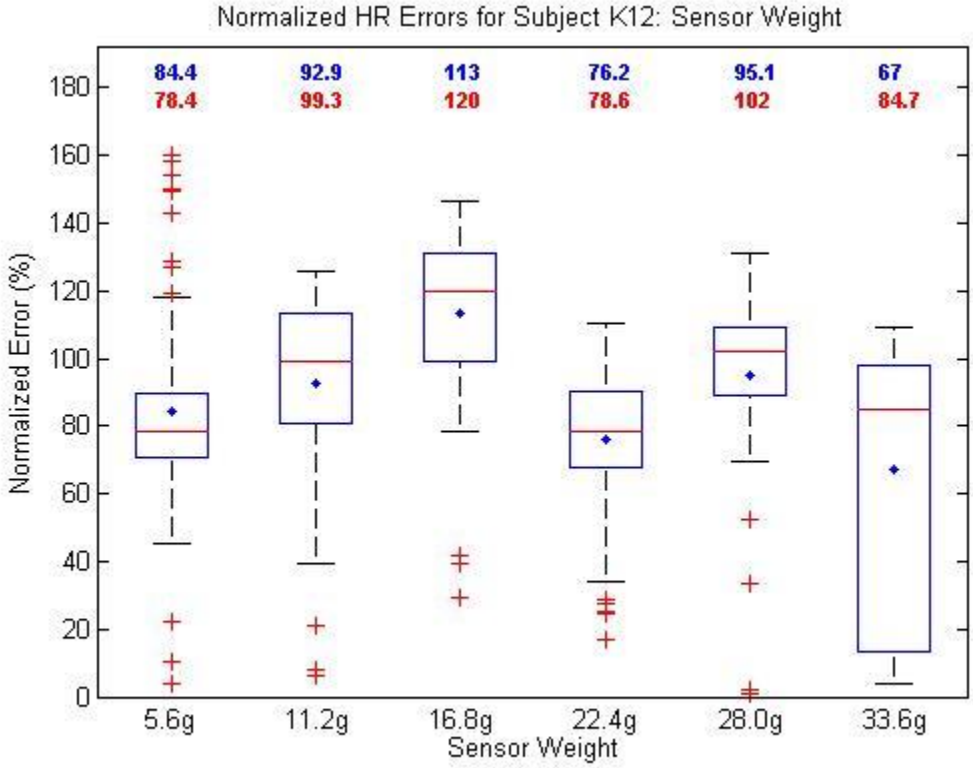
Normalized HR Errors for Subject K12: Sensor Weight
84.4
92.9
113
76.2
95.1
67
78.4
99.3
120
78.6
102
84.7
Normalized Error (%)
0
20
40
60
80
100
120
140
160
180
5.6g
11.2g
16.8g
22.4g
28.0g
33.6g
Sensor Weight

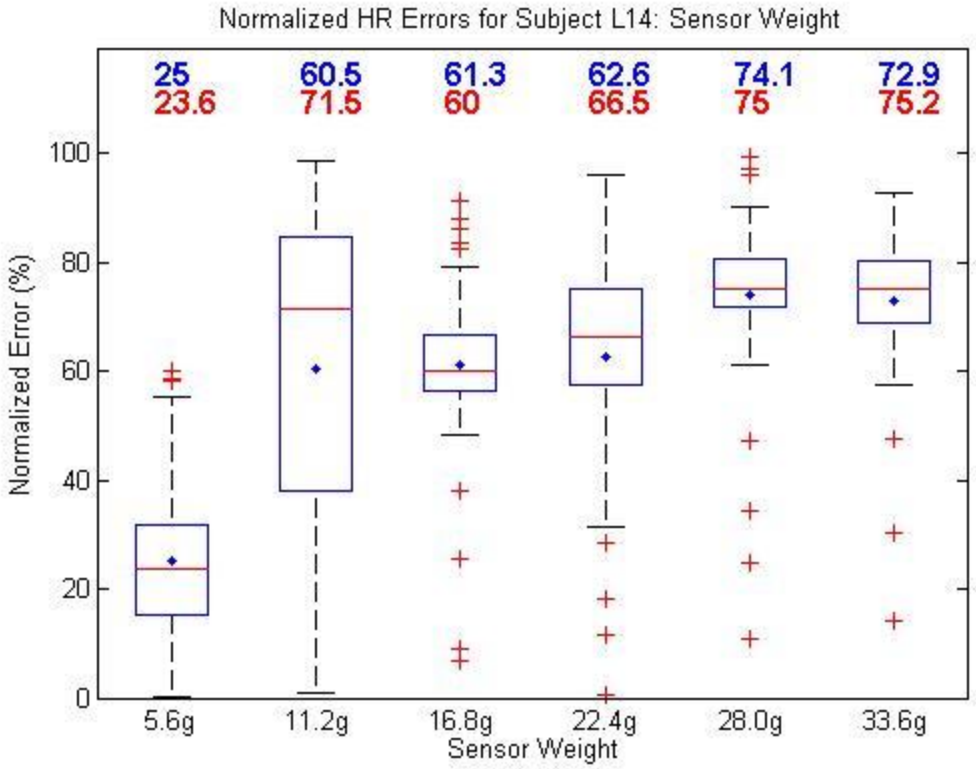
Normalized HR Errors for Subject L14: Sensor Weight
25
23.6
60.5
71.5
61.3
60
62.6
66.5
74.1
75
72.9
75.2
Normalized Error (%)
0
20
40
60
80
100
5.6g
11.2g
16.8g
22.4g
28.0g
33.6g
Sensor Weight

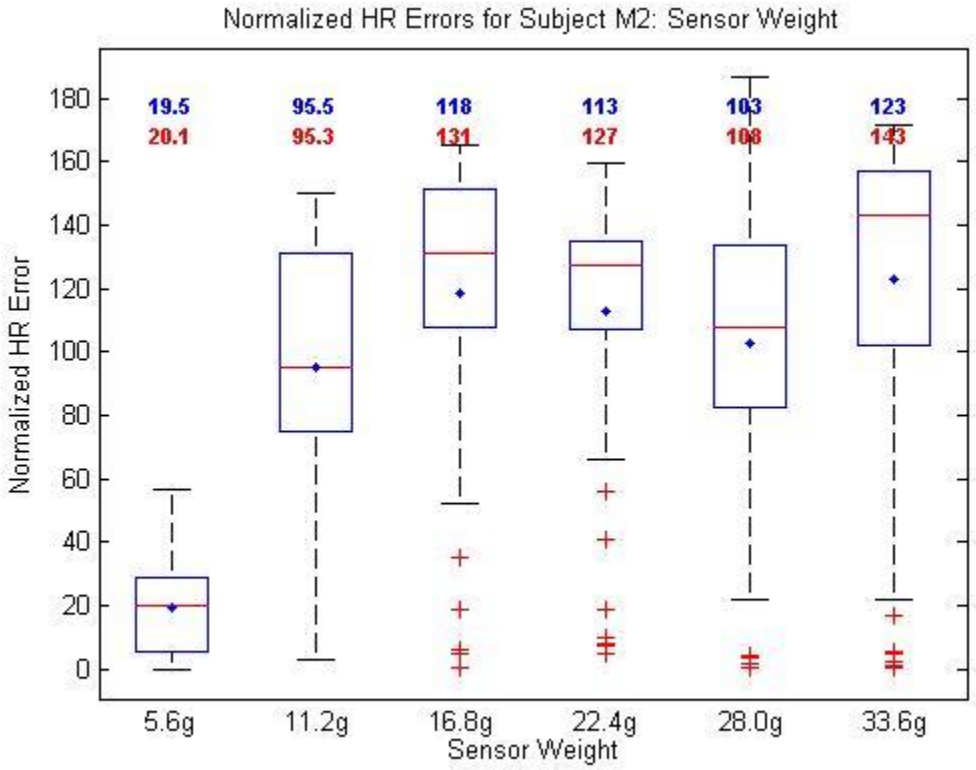
Normalized HR Errors for Subject M2: Sensor Weight
19.5
20.1
95.5
95.3
118
131
113
127
103
108
123
143
Normalized HR Error
0
20
40
60
80
100
120
140
160
180
5.6g
11.2g
16.8g
22.4g
28.0g
33.6g
Sensor Weight

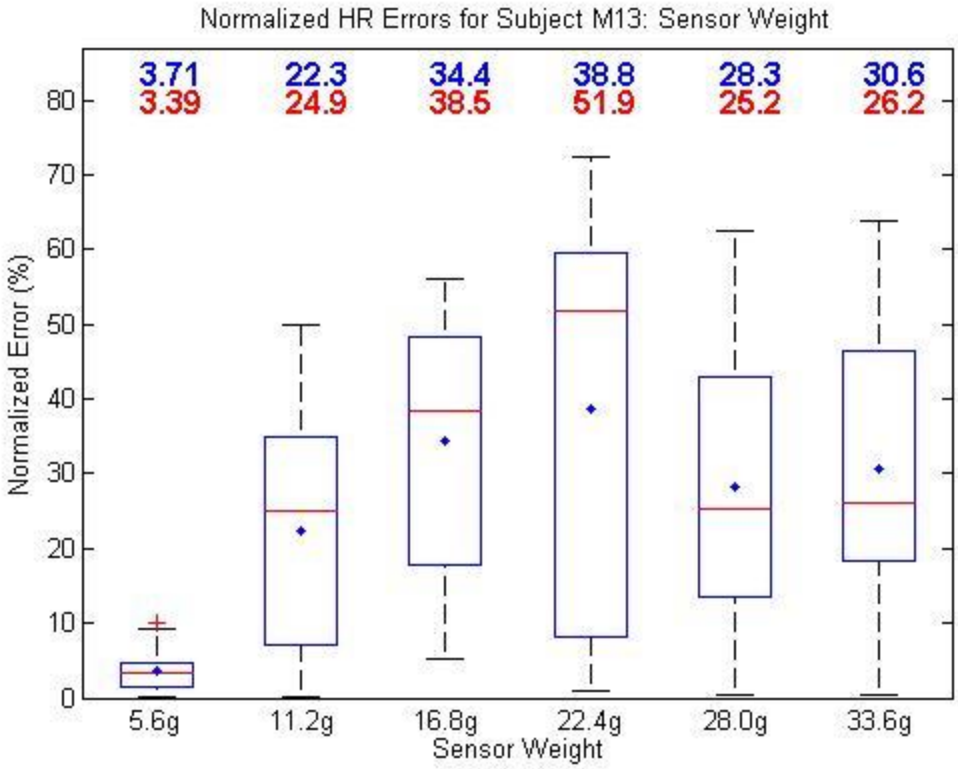
Normalized HR Errors for Subject M13: Sensor Weight
3.71
3.39
22.3
24.9
34.4
38.5
38.8
51.9
28.3
25.2
30.6
26.2
Normalized Error (%)
0
10
20
30
40
50
60
70
80
5.6g
11.2g
16.8g
22.4g
28.0g
33.6g
Sensor Weight

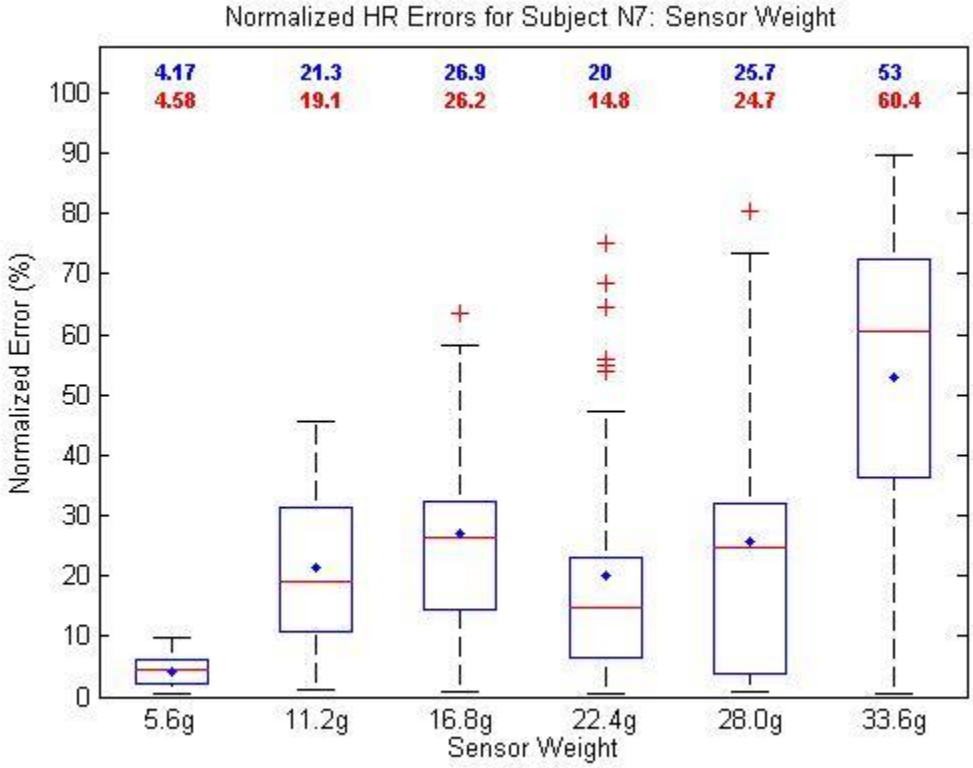
Normalized HR Errors for Subject N7: Sensor Weight
4.17
4.58
21.3
19.1
26.9
26.2
20
14.8
25.7
24.7
53
60.4
Normalized Error (%)
0
10
20
30
40
50
60
70
80
90
100
5.6g
11.2g
16.8g
22.4g
28.0g
33.6g
Sensor Weight

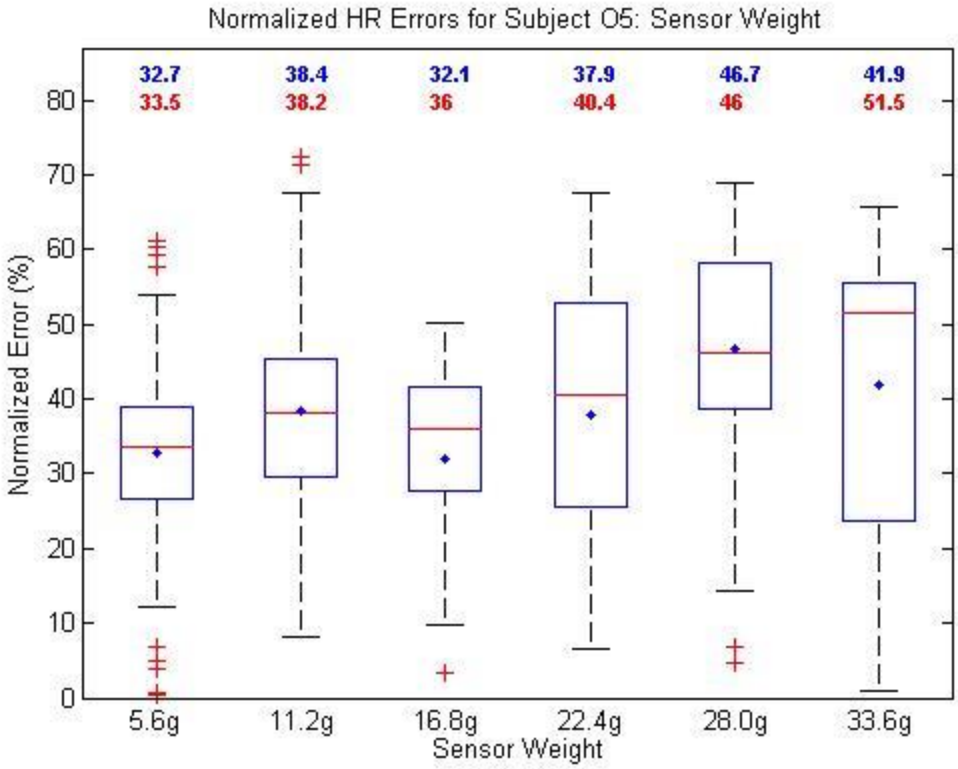
Normalized HR Errors for Subject O5: Sensor Weight
32.7
33.5
38.4
38.2
32.1
36
37.9
40.4
46.7
46
41.9
51.5
Normalized Error (%)
0
10
20
30
40
50
60
70
80
5.6g
11.2g
16.8g
22.4g
28.0g
33.6g
Sensor Weight

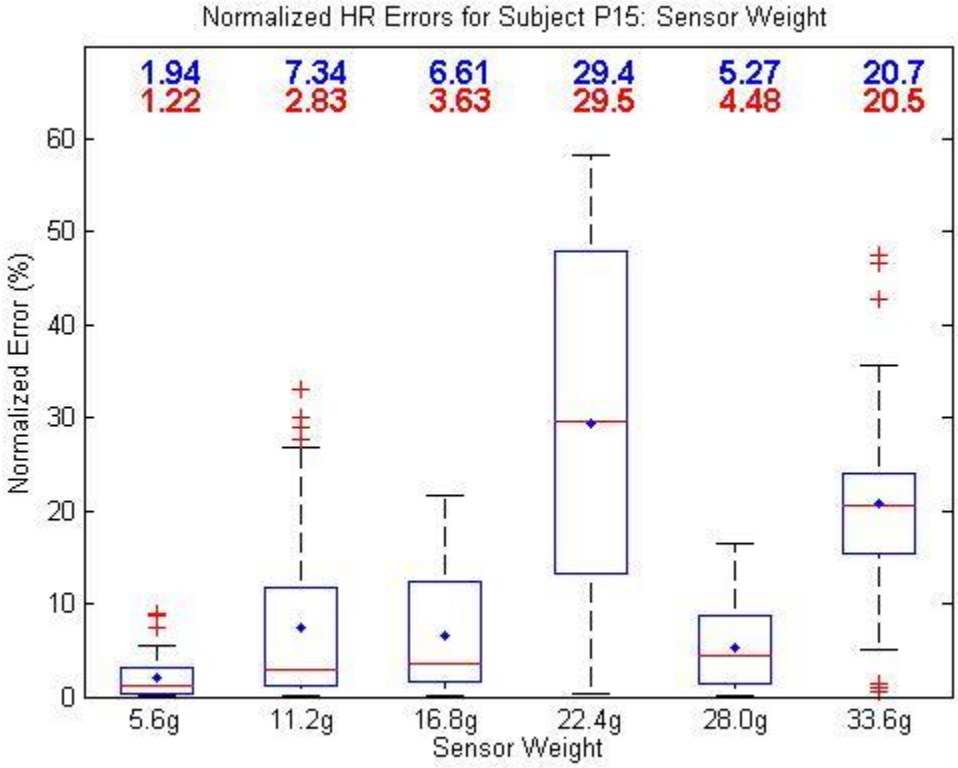
Normalized HR Errors for Subject P15: Sensor Weight
1.94
1.22
7.34
2.83
6.61
3.63
29.4
29.5
5.27
4.48
20.7
20.5
Normalized Error (%)
0
10
20
30
40
50
60
5.6g
11.2g
16.8g
22.4g
28.0g
33.6g
Sensor Weight

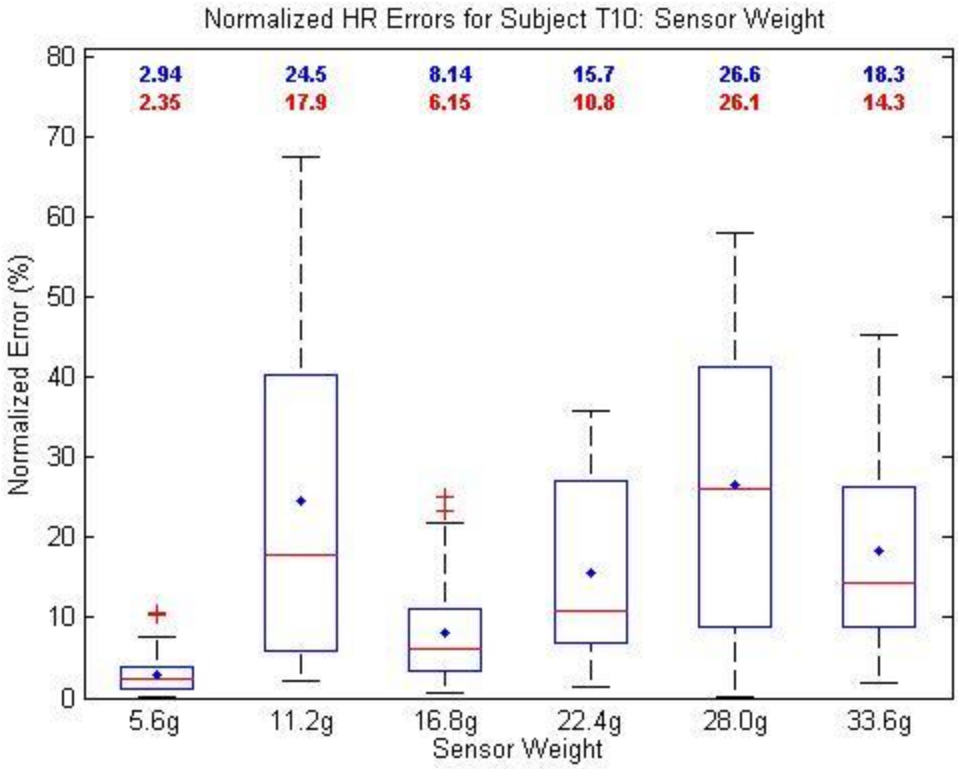
Normalized HR Errors for Subject T10: Sensor Weight
2.94
2.35
24.5
17.9
8.14
6.15
15.7
10.8
26.6
26.1
18.3
14.3
Normalized Error (%)
0
10
20
30
40
50
60
70
80
5.6g
11.2g
16.8g
22.4g
28.0g
33.6g
Sensor Weight

Appendix D: Sensor Weight SpO_2 Box Plots

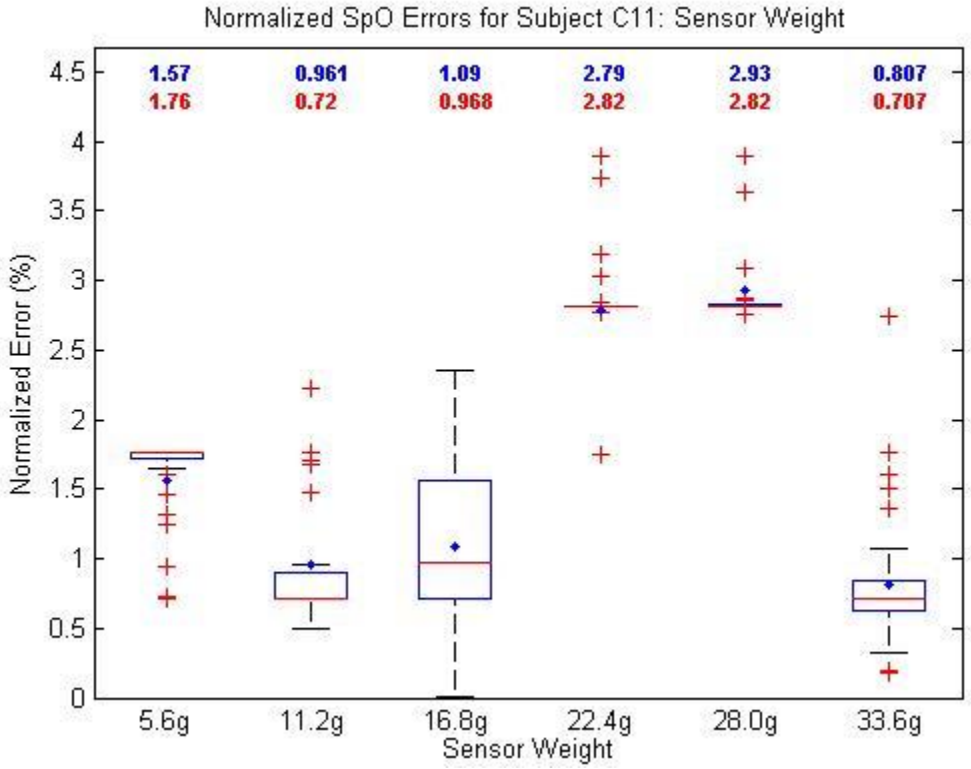

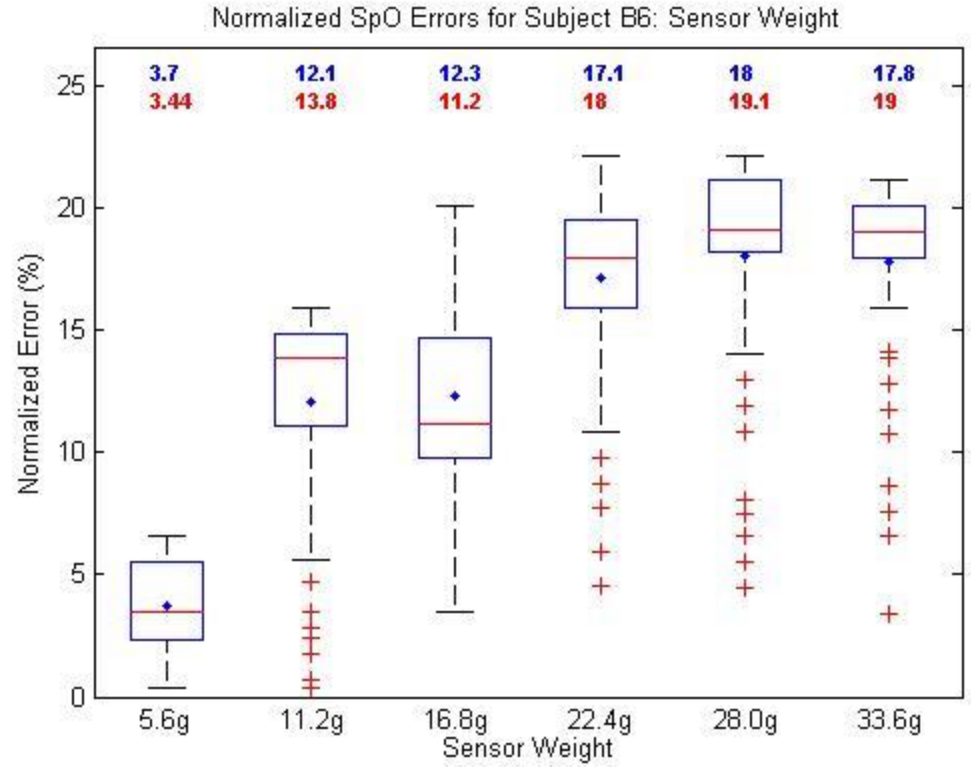

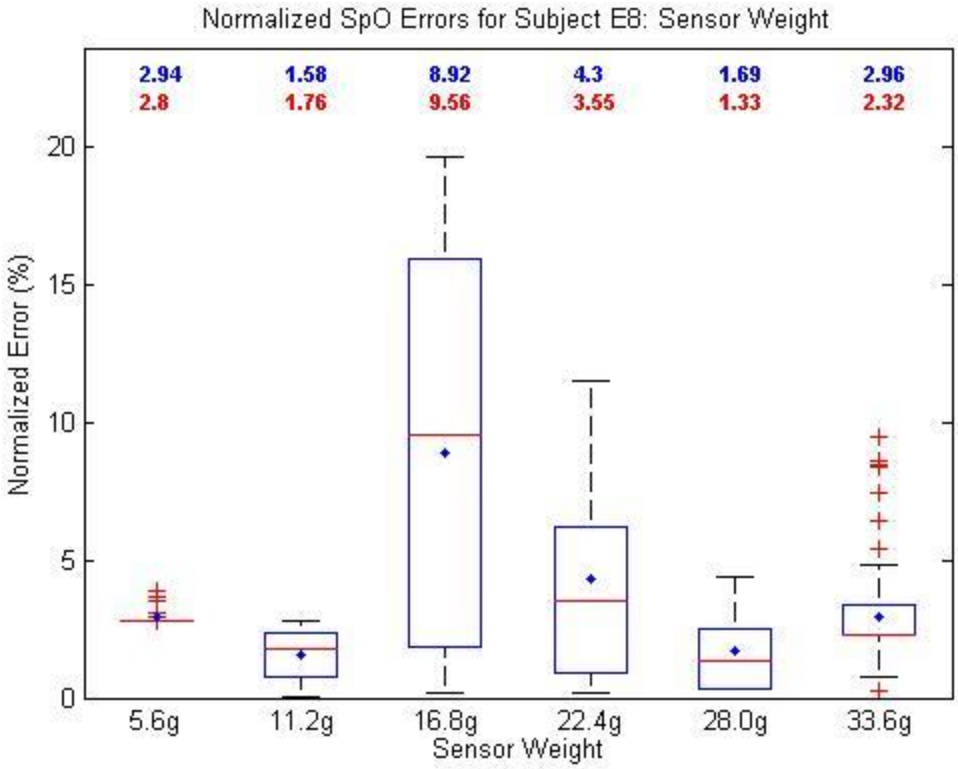
Normalized SpO Errors for Subject E8: Sensor Weight
2.94
1.58
8.92
4.3
1.69
2.96
2.8
1.76
9.56
3.55
1.33
2.32
Normalized Error (%)
0
5
10
15
20
5.6g
11.2g
16.8g
22.4g
28.0g
33.6g
Sensor Weight

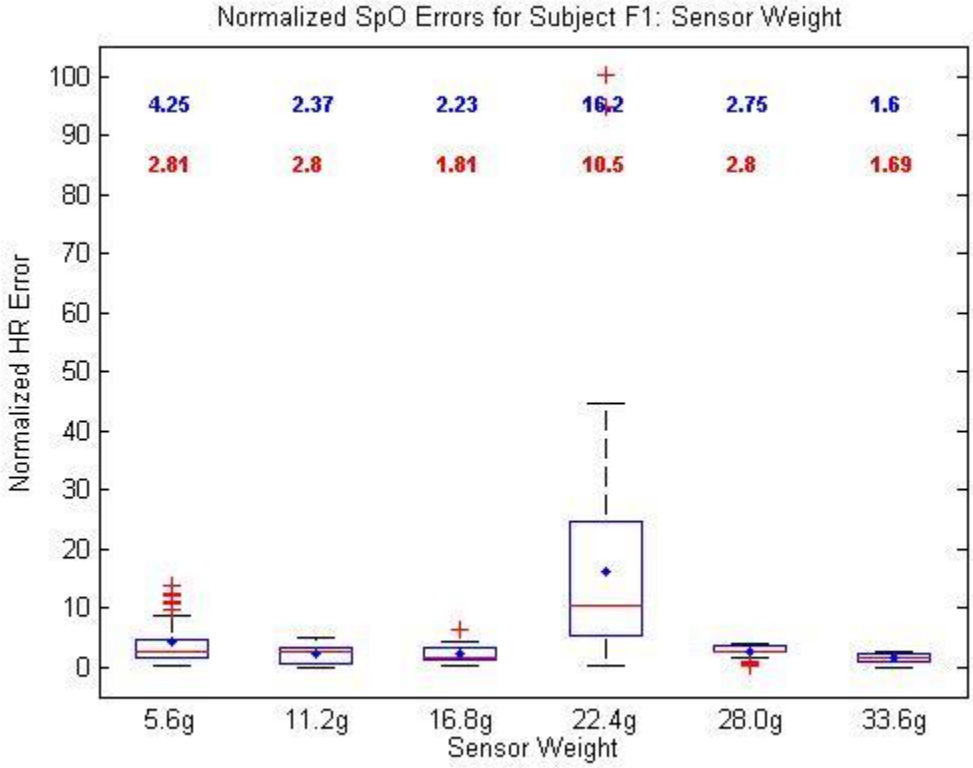
Normalized SpO Errors for Subject F1: Sensor Weight
4.25
2.37
2.23
16.2
2.75
1.6
2.81
2.8
1.81
10.5
2.8
1.69
Normalized HR Error
0
10
20
30
40
50
60
70
80
90
100
5.6g
11.2g
16.8g
22.4g
28.0g
33.6g
Sensor Weight

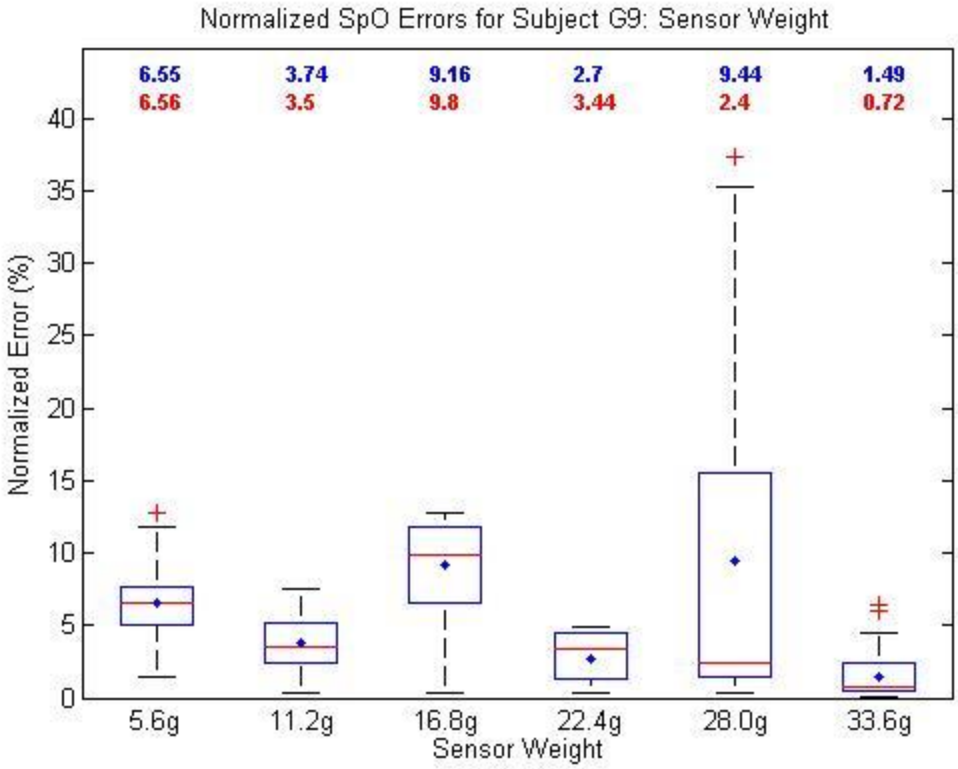
Normalized SpO Errors for Subject G9: Sensor Weight
6.55
6.56
3.74
3.5
9.16
9.8
2.7
3.44
9.44
2.4
1.49
0.72
Normalized Error (%)
0
5
10
15
20
25
30
35
40
5.6g
11.2g
16.8g
22.4g
28.0g
33.6g
Sensor Weight

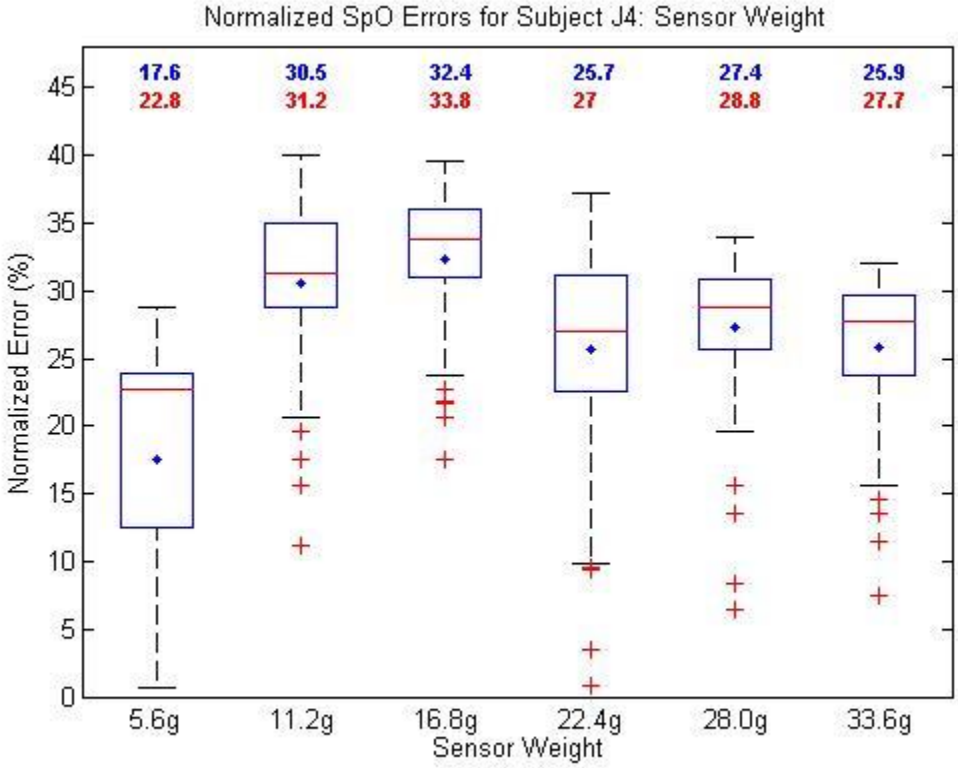
Normalized SpO Errors for Subject J4: Sensor Weight
17.6
22.8
30.5
31.2
32.4
33.8
25.7
27
27.4
28.8
25.9
27.7
Normalized Error (%)
0
5
10
15
20
25
30
35
40
45
5.6g
11.2g
16.8g
22.4g
28.0g
33.6g
Sensor Weight

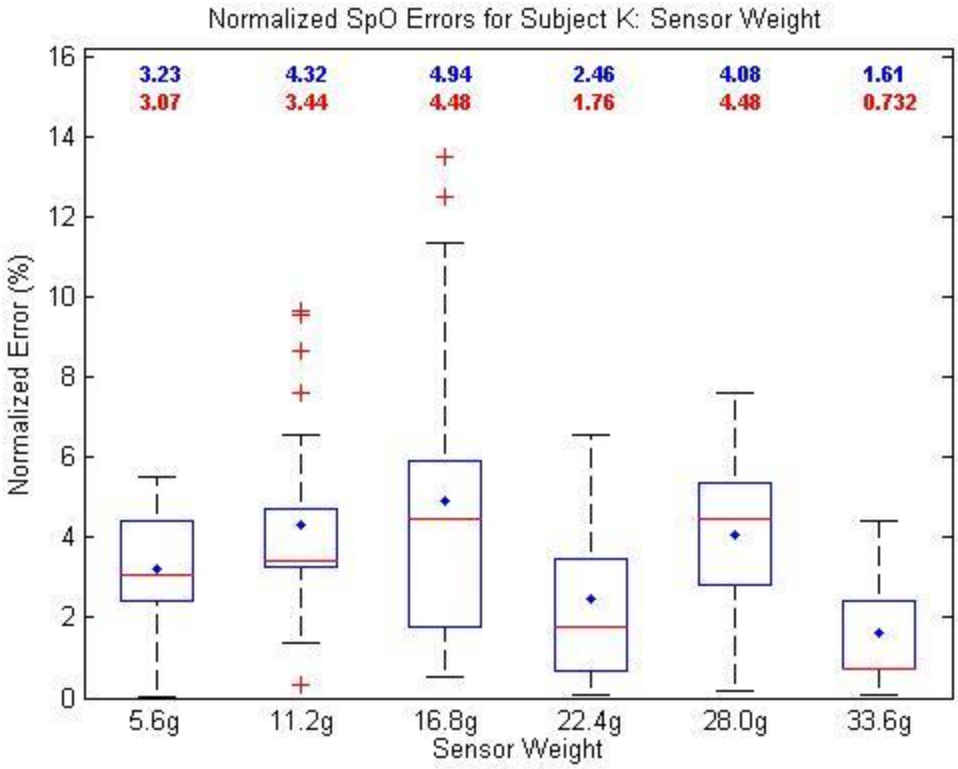
Normalized SpO Errors for Subject K: Sensor Weight
3.23
3.07
4.32
3.44
4.94
4.48
2.46
1.76
4.08
4.48
1.61
0.732
Normalized Error (%)
0
2
4
6
8
10
12
14
16
5.6g
11.2g
16.8g
22.4g
28.0g
33.6g
Sensor Weight

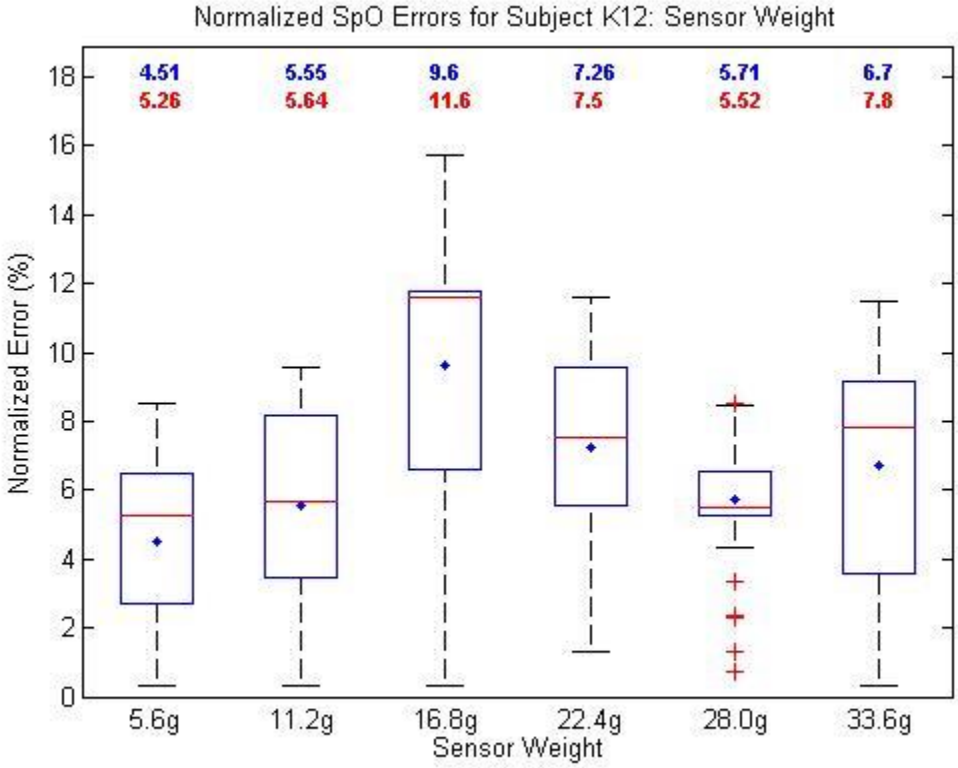
Normalized SpO Errors for Subject K12: Sensor Weight
4.51
5.26
5.55
5.64
9.6
11.6
7.26
7.5
5.71
5.52
6.7
7.8
Normalized Error (%)
0
2
4
6
8
10
12
14
16
18
5.6g
11.2g
16.8g
22.4g
28.0g
33.6g
Sensor Weight

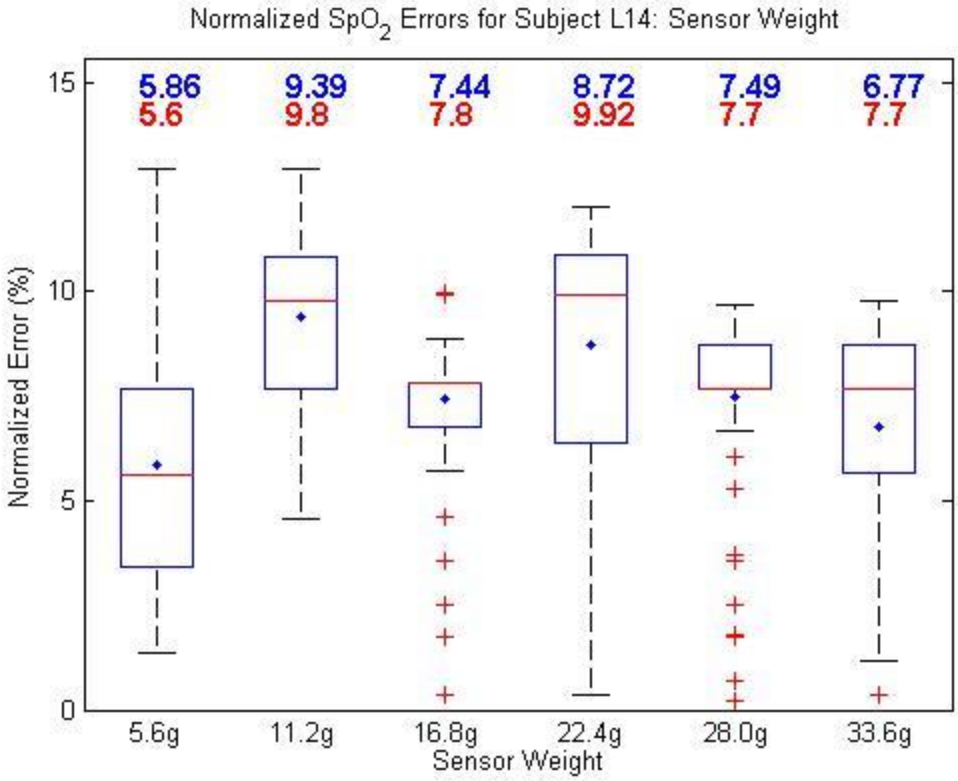
Normalized SpO_2 Errors for Subject L14: Sensor Weight
5.86
5.6
9.39
9.8
7.44
7.8
8.72
9.92
7.49
7.7
6.77
7.7
Normalized Error (%)
0
5
10
15
5.6g
11.2g
16.8g
22.4g
28.0g
33.6g
Sensor Weight

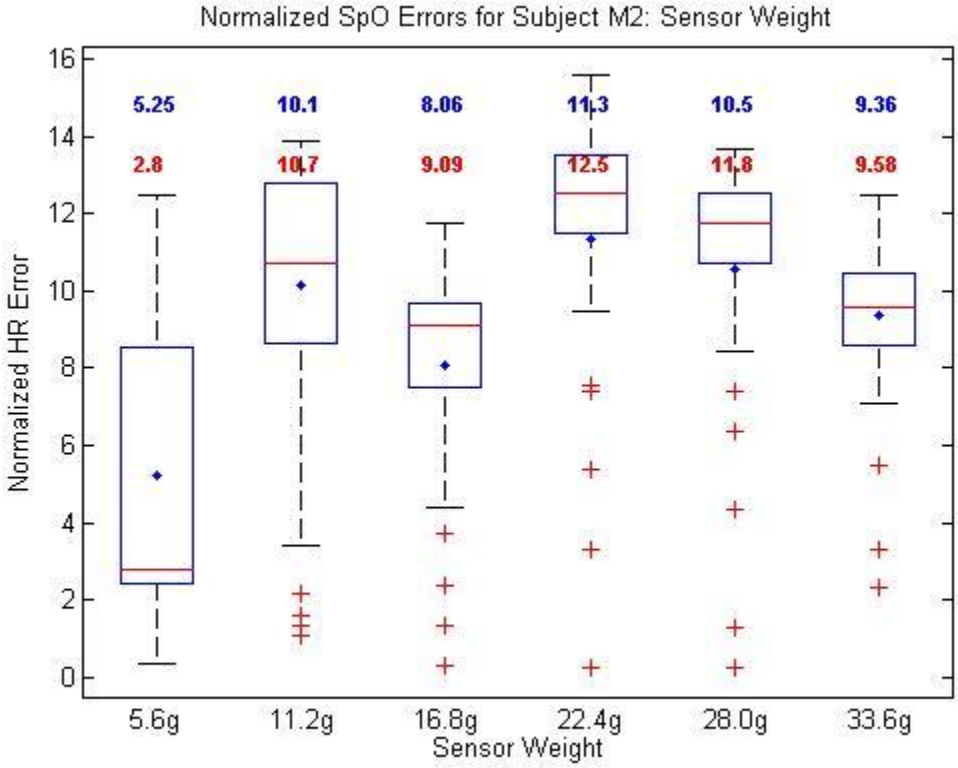
Normalized SpO Errors for Subject M2: Sensor Weight
5.25
2.8
10.1
10.7
8.06
9.09
11.3
12.5
10.5
11.8
9.36
9.58
Normalized HR Error
0
2
4
6
8
10
12
14
16
5.6g
11.2g
16.8g
22.4g
28.0g
33.6g
Sensor Weight

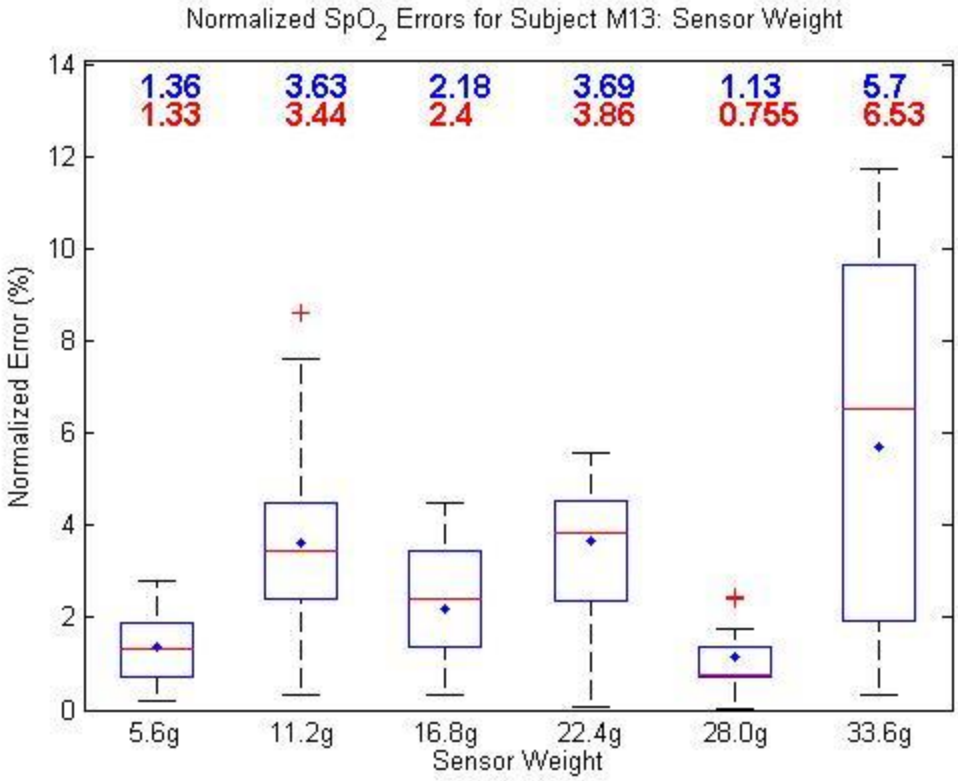
Normalized SpO2 Errors for Subject M13: Sensor Weight
1.36
1.33
3.63
3.44
2.18
2.4
3.69
3.86
1.13
0.755
5.7
6.53
Normalized Error (%)
0
2
4
6
8
10
12
14
5.6g
11.2g
16.8g
22.4g
28.0g
33.6g
Sensor Weight

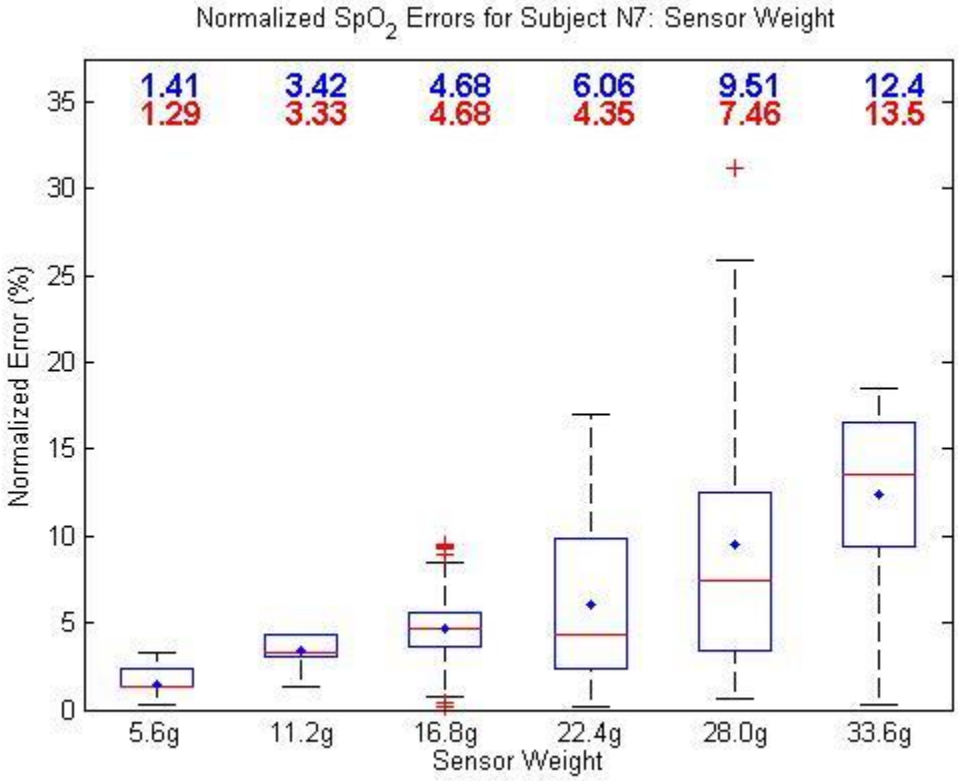
Normalized SpO2 Errors for Subject N7: Sensor Weight
1.41
1.29
3.42
3.33
4.68
4.68
6.06
4.35
9.51
7.46
12.4
13.5
Normalized Error (%)
0
5
10
15
20
25
30
35
5.6g
11.2g
16.8g
22.4g
28.0g
33.6g
Sensor Weight

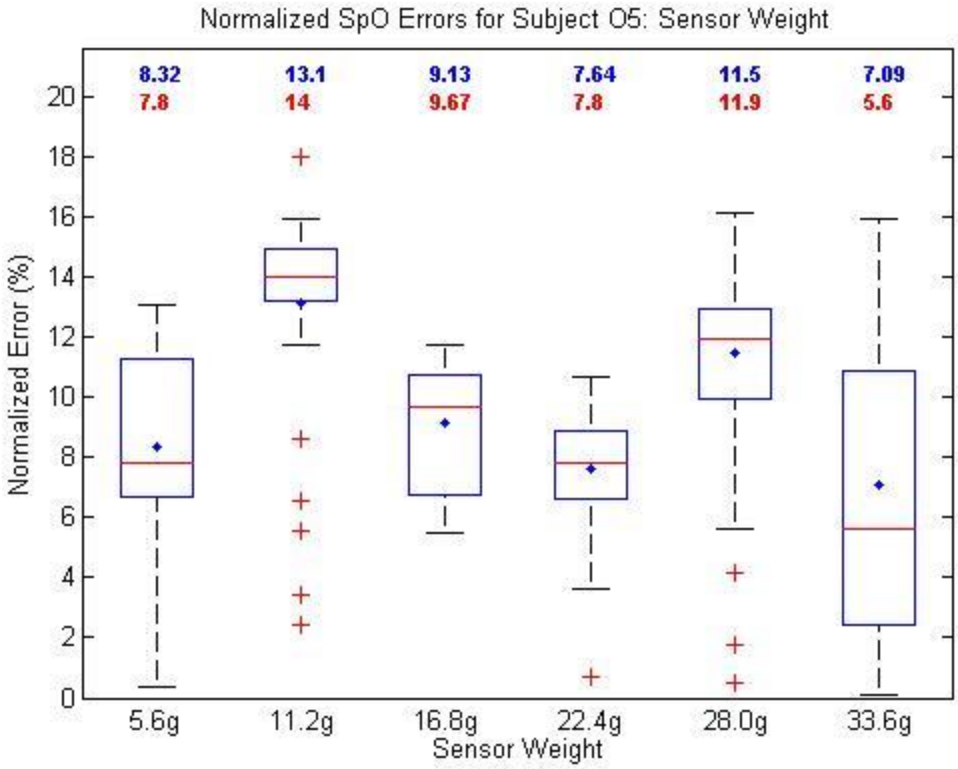
Normalized SpO Errors for Subject O5: Sensor Weight
8.32
7.8
13.1
14
9.13
9.67
7.64
7.8
11.5
11.9
7.09
5.6
Normalized Error (%)
0
2
4
6
8
10
12
14
16
18
20
5.6g
11.2g
16.8g
22.4g
28.0g
33.6g
Sensor Weight

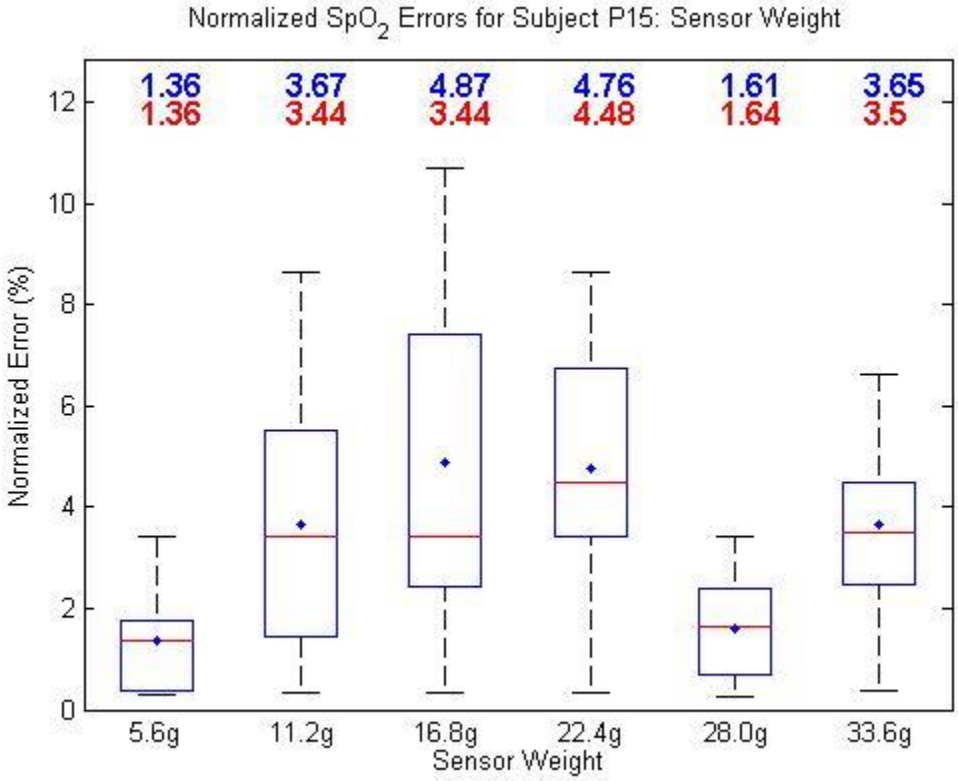
Normalized SpO2 Errors for Subject P15: Sensor Weight
1.36
1.36
3.67
3.44
4.87
3.44
4.76
4.48
1.61
1.64
3.65
3.5
Normalized Error (%)
0
2
4
6
8
10
12
5.6g
11.2g
16.8g
22.4g
28.0g
33.6g
Sensor Weight

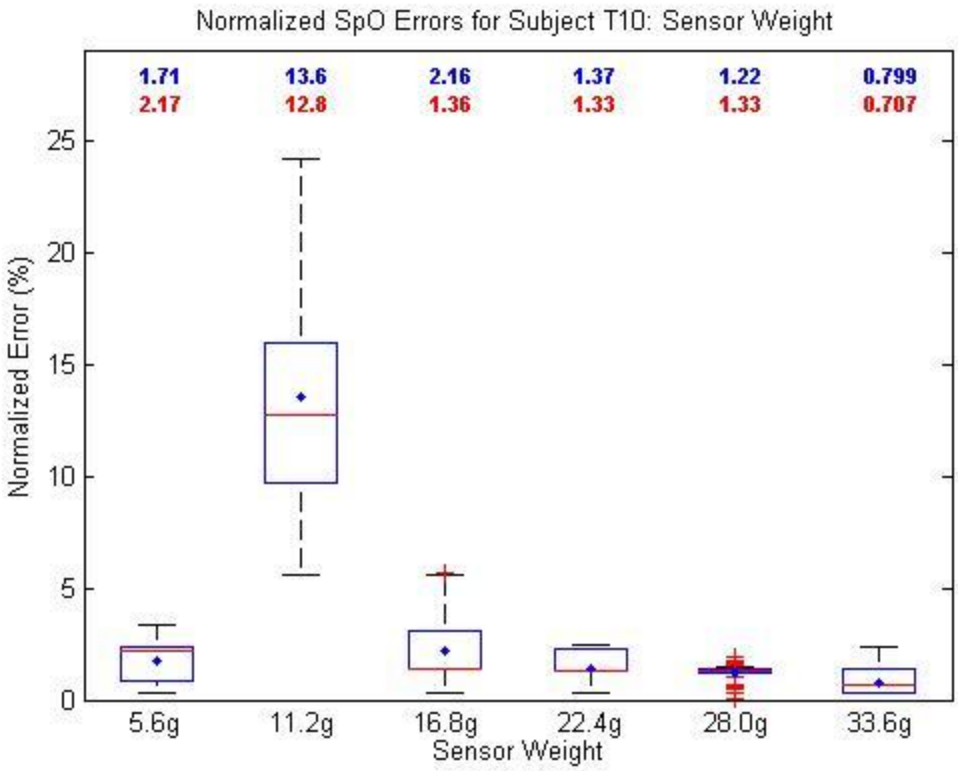
Normalized SpO Errors for Subject T10: Sensor Weight
1.71
2.17
13.6
12.8
2.16
1.36
1.37
1.33
1.22
1.33
0.799
0.707
25
20
15
10
5
0
Normalized Error (%)
5.6g
11.2g
16.8g
22.4g
28.0g
33.6g
Sensor Weight

Appendix E: Applied Heat HR Box Plots

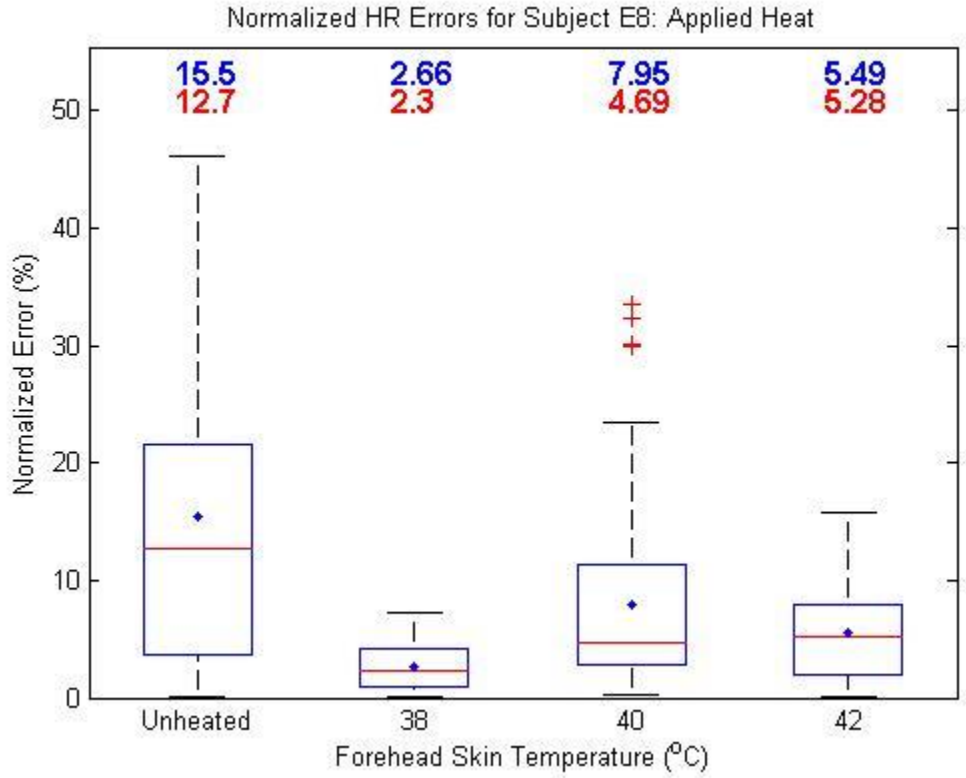

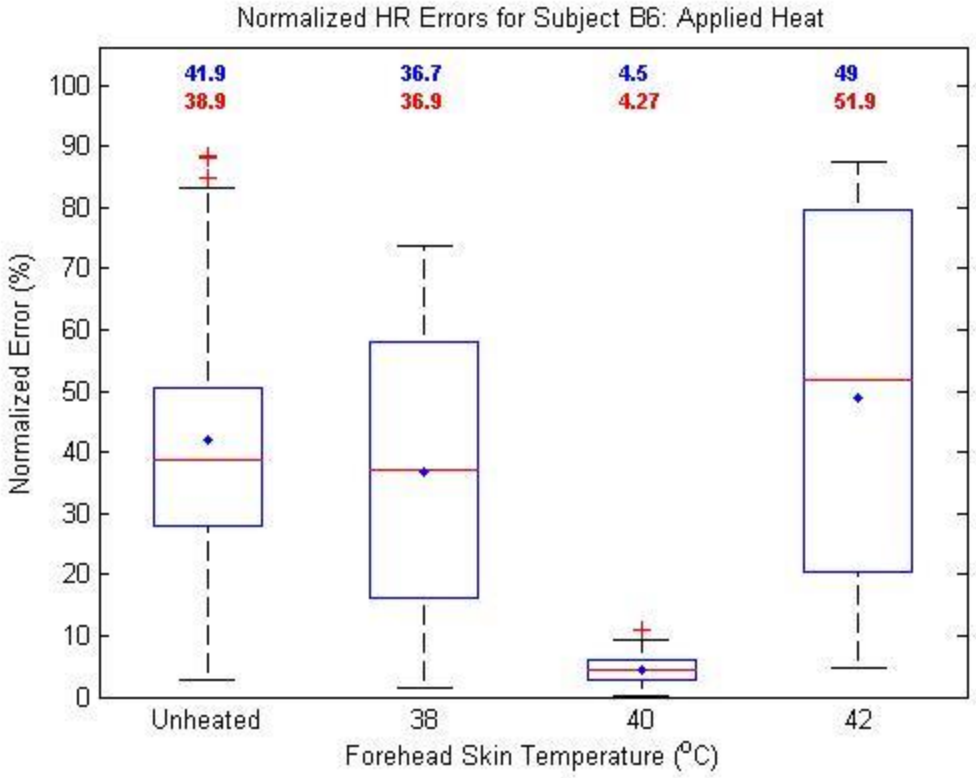

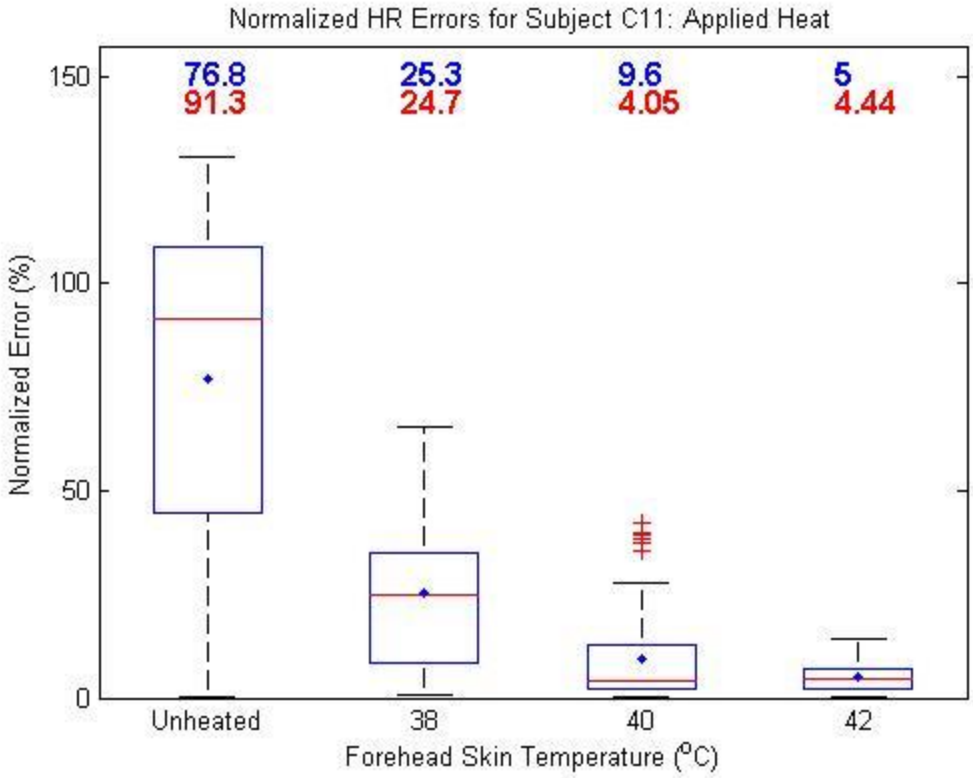
Normalized HR Errors for Subject C11: Applied Heat
76.8
91.3
25.3
24.7
9.6
4.05
5
4.44
150
100
50
0
Normalized Error (%)
Unheated
38
40
42
Forehead Skin Temperature (°C)

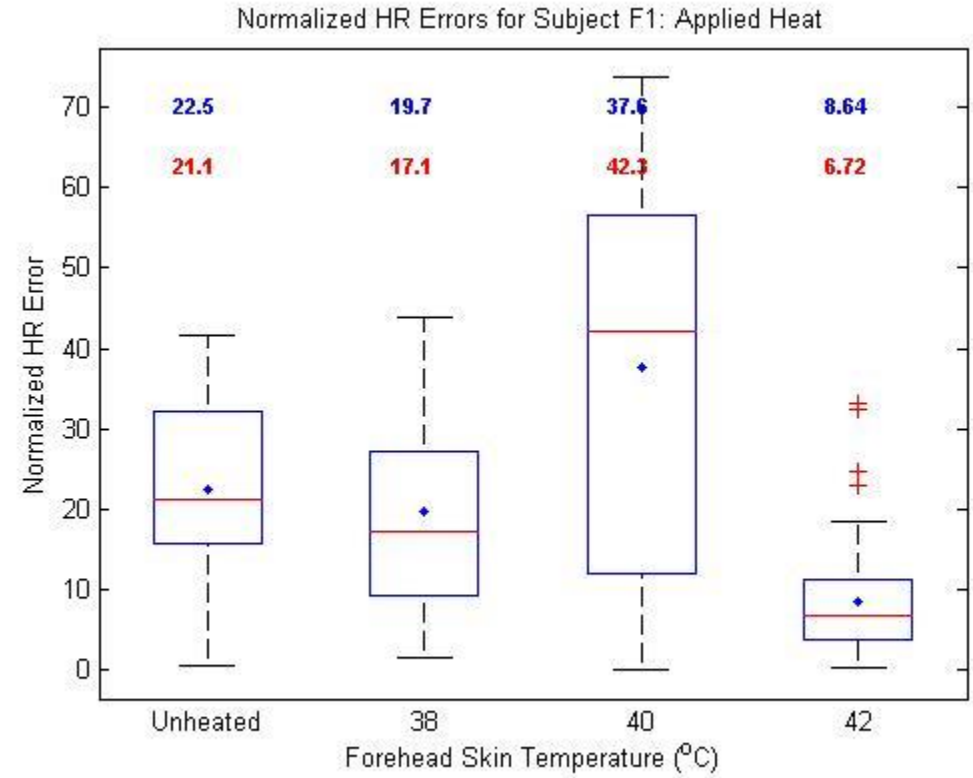
Normalized HR Errors for Subject F1: Applied Heat
22.5
21.1
19.7
17.1
37.6
42.3
8.64
6.72
70
60
50
40
30
20
10
0
Normalized HR Error
Unheated
38
40
42
Forehead Skin Temperature (°C)

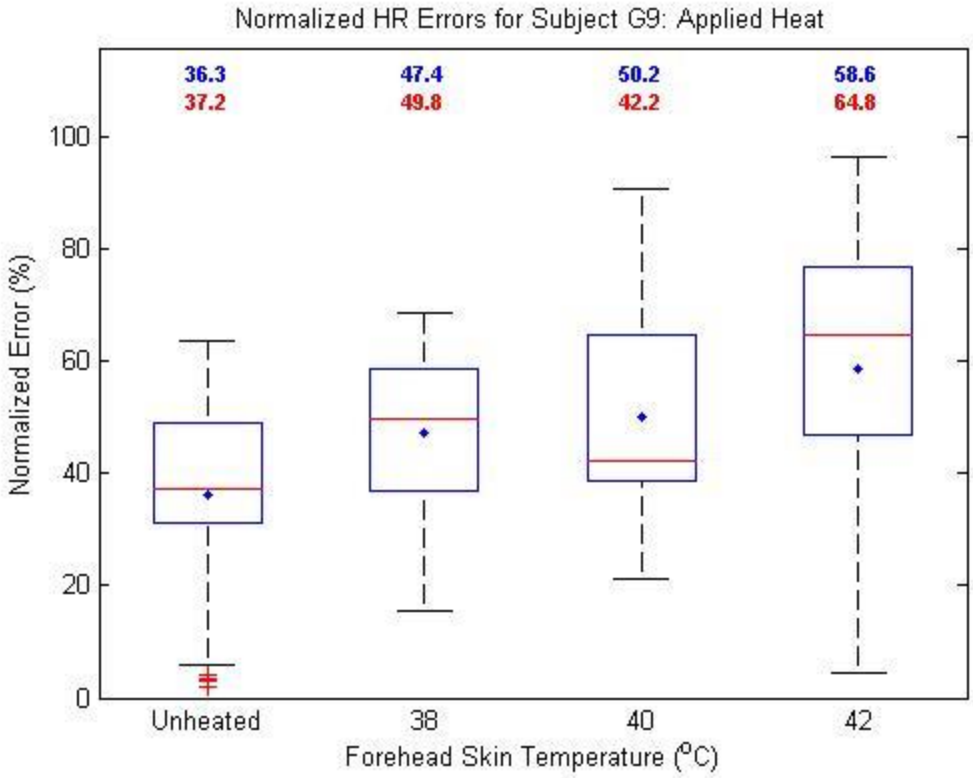
Normalized HR Errors for Subject G9: Applied Heat
36.3
37.2
47.4
49.8
50.2
42.2
58.6
64.8
Normalized Error (%)
0
20
40
60
80
100
Unheated
38
40
42
Forehead Skin Temperature (°C)

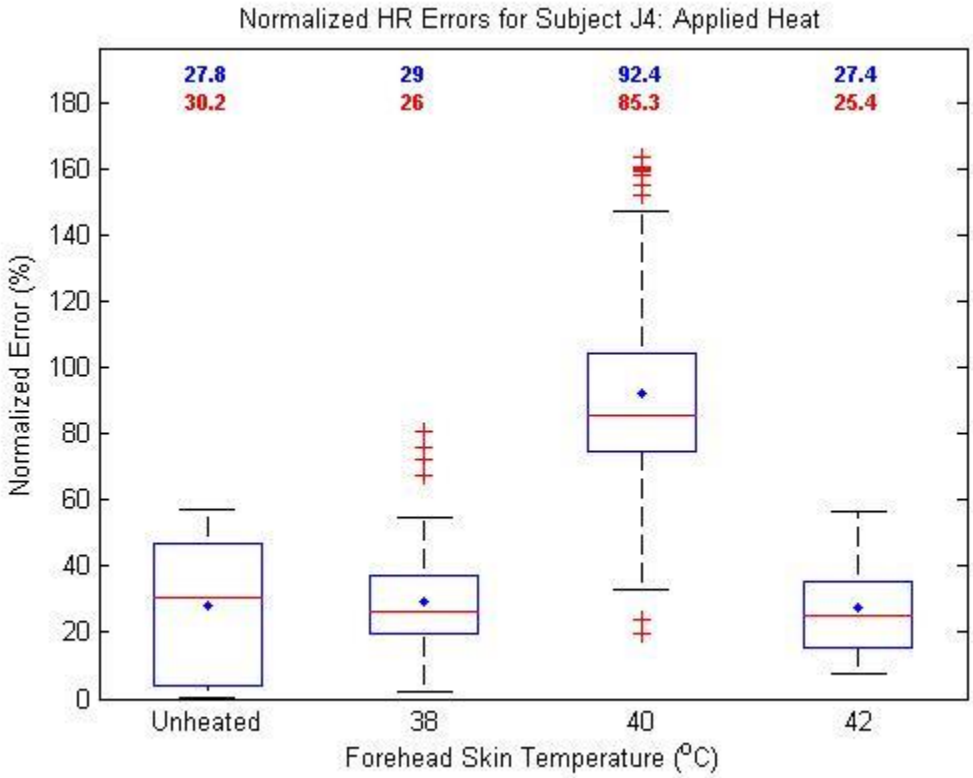
Normalized HR Errors for Subject J4: Applied Heat
27.8
30.2
29
26
92.4
85.3
27.4
25.4
Normalized Error (%)
0
20
40
60
80
100
120
140
160
180
Unheated
38
40
42
Forehead Skin Temperature (°C)

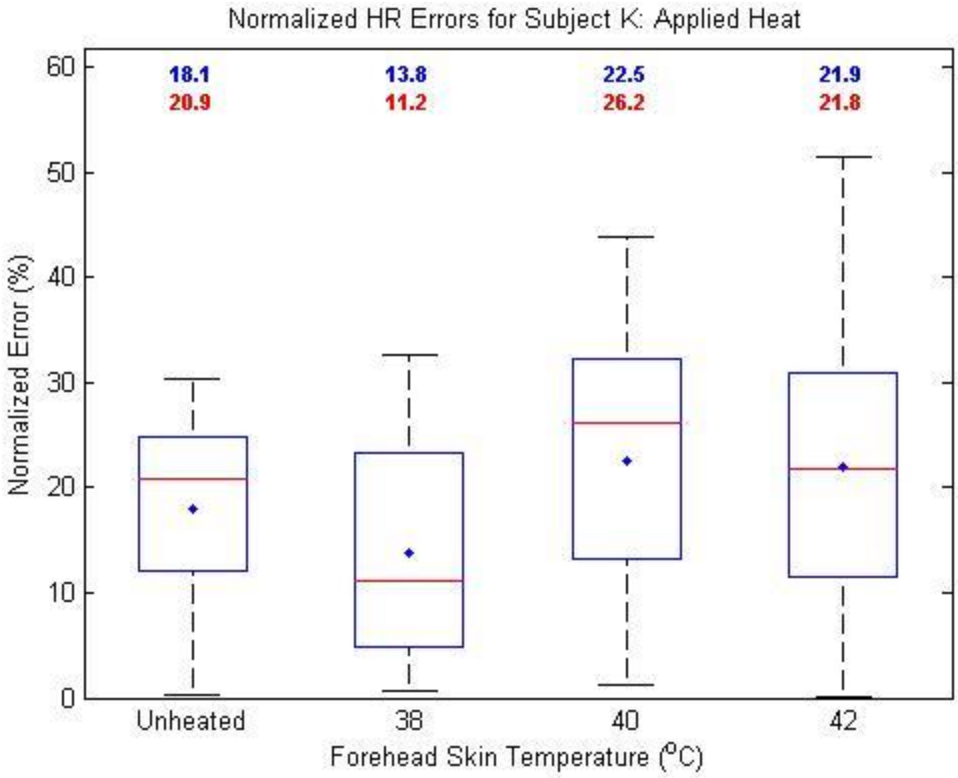
Normalized HR Errors for Subject K: Applied Heat
18.1
20.9
13.8
11.2
22.5
26.2
21.9
21.8
Normalized Error (%)
0
10
20
30
40
50
60
Unheated
38
40
42
Forehead Skin Temperature (°C)

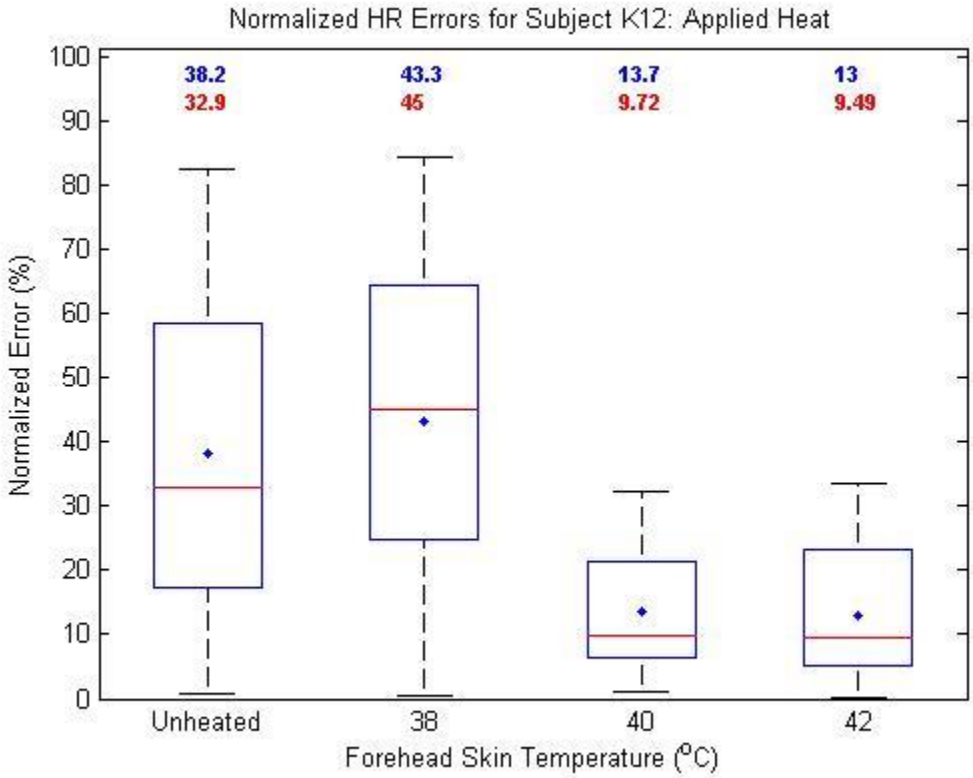
Normalized HR Errors for Subject K12: Applied Heat
38.2
32.9
43.3
45
13.7
9.72
13
9.49
Normalized Error (%)
0
10
20
30
40
50
60
70
80
90
100
Unheated
38
40
42
Forehead Skin Temperature (°C)

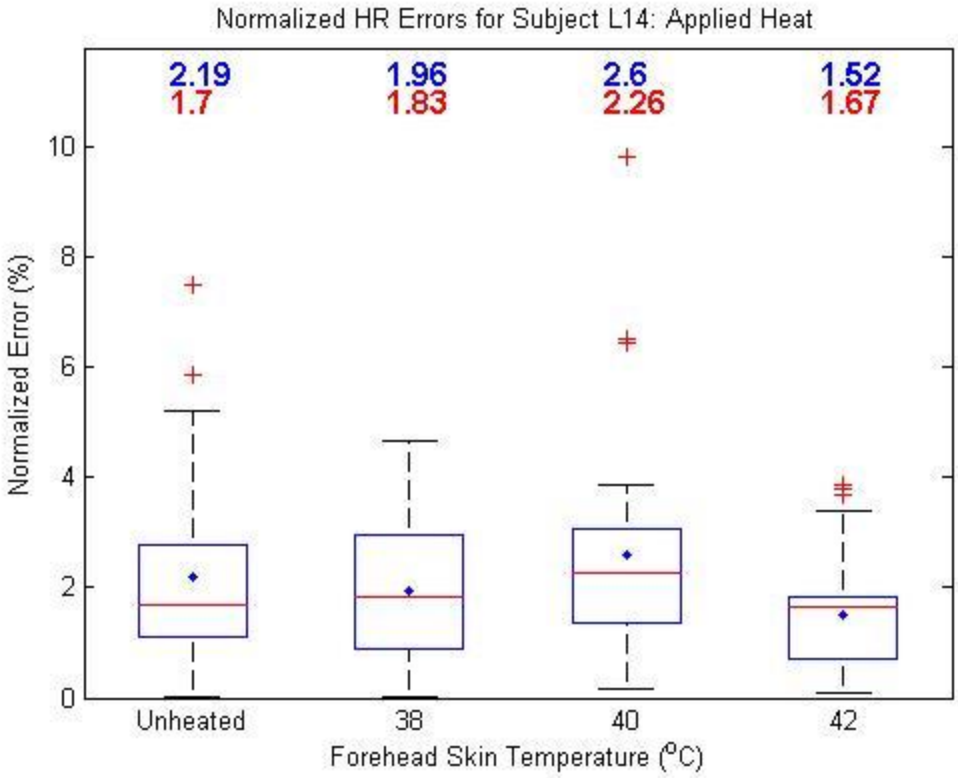
Normalized HR Errors for Subject L14: Applied Heat
2.19
1.7
1.96
1.83
2.6
2.26
1.52
1.67
Normalized Error (%)
0
2
4
6
8
10
Unheated
38
40
42
Forehead Skin Temperature (°C)

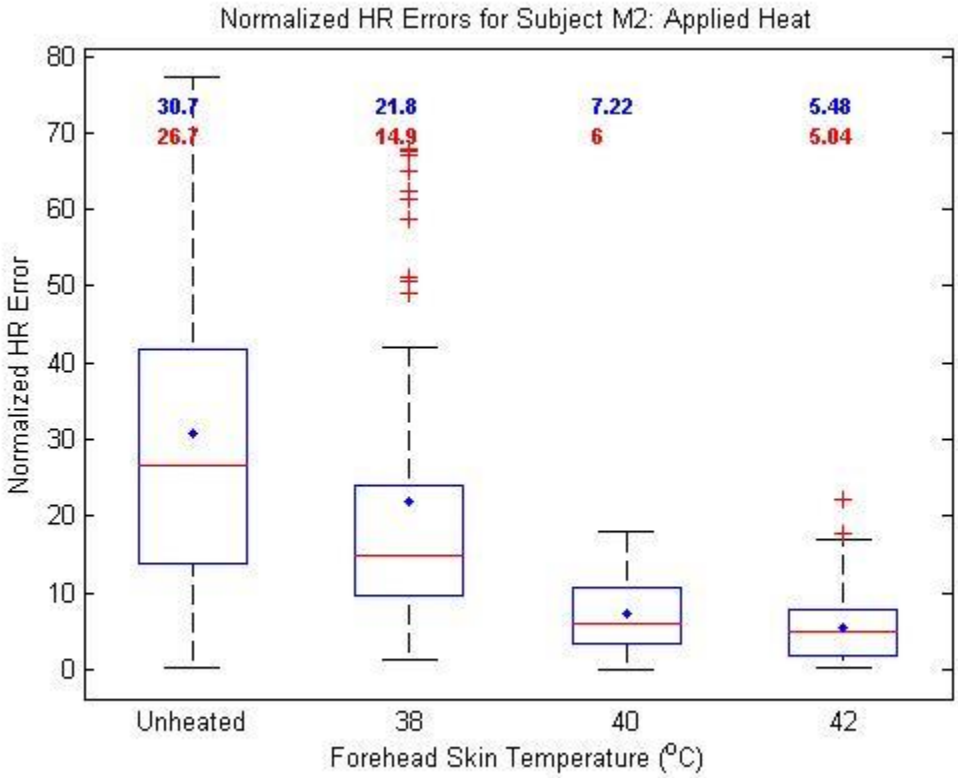
Normalized HR Errors for Subject M2: Applied Heat
30.7
26.7
21.8
14.9
7.22
6
5.48
5.04
Normalized HR Error
0
10
20
30
40
50
60
70
80
Unheated
38
40
42
Forehead Skin Temperature (°C)

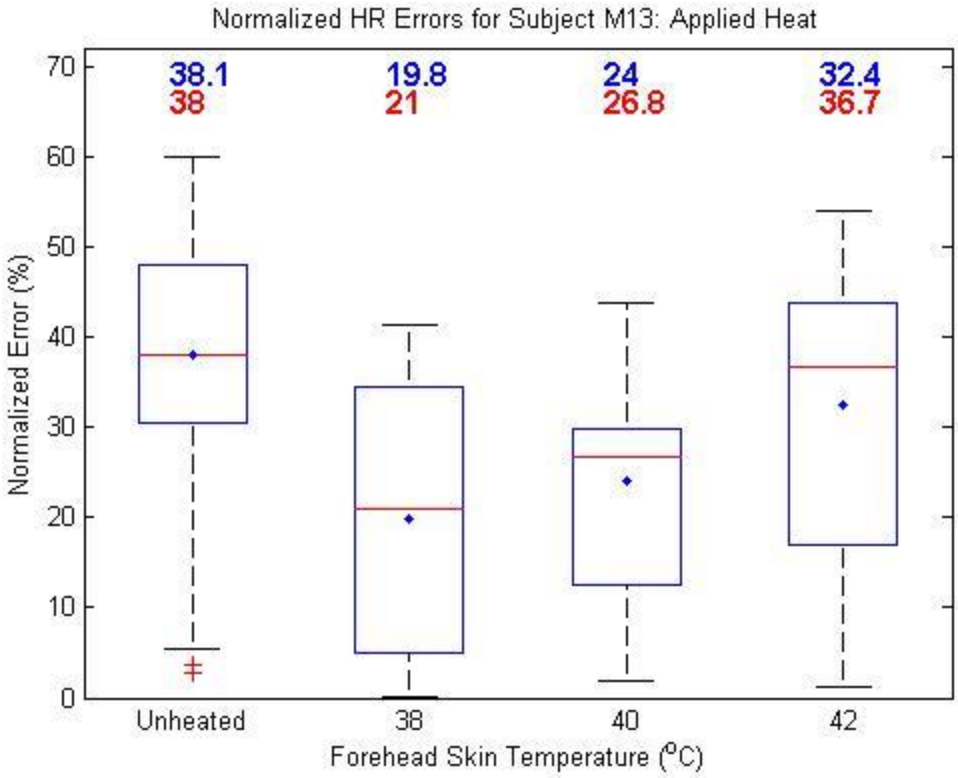
Normalized HR Errors for Subject M13: Applied Heat
38.1
38
19.8
21
24
26.8
32.4
36.7
Normalized Error (%)
0
10
20
30
40
50
60
70
Unheated
38
40
42
Forehead Skin Temperature (°C)

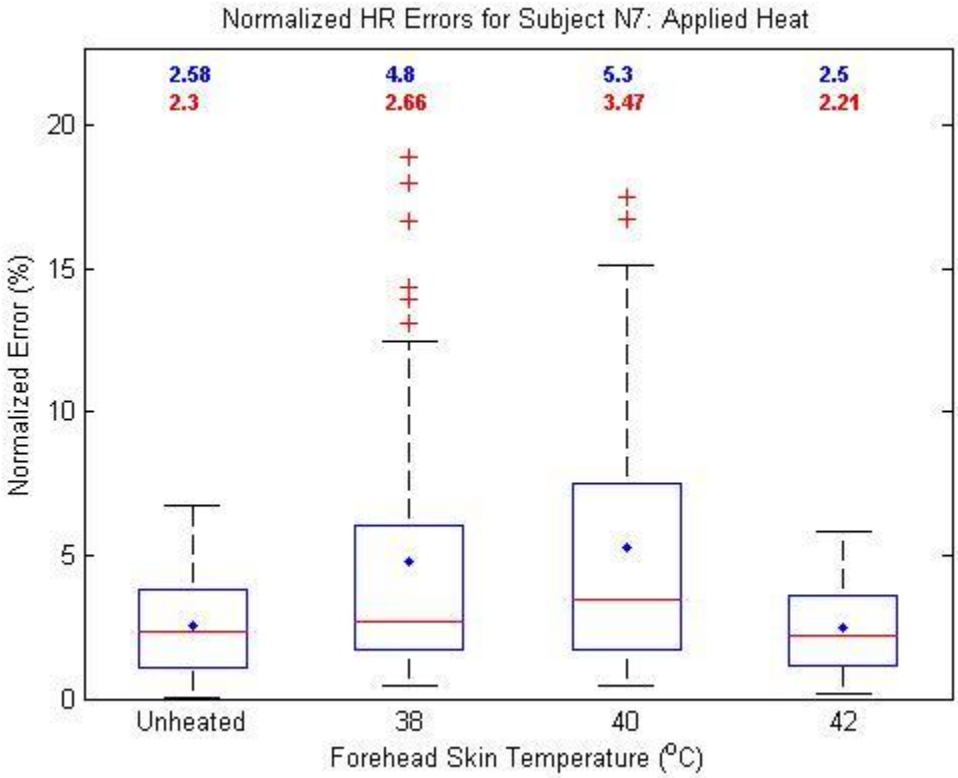
Normalized HR Errors for Subject N7: Applied Heat
2.58
2.3
4.8
2.66
5.3
3.47
2.5
2.21
Normalized Error (%)
0
5
10
15
20
Unheated
38
40
42
Forehead Skin Temperature (°C)

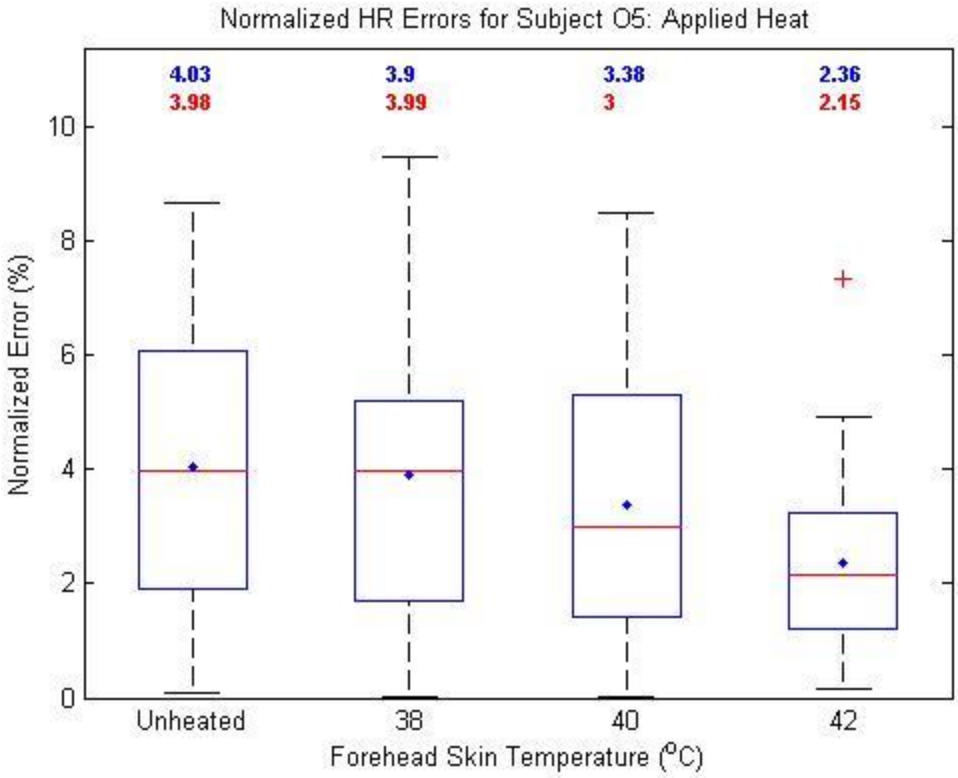
Normalized HR Errors for Subject O5: Applied Heat
4.03
3.98
3.9
3.99
3.38
3
2.36
2.15
Normalized Error (%)
0
2
4
6
8
10
Unheated
38
40
42
Forehead Skin Temperature (°C)

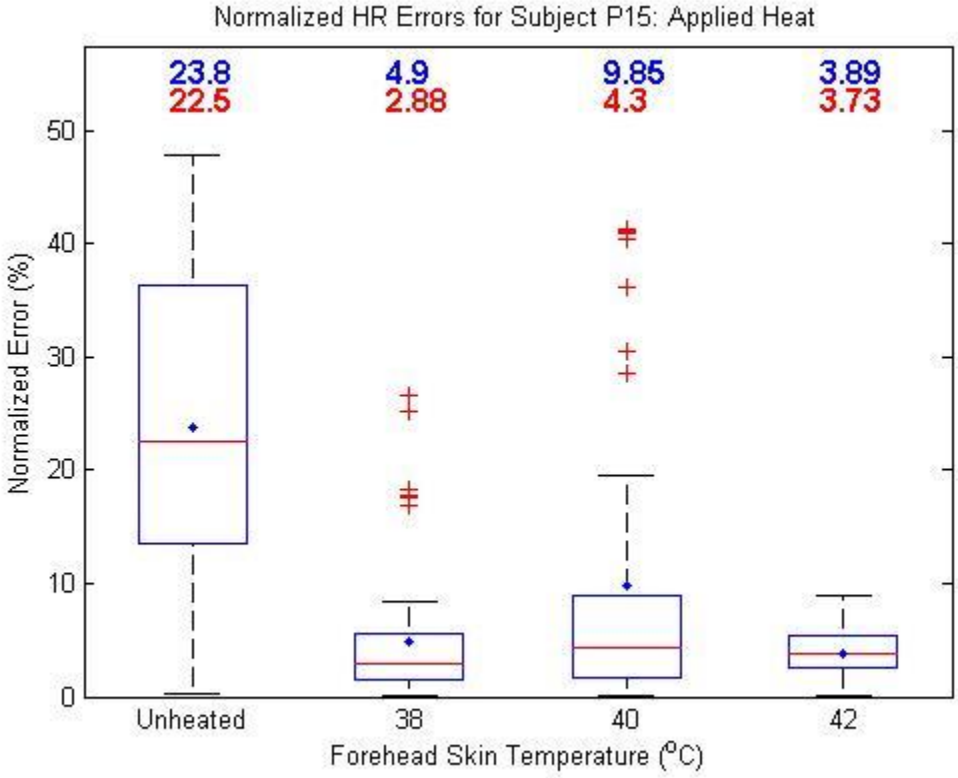
Normalized HR Errors for Subject P15: Applied Heat
23.8
22.5
4.9
2.88
9.85
4.3
3.89
3.73
Normalized Error (%)
0
10
20
30
40
50
Unheated
38
40
42
Forehead Skin Temperature (°C)

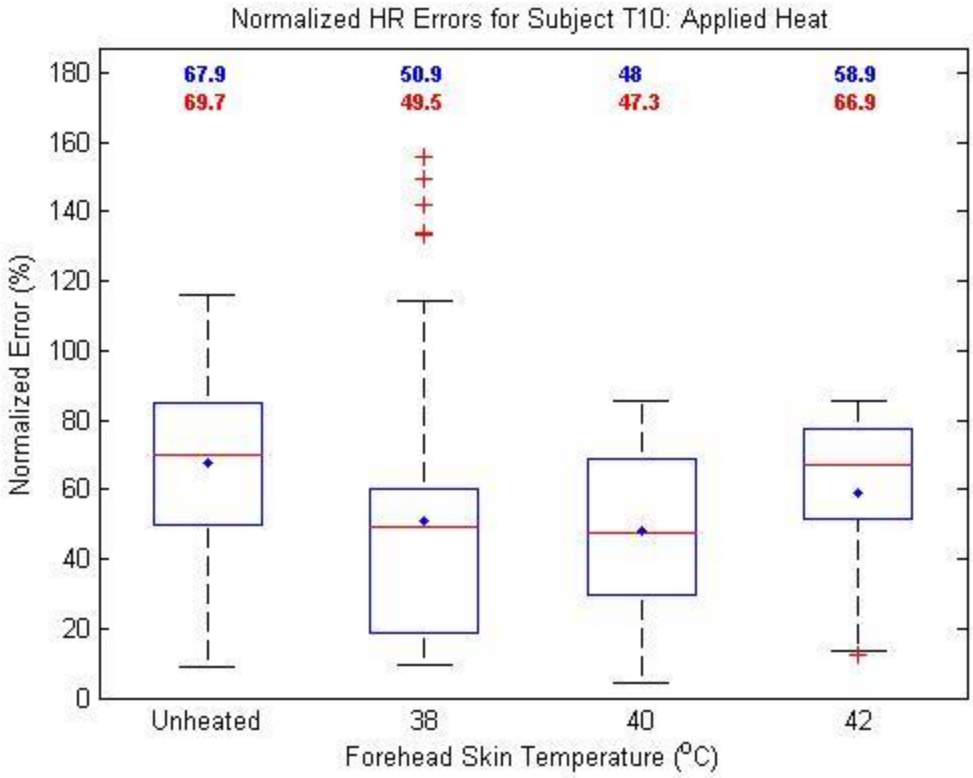
Normalized HR Errors for Subject T10: Applied Heat
67.9
69.7
50.9
49.5
48
47.3
58.9
66.9
180
160
140
120
100
80
60
40
20
0
Normalized Error (%)
Unheated
38
40
42
Forehead Skin Temperature (°C)

Appendix F: Applied Heat SpO_2 Box Plots

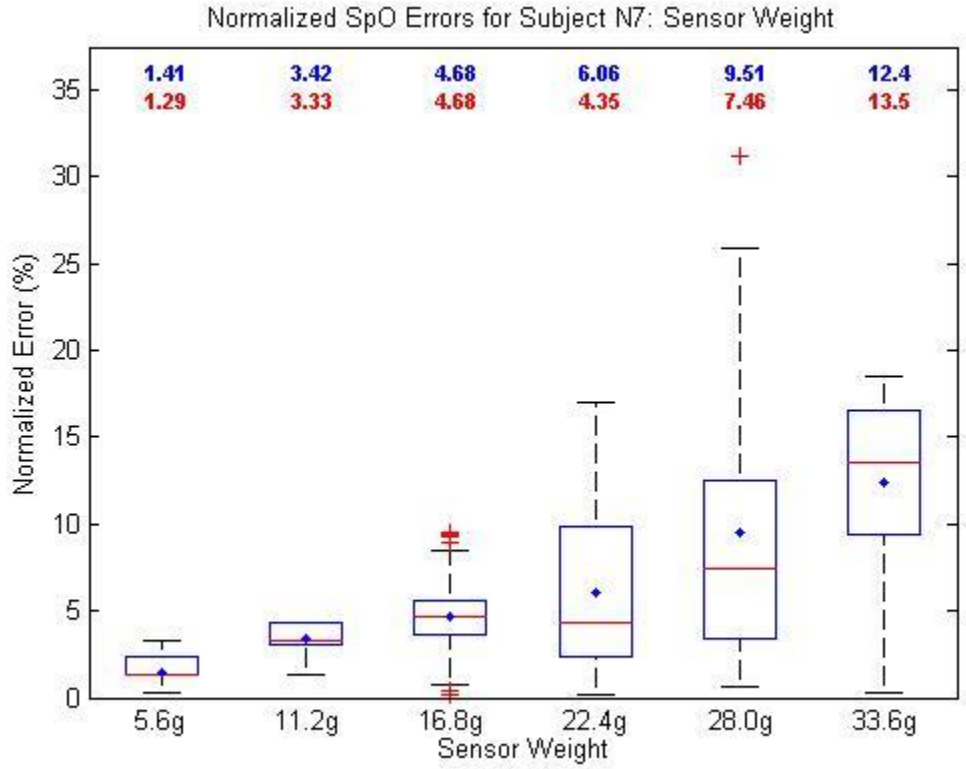

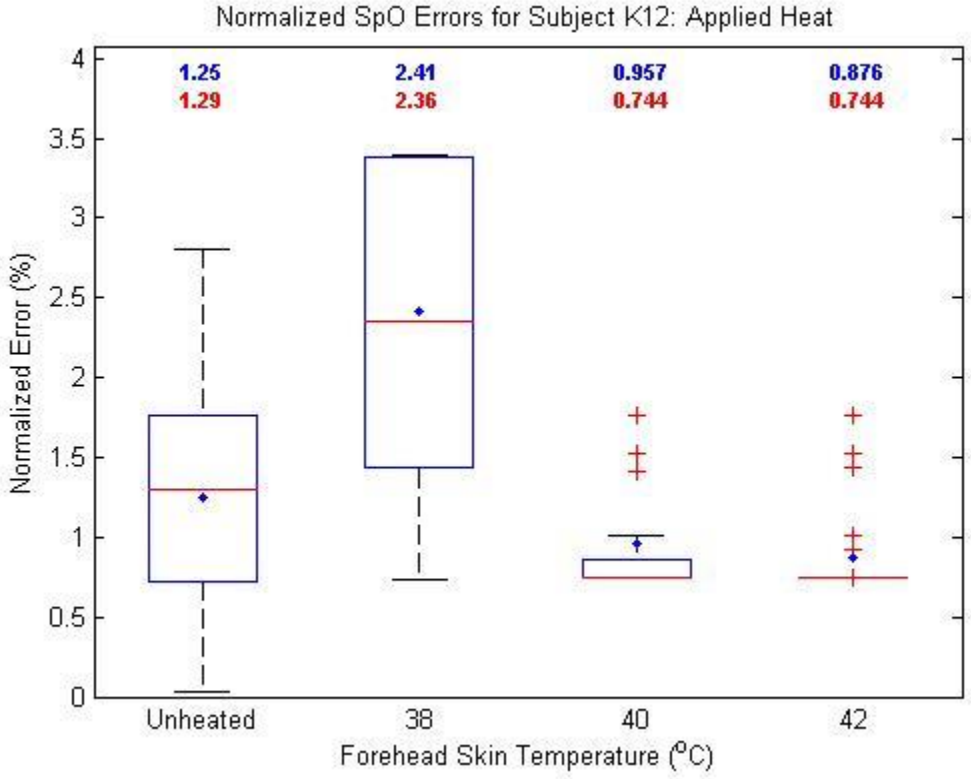

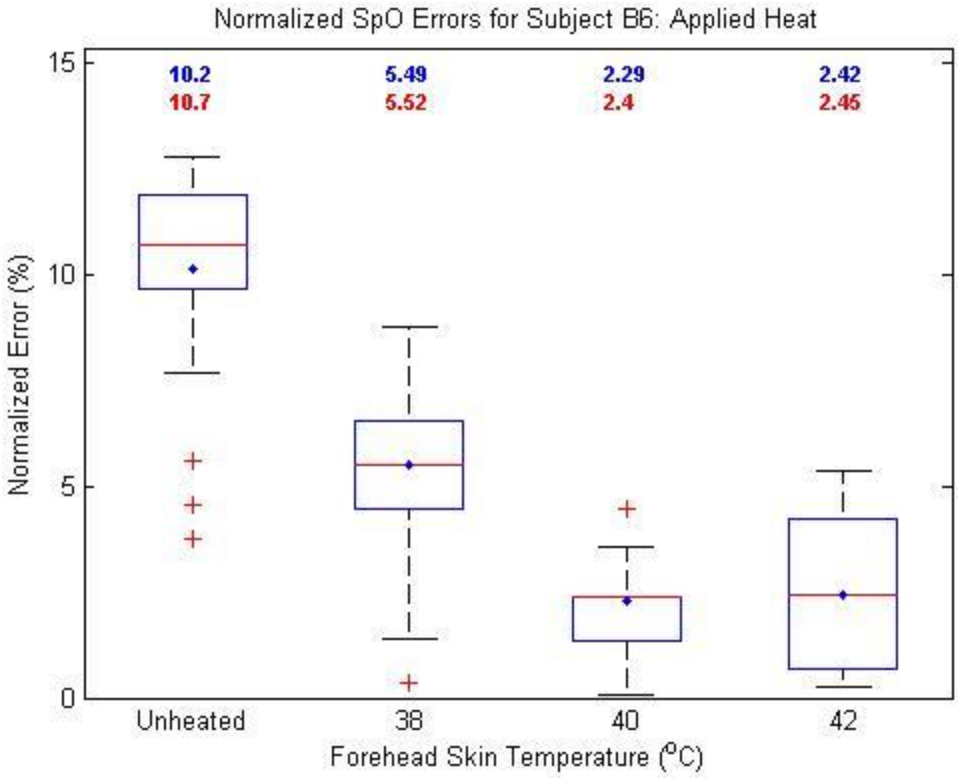
Normalized SpO Errors for Subject B6: Applied Heat
10.2
10.7
5.49
5.52
2.29
2.4
2.42
2.45
Normalized Error (%)
0
5
10
15
Unheated
38
40
42
Forehead Skin Temperature (°C)

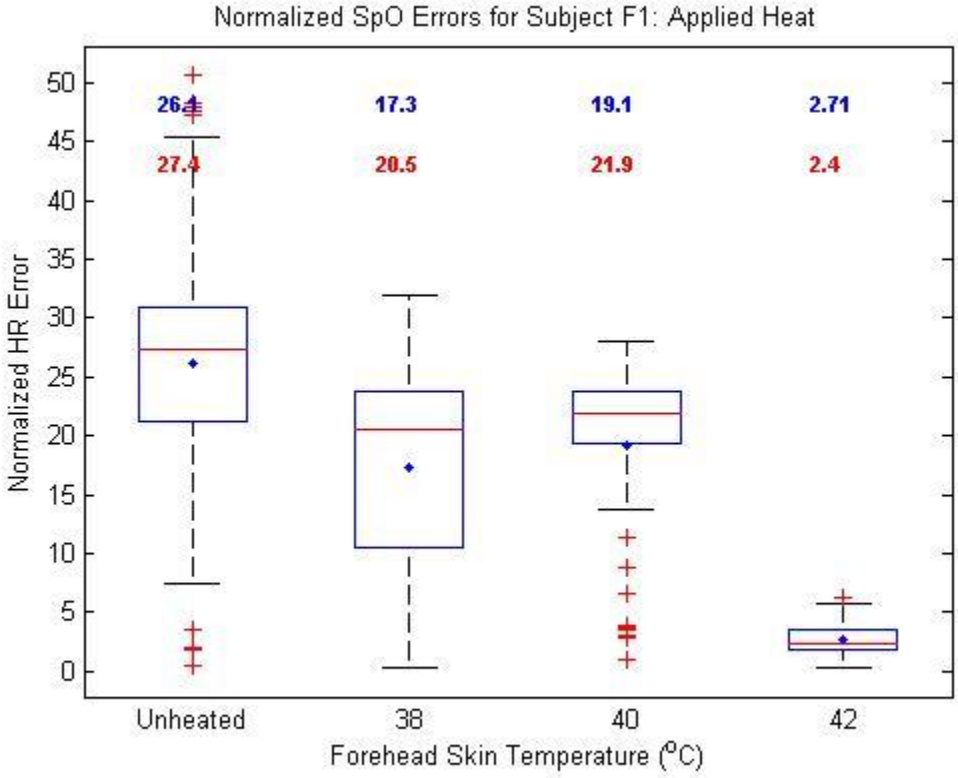
Normalized SpO Errors for Subject F1: Applied Heat
26.4
27.4
17.3
20.5
19.1
21.9
2.71
2.4
Normalized HR Error
0
5
10
15
20
25
30
35
40
45
50
Unheated
38
40
42
Forehead Skin Temperature (°C)

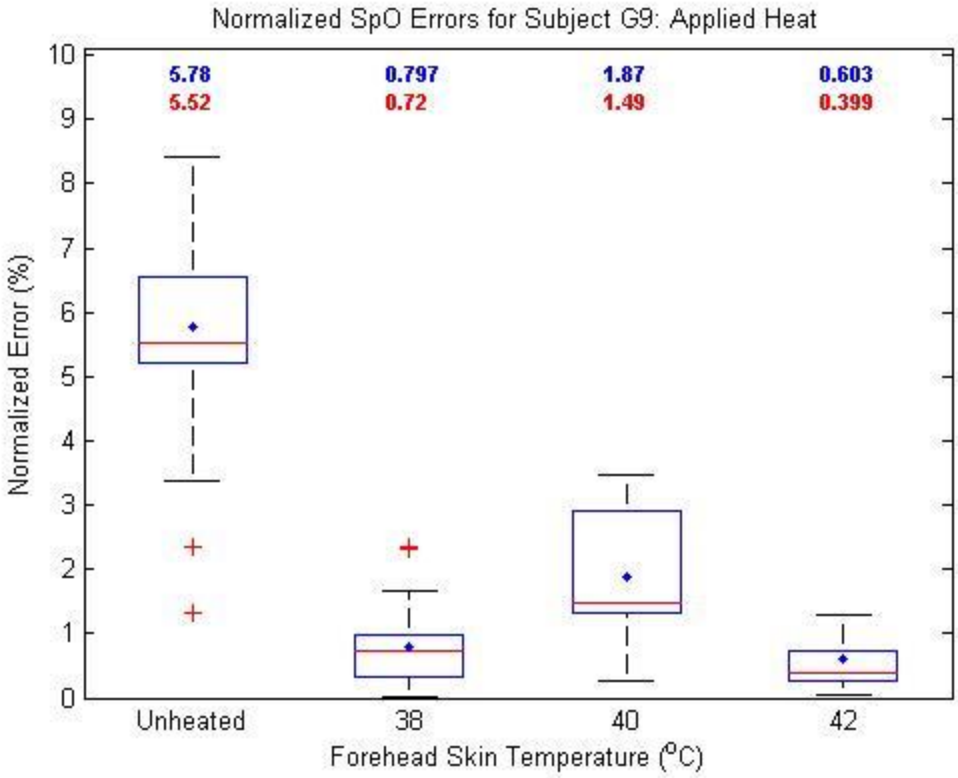
Normalized SpO Errors for Subject G9: Applied Heat
5.78
5.52
0.797
0.72
1.87
1.49
0.603
0.399
Normalized Error (%)
Unheated
38
40
42
Forehead Skin Temperature (°C)

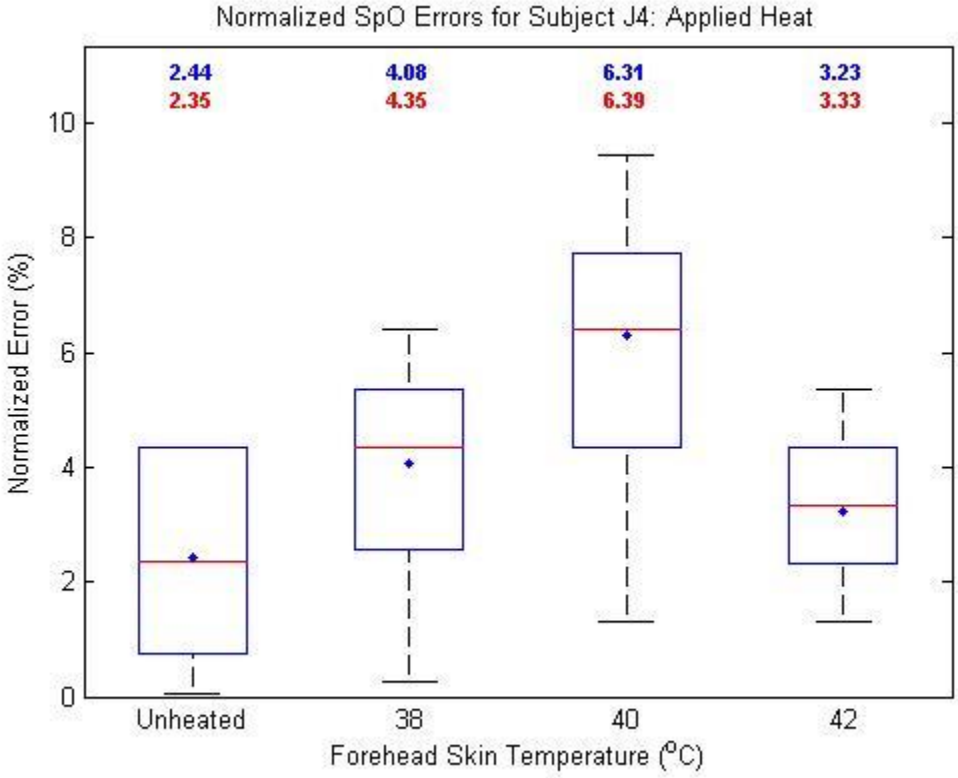
Normalized SpO Errors for Subject J4: Applied Heat
2.44
2.35
4.08
4.35
6.31
6.39
3.23
3.33
Normalized Error (%)
Unheated
38
40
42
Forehead Skin Temperature (°C)

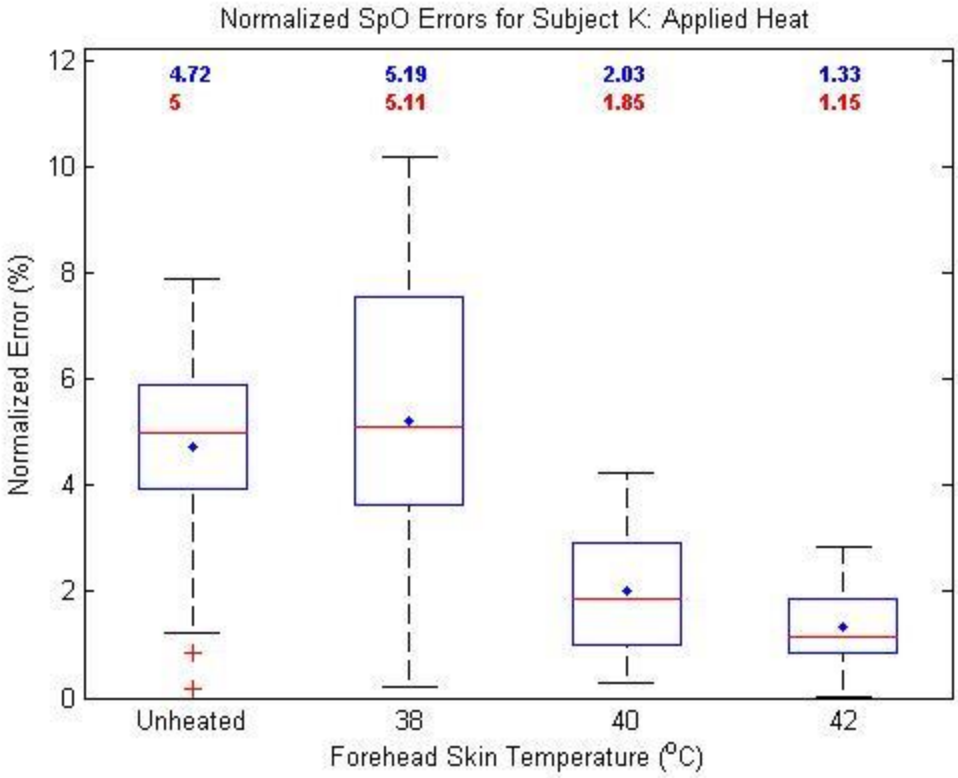
Normalized SpO Errors for Subject K: Applied Heat
4.72
5
5.19
5.11
2.03
1.85
1.33
1.15
Normalized Error (%)
Unheated
38
40
42
Forehead Skin Temperature (°C)

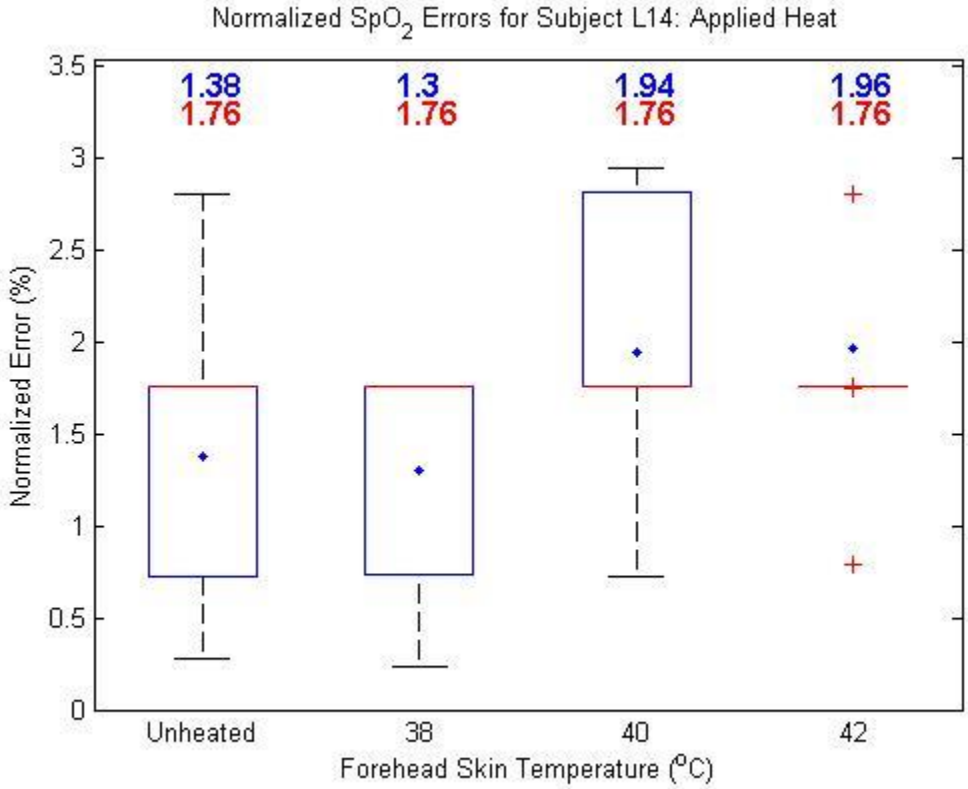
Normalized SpO2 Errors for Subject L14: Applied Heat
1.38
1.76
1.3
1.76
1.94
1.76
1.96
1.76
Normalized Error (%)
Unheated
38
40
42
Forehead Skin Temperature (°C)

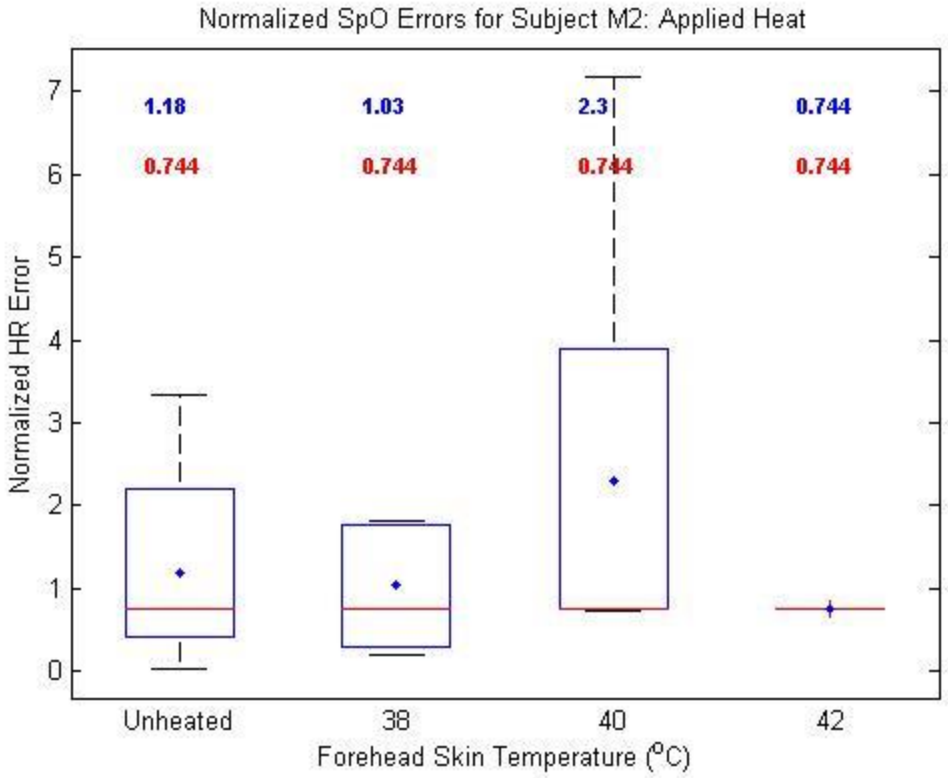
Normalized SpO Errors for Subject M2: Applied Heat
1.18
1.03
2.3
0.744
0.744
0.744
0.744
0.744
Normalized HR Error
0
1
2
3
4
5
6
7
Unheated
38
40
42
Forehead Skin Temperature (°C)

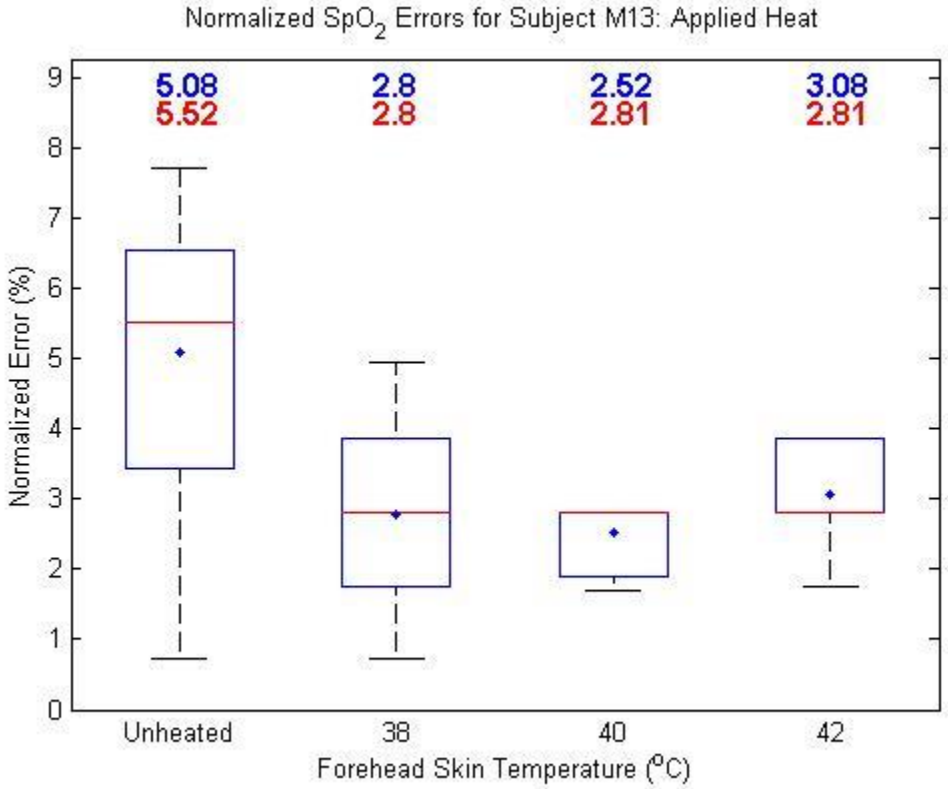
Normalized SpO2 Errors for Subject M13: Applied Heat
5.08
5.52
2.8
2.8
2.52
2.81
3.08
2.81
Normalized Error (%)
0
1
2
3
4
5
6
7
8
9
Unheated
38
40
42
Forehead Skin Temperature (°C)

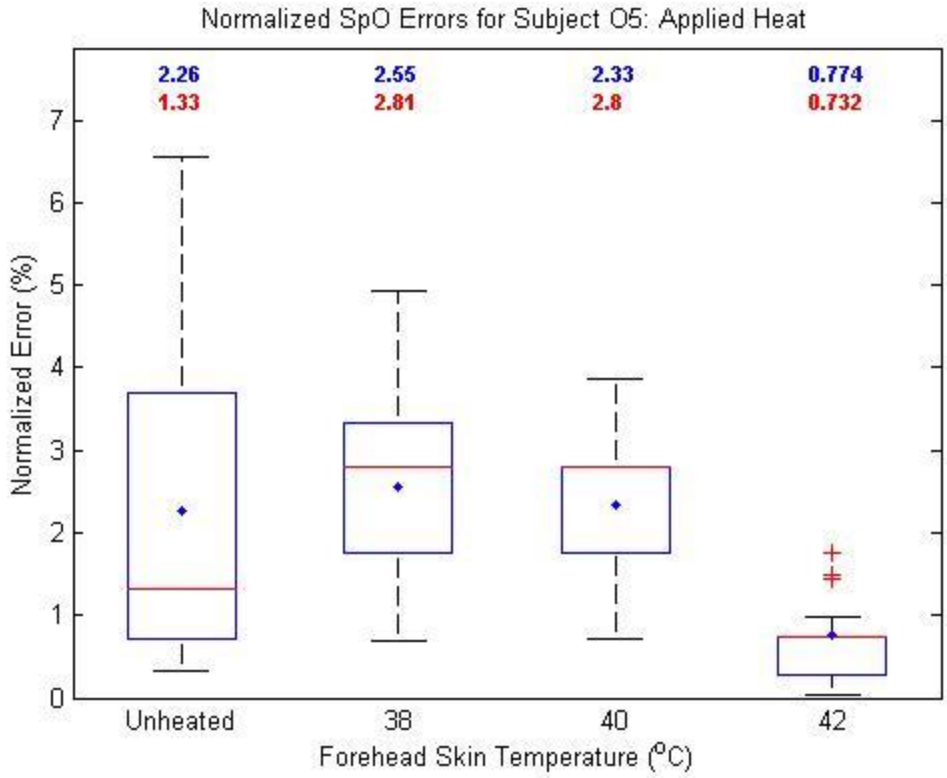
Normalized SpO Errors for Subject O5: Applied Heat
2.26
1.33
2.55
2.81
2.33
2.8
0.774
0.732
Normalized Error (%)
0
1
2
3
4
5
6
7
Unheated
38
40
42
Forehead Skin Temperature (°C)

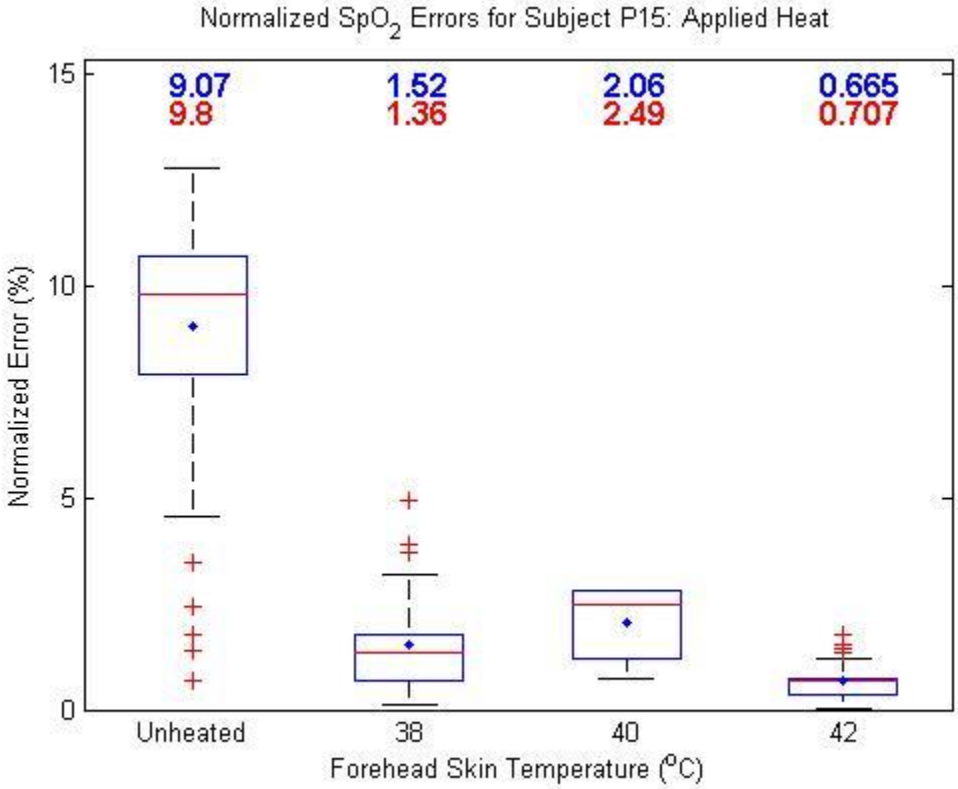
Normalized SpO2 Errors for Subject P15: Applied Heat
9.07
9.8
1.52
1.36
2.06
2.49
0.665
0.707
Normalized Error (%)
0
5
10
15
Unheated
38
40
42
Forehead Skin Temperature (°C)

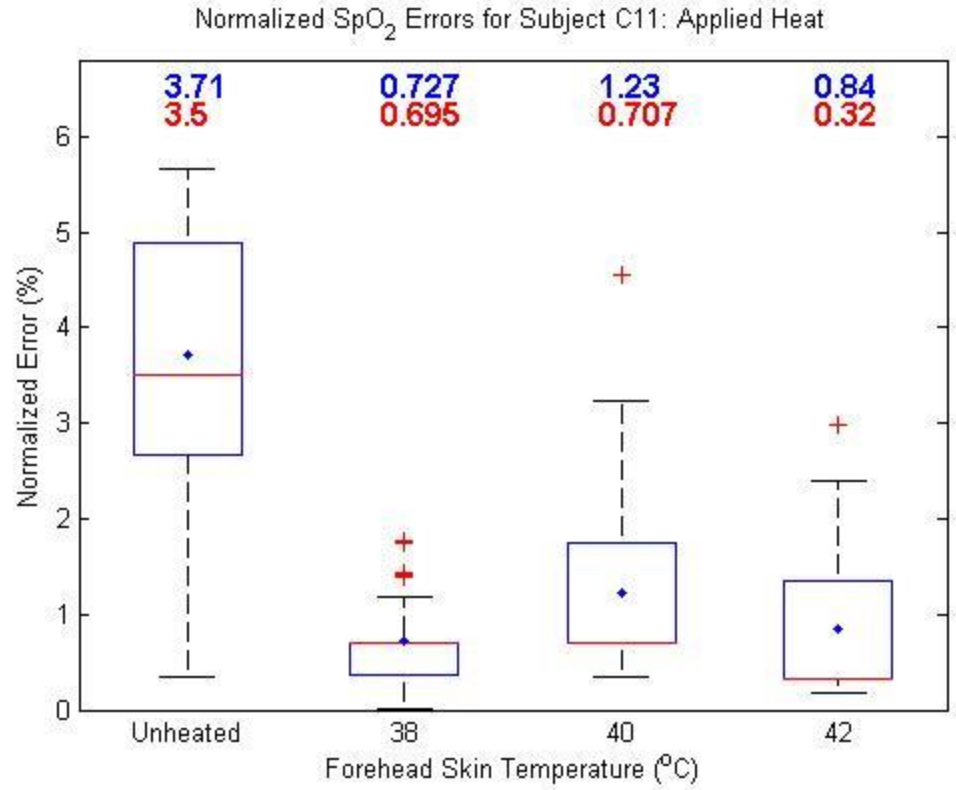
Normalized SpO2 Errors for Subject C11: Applied Heat
3.71
3.5
0.727
0.695
1.23
0.707
0.84
0.32
Normalized Error (%)
0
1
2
3
4
5
6
Unheated
38
40
42
Forehead Skin Temperature (°C)

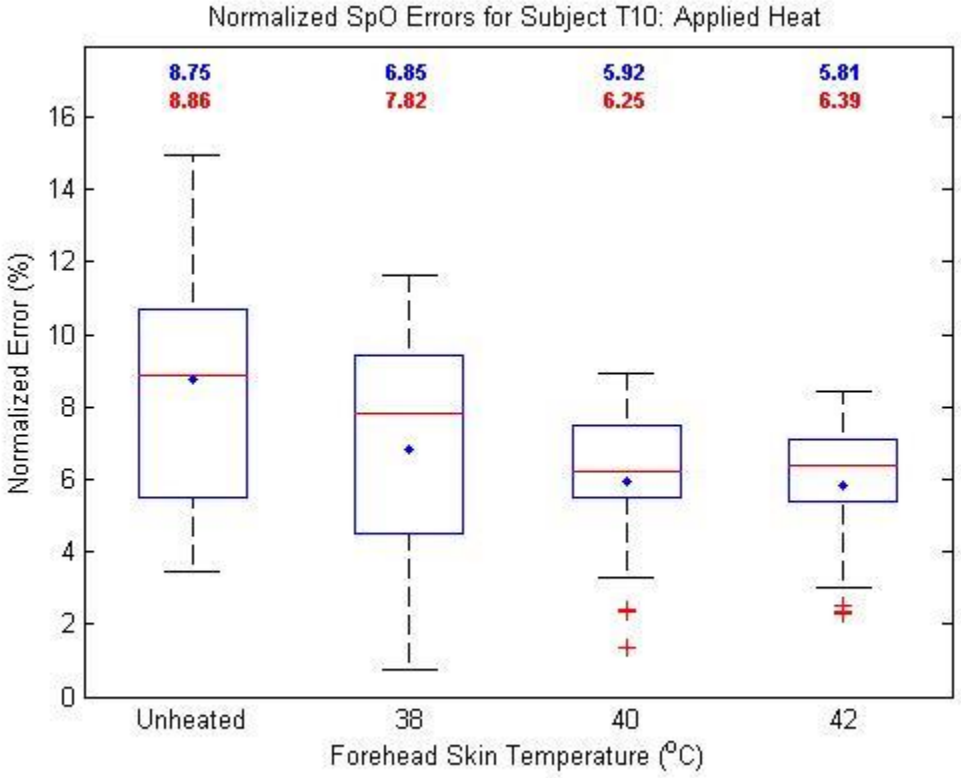
Normalized SpO Errors for Subject T10: Applied Heat
8.75
8.86
6.85
7.82
5.92
6.25
5.81
6.39
Normalized Error (%)
0
2
4
6
8
10
12
14
16
Unheated
38
40
42
Forehead Skin Temperature (°C)

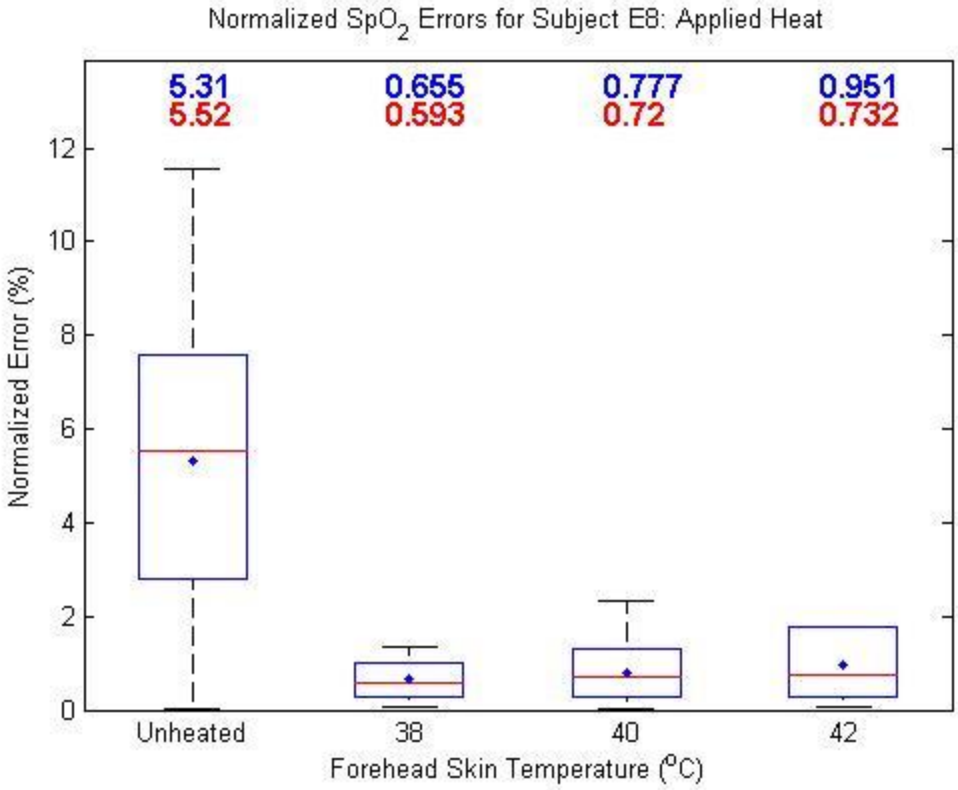
Normalized SpO2 Errors for Subject E8: Applied Heat
5.31
5.52
0.655
0.593
0.777
0.72
0.951
0.732
Normalized Error (%)
0
2
4
6
8
10
12
Unheated
38
40
42
Forehead Skin Temperature (°C)

Appendix G: Applied Pressure HR Box Plots

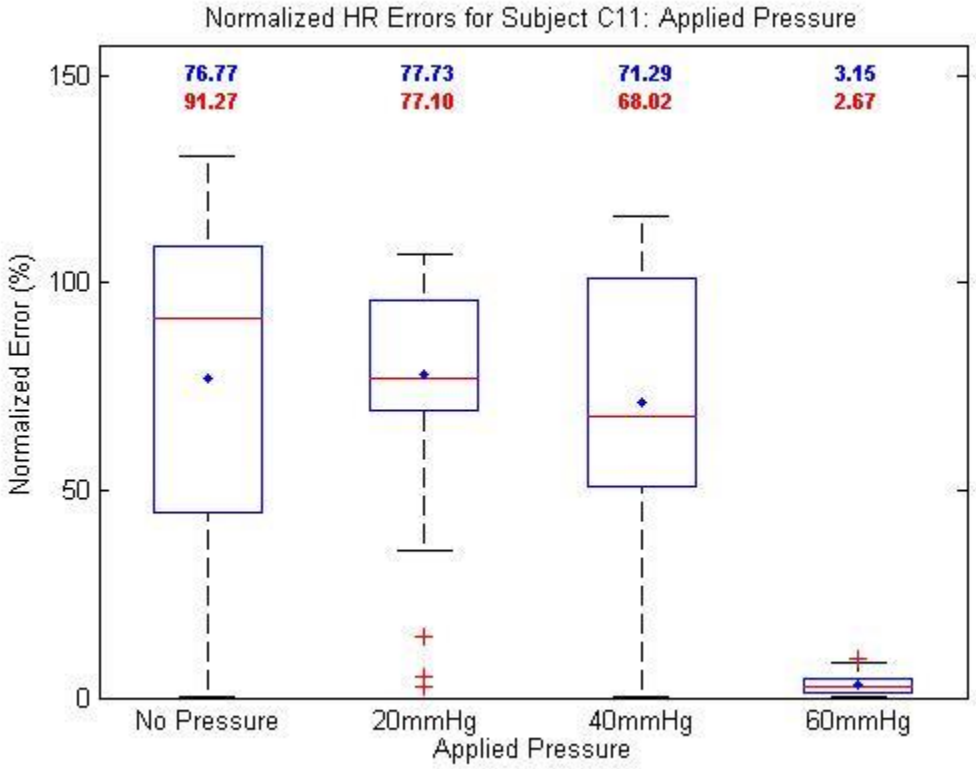

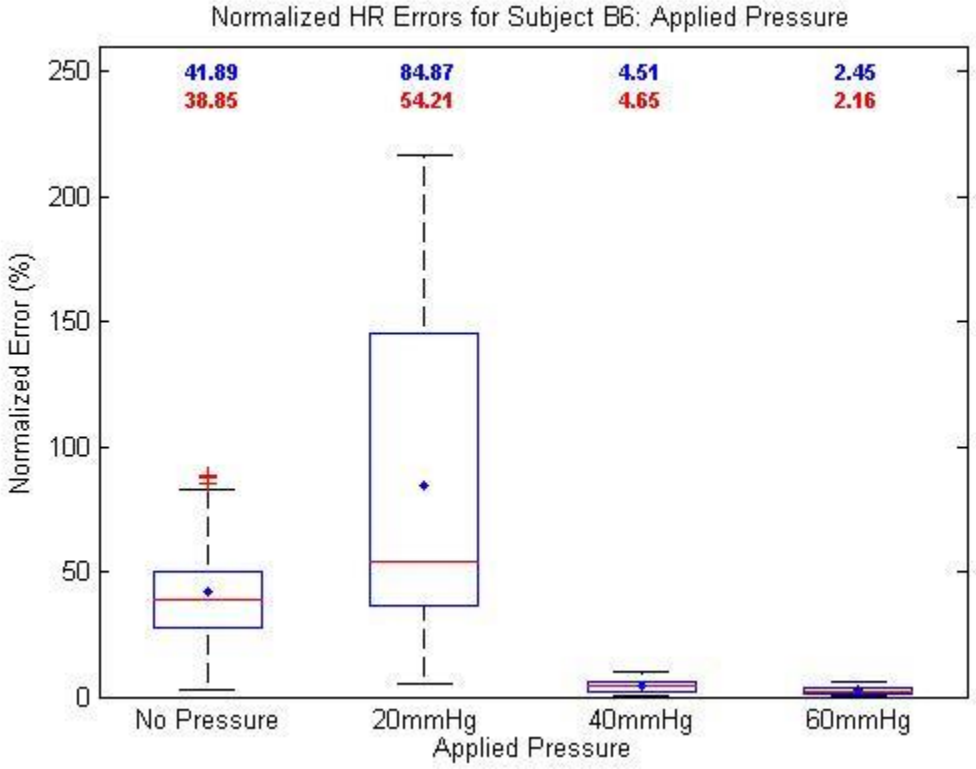

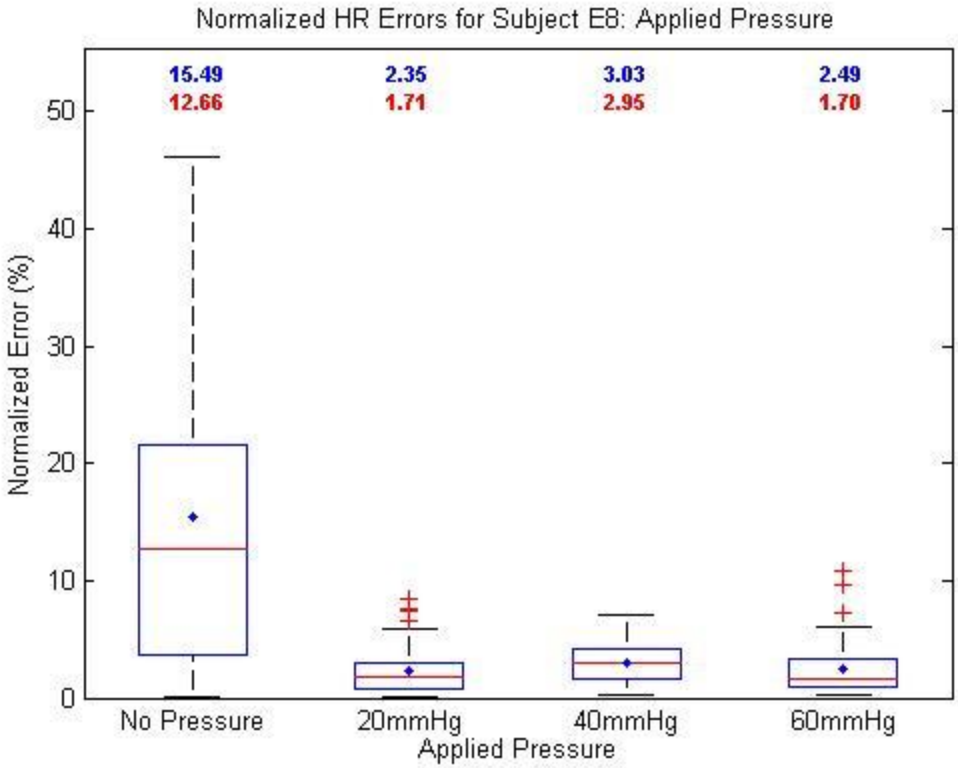
Normalized HR Errors for Subject E8: Applied Pressure
15.49
12.66
2.35
1.71
3.03
2.95
2.49
1.70
Normalized Error (%)
0
10
20
30
40
50
No Pressure
20mmHg
40mmHg
60mmHg
Applied Pressure

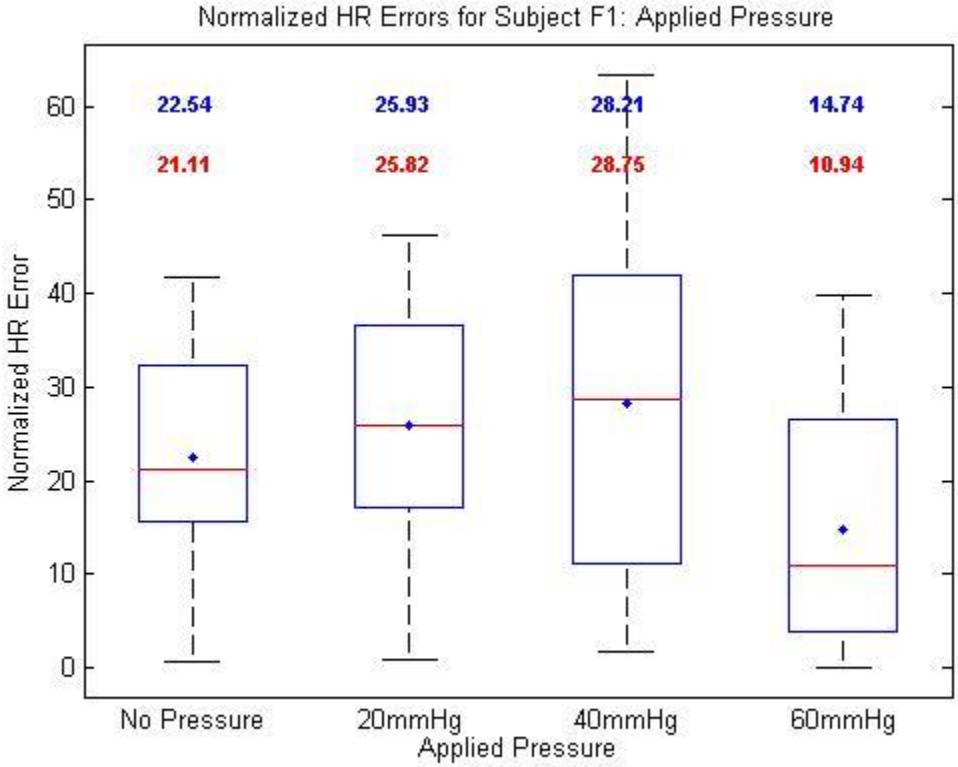
Normalized HR Errors for Subject F1: Applied Pressure
22.54
21.11
25.93
25.82
28.21
28.75
14.74
10.94
Normalized HR Error
0
10
20
30
40
50
60
No Pressure
20mmHg
40mmHg
60mmHg
Applied Pressure

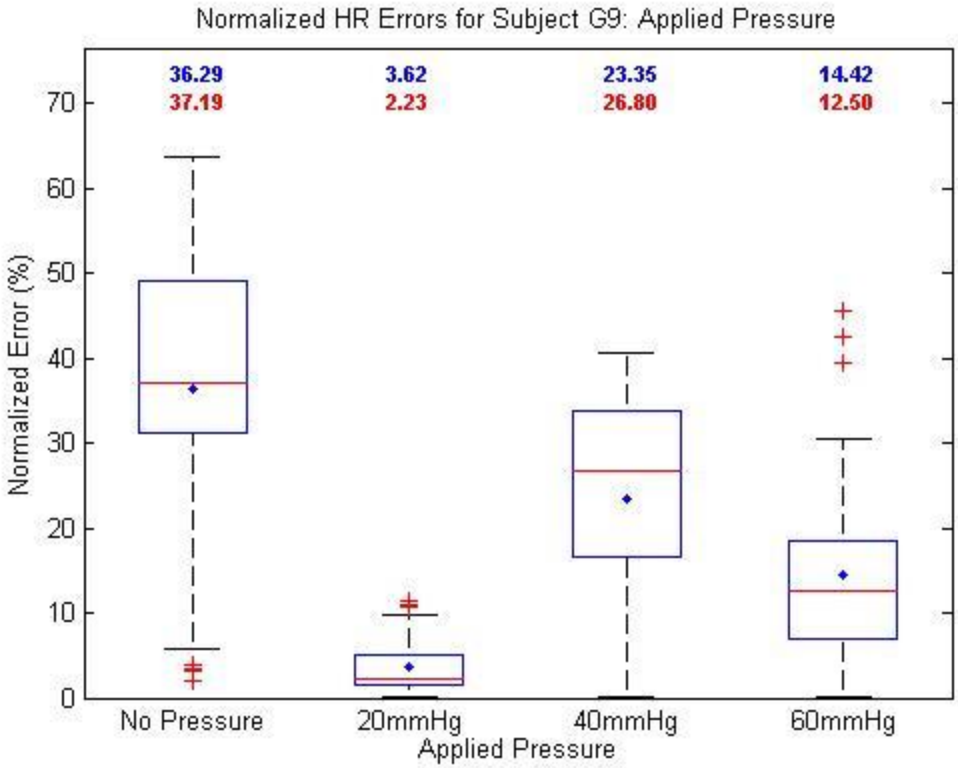
Normalized HR Errors for Subject G9: Applied Pressure
36.29
37.19
3.62
2.23
23.35
26.80
14.42
12.50
Normalized Error (%)
0
10
20
30
40
50
60
70
No Pressure
20mmHg
40mmHg
60mmHg
Applied Pressure

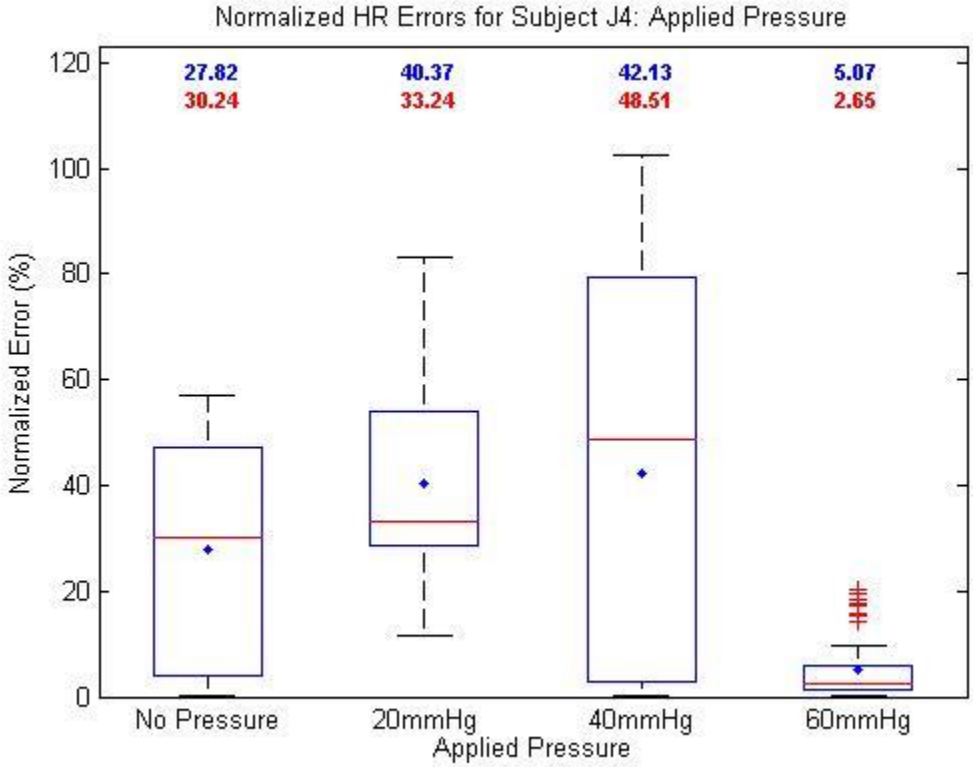
Normalized HR Errors for Subject J4: Applied Pressure
27.82
30.24
40.37
33.24
42.13
48.51
5.07
2.65
Normalized Error (%)
0
20
40
60
80
100
120
No Pressure
20mmHg
40mmHg
60mmHg
Applied Pressure

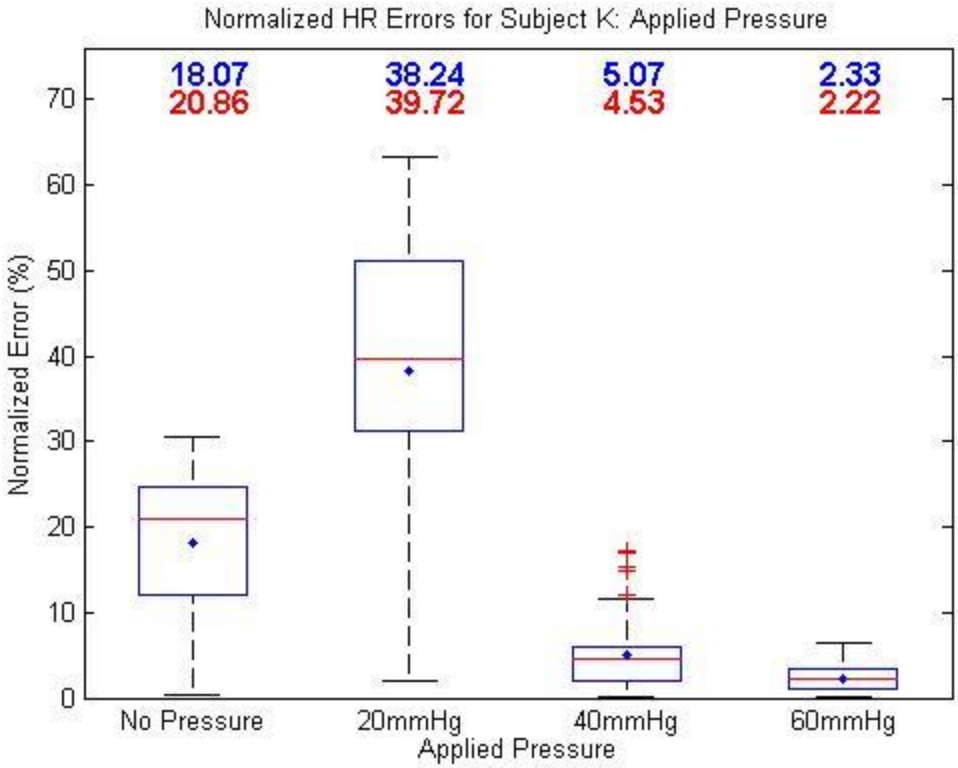
Normalized HR Errors for Subject K: Applied Pressure
18.07
20.86
38.24
39.72
5.07
4.53
2.33
2.22
Normalized Error (%)
0
10
20
30
40
50
60
70
No Pressure
20mmHg
40mmHg
60mmHg
Applied Pressure

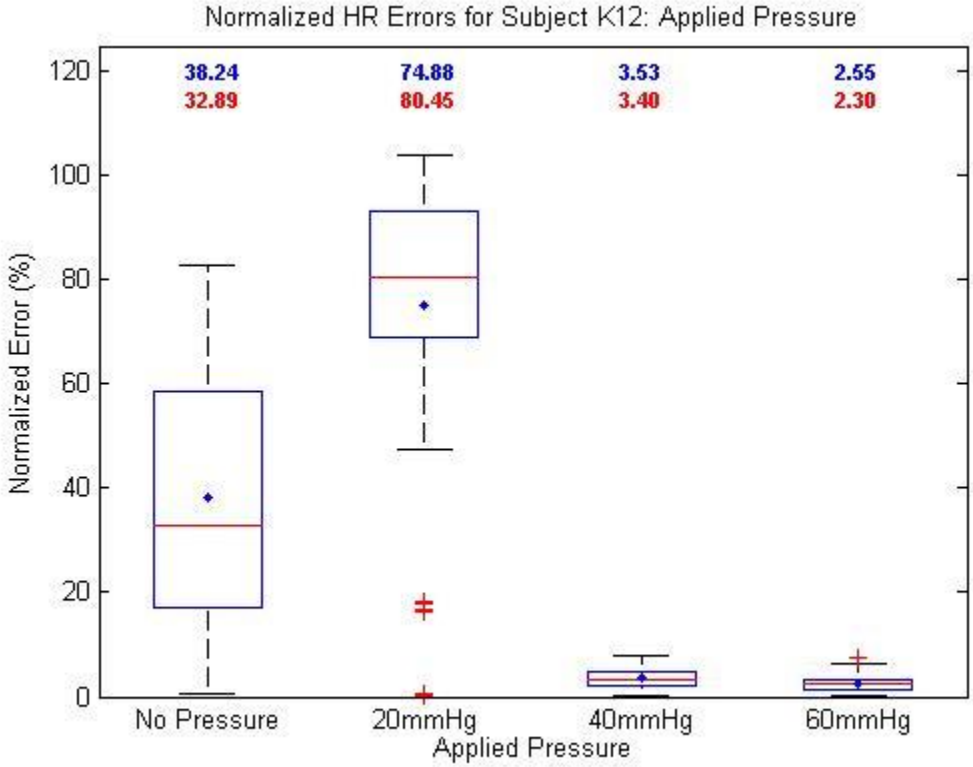
Normalized HR Errors for Subject K12: Applied Pressure
38.24
32.89
74.88
80.45
3.53
3.40
2.55
2.30
Normalized Error (%)
0
20
40
60
80
100
120
No Pressure
20mmHg
40mmHg
60mmHg
Applied Pressure

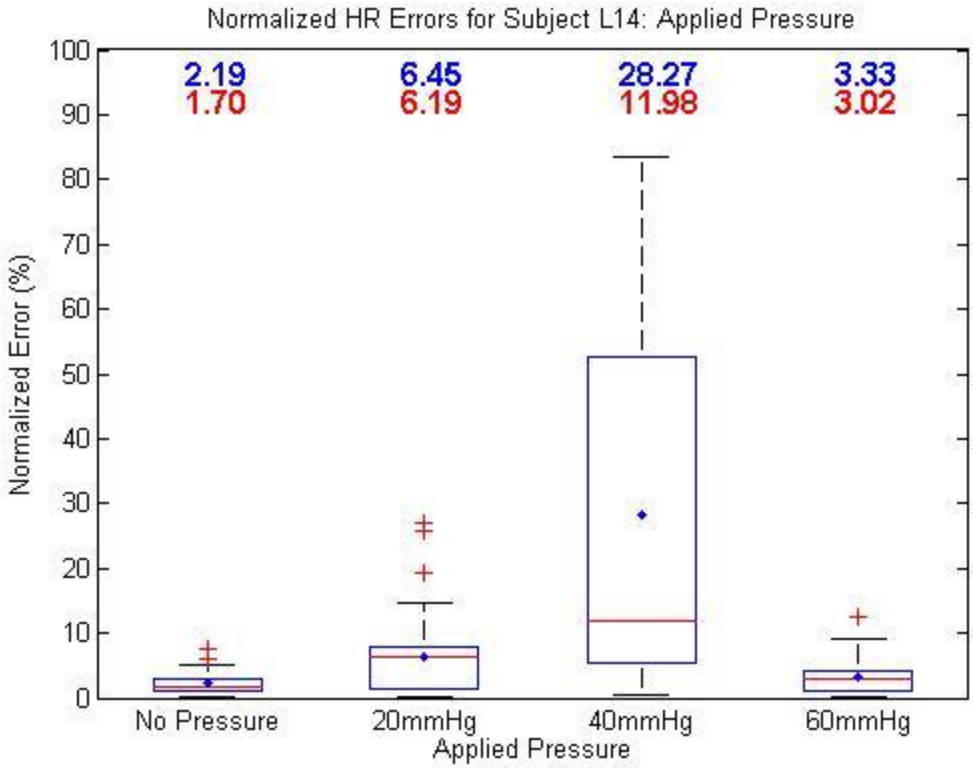
Normalized HR Errors for Subject L14: Applied Pressure
2.19
1.70
6.45
6.19
28.27
11.98
3.33
3.02
Normalized Error (%)
No Pressure
20mmHg
40mmHg
60mmHg
Applied Pressure

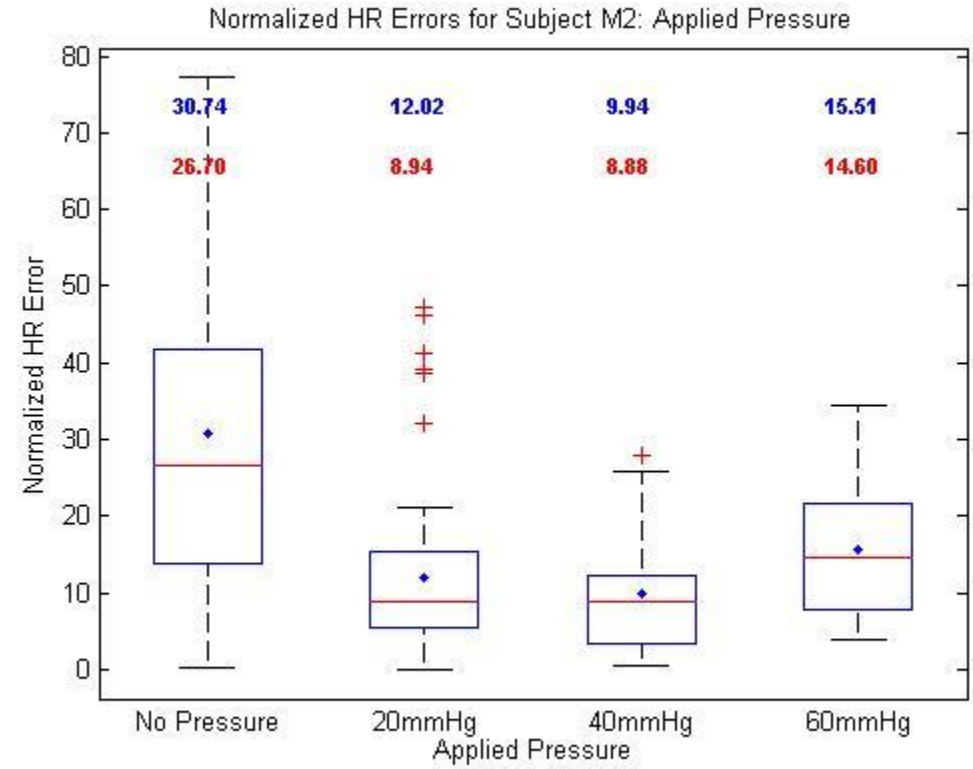
Normalized HR Errors for Subject M2: Applied Pressure
30.74
26.70
12.02
8.94
9.94
8.88
15.51
14.60
Normalized HR Error
No Pressure
20mmHg
40mmHg
60mmHg
Applied Pressure

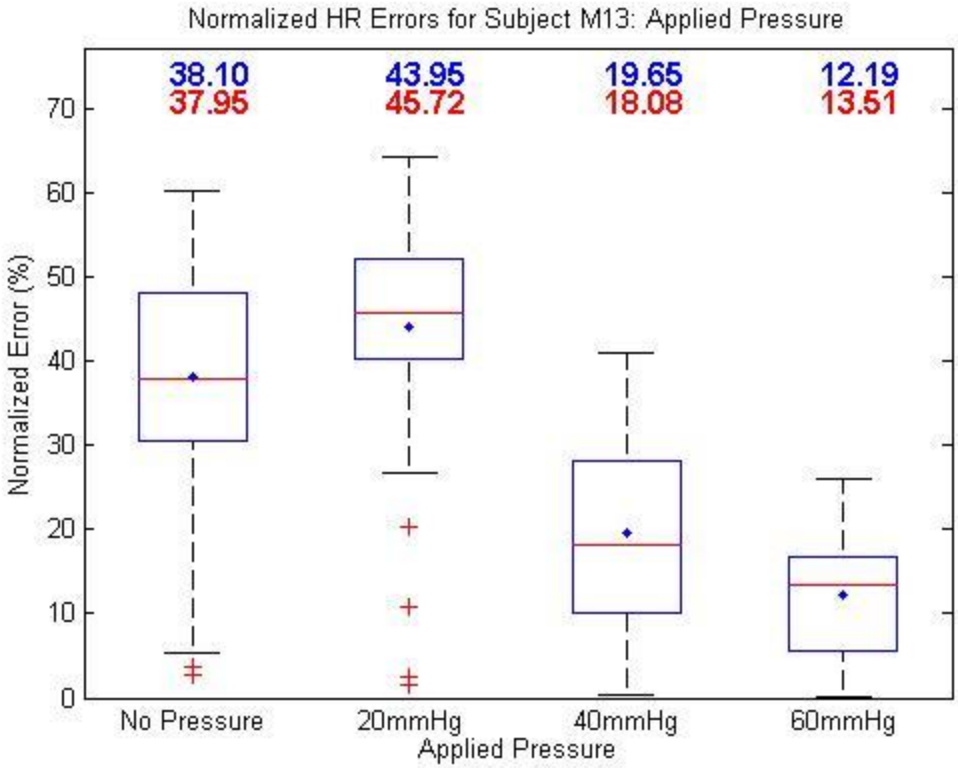
Normalized HR Errors for Subject M13: Applied Pressure
38.10
37.95
43.95
45.72
19.65
18.08
12.19
13.51
Normalized Error (%)
0
10
20
30
40
50
60
70
No Pressure
20mmHg
40mmHg
60mmHg
Applied Pressure

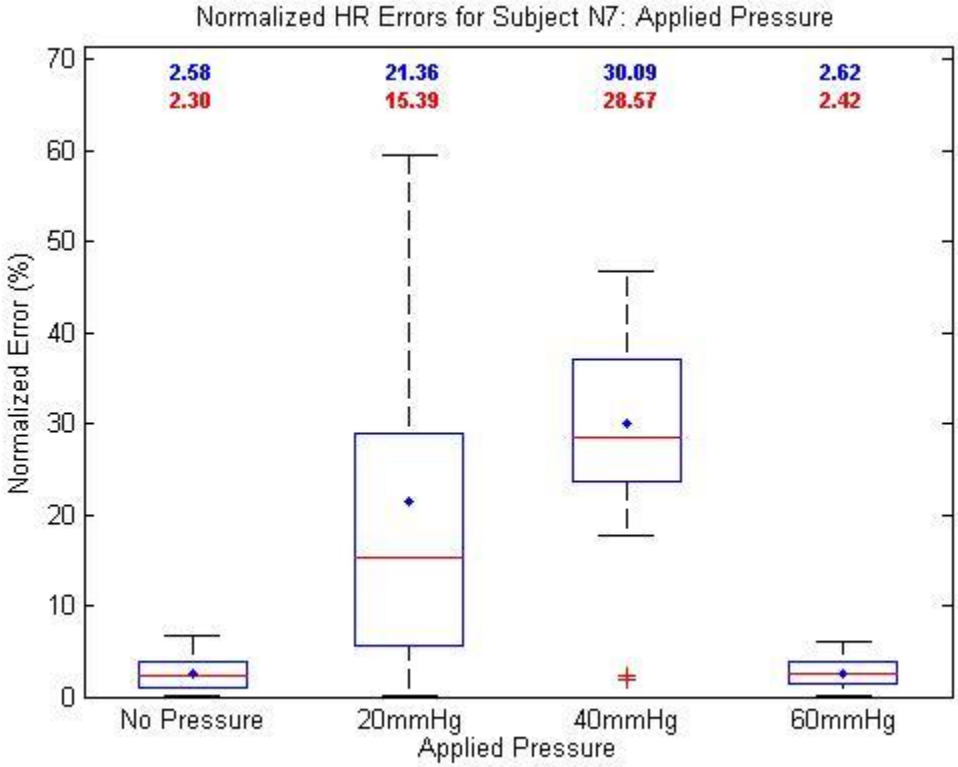
Normalized HR Errors for Subject N7: Applied Pressure
2.58
2.30
21.36
15.39
30.09
28.57
2.62
2.42
Normalized Error (%)
0
10
20
30
40
50
60
70
No Pressure
20mmHg
40mmHg
60mmHg
Applied Pressure

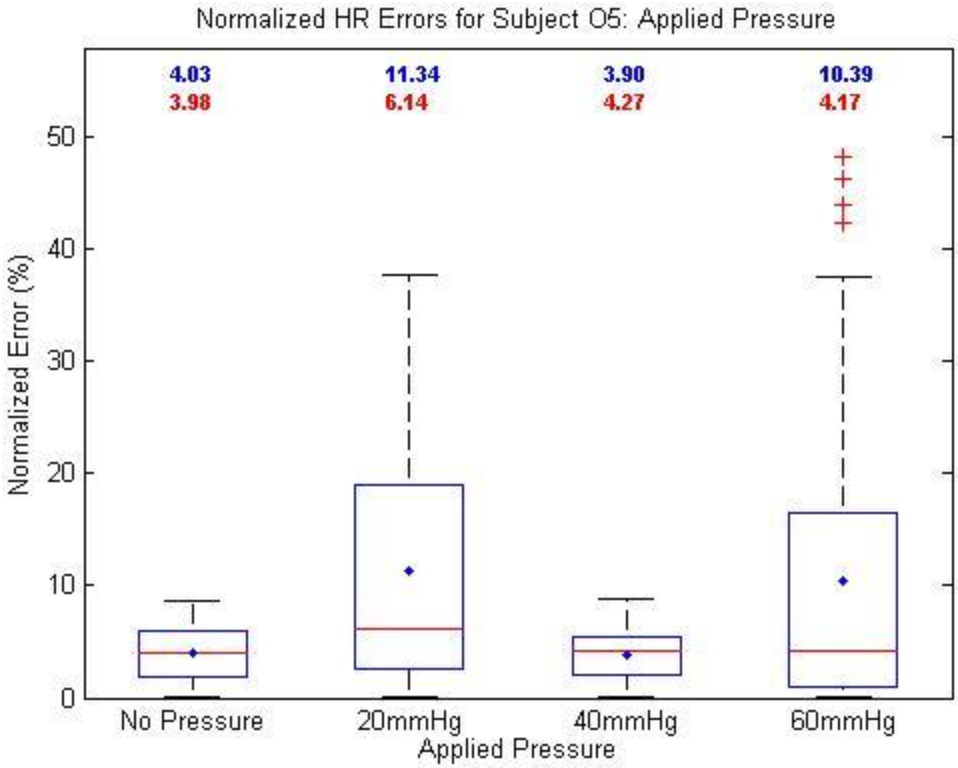
Normalized HR Errors for Subject O5: Applied Pressure
4.03
3.98
11.34
6.14
3.90
4.27
10.39
4.17
Normalized Error (%)
0
10
20
30
40
50
No Pressure
20mmHg
40mmHg
60mmHg
Applied Pressure

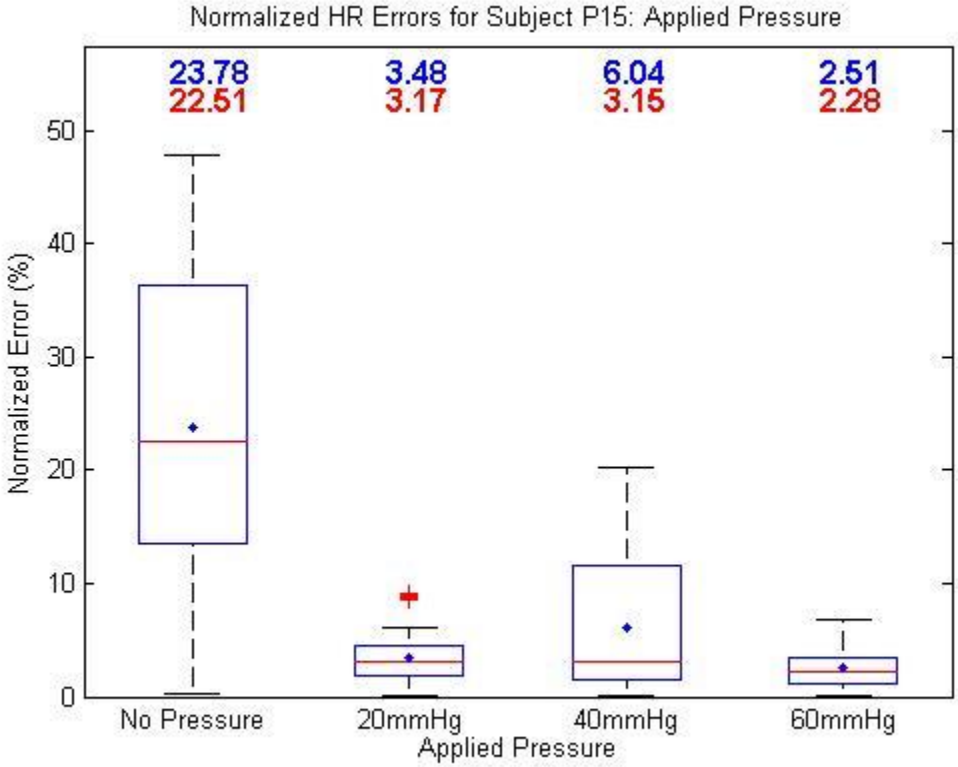
Normalized HR Errors for Subject P15: Applied Pressure
23.78
22.51
3.48
3.17
6.04
3.15
2.51
2.28
Normalized Error (%)
0
10
20
30
40
50
No Pressure
20mmHg
40mmHg
60mmHg
Applied Pressure

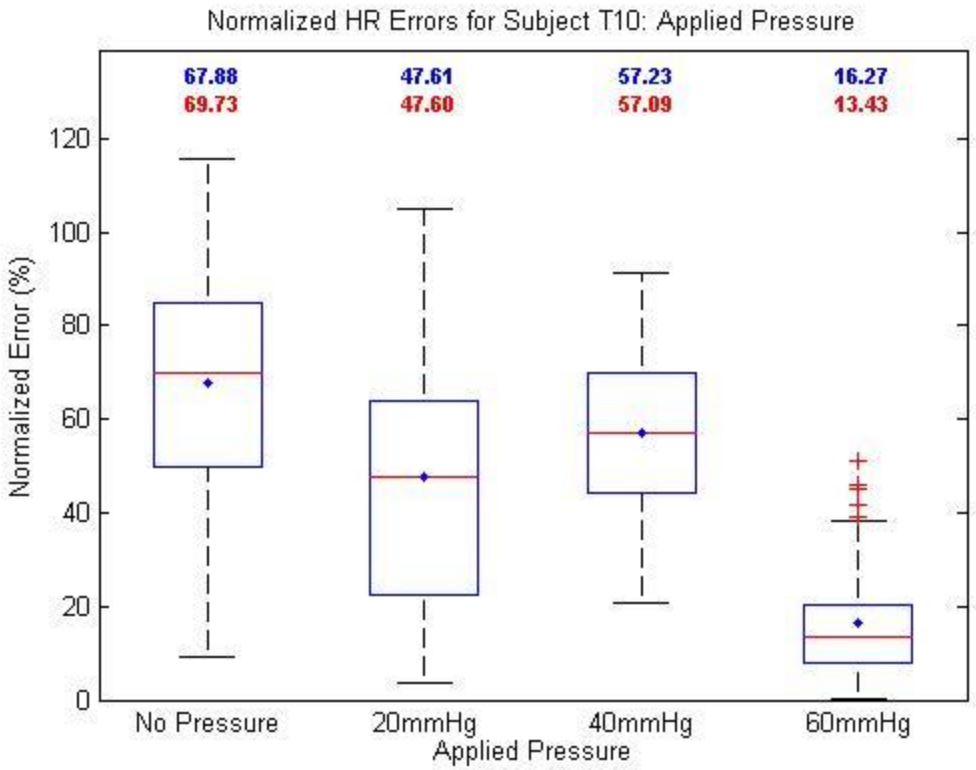
Normalized HR Errors for Subject T10: Applied Pressure
67.88
69.73
47.61
47.60
57.23
57.09
16.27
13.43
120
100
80
60
40
20
0
Normalized Error (%)
No Pressure
20mmHg
40mmHg
60mmHg
Applied Pressure

Appendix H: Applied Pressure SpO_2 Box Plots

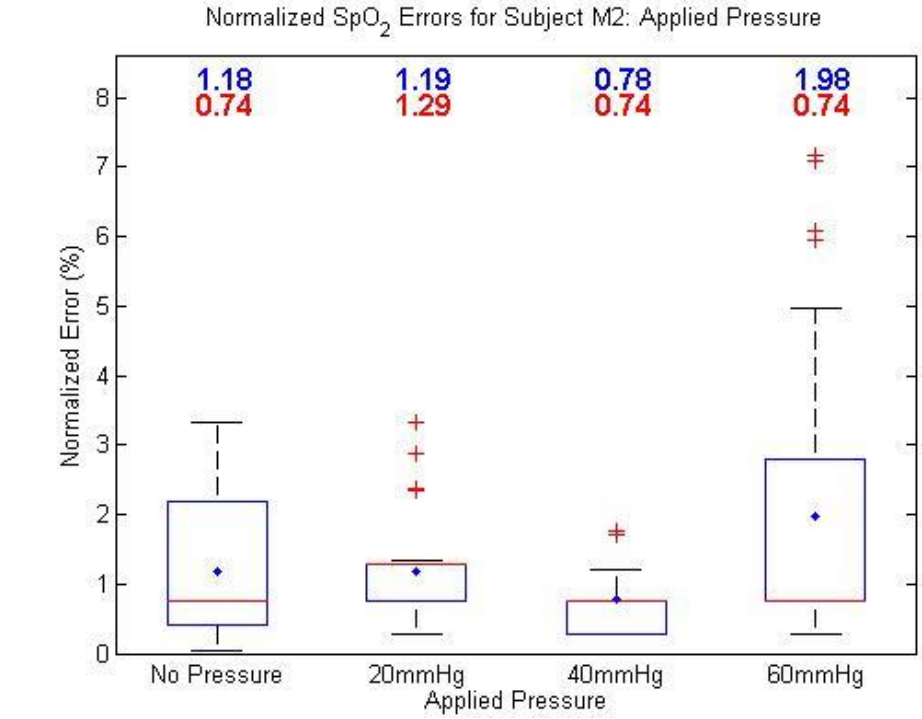

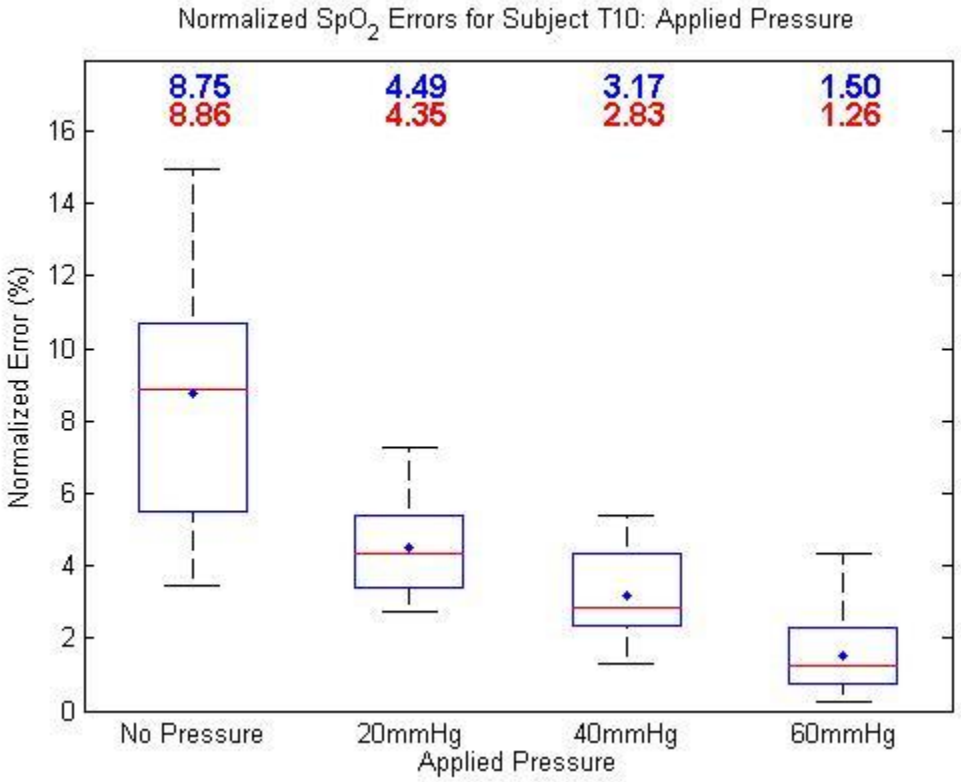

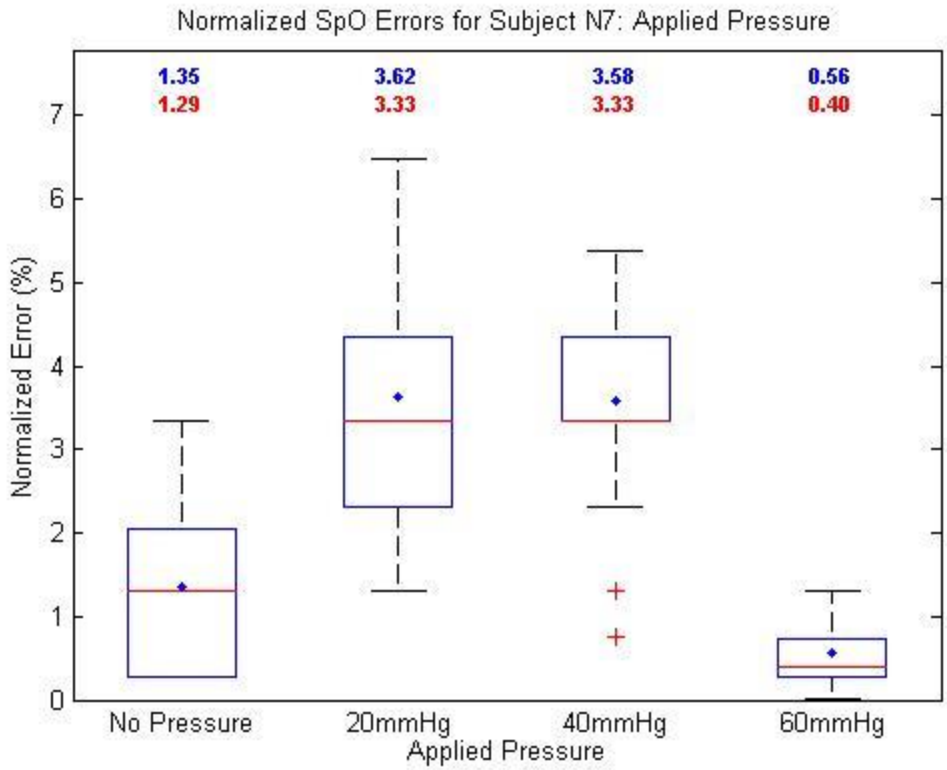
Normalized SpO Errors for Subject N7: Applied Pressure
1.35
1.29
3.62
3.33
3.58
3.33
0.56
0.40
Normalized Error (%)
0
1
2
3
4
5
6
7
No Pressure
20mmHg
40mmHg
60mmHg
Applied Pressure

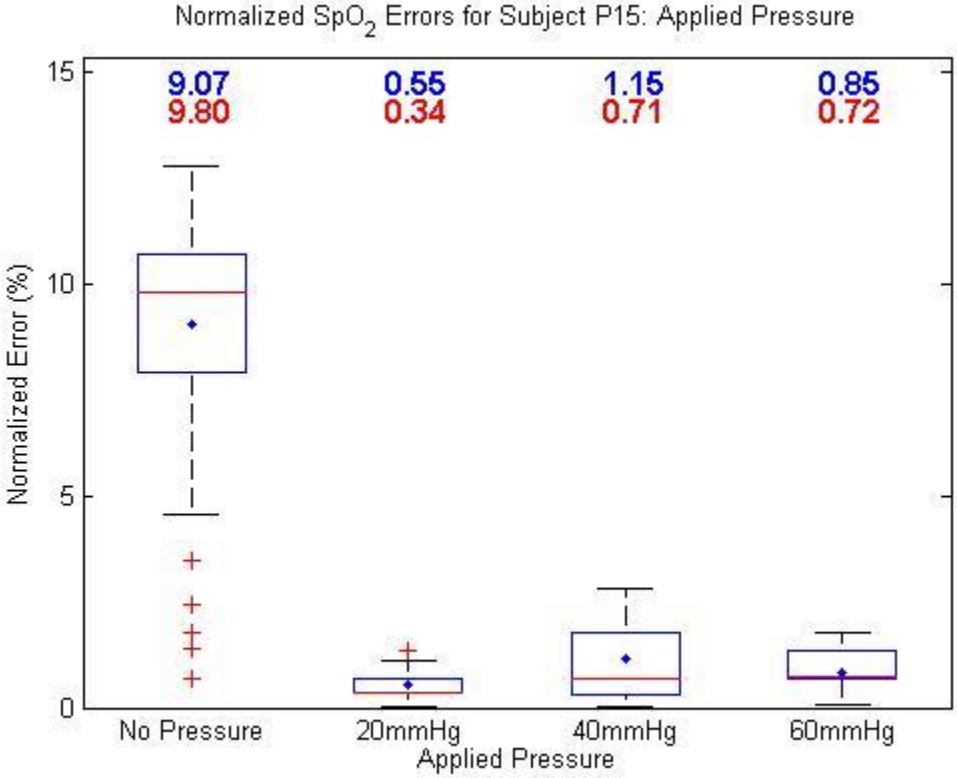
Normalized SpO2 Errors for Subject P15: Applied Pressure
9.07
9.80
0.55
0.34
1.15
0.71
0.85
0.72
Normalized Error (%)
0
5
10
15
No Pressure
20mmHg
40mmHg
60mmHg
Applied Pressure

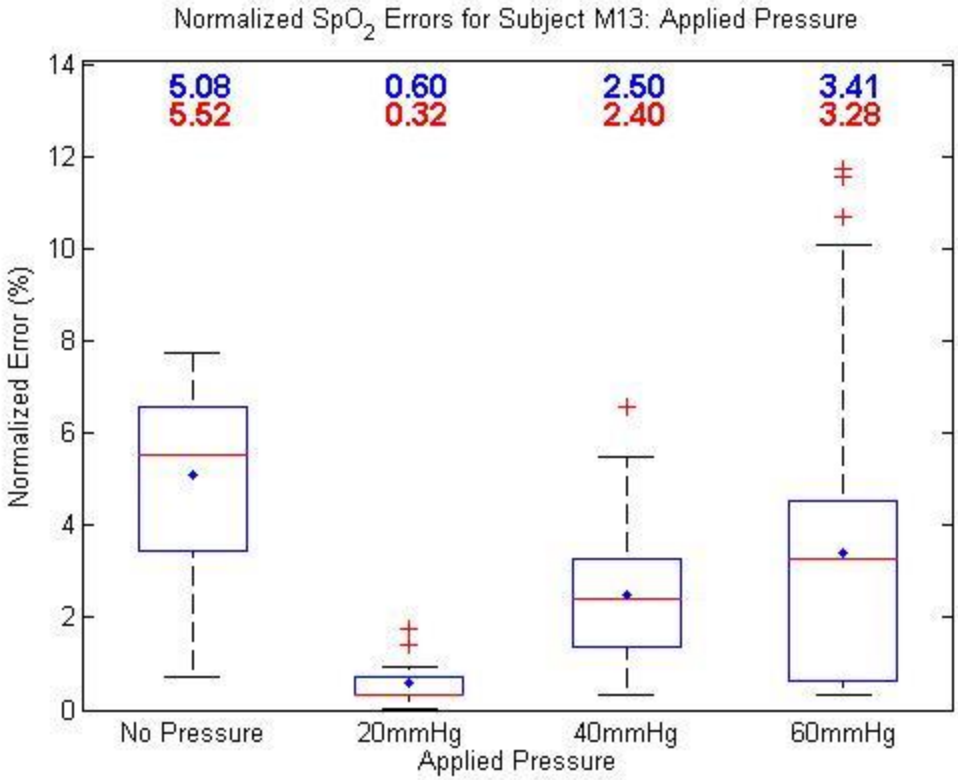
Normalized SpO2 Errors for Subject M13: Applied Pressure
5.08
5.52
0.60
0.32
2.50
2.40
3.41
3.28
Normalized Error (%)
No Pressure
20mmHg
40mmHg
60mmHg
Applied Pressure

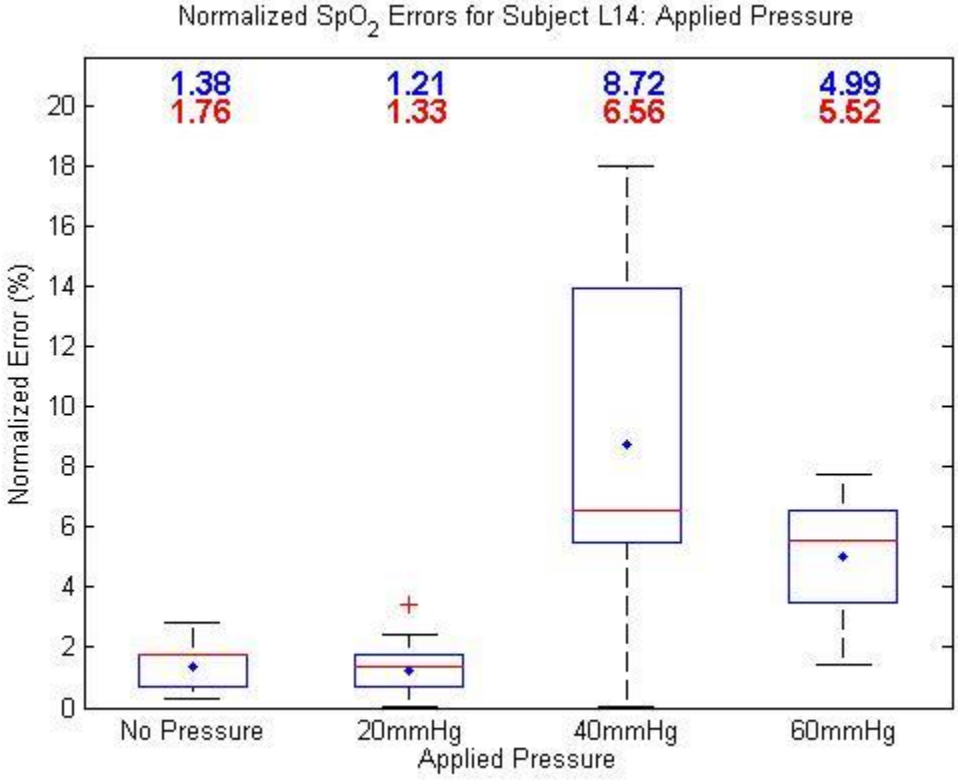
Normalized SpO2 Errors for Subject L14: Applied Pressure
1.38
1.76
1.21
1.33
8.72
6.56
4.99
5.52
Normalized Error (%)
No Pressure
20mmHg
40mmHg
60mmHg
Applied Pressure

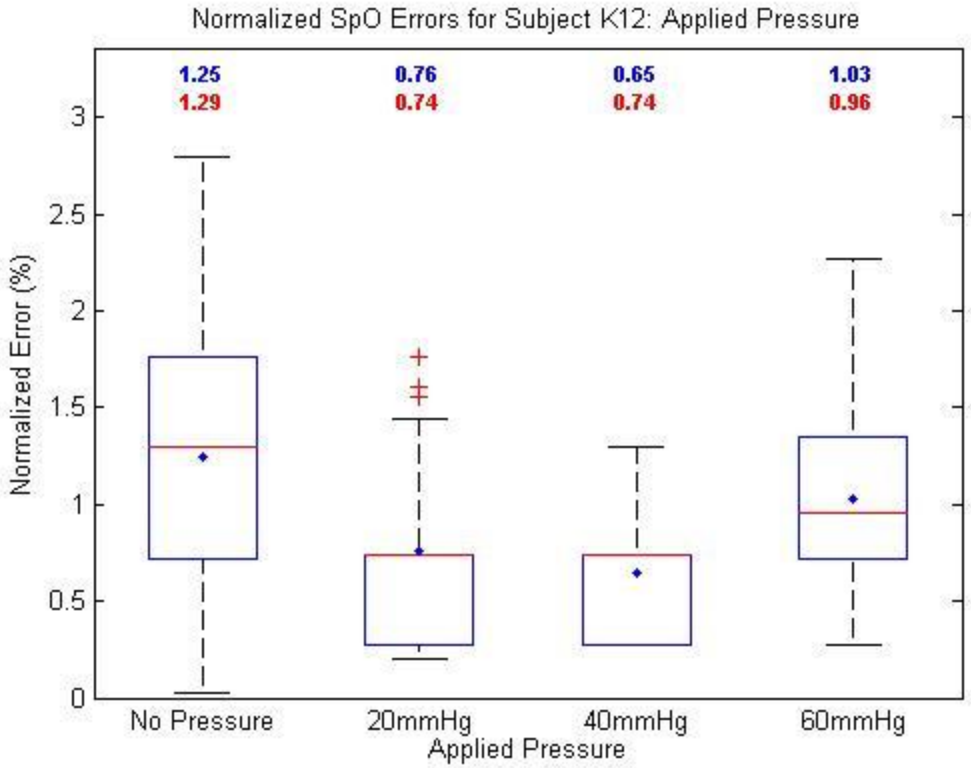
Normalized SpO Errors for Subject K12: Applied Pressure
1.25
1.29
0.76
0.74
0.65
0.74
1.03
0.96
Normalized Error (%)
0
0.5
1
1.5
2
2.5
3
No Pressure
20mmHg
40mmHg
60mmHg
Applied Pressure

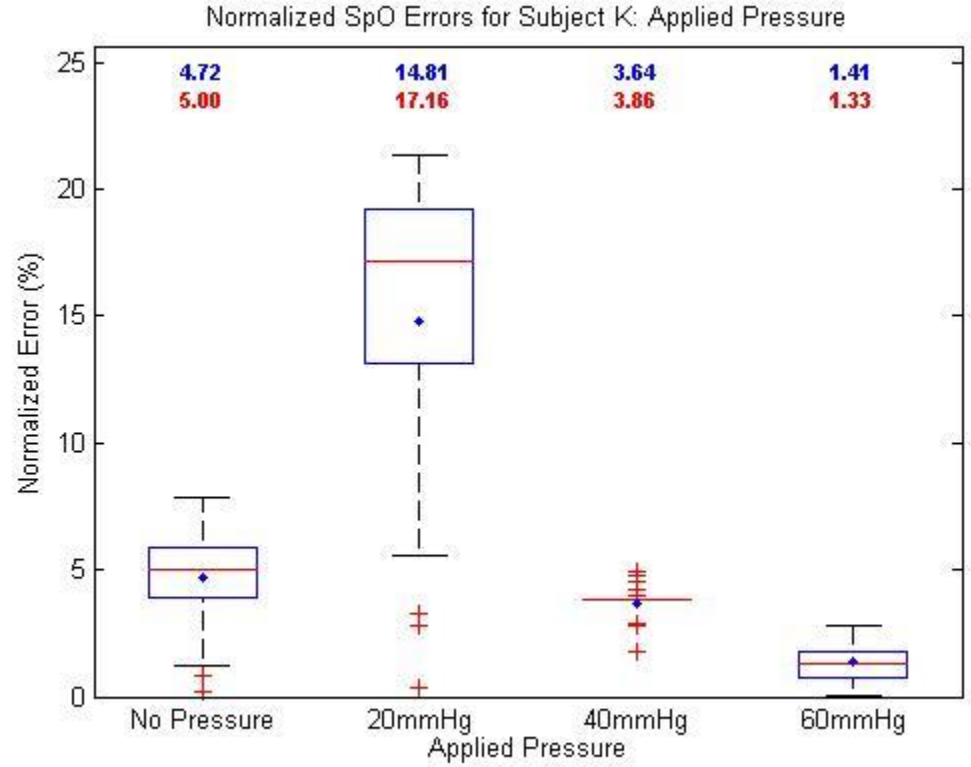
Normalized SpO Errors for Subject K: Applied Pressure
4.72
5.00
14.81
17.16
3.64
3.86
1.41
1.33
Normalized Error (%)
0
5
10
15
20
25
No Pressure
20mmHg
40mmHg
60mmHg
Applied Pressure

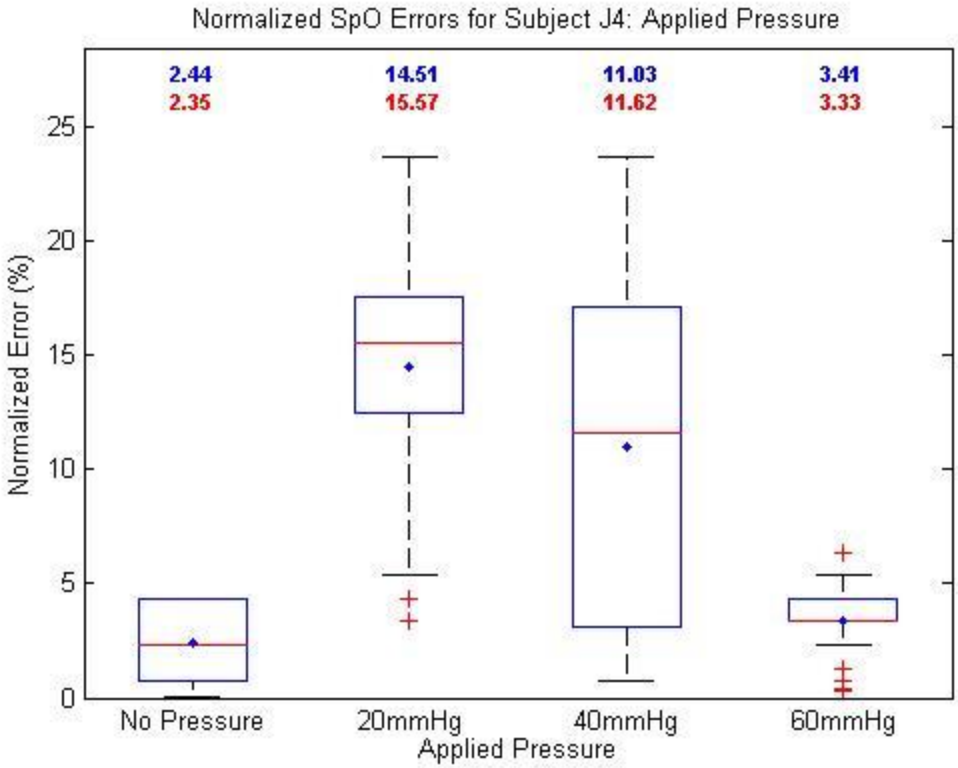
Normalized SpO Errors for Subject J4: Applied Pressure
2.44
2.35
14.51
15.57
11.03
11.62
3.41
3.33
Normalized Error (%)
0
5
10
15
20
25
No Pressure
20mmHg
40mmHg
60mmHg
Applied Pressure

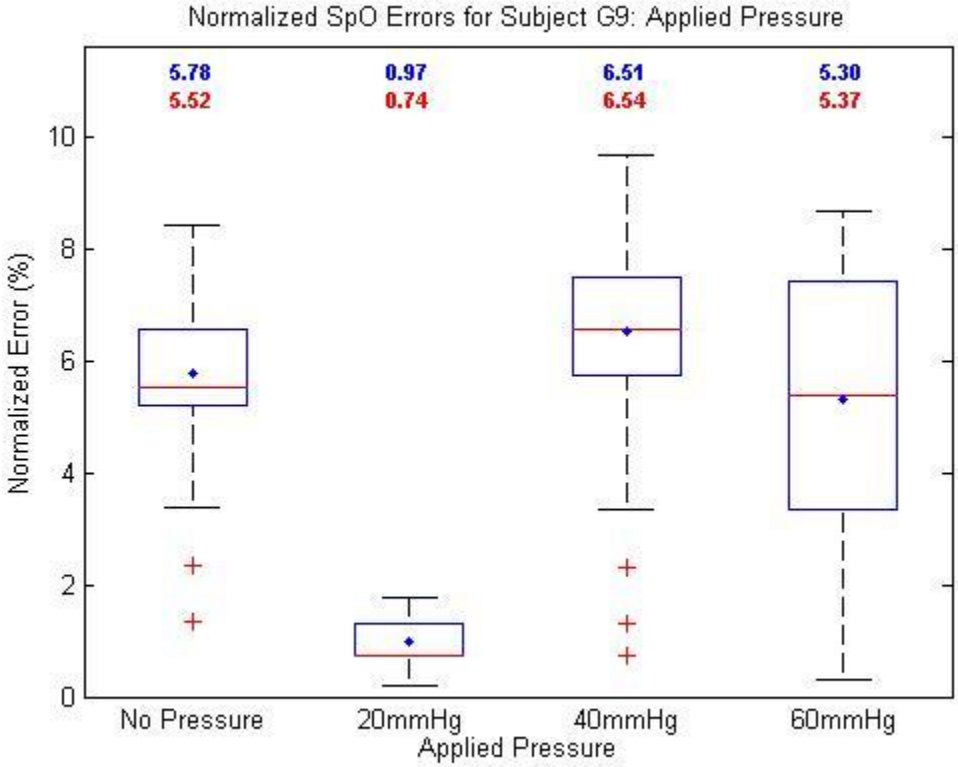
Normalized SpO Errors for Subject G9: Applied Pressure
5.78
5.52
0.97
0.74
6.51
6.54
5.30
5.37
Normalized Error (%)
0
2
4
6
8
10
No Pressure
20mmHg
40mmHg
60mmHg
Applied Pressure

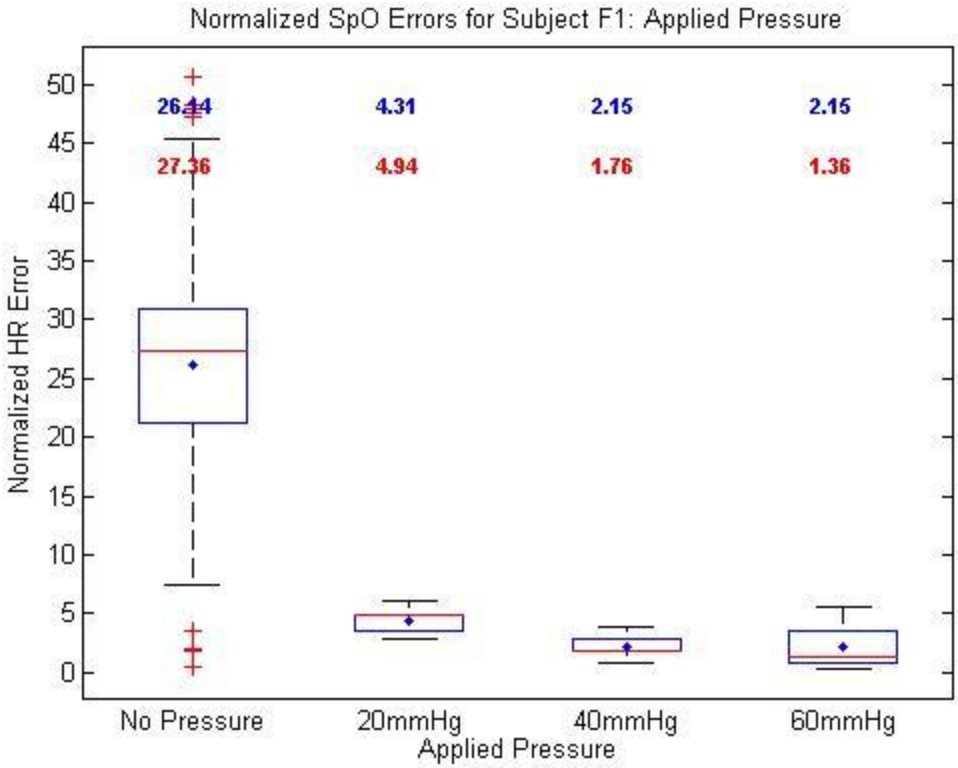
Normalized SpO Errors for Subject F1: Applied Pressure
26.44
4.31
2.15
2.15
27.36
4.94
1.76
1.36
Normalized HR Error
0
5
10
15
20
25
30
35
40
45
50
No Pressure
20mmHg
40mmHg
60mmHg
Applied Pressure

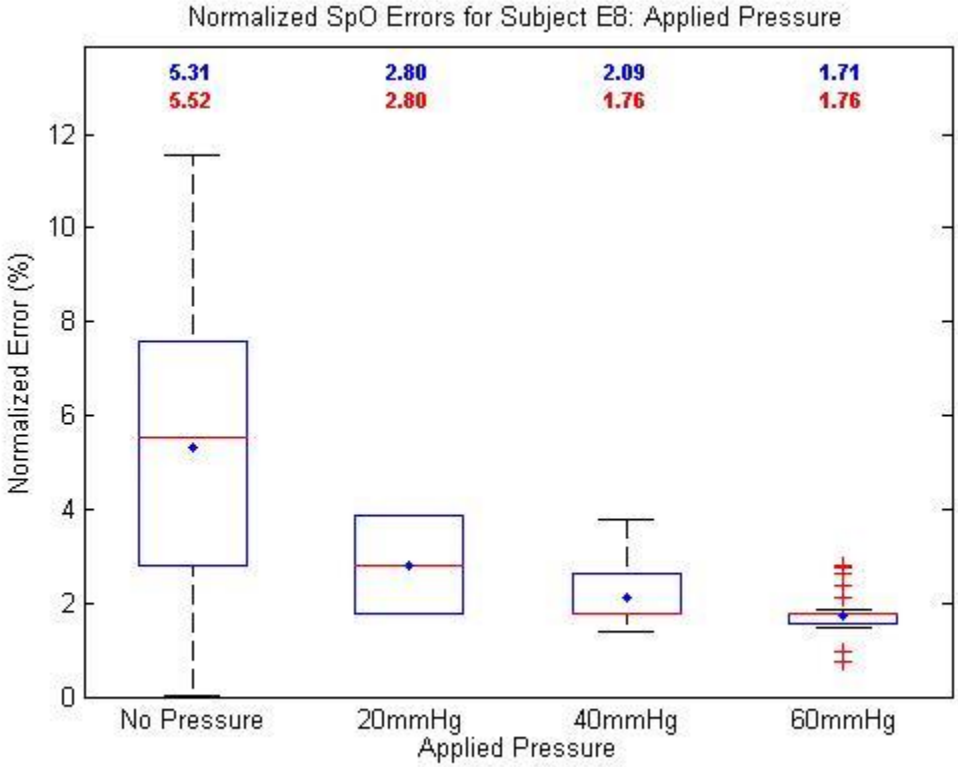
Normalized SpO Errors for Subject E8: Applied Pressure
5.31
2.80
2.09
1.71
5.52
2.80
1.76
1.76
Normalized Error (%)
0
2
4
6
8
10
12
No Pressure
20mmHg
40mmHg
60mmHg
Applied Pressure

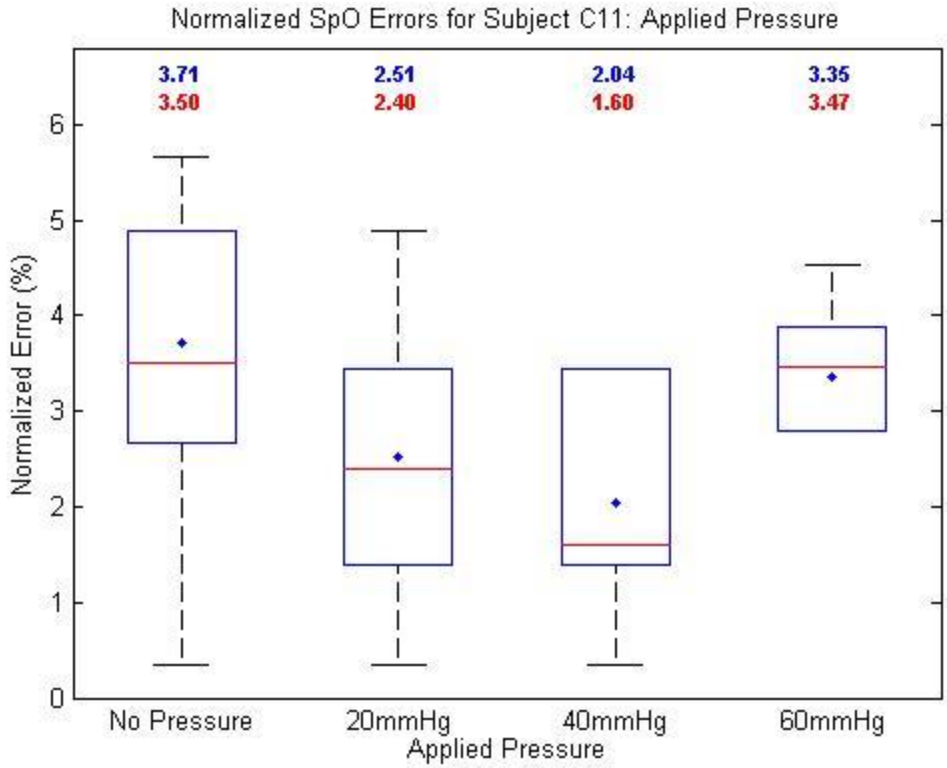
Normalized SpO Errors for Subject C11: Applied Pressure
3.71
3.50
2.51
2.40
2.04
1.60
3.35
3.47
Normalized Error (%)
0
1
2
3
4
5
6
No Pressure
20mmHg
40mmHg
60mmHg
Applied Pressure

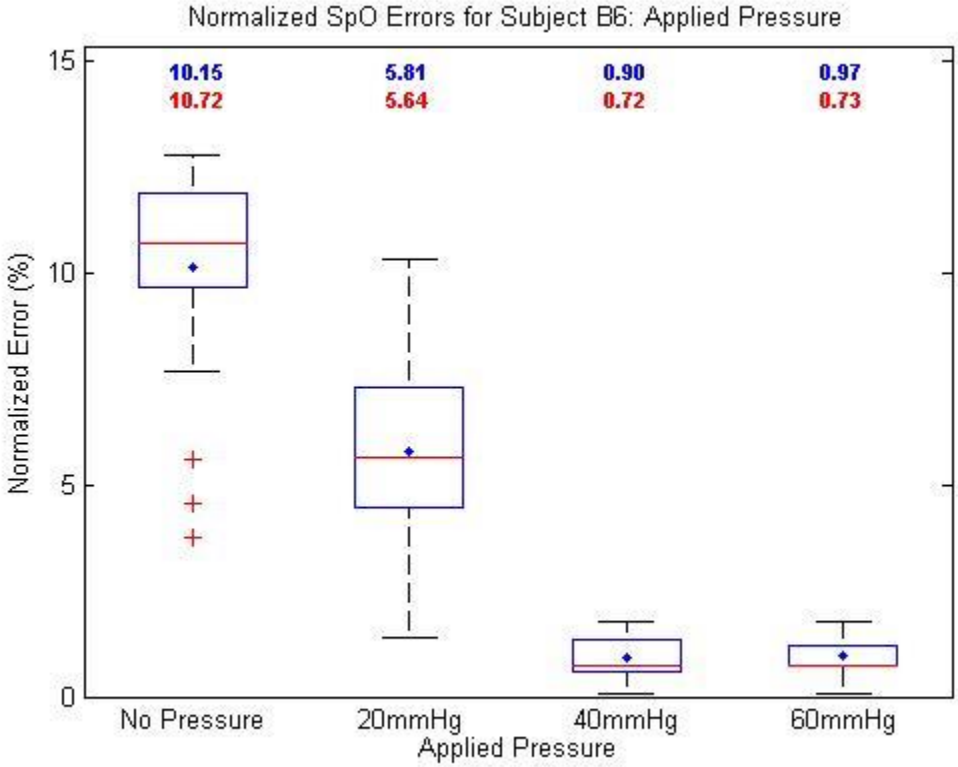
Normalized SpO Errors for Subject B6: Applied Pressure
10.15
10.72
5.81
5.64
0.90
0.72
0.97
0.73
Normalized Error (%)
0
5
10
15
No Pressure
20mmHg
40mmHg
60mmHg
Applied Pressure

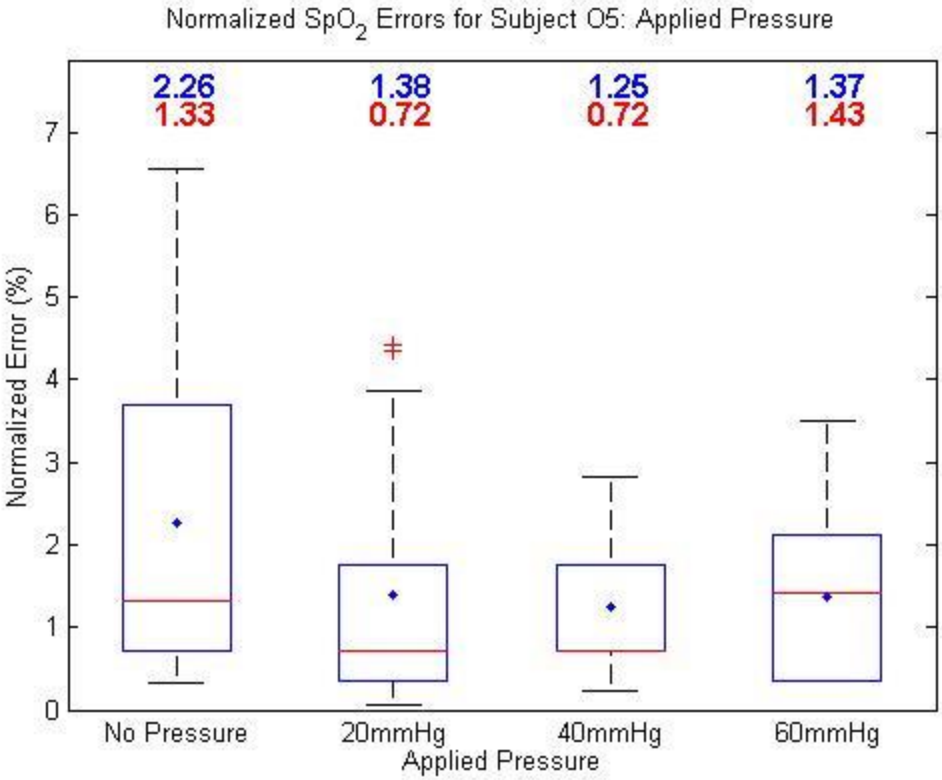
Normalized SpO2 Errors for Subject O5: Applied Pressure
2.26
1.33
1.38
0.72
1.25
0.72
1.37
1.43
Normalized Error (%)
0
1
2
3
4
5
6
7
No Pressure
20mmHg
40mmHg
60mmHg
Applied Pressure

Appendix I: Sensor Weight Frequency Spectra

Subject B6:

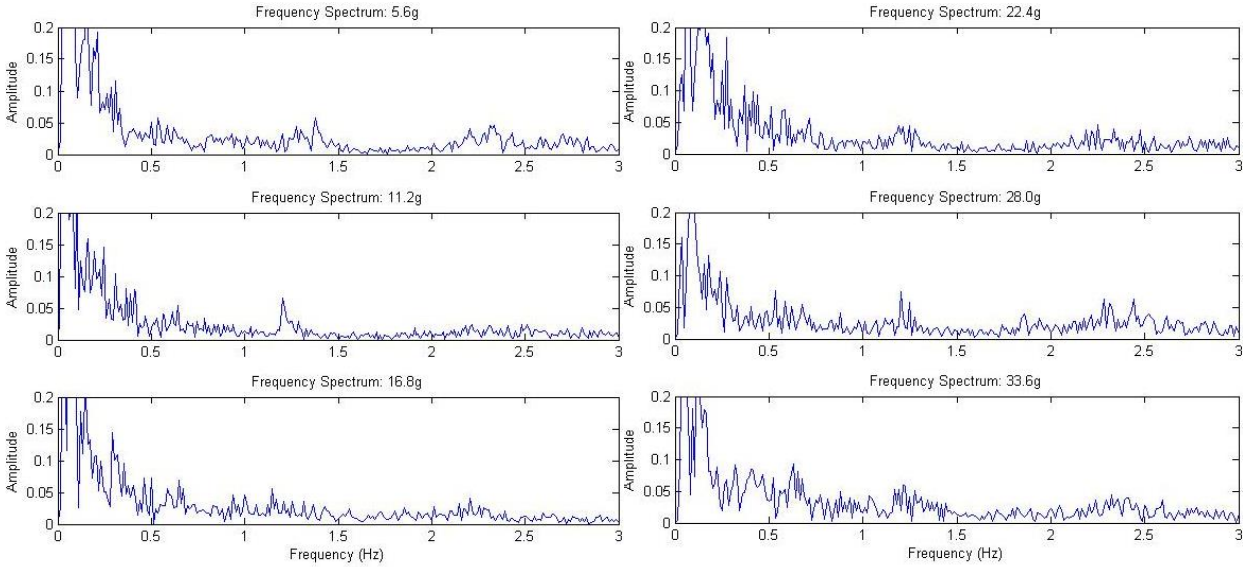

Subject C11:

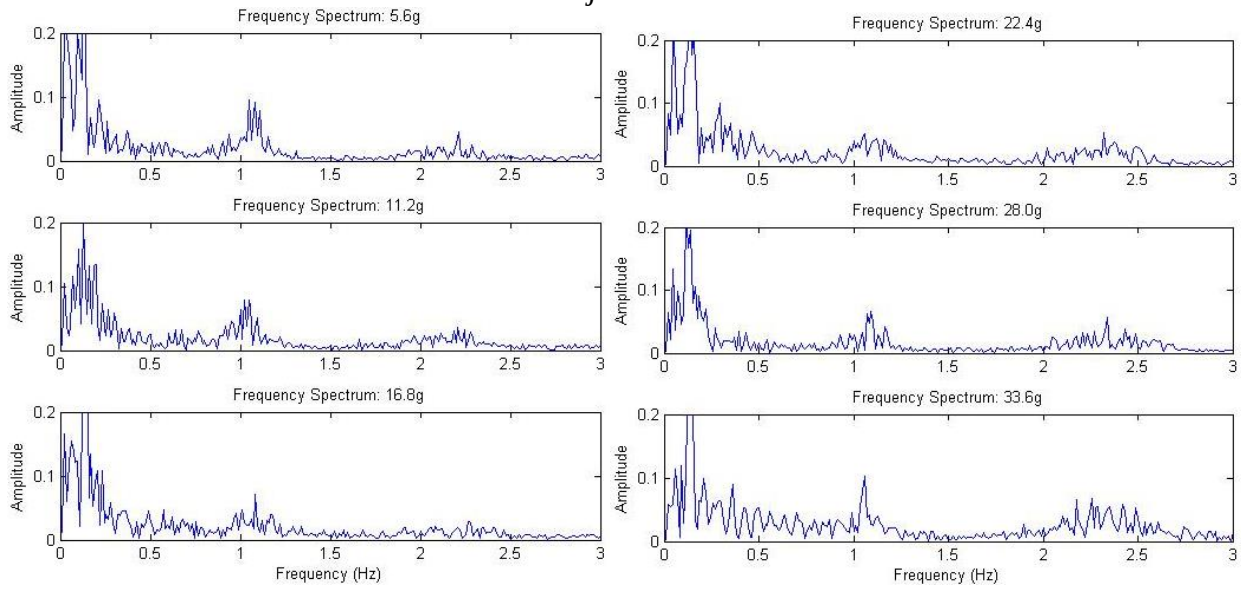

Subject E8:

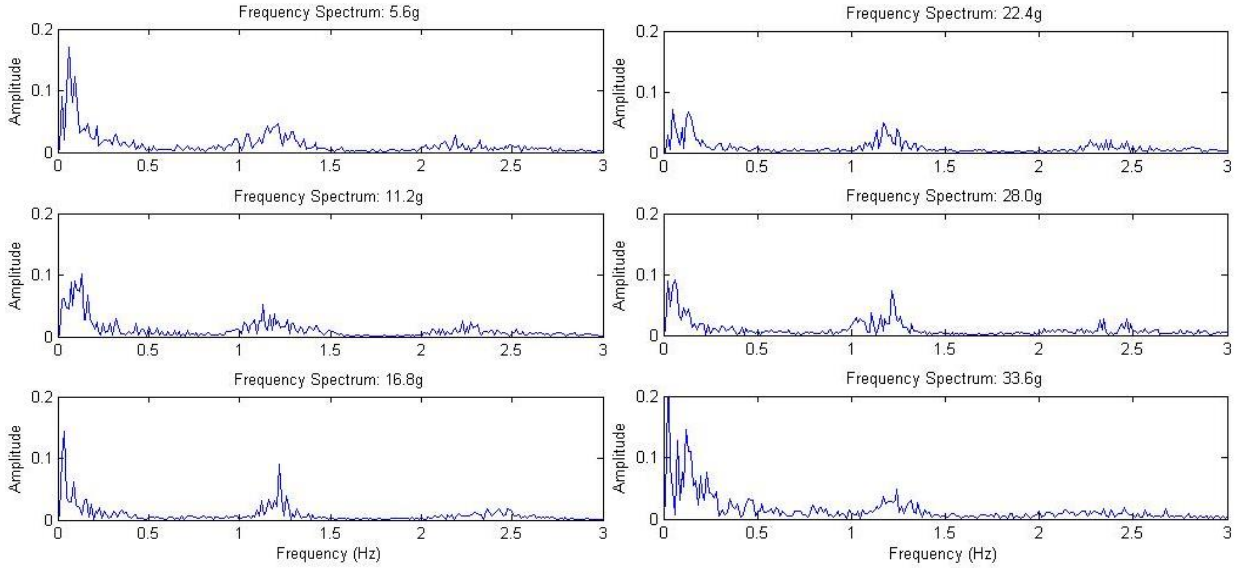

Subject F1:

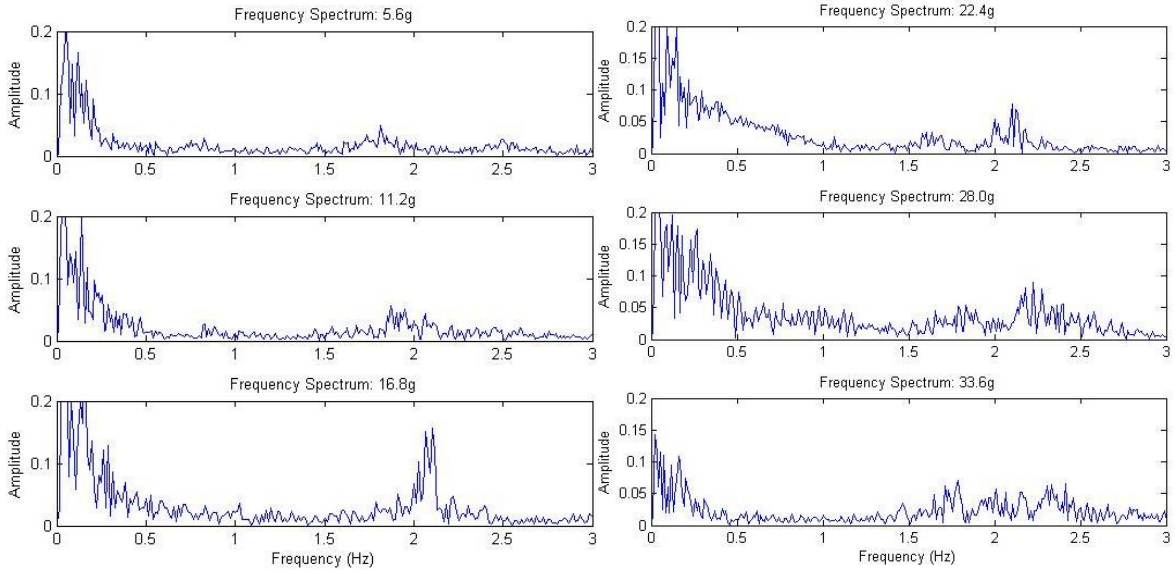

Subject J4:

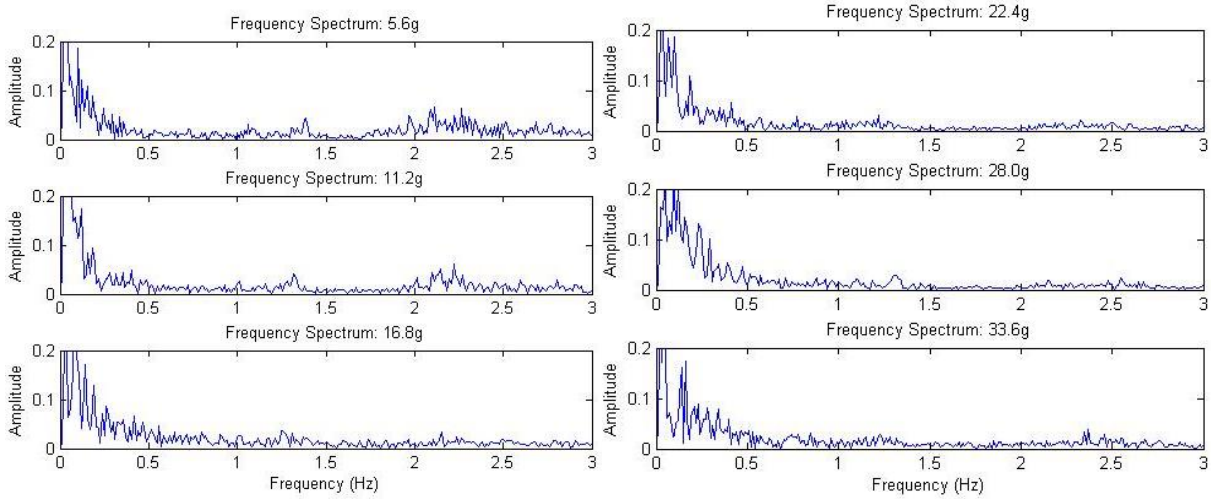

Subject K:

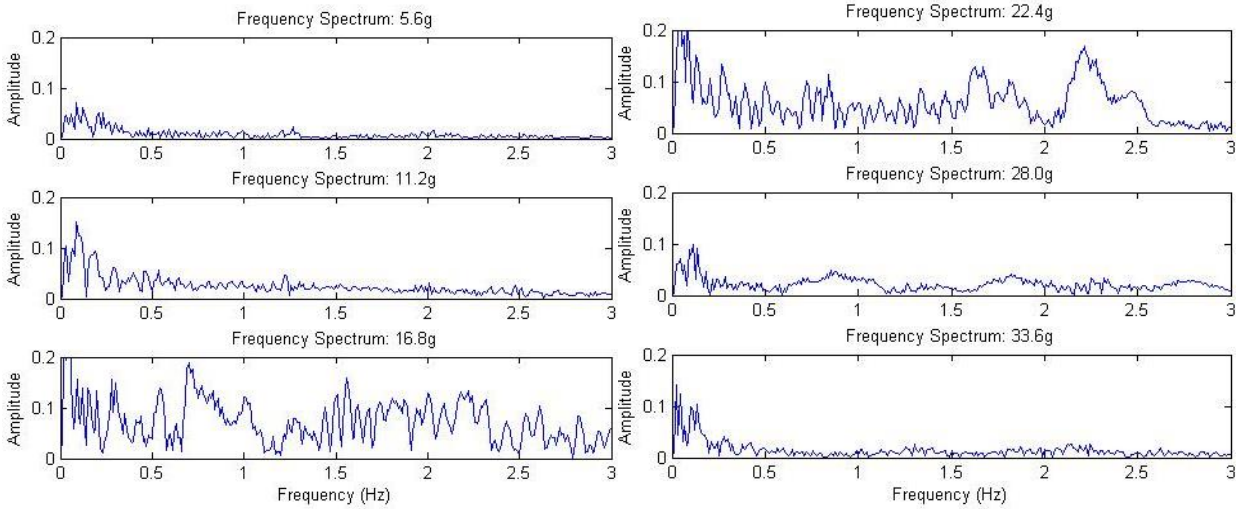

Subject K12:

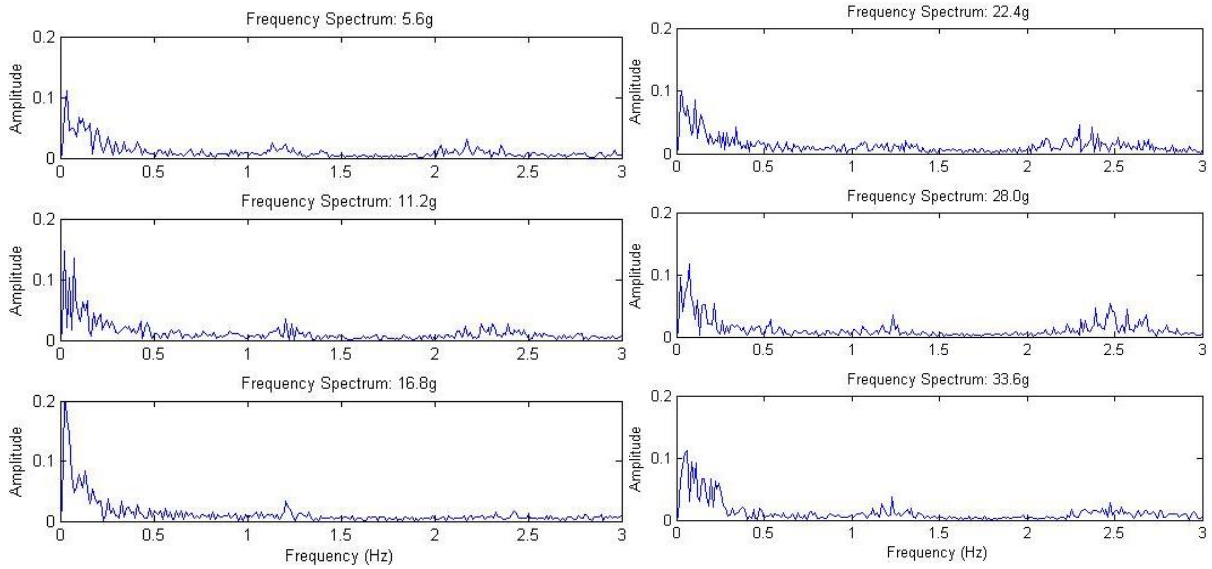

Subject L14:

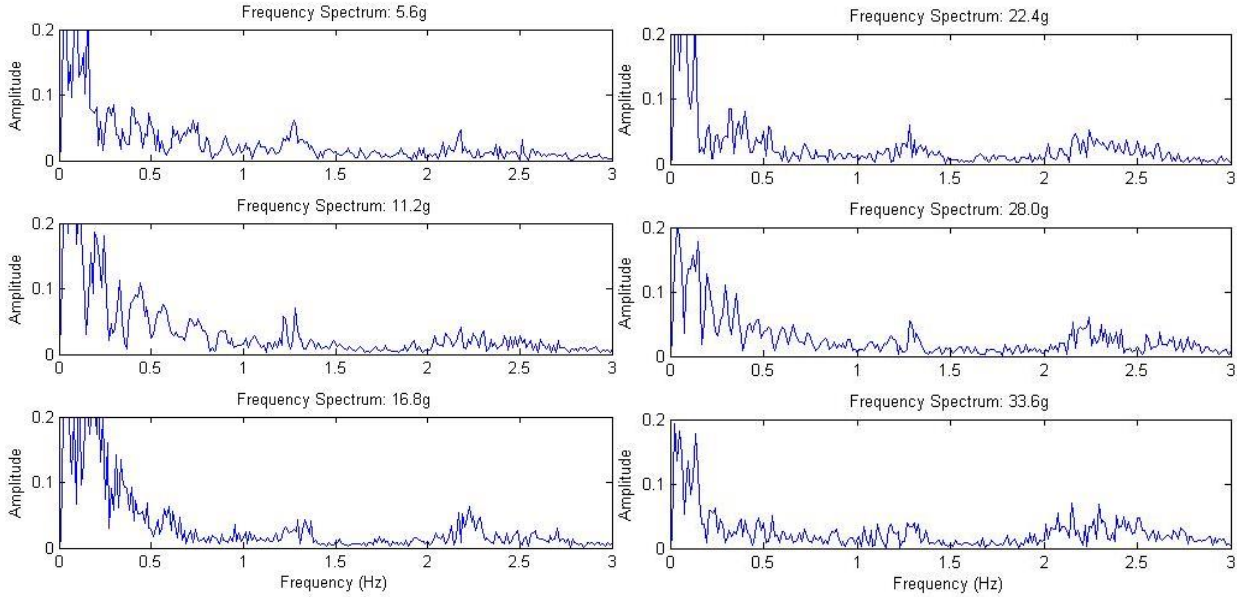

Subject M13:

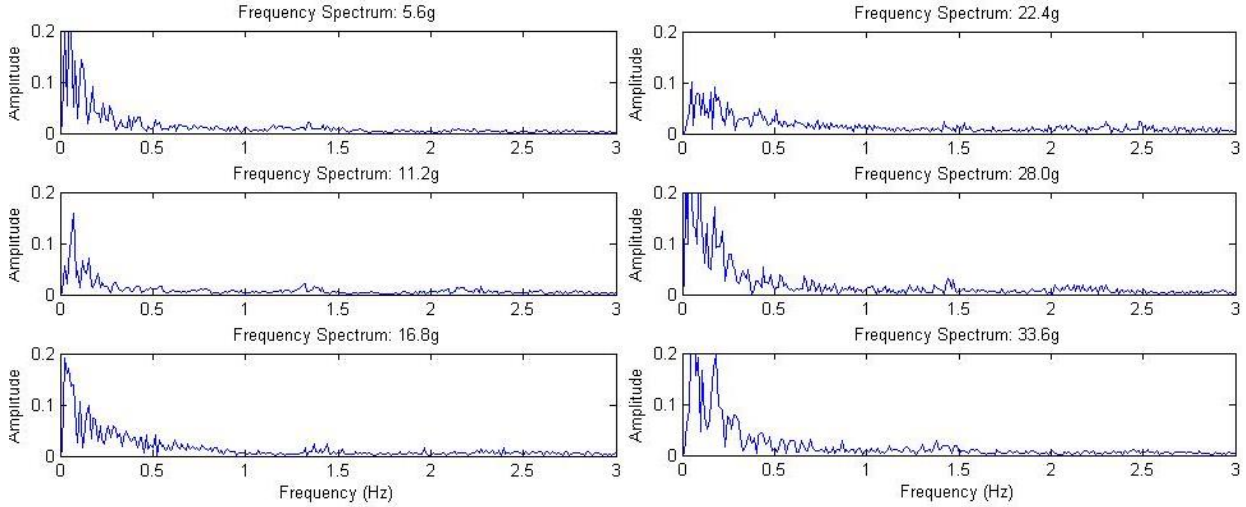

Subject N7:

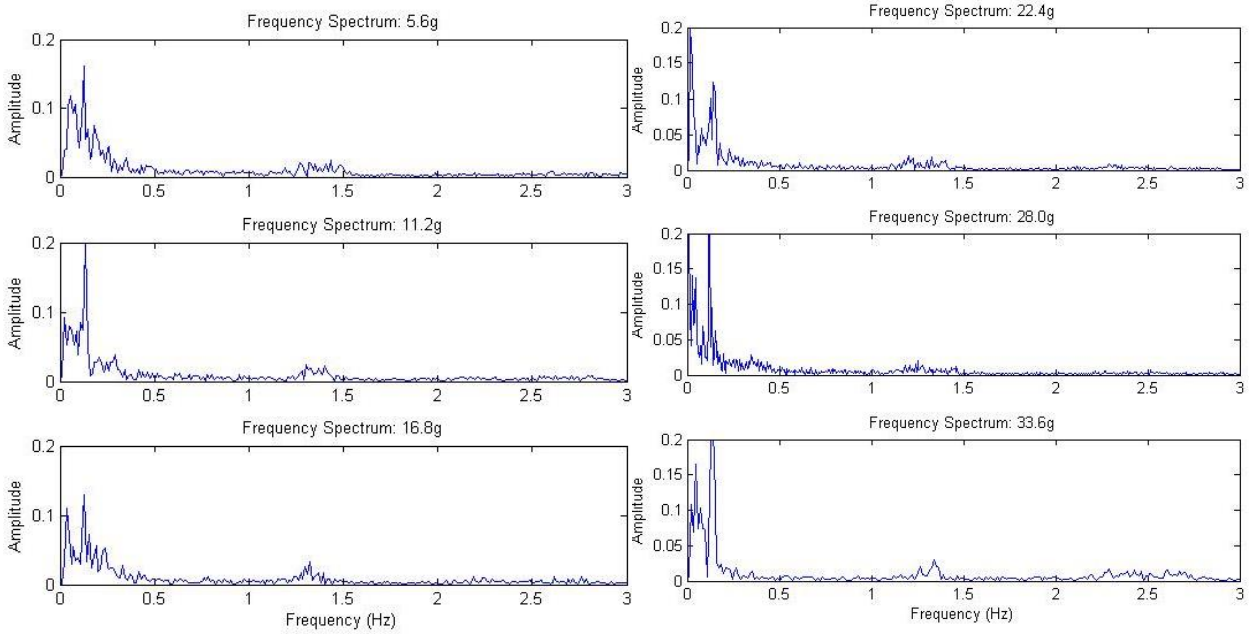

Subject O5:

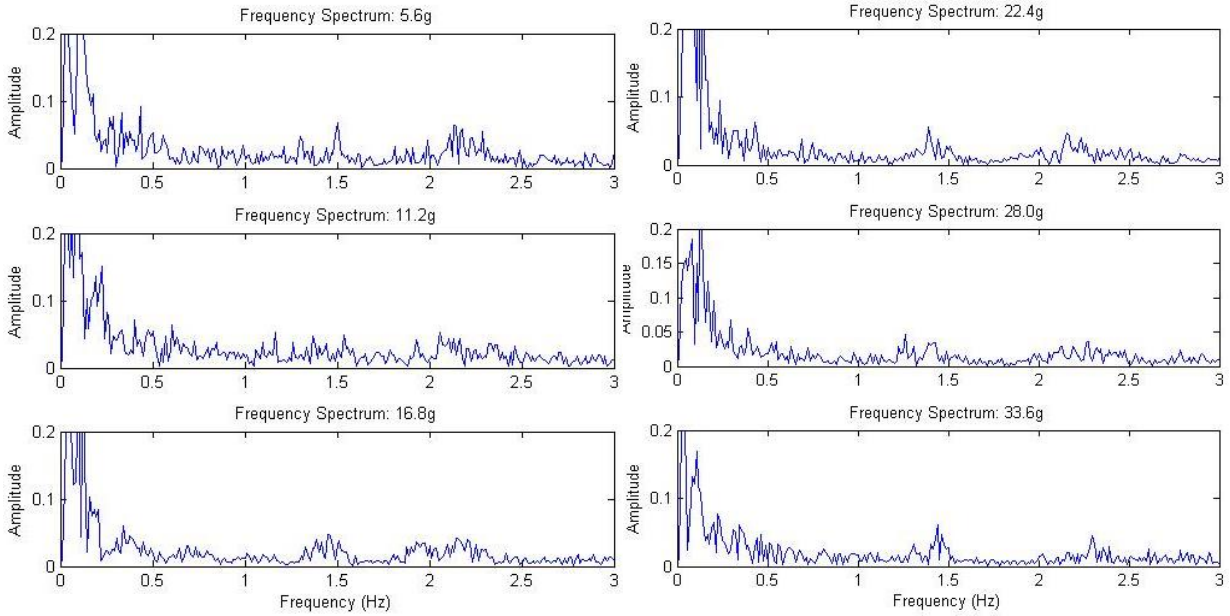

Subject P15:

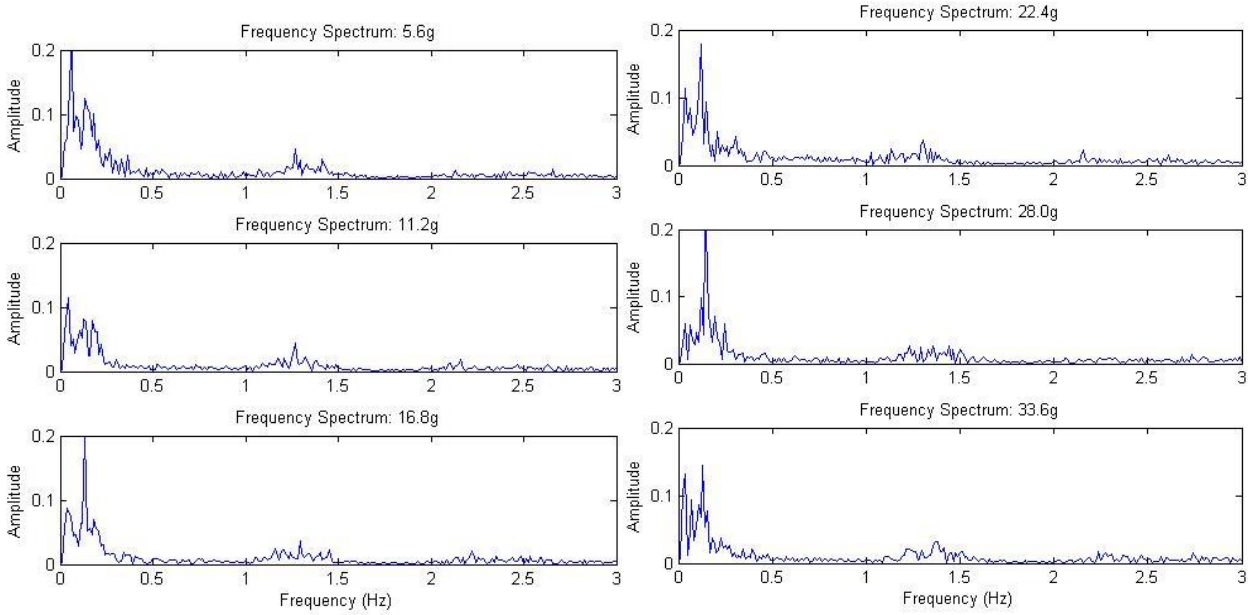

Subject T10:

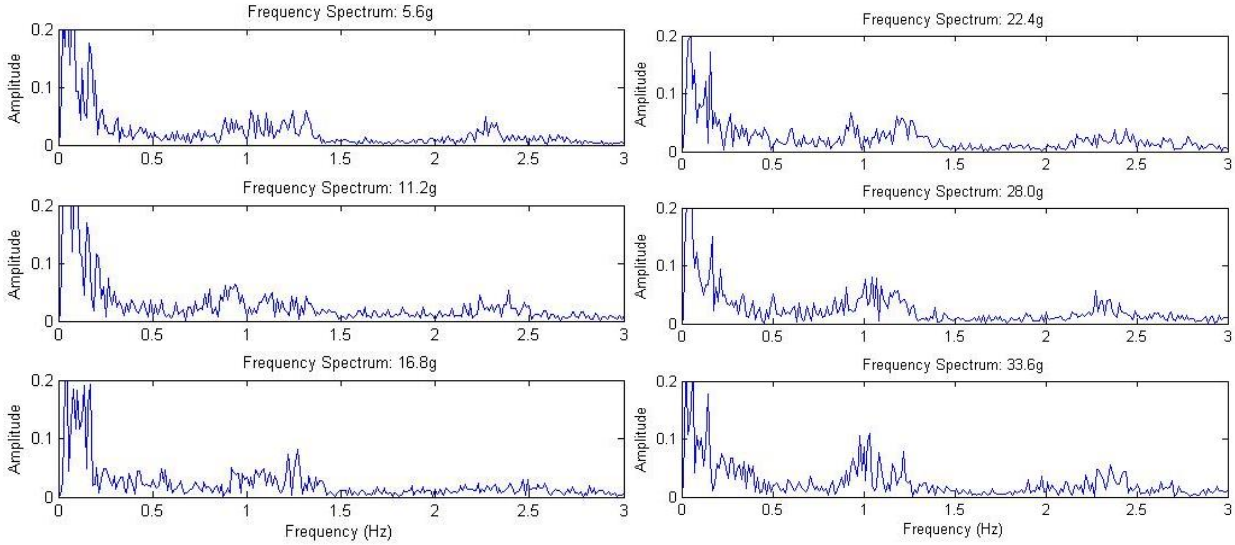
Frequency Spectrum: 5.6g
Frequency Spectrum: 22.4g
Frequency Spectrum: 11.2g
Frequency Spectrum: 28.0g
Frequency Spectrum: 16.8g
Frequency Spectrum: 33.6g
Amplitude
Frequency (Hz)
0
0.1
0.2
0.5
1
1.5
2
2.5
3

Appendix J: Applied Heat Frequency Spectra

Subject B6:

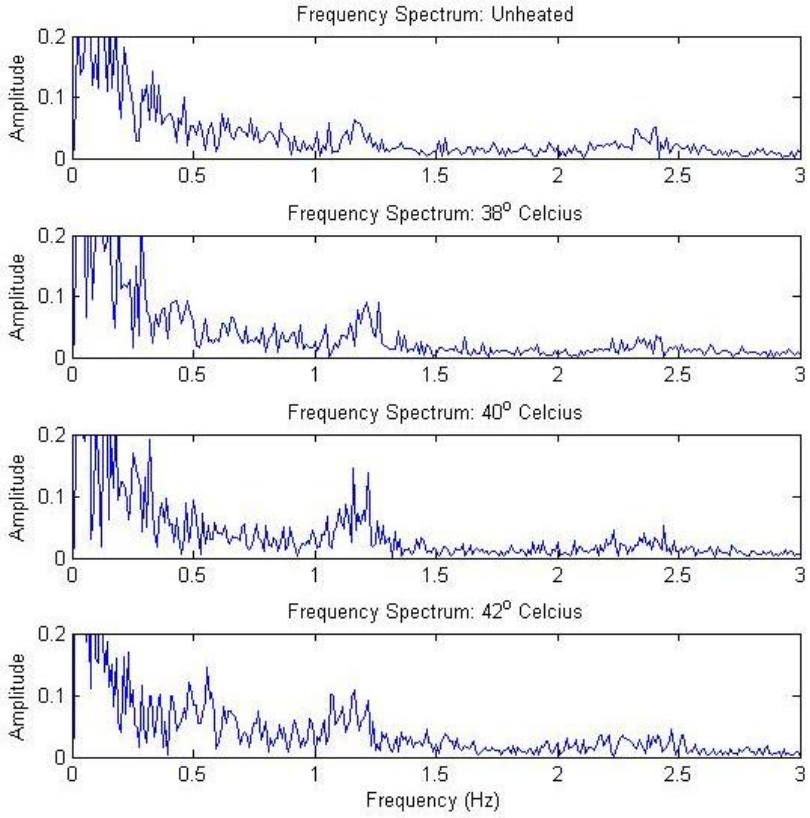

Subject C11:

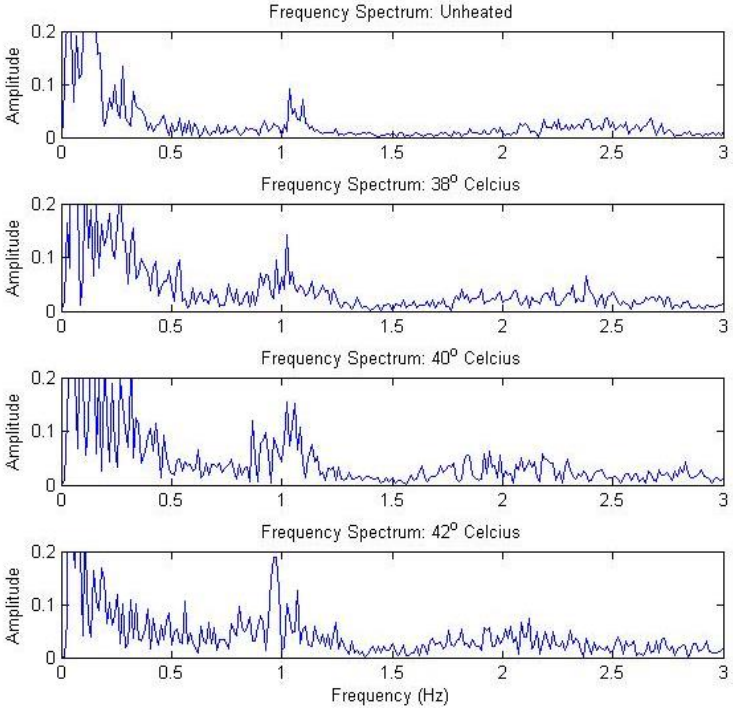

Subject E8:

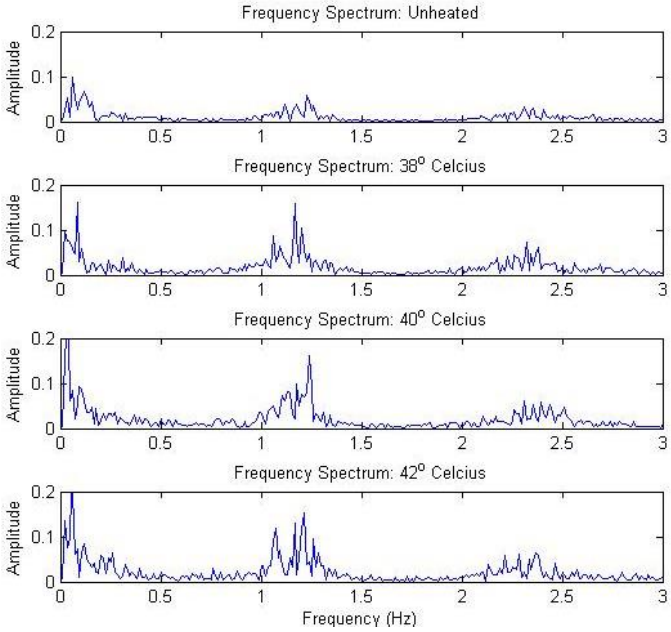

Subject F1:

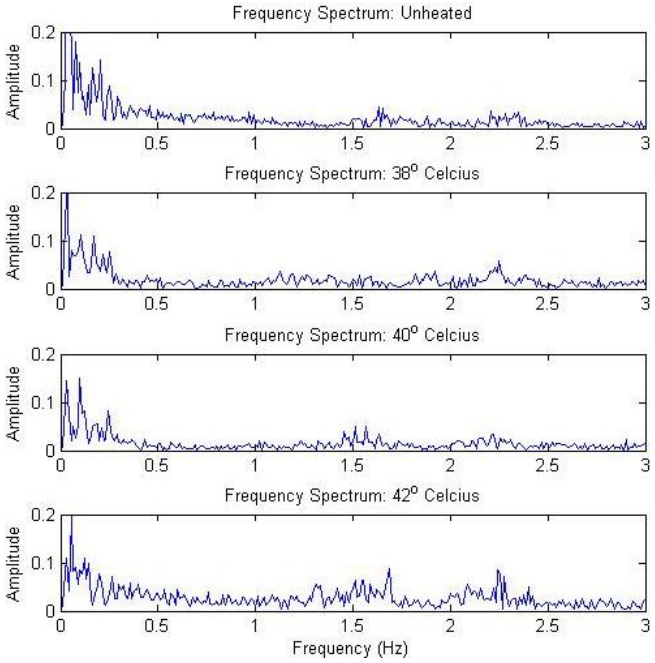

Subject G9:

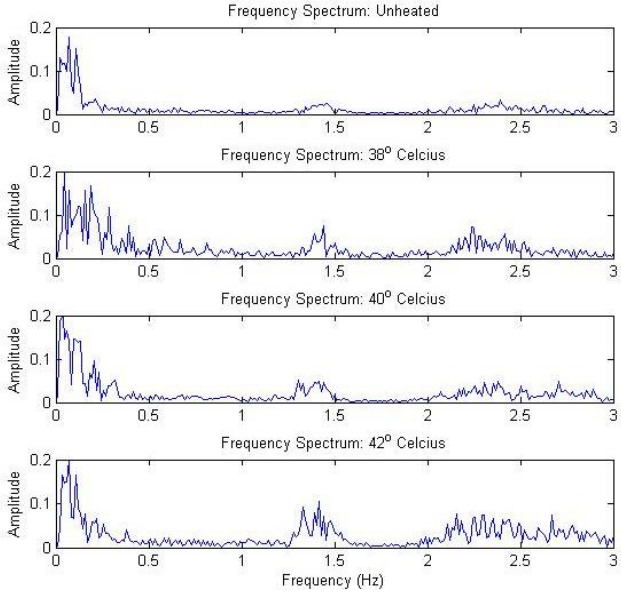

Subject J4

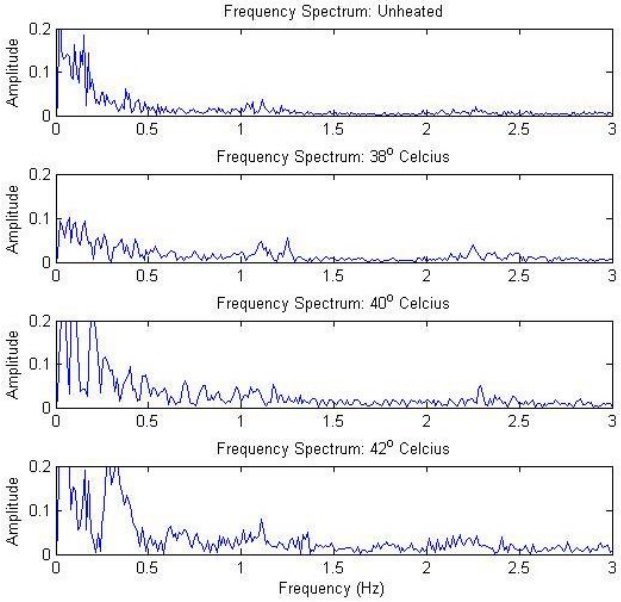

Subject K12:

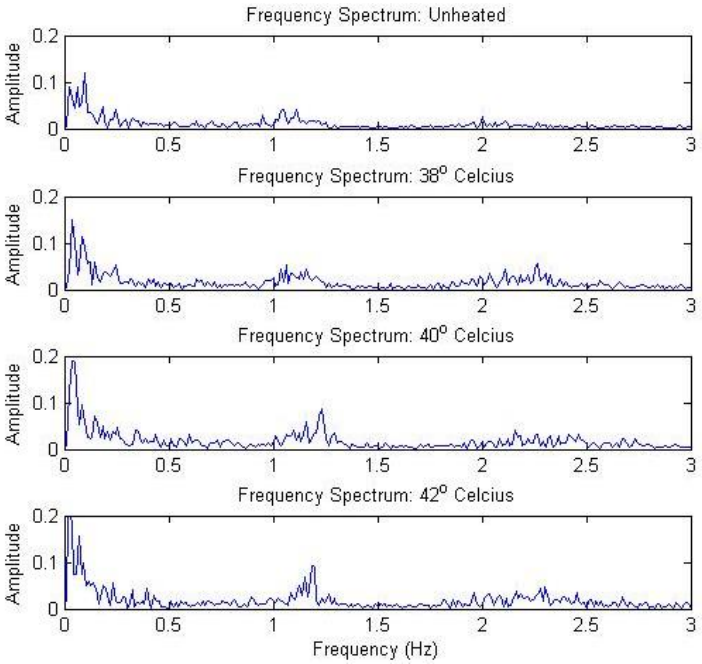

Subject L14:

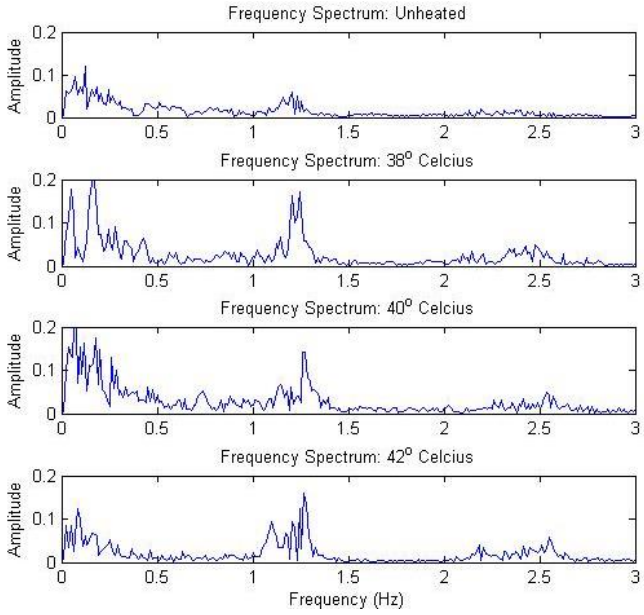

Subject M2:

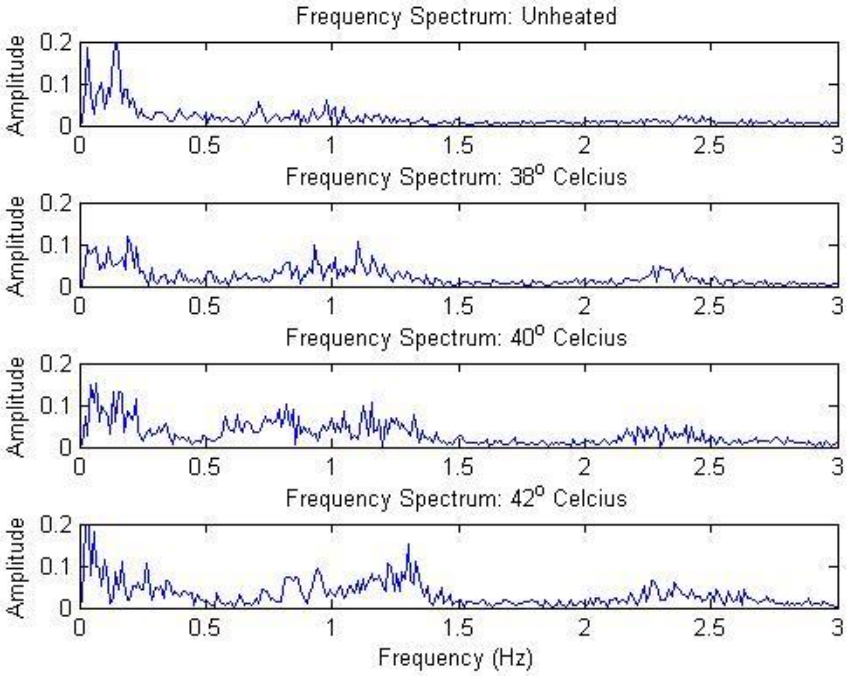

Subject M13:

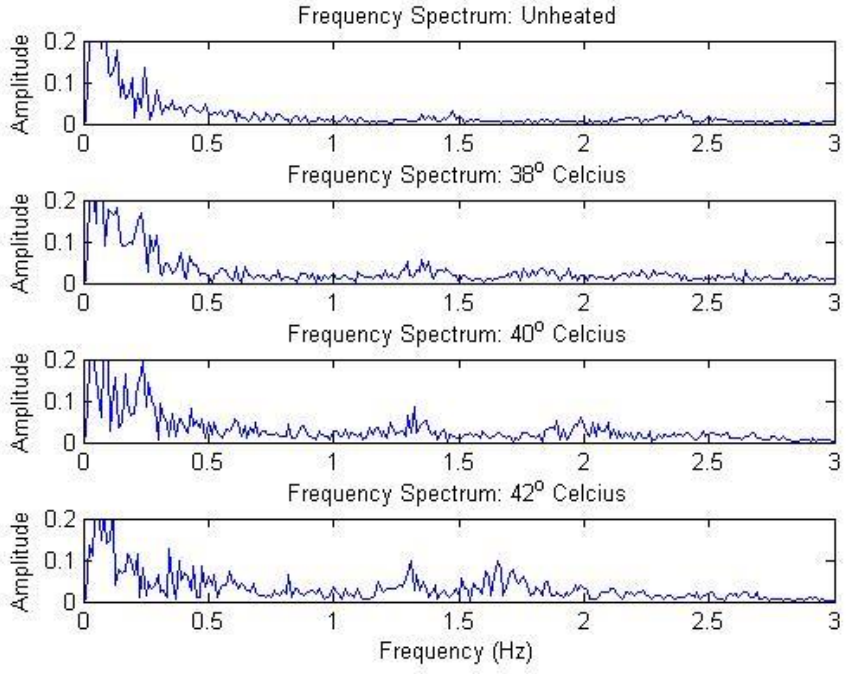

Subject N7:

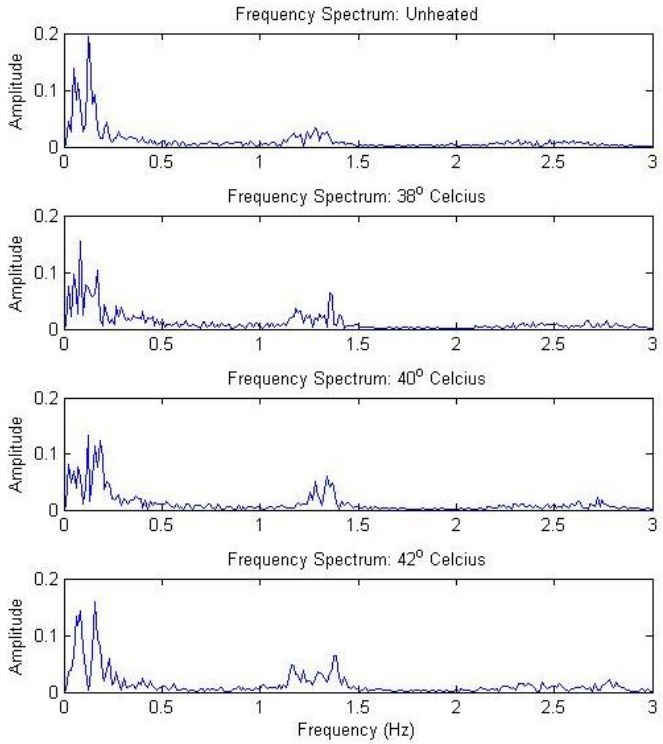

Subject O5:

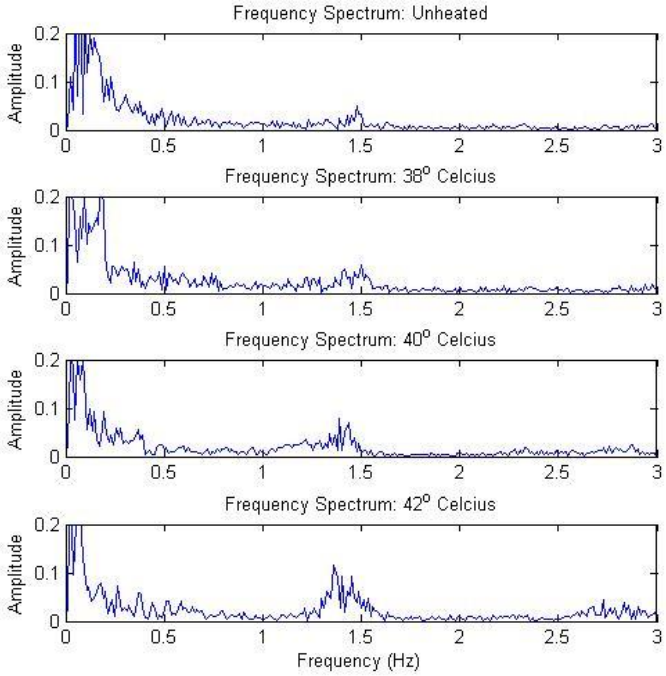

Subject P15:

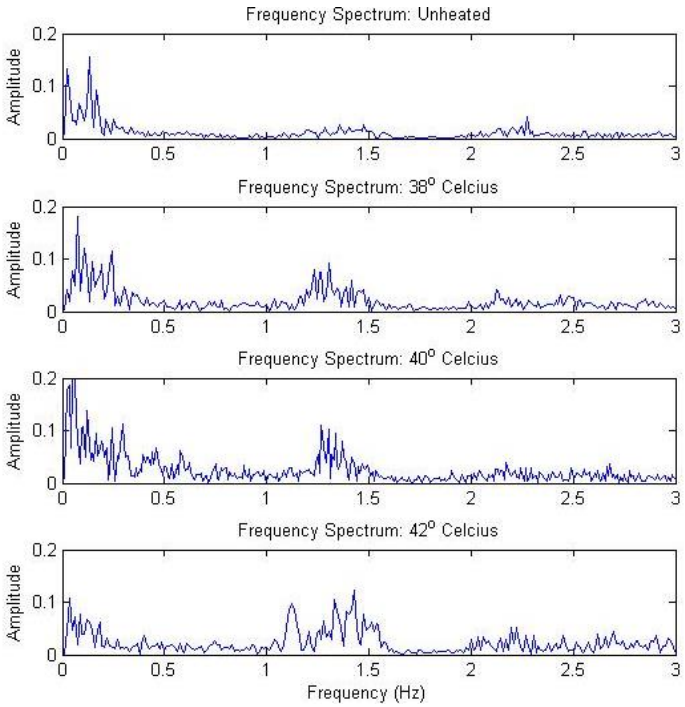

Subject T10:

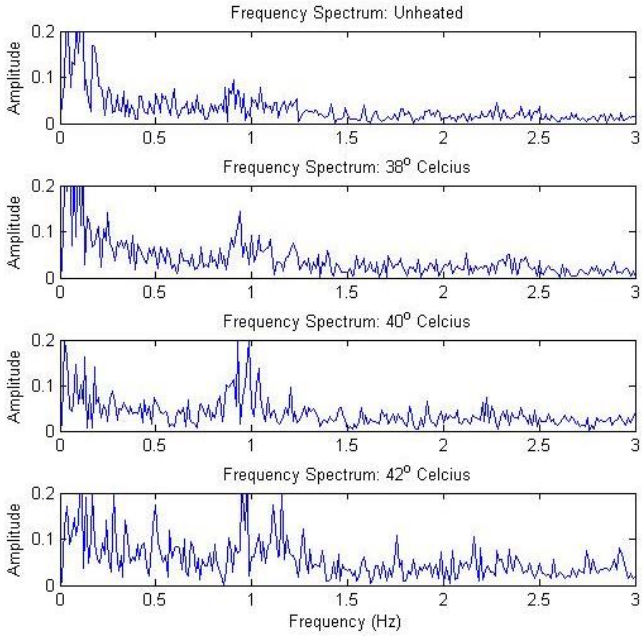

Appendix K: Applied Pressure Frequency Spectra

Subject B6:

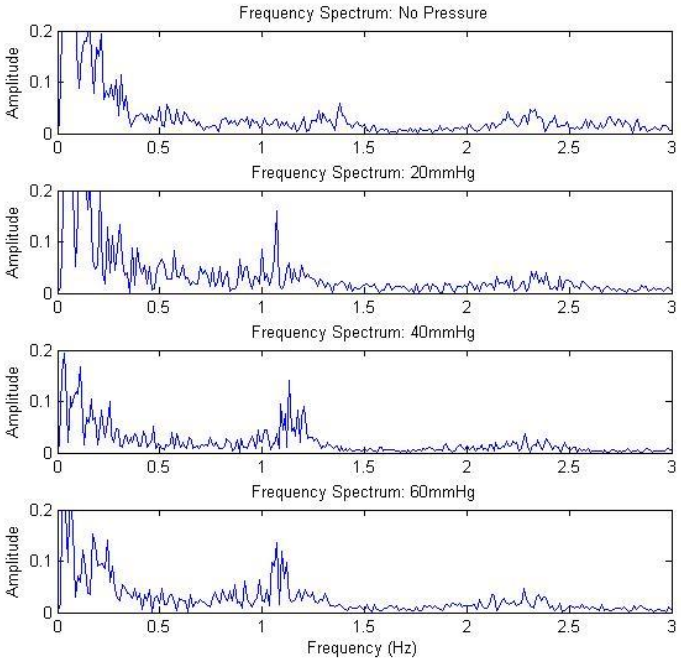

Subject C11:

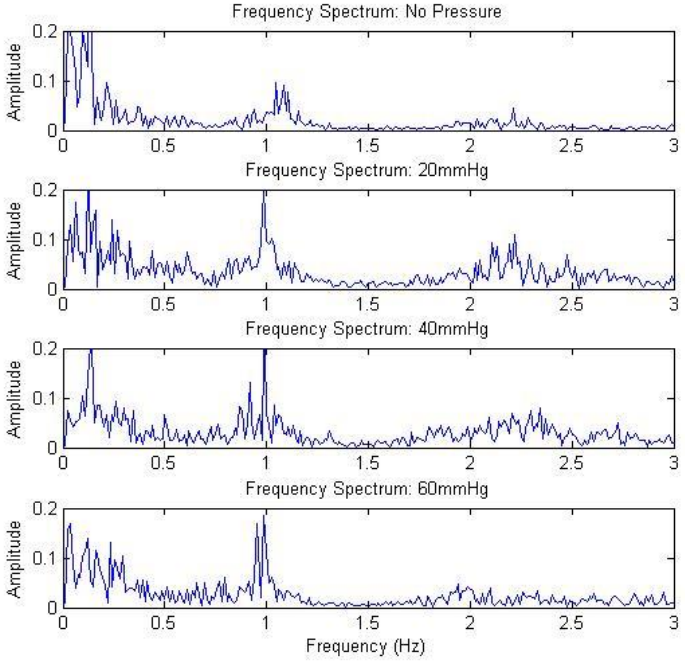

Subject E8:

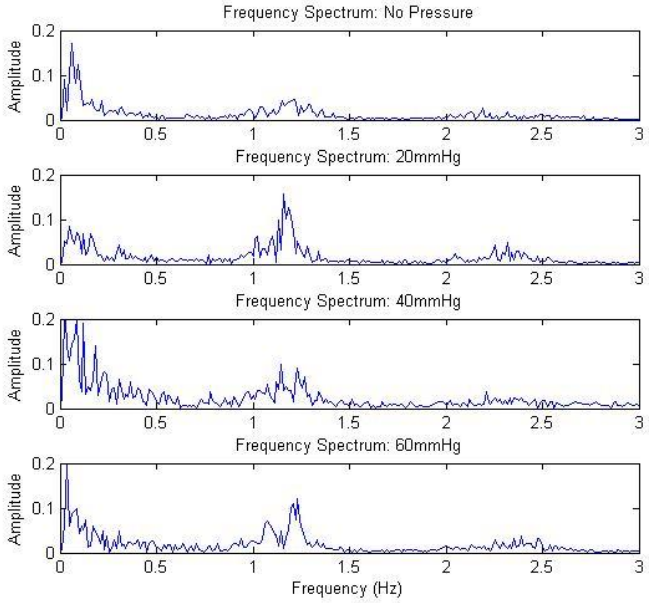

Subject F1:

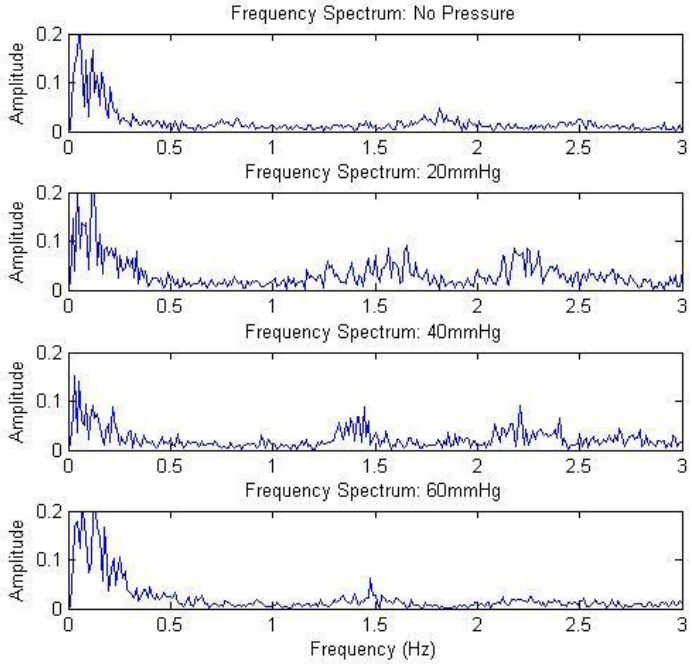

Subject G9:

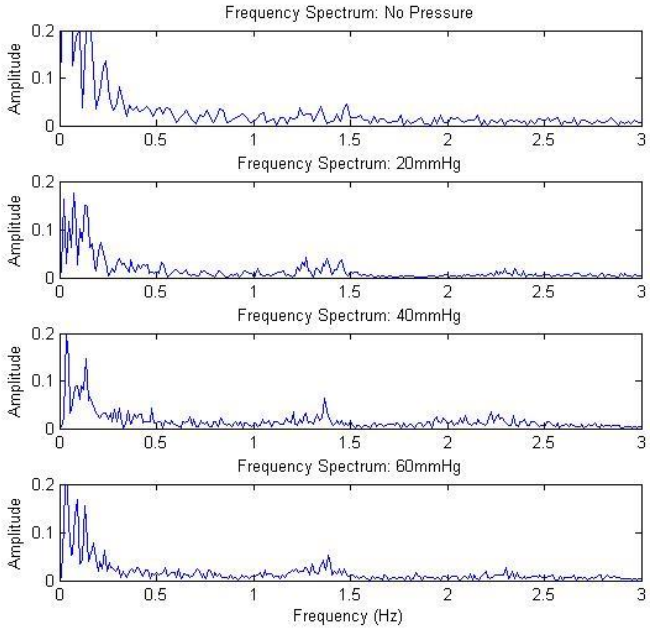

Subject J4:

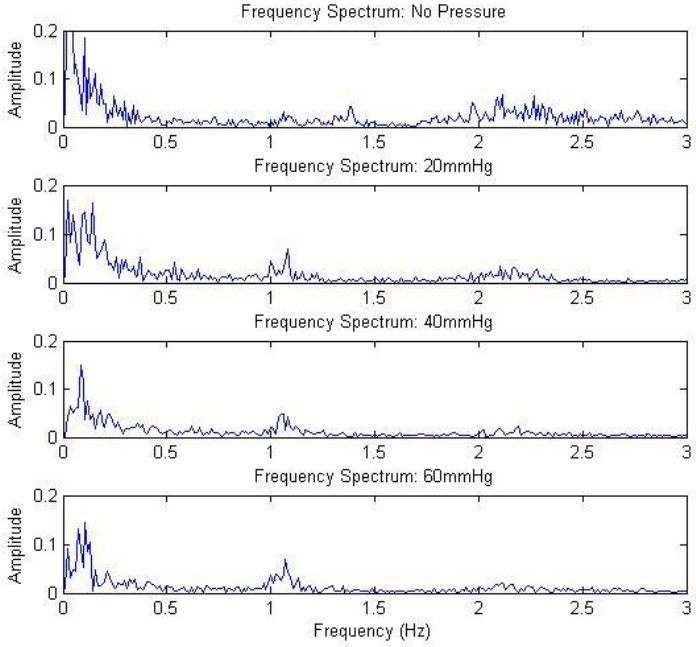

Subject K:

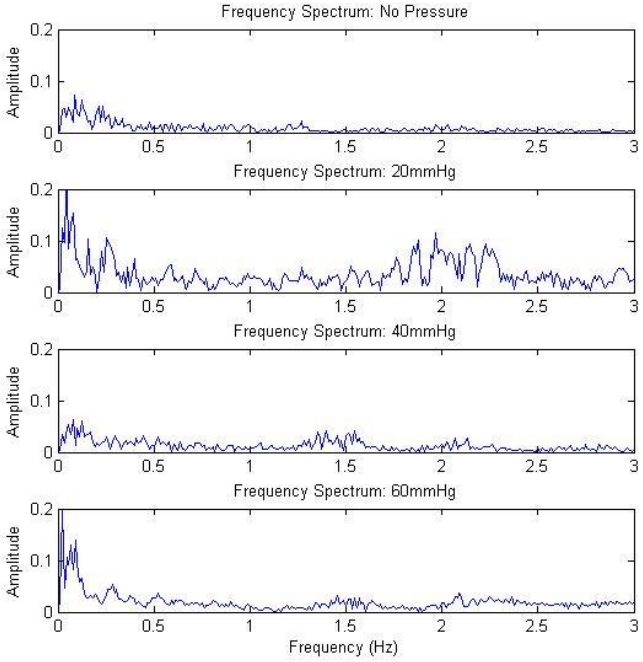

Subject K12:

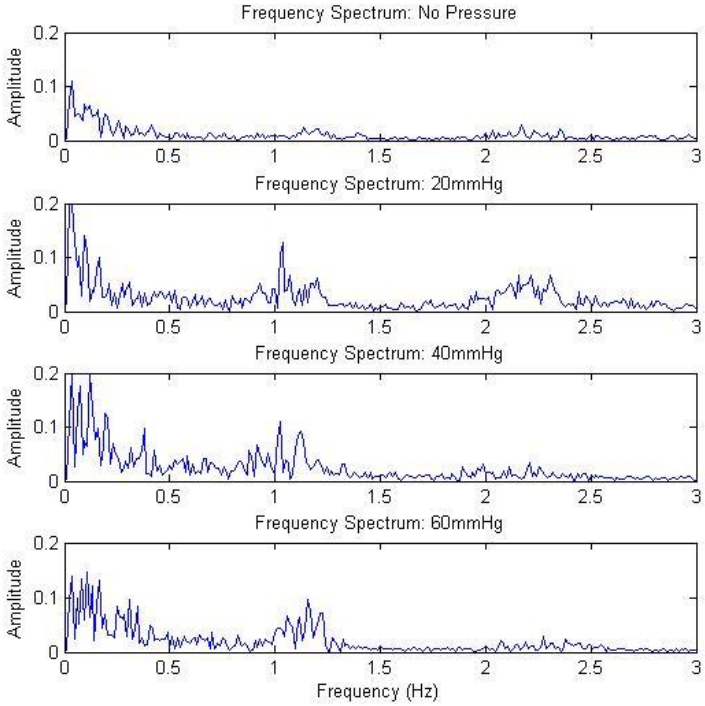

Subject L14:

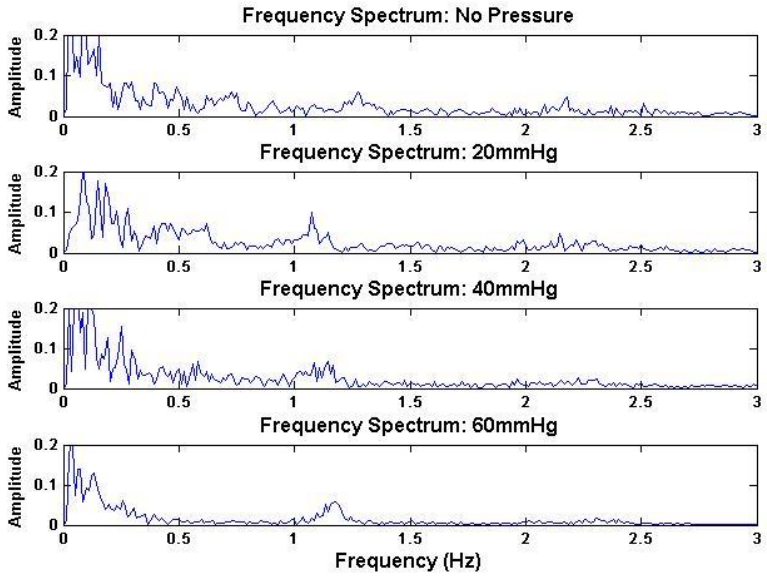

Subject M2:

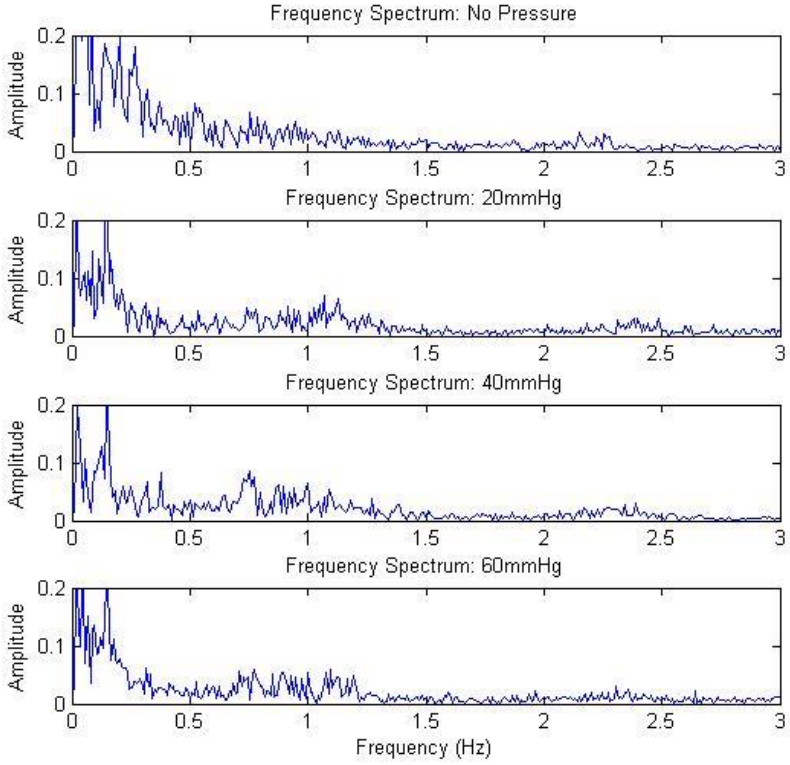

Subject M13:

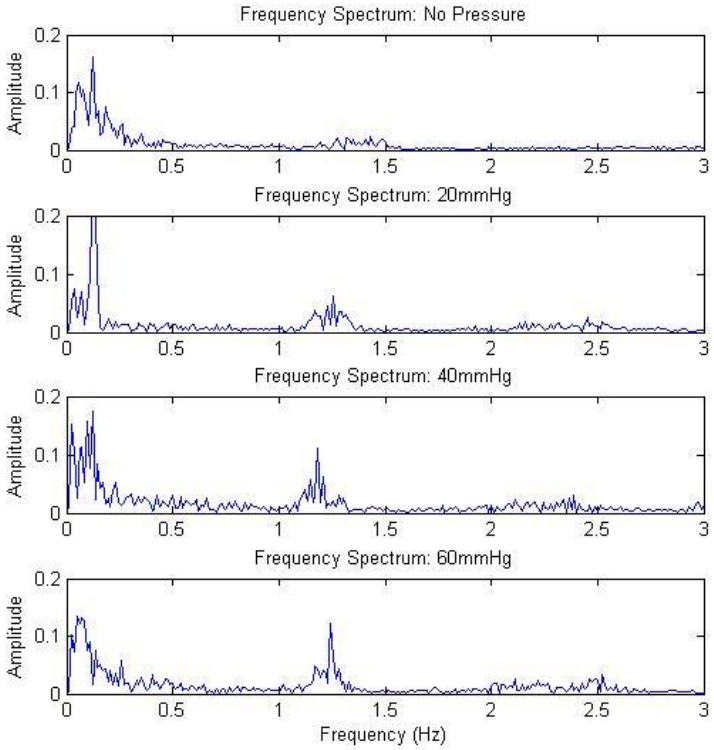

Subject N7:

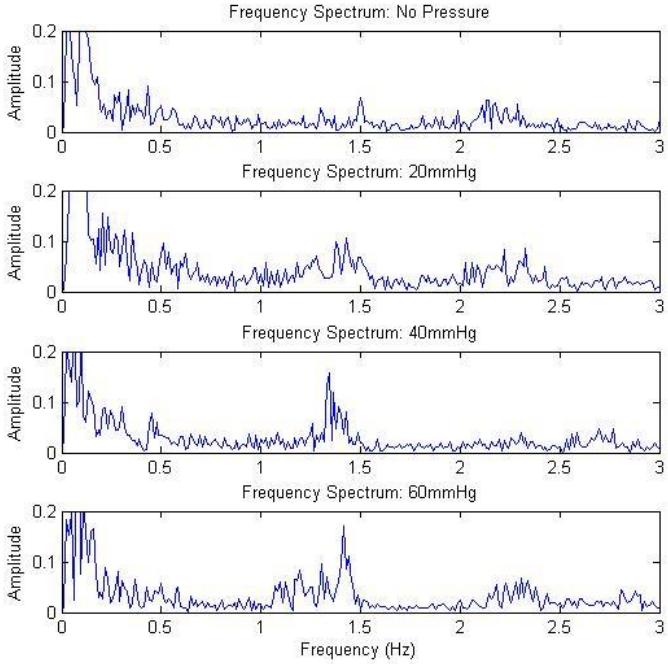

Subject O5:

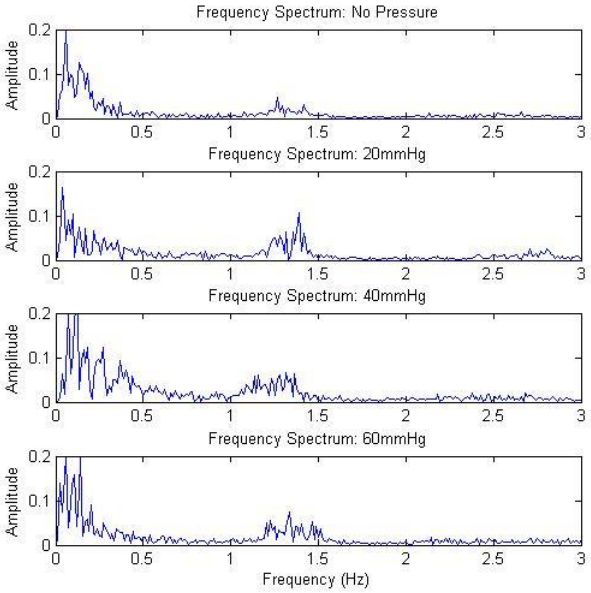

Subject P15: